



NARODOWE CENTRUM BADAŃ JĄDROWYCH
National Centre for Nuclear Research

MONOGRAFIE NCBJ

**Understanding the Nucleon's Spin Structure
The Direct Gluon Polarisation Measurement
at the COMPASS Experiment**

Krzysztof Kurek

National Centre for Nuclear Research

Theoretical Physics Department

D. Sc. Thesis

Świerk, November 2011

Abstract

A modern understanding of the nucleon's spin structure is presented. Polarisation dependent deep inelastic experiments have shown that the helicity contribution of quarks to the nucleon spin is much smaller than expected from the simple quark model. This observation and the role of the triangle anomaly lead to the conclusion that gluons - if strongly polarised, might solve the spin problem of the nucleon. Therefore a direct gluon polarisation measurement is the one of main goals of the COMPASS experiment spin physics programme. Gluon polarisation is determined from the longitudinal double spin asymmetry in the scattering of 160 GeV polarised muons off a polarised ${}^6\text{LiD}$ and a polarised proton target. The gluons are accessible by the selection of photon-gluon fusion events. The well-known processes to tag the photon-gluon fusion events in the energy range covered by the COMPASS experiment are: the production of open-charm D^0 mesons and of light hadron pairs with large transverse momenta. A special emphasis is put on a Neural Network approach that has been widely used in both gluon polarisation determination methods. Thanks to a weighting method and the Neural Network used in the signal selection, as well as in the parameterization of an analyzing powers, the statistical precision of the results is significantly increased. The application of Next-to-Leading Order Quantum Chromodynamics corrections to the polarisation dependent and polarisation averaged partonic cross sections for open-charm production is discussed. These higher order contributions are non-negligible in the COMPASS kinematical domain. New results for the gluon polarisation, including these contributions, are obtained. The results strongly support the hypothesis, that the gluons inside the nucleon are weakly or not polarised. Therefore, the possible importance of quark and gluon angular momenta are also discussed. Combining new results obtained in a Lattice Quantum Chromodynamics approach, the possible scenario of the nucleon spin decomposition as a sum of the valence quarks helicity and the orbital angular momentum of the gluons is discussed. The new concept that the presence of the angular momentum of quarks inside nucleon is related to the spatial deformation of the quark densities in the transverse plane is also reviewed.

Table of contents

1	Spin degrees of freedom	1
2	Longitudinal spin structure of the nucleon	7
2.1	Measurement of the inclusive asymmetry A_1 and structure function g_1	7
2.1.1	Spin-dependent DIS cross section	7
2.1.2	Longitudinal double-spin asymmetry	15
2.1.3	The polarisation dependent structure function g_1	17
2.2	Decomposition of the nucleon spin	25
2.2.1	The Bjorken and Ellis-Jaffe sum rules	25
2.2.2	The triangle anomaly and the role of gluons	30
2.3	The Gerasimov-Drell-Hearn sum rule	34
2.4	Semi-inclusive asymmetries and the flavour separation	35
2.5	Summary of the nucleon's longitudinal spin structure	46
3	Transverse spin structure of the nucleon	48
3.1	Transversity PDF, Collins and Sivers asymmetries	48
3.2	Catalogue of twist-2 parton distribution functions	59
3.3	Summary of the TMDs and transverse spin structure of the nucleon	66
4	COMPASS experimental set-up	68
5	Open-charm analysis with an Artificial Neural Network	73
5.1	Spin cross section asymmetry for D meson production	75
5.2	Data selection	78

5.3	The weighted analysis	85
5.3.1	Asymmetry determination	85
5.3.2	Parameterization of the analysing power	89
5.3.3	The signal purity	91
5.4	Results	96
5.4.1	Leading Order results for the gluon polarisation	97
5.4.2	Open-charm asymmetry in kinematic bins	101
5.4.3	NLO QCD corrections for spin-dependent charm muoproduction	107
5.5	The D^0 and \bar{D}^0 meson production asymmetry	115
5.6	Summary of the gluon polarisation measurement from open-charm D meson production	118
6	Determination of the gluon polarization from DIS events with high-p_T hadron pairs	120
6.1	Spin cross section asymmetry for high- p_T hadron pairs	122
6.2	Data sample and event selection	126
6.3	The analysis method	127
6.4	Monte-Carlo simulations and ANN training	128
6.5	Systematic studies	131
6.6	The gluon polarisation results	134
6.7	Summary of the gluon polarisation measurement	136
7	The spin structure of the nucleon; GPDs and orbital motion	138
7.1	Transverse distortion, QCD lensing and the Sivers effect	141
7.2	Controversy on the definition of orbital and total angular momentum	144
7.3	Lattice QCD results	146
8	Summary and outlook	151
9	Appendices	155
9.1	The helicity dependent DIS cross sections	155
9.2	A Neural Network approach	156

9.3	NLO QCD fits of $g_1(x, Q^2)$ updated with the NLO open-charm result on $\Delta G/G$	158
9.4	Angular momentum operator in QED	159
	Bibliography	161
	Acknowledgements	1

Chapter 1

Spin degrees of freedom

Spin is a fundamental degree of freedom originating from a space-time symmetry. It plays a critical role in determining the basic structure of fundamental interactions. Spin is a relativistic, quantum object. Effects related to spin survive also in the high-energy limit. Spin also provides an opportunity to probe the inner structure of composite systems such as the nucleon. After more than 25 years of measurements of the spin-dependent structure functions of the nucleon the third generation of polarised experiments is now running and delivering more precise data. Although our knowledge about the spin decomposition in the frame of quark parton model (QPM) and Quantum Chromodynamics (QCD) is now more complete and the polarisation dependent parton distribution functions (polarised PDFs) are better constrained by data, the driving question for QCD spin physics still has no answer: where does the nucleon spin come from? Pioneering experiments on the spin structure were performed in the seventies at SLAC [1]. The famous EMC double spin asymmetry measurement [2] and the naive interpretation of the results based on the Ellis-Jaffe sum rule [3] have introduced the so-called "spin crisis" to Particle Physics : quark spins carry only a small fraction of the nucleon helicity. A lot of theoretical work has been done to understand the spin crisis in the framework of QCD, e.g. higher order corrections to the Ellis-Jaffe sum rule [4].

The quark helicity distributions $\Delta q_i(x, Q^2)$ are related to the vector-axial quark current. This current is not conserved due to the Adler-Bell-Jackiw anomaly [5]. The anomaly can explain the spin crisis by changing the interpretation of the measurement: instead of the quark spin content $\Delta\Sigma = \int_0^1 \sum_{i=1}^{n_f} \Delta q_i(x, Q^2) dx$ the flavor-singlet axial current matrix el-

ement $a_0 = \Delta\Sigma - \frac{3\alpha_s}{2\pi}\Delta G$ is measured, where $\Delta G = \int_0^1 \Delta G(x, Q^2)dx$ is a gluon helicity inside the nucleon. The spin crisis can be then avoided if ΔG is large enough. This interpretation was the driving force in the preparation of a series of new polarisation dependent Deep Inelastic Scattering (DIS) experiments dedicated to the precise measurement of parton helicity distributions, transverse nucleon structure, and to the direct measurements of gluon polarization: HERMES [6] at DESY, SMC [7] and COMPASS [8] at CERN, E155 [9] at SLAC and CLAS [10] at JLAB. The collider experiments STAR [11] and PHENIX [12] at RHIC measure the gluon polarisation by observing helicity asymmetries for hadrons and jets in polarised proton-proton collisions. In the light of the results obtained by these new spin-dependent experiments the role of the axial anomaly seems to be marginal as data prefer the gluon helicity contribution to the nucleon's spin to be small.

Beside the quark and gluon helicities, also Orbital Angular Momenta (OAM) can contribute the nucleon spin structure. The definition of the angular momentum of quarks and gluons, both orbital and total, is a very delicate and nontrivial topic. It should be gauge invariant and expressed in terms of well defined local QCD operators built from quark and gluon fields. A possible solution was recently been proposed [13] although also this approach has difficulty [14]. The presence of OAM inside nucleon requires the extension of the usual QPM beyond the longitudinal approximation.

Complementary measurements to the longitudinal spin structure of the nucleon are performed on transversely polarized targets. New polarisation dependent parton distribution functions called "transversity" are associated with such a "transverse" spin nucleon structure. They are defined by the difference between quark (antiquark) distributions for two different spin projection orientations relative to the transversely polarised target. Transversity probes the relativistic nature of quarks. For models with non-relativistic quarks there is no difference of the helicity and transversity distributions due to rotation symmetry. Relativistic quarks make a difference (relativistic Lorentz boosts and rotations don't commute) which can be easily calculated in relativistic models. A good "textbook" example is the MIT bag model (see e.g.[15]). This model explains why $\Delta\Sigma \sim 0.6$ is below the naive expectation $\Delta\Sigma = 1$ and predicts the reduction factor of about 0.83 for transversity. There is no transversity analog of the gluon helicity distribution due to angular momentum conservation (the nucleon spin decomposition in the case of transversity does not contain gluons). Because transversity is a C-odd and chiral-odd distribution it cannot be accessed in inclusive DIS experiments. The Collins effect [16] uses the spin-dependent part of the hadronization process as a "polarimeter". The Collins chiral-odd and T-even fragmentation functions are associated with a correlation between the transverse momentum of the produced hadron and the transversely oriented fragmenting quark spin. The semi exclusive processes with observed

e.g. ρ mesons are also considered to be a good reactions for accessing transverse structure of the nucleon. In proton-proton collisions there is a possibility to study transversity function measuring double transverse spin asymmetry (but the effect is "double" small comparing to DIS single spin asymmetry measurement), and an azimuthal distribution of hadrons in jets. The Drell-Yan (DY) lepton pair production seems to be also interesting process. The observation of the Collins effect requires the non-zero Collins fragmentation function. The existence of this finite fragmentation function has measured by BELLE Collaboration in e^+e^- collisions at KEK accelerator [17].

To go beyond the collinear approximation in the QPM, the transverse internal momentum of partons inside the nucleon, k_\perp , should be taken into account in the description of the nucleon structure. Transverse Momentum Dependent parton distribution functions (TMDs) are necessary in generalized decomposition of the semi inclusive cross sections, when azimuthal angle and internal k_\perp are considered. They are mostly accessed via measurements of spin-dependent in particle production at experiments with transversely polarised targets. The interpretation of the TMDs in the framework of the QPM is not straightforward. TMDs describe different types of correlations between transverse spin projection (of quarks or the nucleon) and transverse momentum of quarks. The Boer-Mulders function, for example, quantifies the correlation between quark spin and quark transverse momentum (or the correlation between quark spin and quark orbital angular momentum) and describes transversely polarised quarks inside unpolarised nucleon. This function is accompanied by the kinematical Cahn effect - a reflection of the presence of the k_\perp inside unpolarised nucleon. The Sivers function links quark (parton) internal motion to the nucleon spin inside transversely polarised nucleon. This function describes unpolarised quarks inside transversely polarised nucleon. Another example is the convolution of twist-two parton distribution from the unpolarised hadron with twist-three quark-gluon correlation function from transversely polarised second hadron, together with a short-distance hard partonic processes calculable in the frame of perturbative QCD, The latter is an example of a possible production mechanism for transverse single-spin dependent asymmetries (SSA) for pions, observed by the FermiLab experiment E704 [18] in proton-antiproton collisions and recently measured in proton-proton interactions at RHIC by STAR [19] and PHENIX [20] experiments and - also for kaons and protons - by BRAHMS [21] experiment. Factorization problem for the TMDs for proton-proton collisions has been discussed in [22]. The so-called Pretzelosity and Worm-Gear functions complete the twist-two QCD description of the structure on the nucleon [23].

The Collins and Sivers effects have been recently measured by HERMES [24] and COMPASS [25, 26] experiments. These results together with SSA measurements suggest the

existence of non-zero TMD functions. Their more precise measurement is thus expected to lead to better understanding of factorization and twist-expansion in QCD. The advantage of studying TMD functions lies in the fact that the leading terms cancel in some of them. This provides the unique opportunity to test higher twist contributions. Usually these contributions are very small compared to the leading terms and difficult to measure experimentally. The role of TMDs in understanding the nucleon spin is, however, not completely clear. Some of them can be related to the existence of the quark OAM and maybe also of gluons. On the one hand precise measurement of the TMDs can thus give insight in the role of OAM. On the other hand the relation between the OAM and TMDs (some of them) is rather qualitative and model dependent [27]. The Sivers function [28] seems to be the most promising. In the Sivers effect, associated with the intrinsic quark transverse momentum in a transversely polarized nucleon, final state interactions produce an asymmetry before the struck quark fragments. The Sivers distribution is chiral-even and T-odd. It is not universal because it is generated via final state interactions in DIS and through initial state interactions in DY process. Technically the Sivers effect requires a correlation of the two QCD amplitudes where two different transverse nucleon spin states produce the same final state. To produce a T-odd effect both amplitudes should have different phases and cannot appear at tree level. In addition, the two different nucleon spin state amplitudes can give a non-zero correlation if there is non-zero OAM of the quarks inside the nucleon (see [15] and references therein).

The interesting idea proposed in [30] introduces the relation between TMDs and a Fourier transform of Generalized Parton Distribution functions (GPDs) [29]. In this approach the Fourier transform of the GPDs can be expressed in terms of an Impact Parameter Distributions (IPDs). The IPDs provide a probabilistic interpretation of GPDs¹. These IPDs are transversely distorted when one considers transversely polarised nucleons (Sivers) or quarks (Boer-Mulders). This distortion together with final state interactions (FSI), called "Chromodynamic lensing", produces a Sivers asymmetry and dynamically generates k_{\perp} of partons inside the nucleon. This elegant idea, if exists in nature, makes it possible to interpret the correlations in transversely polarised nucleon described by TMDs in terms of IPDs and their distortions. On the other hand, TMDs and IPDs contain complementary information about three-dimensional images of the nucleon (nucleon "tomography"): in momenta space (TMDs) and in mixed coordinate-momentum space (IPDs). The higher-twist effects like quark-gluon correlations can also be manifested in quark transverse plane distortions (Boer-Mulders)

The GPDs are related to Total Angular Momentum (TAM) as defined in Ji's sum rule [31]. A possible determination of OAM of quarks and gluons can be based on this sum rule.

¹It is essential for the probabilistic interpretation that skewness parameter $\xi = 0$.

The open question is if the OAM of partons can be related to transverse plane distortion of IPDs. The GPDs can be accessed measuring Deeply-Virtual Compton Scattering process (DVCS). The asymmetries for DVCS process were measured by CLAS [32] - [34], HALL A [38, 39] and HERMES [35, 36] experiments. H1 and ZEUS experiments measured DVCS cross section [37]. These initial data on GPDs have given limited insight and future measurements are eagerly awaited [40, 41, 42].

At present one thus relies on models and lattice QCD calculations. The recent results of the Lattice QCD computations [43, 44, 45] suggest that the OAM of quarks however non-zero for u and d quarks separately, cancels out nearly exactly in the sum. Assuming in addition that gluon polarisation ΔG is close to zero the missing part of the nucleon spin should origin from OAM of gluons. Therefore the measurement of the Sivers function on the gluons should be very interesting. The small gluon polarisation is partially confirmed by the data, however the precision of the measurements of gluon polarisation is still not satisfactory. Moreover, these measurements are in the limited range of the nucleon momentum fraction carried by gluons. The gluon polarisation results obtained from QCD evolution of the precise, inclusive and semi-inclusive DIS data, and from the asymmetries measured at RHIC experiments are also consistent with zero but the obtained error is still very large [46, 47], mainly due to lack of precision data at large Bjorken x region. The improvement of the precision of the gluon polarisation measurement will be a very difficult task, probably possible in the future collider experiment [42].

The Lattice QCD results depend on an initial scale parameter and can be evolved with the help of QCD evolution equations. The evolution of the TAM of quarks shows increase the quark contribution to the nucleon spin when the scale is decreasing. At some particular low scale point ($\mu^2 \simeq 0.18 \text{ GeV}^2$) the Lattice and QCD evolution predict that the spin of the nucleon is fully explained by quarks only. Gluons don't contribute to the nucleon spin budget at this scale. These results agree very well with predictions obtained in the relativistic chiral models, where pion cloud is a significant part of the nucleon structure and gluons are not present.[48, 49]. This agreement shows that Lattice QCD approach links the perturbative QCD regime with the non-perturbative chiral limit of QCD.

In this thesis modern understanding of the nucleon spin structure, based on existing and new experimental and theoretical results, is presented. The main part of the thesis is dedicated to the direct gluon polarisation measurements with the COMPASS experiment. The author was deeply involved in these measurements and had key responsibilities for the data analysis.

In the LO QCD approximation, only the Photon Gluon Fusion (PGF) subprocesses have sensitivity to gluons inside the nucleon. Two of such subprocesses were used in COMPASS:

the production of open-charm D^0 mesons and the production of two hadrons in the final state with relatively high transverse momenta p_T , with respect to the photon direction. New methods using statistical weighting and an Artificial Neural Network (ANN) approach have been developed to increase the statistical precision and to optimize the usage of the collected data.

Gluon polarisation was determined from open-charm muoproduction in LO and NLO QCD approximations. The application of NLO QCD calculations and the modification of the weighted method are discussed in detail in this thesis. The decomposition of double helicity asymmetry decomposition for the high- p_T data samples in the DIS domain with $Q^2 > 1 \text{ GeV}/c^2$ is discussed in LO QCD approximation and the new method to extract gluon polarisation from the measured asymmetries for inclusive and high- p_T events is presented. The new result of the gluon polarisation obtained from the large Q^2 high- p_T hadron pairs is discussed. New gluon polarisation results are presented.

This thesis is organized in the following way: in chapter 2 the longitudinal spin structure of the nucleon is reviewed as it is based on inclusive measurements of the spin-dependent structure function g_1 and on semi-inclusive measurements of the quark helicity distributions in DIS experiments. The role of the axial anomaly, the Operator Product Expansion (OPE) and QCD evolution are also discussed in this chapter. In chapter 3 the recent results of Collins and Sivers effects measurements performed on transversely polarised targets are discussed. The review of the leading TMDs is also presented. The COMPASS experimental setup is shortly described in chapter 4. In chapter 5 the determination of the gluon polarisation from the open-charm D^0 mesons production is discussed in the QCD LO and QCD NLO approximations. Chapter 6 is dedicated to the determination of gluon polarisation determination from high- p_T hadron pairs at large scale Q^2 , $Q^2 > 1 \text{ GeV}^2$. The COMPASS result of the gluon polarisation, obtained from the observation of the high- p_T hadron pairs at low Q^2 , $Q^2 < 1 \text{ GeV}^2$, is also shortly discussed in this chapter. Chapter 7 is dedicated to the interpretation of the Sivers effect in terms of Chromodynamics Lensing. The controversy on the definition of orbital and total angular momentum of quarks and gluons and recent Lattice QCD results for the spin structure of the nucleon are discussed. The summary and concluding remarks are in chapter 8.

The convention of units used in the reminder of this thesis is: $\hbar = c = 1$.

Chapter 2

Longitudinal spin structure of the nucleon

A description of the longitudinal nucleon spin structure in the framework of the QPM with QCD as a theory of parton interactions is presented in this chapter. A short review of the experimental results on the polarisation dependent structure functions and on the helicity distributions of quarks and gluons is given. QCD evolution and corrections to the naive QPM approach are discussed. It is shown that the inclusive as well as the semi-inclusive polarised data obtained by different experiments agree well and lead to the intriguing observation that quarks are responsible for not more than 1/3 of the nucleon spin.

The review of the experimental results is far from being complete. The selected results showed here are used to illustrate the modern understanding of the spin structure of the nucleon.

2.1 Measurement of the inclusive asymmetry A_1 and structure function g_1

2.1.1 Spin-dependent DIS cross section

Our present knowledge about the structure of the nucleon in the perturbative regime (large probing scales) comes mostly from DIS experiments. A point-like lepton projectile interacts with a target particle via the exchange of photons and weak bosons which penetrate the internal structure of the nucleon. The energy range covered by fixed-target experiments like COMPASS is not large enough to have a significant fraction of the subprocesses with an exchange of the W and Z bosons between lepton and the nucleon. The interference between

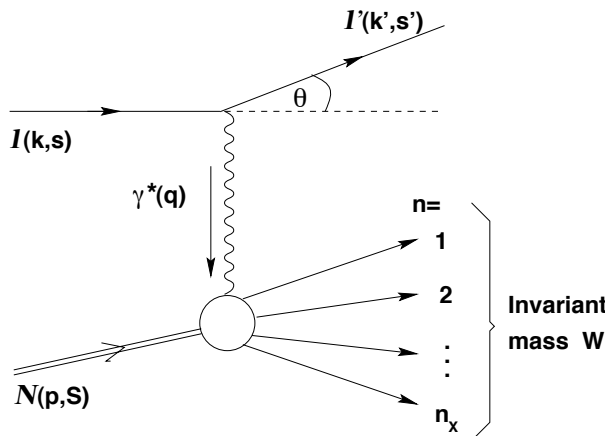


Figure 2.1: Inelastic scattering $lN \rightarrow l'X$ in one-photon approximation.

γ and Z bosons are also negligible. The probability of double-photon exchange as a higher order QED correction is very small and can be neglected, except the case of heavy targets [50]. The other QED corrections: real photon emissions from the lepton and virtual/soft corrections are taken into account in a radiative corrections scheme used by the experimental groups to correct their results and to present them as one-photon data (e.g.[51]). The weak interactions become important for larger Center-of-Mass-System (CMS) energy in collider experiments ZEUS and H1 at HERA. Since all spin-dependent DIS experiments are thus far the fixed-target experiments the one-photon exchange is a very good approximation. The virtuality of the exchanged photon, Q^2 , is usually considered as the perturbative scale and the DIS perturbative regime is defined by $Q^2 > 1 \text{ GeV}^2$. The perturbative scale can be defined not only by the photon virtuality but also by other momenta or large masses in the system. A good example is photo-production of heavy flavour where the mass of the heavy quark pair forms the perturbative scale while the photon virtuality can be close to zero. Photo-production of high- p_T hadrons belongs to the same category; here the perturbative scale is defined by the large p_T of the hadron(s) observed in the final state. In these cases it is more convenient to speak of Inelastic Scattering rather than Deep Inelastic Scattering, nevertheless the presence of a hard scale allows one to probe the internal nucleon structure described by Quark Parton Model (QPM) and perturbative QCD. Instead of the photon a virtual heavy quark or a quark with high p_T is the "hard" probe here. The DIS process is shown schematically in Fig. 2.1

To describe the inclusive DIS cross section at the CMS energy, \sqrt{s} , in the one-photon approximation it is enough to use two independent Lorentz invariant variables. They can be chosen as: Q^2 , the virtuality of the photon and, the virtual photon energy transferred to

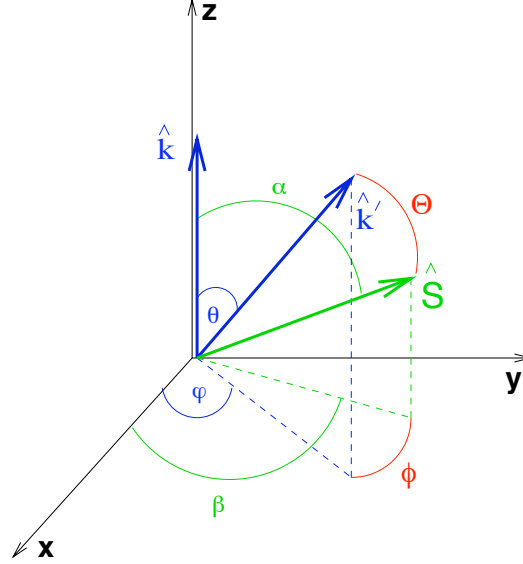


Figure 2.2: The Definition of angles in the laboratory frame (Figure from [52]).

the nucleon:

$$-Q^2 = q^2 = (k - k')^2 \stackrel{lab}{=} 2(|\tilde{\mathbf{k}}||\tilde{\mathbf{k}}'| \cos \theta - EE' + m^2), \quad (2.1)$$

$$\nu = \frac{p \cdot q}{M} \stackrel{lab}{=} E - E', \quad (2.2)$$

where the momenta of the incoming and outgoing lepton, cf. Fig. 2.1, are:

$$k^\mu = (E, \tilde{\mathbf{k}}) \stackrel{lab}{=} (E, 0, 0, |\tilde{\mathbf{k}}|), \quad (2.3)$$

$$k'^\mu = (E', \tilde{\mathbf{k}}') \stackrel{lab}{=} (E', |\tilde{\mathbf{k}}'| \sin \theta \cos \varphi, |\tilde{\mathbf{k}}'| \sin \theta \sin \varphi, |\tilde{\mathbf{k}}'| \cos \theta). \quad (2.4)$$

The definition of the angles in the laboratory frame (the rest frame of the nucleon) is shown in Fig. 2.2.

Instead of Q^2 and ν the two dimensionless variables: x , the Bjorken scaling variable and y , the virtual photon energy fraction transferred to the nucleon, can be defined:

$$x = \frac{Q^2}{2p \cdot q} \stackrel{lab}{=} \frac{Q^2}{2M\nu}, \quad y = \frac{p \cdot q}{p \cdot k} \stackrel{lab}{=} \frac{\nu}{E}. \quad (2.5)$$

The interpretation of the Bjorken x variable ($0 < x \leq 1$) was first given within the framework of the Quark Parton Model by Feynman [53]: it corresponds to the fraction of the nucleon

momentum carried by the parton interacting with the virtual photon.¹ The helicity of the incoming lepton can be defined with the help of the four-vector s^μ such that it is orthogonal to the lepton momentum $s \cdot k = 0$ and is normalised so that $s^2 = -1$:

$$s^\mu \stackrel{lab}{=} h_l \frac{1}{m} (|\tilde{\mathbf{k}}|, 0, 0, E), \quad (2.6)$$

where $h_l = \pm 1$ is the lepton helicity and m denotes its mass. Since the nucleon is at rest, it can be polarised in any arbitrary direction, cf. Fig. 2.2:

$$S^\mu \stackrel{lab}{=} (0, \sin \alpha \cos \beta, \sin \alpha \sin \beta, \cos \alpha). \quad (2.7)$$

The spin four-vector of the target S^μ satisfies $S \cdot p = 0$ and $S^2 = -1$.

The DIS inclusive cross section can be decomposed into leptonic and hadronic parts as follows:

$$\frac{d\sigma}{dE'd\Omega} = \left(\frac{E'}{M\nu} \right) \frac{d\sigma}{dx dy d\varphi} = \left(\frac{Q^2 E'}{y M \nu} \right) \frac{d\sigma}{dx dQ^2 d\varphi} = \frac{e^4}{16\pi^2 Q^4} \frac{E'}{ME} L_{\mu\nu} W^{\mu\nu}, \quad (2.8)$$

where $\Omega(\theta, \varphi)$ is the solid angle of the lepton scattered from the nucleon target. The leptonic tensor $L_{\mu\nu}$ in general is a sum of symmetric and antisymmetric parts, calculable in QED:

$$L^{\mu\nu} = L_{(S)}^{\mu\nu} + iL_{(A)}^{\mu\nu}, \quad (2.9)$$

where

$$L_{(S)}^{\mu\nu} = 2k'^\mu k^\nu + 2k'^\nu k^\mu + 2(m^2 - k' \cdot k)g^{\mu\nu}, \quad (2.10)$$

$$L_{(A)}^{\mu\nu} = -2m\epsilon^{\mu\nu\rho\sigma} q_\rho s_\sigma, \quad (2.11)$$

with $\epsilon^{\mu\nu\rho\sigma}$ - the antisymmetric Levi-Civita tensor. Only the antisymmetric part of $L^{\mu\nu}$ depends on the lepton spin four-vector s^μ . The hadronic tensor $W^{\mu\nu}$, which describes the internal structure of the hadron, can also be written as a sum of symmetric and antisymmetric parts:

$$W^{\mu\nu} = W_{(S)}^{\mu\nu} + iW_{(A)}^{\mu\nu}. \quad (2.12)$$

The most general form of the hadronic tensor $W^{\mu\nu}$ depends on non-perturbative QCD dynamics and cannot be calculated directly. However, It can be written in terms of the variables p^μ , q^μ , S^μ , $g^{\mu\nu}$ and $\epsilon^{\mu\nu\rho\sigma}$ and can be parameterized by certain hadron spin-averaged and spin-dependent structure functions, that respect the Lorentz covariant structure, gauge

¹This nice interpretation (simple consequence of the energy-momentum conservation law) is correct only if the QCD corrections can be absorbed into an effective definition of the structure functions; it is not true e.g. for the PGF process.

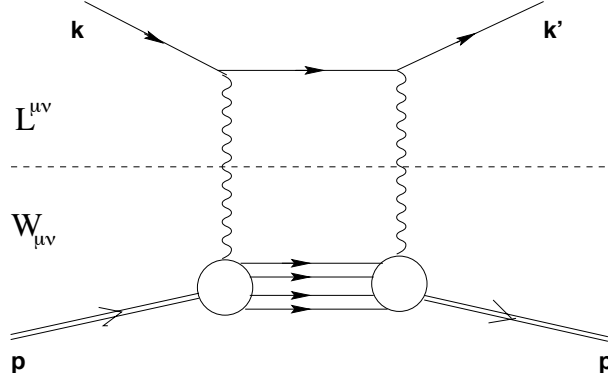


Figure 2.3: The squared amplitude for lepton-nucleon inelastic scattering and its factorisation into leptonic and hadronic tensors $L_{\mu\nu}$ and $W^{\mu\nu}$.

invariance, parity and time reversal invariance, and electromagnetic current conservation ($q_\mu L^{\mu\nu} = 0$ and $q_\mu W^{\mu\nu} = 0$) [54, 15]. To parameterize the hadronic tensor $W^{\mu\nu}$ four independent structure functions are used: F_1 and F_2 are unpolarised and g_1 and g_2 are polarisation dependent [54]. Each of them depends on two independent kinematic variables, e.g. (x, Q^2) , but the explicit dependence will be omitted here for simplicity of the notation. The symmetric and antisymmetric terms of $W^{\mu\nu}$ are given by:

$$W_{(S)}^{\mu\nu} = -g^{\mu\nu} F_1 + \frac{F_2}{p \cdot q} p^\mu p^\nu, \quad (2.13)$$

$$W_{(A)}^{\mu\nu} = g_1 \frac{M}{p \cdot q} \epsilon^{\mu\nu\lambda\delta} q_\lambda S_\delta + g_2 \frac{M}{(p \cdot q)^2} \epsilon^{\mu\nu\lambda\delta} q_\lambda (p \cdot q S_\delta - S \cdot q p_\delta), \quad (2.14)$$

in which terms proportional to q_μ, q_ν have been omitted since $q_\mu L^{\mu\nu} = 0$.

The Lorentz invariant differential cross section for polarised inelastic lepton-nucleon inclusive scattering is then given by :

$$\begin{aligned} \frac{d\sigma}{dx dQ^2 d\phi} &= \frac{e^4 y^2}{16\pi^2 Q^6} \left(2Q^2 \left(1 - \frac{2m^2}{Q^2} \right) F_1 + 4M \left(\frac{E'}{y} - \frac{Q^2}{4Ey} \right) F_2 \right. \\ &+ 4mM^2 Ey \left[\frac{(s \cdot q)(S \cdot q)}{(p \cdot q)(p \cdot q)} + 2x \frac{(s \cdot S)}{p \cdot q} \right] g_1 \\ &\left. + 4mMQ^2 \left[\frac{s \cdot S}{p \cdot q} - \frac{(s \cdot p)(S \cdot q)}{(p \cdot q)(p \cdot q)} \right] g_2 \right). \end{aligned} \quad (2.15)$$

In a fixed target laboratory frame with the angles defined as in Fig.2.2 the polarised lepton-nucleon inclusive scattering cross section can be written as a sum of a spin-averaged term $\bar{\sigma}$

and a spin-dependent term $\Delta\sigma$, which can be further decomposed in $\Delta\sigma_{\parallel}$ and $\Delta\sigma_T$:

$$\sigma = \bar{\sigma} - \frac{1}{2}h_l\Delta\sigma = \bar{\sigma} - \frac{1}{2}h_l(\cos\alpha\Delta\sigma_{\parallel} + \sin\alpha\cos\phi\Delta\sigma_{\perp}), \quad (2.16)$$

where:

$$\bar{\sigma} \equiv \frac{d^3\bar{\sigma}}{dx dQ^2 d\phi} = \frac{e^4 y}{4\pi^2 Q^4} \left[\frac{y}{2} \left(1 - \frac{2m^2}{Q^2}\right) F_1 + \frac{1}{2xy} \left(1 - y - \frac{\gamma^2 y^2}{4}\right) F_2 \right], \quad (2.17)$$

$$\Delta\sigma_{\parallel} \equiv \frac{d^3\Delta\sigma_{\parallel}}{dx dQ^2 d\phi} = \frac{e^4 y}{4\pi^2 Q^4} \left[\left(2 - y - \frac{\gamma^2 y^2}{2} - \frac{2m^2}{Q^2} y^2\right) g_1 - \gamma^2 y g_2 \right], \quad (2.18)$$

$$\Delta\sigma_T = \cos\phi\Delta\sigma_{\perp} \equiv \frac{d^3\Delta\sigma_T}{dx dQ^2 d\phi} = \cos\phi \frac{e^4 y}{4\pi^2 Q^4} \gamma \sqrt{1 - y - \frac{\gamma^2 y^2}{4}} \left[y \left(1 + \frac{2m^2}{Q^2} y\right) g_1 + 2g_2 \right]. \quad (2.19)$$

Here $\gamma = \frac{2Mx}{\sqrt{Q^2}} = \frac{2Mx}{Q} = \frac{Q}{Ey}$. The cross sections $\Delta\sigma_{\parallel}$ and $\Delta\sigma_{\perp}$, given by Eqs (2.18, 2.19) can only be measured in experiments with a polarised target and a polarised beam. They refer to the two configurations where the nucleon spin is (anti) parallel or orthogonal to the lepton momentum direction and have been determined up to terms of order m^2/Q^2 ($\sim 10^{-7}$ in the SMC and COMPASS kinematic domain). The structure function g_1 is measured in the (anti) parallel configuration, where g_2 is suppressed by a factor γ which is small since the energy of the beam is high, . The structure function g_2 is determined by combination of a measurement of $\Delta\sigma_{\perp}$ with the results on g_1 .

The inclusive polarisation dependent DIS cross section, discussed so far, has been obtained for a nucleon target with spin 1/2. Among the data collected by high-energy polarised DIS experiments, the data collected on a deuteron target (e.g. SMC and COMPASS polarised targets, [55, 56]) are a significant fraction. Since the deuteron is spin-1 particle, the polarisation dependent cross section formulae for lepton-deuteron inclusive scattering are slightly more complicated; instead of four structure functions, the eight independent structure functions are needed to parameterize the cross section. Since the additional four structure functions, called quadrupole structure functions, b_{1-4} , are very small their contribution can be neglected [57, 58]. The details of the spin-1 target are not further discussed in this thesis. A review of the formulae for the differential cross sections and asymmetries for the nucleon as well as for the deuteron target can be found in [59], where all approximations used in the SMC fixed-target experiment are discussed in detail. It is easy to show that the asymmetry decomposition for nucleon and deuteron targets are the same if the deuteron quadrupole structure functions are neglected.

The g_1 and g_2 structure functions contain all information about the spin structure of the nucleon available in inclusive measurements. The g_1 structure function can be interpreted in terms of the parton helicities. It will be discussed in the next sections in detail. The g_2 structure function is a more complicated object with no direct QPM interpretation. Because of the Optical Theorem the inclusive hadronic tensor $W^{\mu\nu}$ is related to the imaginary part of the forward Compton scattering amplitude. This amplitude can be then expressed in terms of the matrix elements of local operators within Operator Product Expansion (OPE) approach. When $Q^2 \rightarrow \infty$ (light-cone regime) the leading contribution to the forward Compton amplitude comes from the nucleon matrix elements of a tower of gauge invariant, local operators multiplied by Wilson Coefficients. These twist-2 operators are constructed from the quark and gluon fields. The higher-twist operators are suppressed on the light-cone. The OPE is an equation relating operators and does not depend on the states between the operator matrix elements are evaluated. The Wilson coefficients are target independent and may be calculated in the framework of perturbative QCD. The OPE method is more general than the QCD improved QPM and allows one to discuss the asymptotic properties and QCD evolution of the Compton amplitude in terms of Quantum Field Theory (QCD) without the additional assumptions as used in the definition of the QPM. The g_1 and g_2 structure functions can be discussed in the framework of the OPE with a dispersion relations techniques. A set of sum rules for the moments of g_1 and g_2 can be established. In particular the integral over x of the g_2 structure function should vanish for all Q^2 (Burkhardt-Cottingham sum rule, [60]) and g_2 can be split into two parts, the so-called Wandzura-Wilczek part [61], expressed in terms of the twist-2 structure function g_1 and its integral, and the twist-3 part, which contains a non-trivial higher twist contribution and a "transversity" term h_1 (see chapter 3). The higher twist contributions represent quark and gluon correlations in the nucleon. The most precise measurements of the structure function g_2 come from SLAC proton and deuteron experiments (E155 and E143 [62]) and from a JLAB measurement using a ^3He (neutron) target [63]. Since the structure function g_2 measures correlations between quarks and gluons and higher-twist effects, its contribution to the nucleon spin structure is marginal.

Additional details of the OPE method and of the dispersion relations in the context of nucleon spin physics can be found in [64] and [15]. The OPE method is limited to inclusive processes. Semi-inclusive measurements, where some hadrons are observed in the final state, require a description based on so-called "hard factorization" and the QPM. As seen in Fig. 2.3 the final states must be resummed to reduce the Compton amplitude to the matrix elements of the product of two quark currents which can then be decomposed into an OPE series. The observation of the final state hadrons makes this impossible. The other limitation of the use of the OPE concerns experimental input: the measurement of the matrix elements

of the higher-twist operators is still an experimental challenge.

It is convenient to introduce the virtual photon-nucleon cross section before one defines the asymmetry measured in polarisation dependent experiments. Since the virtual photon flux is an ill defined object some convention is needed to define the virtual photon-nucleon cross section. The Hand convention, where the flux K is:

$$K = \frac{W^2 - M^2}{2M} = \nu - \frac{Q^2}{2M}, \quad (2.20)$$

is used in this thesis. The virtual photon-nucleon cross section is obtained from the forward Compton amplitudes, calculated as a contraction of the hadronic tensor $W^{\mu\nu}$ and the virtual photon polarisation vectors. For a spin-1/2 nucleon there are ten helicity amplitudes. Among them only four are independent. This reduction results from conservation of TAM, the time reversal and the parity invariance. The number of these amplitudes is the same as the number of structure functions that parameterize the hadronic tensor $W_{\mu\nu}$. This means that all the structure functions can be expressed as linear combinations of the amplitudes and *vice versa*. The calculations and discussion of the helicity virtual photon-nucleon amplitudes can be found in [57] and [59].

The virtual photon-nucleon cross sections are defined in the following way [57]:

$$\sigma_{3/2}^T = \frac{4\pi^2\alpha}{MK} \mathcal{A}(+1, +\frac{1}{2}; +1, +\frac{1}{2}) = \frac{4\pi^2\alpha}{MK} [F_1 - g_1 + (\kappa - 1)g_2], \quad (2.21)$$

$$\sigma_{1/2}^T = \frac{4\pi^2\alpha}{MK} \mathcal{A}(+1, -\frac{1}{2}; +1, -\frac{1}{2}) = \frac{4\pi^2\alpha}{MK} [F_1 + g_1 - (\kappa - 1)g_2], \quad (2.22)$$

$$\sigma_{1/2}^{TL} = \frac{4\pi^2\alpha}{MK} \mathcal{A}(+1, -\frac{1}{2}; 0, +\frac{1}{2}) = \frac{4\pi^2\alpha}{MK} \sqrt{\kappa - 1} [g_1 + g_2], \quad (2.23)$$

$$\sigma_{1/2}^L = \frac{4\pi^2\alpha}{MK} \mathcal{A}(0, +\frac{1}{2}; 0, +\frac{1}{2}) = \frac{4\pi^2\alpha}{MK} \left[-F_1 + \frac{\kappa}{2x} F_2 \right], \quad (2.24)$$

where $\kappa = 1 + \frac{4x^2 M^2}{Q^2} = 1 + \frac{Q^2}{\nu^2} = 1 + \gamma^2$. Here the subscript is the total spin of the photon-nucleon system and the superscript corresponds to the polarisation of the photon in the initial and the final states.

It is also useful to define the total absorption cross section of longitudinally and transversely polarised photons:

$$\sigma^L = \sigma_{1/2}^L = \frac{4\pi^2\alpha}{MK} \left[-F_1 + (1 + \gamma^2) \frac{F_2}{2x} \right], \quad (2.25)$$

$$\sigma^T = \frac{1}{2} (\sigma_{1/2}^T + \sigma_{3/2}^T) = \frac{4\pi^2\alpha}{MK} F_1, \quad (2.26)$$

and the function $R = \sigma^L/\sigma^T$, the ratio of the cross sections for longitudinal and transverse photon absorption by the nucleon:

$$R = (1 + \gamma^2) \frac{F_2}{2xF_1} - 1. \quad (2.27)$$

2.1.2 Longitudinal double-spin asymmetry

The double-spin cross section asymmetries in longitudinally polarised lepton (\rightarrow) and longitudinally/transversely polarised target (\Rightarrow / $\uparrow\uparrow$) systems are defined as follows:

$$A_{\parallel} = \frac{\Delta\sigma_{\parallel}}{2\bar{\sigma}} = \frac{\sigma_{\rightarrow\Rightarrow}^{\rightarrow} - \sigma_{\rightarrow\Rightarrow}^{\leftarrow}}{\sigma_{\rightarrow\Rightarrow}^{\rightarrow} + \sigma_{\rightarrow\Rightarrow}^{\leftarrow}}, \quad A_{\perp} = \frac{\Delta\sigma_{\perp}}{2\bar{\sigma}} = \frac{\sigma_{\rightarrow\uparrow}^{\rightarrow} - \sigma_{\rightarrow\downarrow}^{\rightarrow}}{\sigma_{\rightarrow\uparrow}^{\rightarrow} + \sigma_{\rightarrow\downarrow}^{\rightarrow}}. \quad (2.28)$$

where the cross sections $\bar{\sigma}$ and $\Delta\sigma_{\parallel}$, $\Delta\sigma_{\perp}$, calculated in the one-photon exchange approximation, are given by Eqs (2.17–2.19). The above formulae are exact for a spin-1/2 nucleon target and only approximate for a spin-1 deuteron target. That is $\Delta\sigma_{\parallel}$ and $\bar{\sigma}$ Eq. (2.28) are expressed in terms of the same structure functions $g_{1,2}$ and $F_{1,2}$ only when the deuteron quadrupole structure functions b_{1-4} are neglected. As discussed in the previous section this approximation is justified in view of the size of experimental uncertainties.

The virtual photon-nucleon asymmetries A_1 and A_2 can be defined in the following way:

$$A_1 = \frac{\sigma_{1/2}^T - \sigma_{3/2}^T}{\sigma_{1/2}^T + \sigma_{3/2}^T} = \frac{\sigma_{1/2}^T - \sigma_{3/2}^T}{2\sigma^T}, \quad A_2 = \frac{\sigma_{1/2}^{TL}}{\sigma_{1/2}^T + \sigma_{3/2}^T} = \frac{\sigma_{1/2}^{TL}}{2\sigma^T}. \quad (2.29)$$

where the photon cross sections are given by Eqs (2.21–2.23) and Eq (2.26) for a spin-1/2 nucleon target. The asymmetries A_1 and A_2 for a deuteron (spin-1) target are as follows:

$$A_1^d = \frac{3}{2} \frac{\sigma_0^T - \sigma_2^T}{\sigma_0^T + \sigma_1^T + \sigma_2^T} = \frac{\sigma_0^T - \sigma_2^T}{2\sigma^T}, \quad A_2^d = \frac{3}{2} \frac{\sigma_0^{TL} + \sigma_1^{TL}}{\sigma_0^T + \sigma_1^T + \sigma_2^T} = \frac{\sigma_0^{TL} + \sigma_1^{TL}}{2\sigma^T}. \quad (2.30)$$

Here the quadrupole structure functions b_{1-4} are neglected and the corresponding photon cross section formulae can be found in [57] and [59]. σ_J^T is the virtual photon-deuteron absorption cross section for a total spin projection J in the photon direction. σ_J^{TL} results from the interference between transverse and longitudinal amplitudes for $J = 0, 1$, and $\sigma^T = (\sigma_0^T + \sigma_1^T + \sigma_2^T)/3$ is the total transverse photo-absorption cross section.

There are bounds on the absolute values of A_1 and A_2 [66, 67]:

$$|A_1| \leq 1, \quad |A_2| \leq \sqrt{R}. \quad (2.31)$$

The virtual photon asymmetries A_1 and A_2 are directly related to the spin-dependent structure functions g_1 and g_2 :

$$A_1 = \frac{g_1 - \gamma^2 g_2}{F_1}, \quad A_2 = \gamma \frac{g_1 + g_2}{F_1}. \quad (2.32)$$

Conversely, the structure functions g_1 and g_2 can be expressed in terms of the asymmetries A_1 and A_2 :

$$g_1 = \frac{F_1}{(1 + \gamma^2)} (A_1 + \gamma A_2), \quad g_2 = \frac{F_1}{(1 + \gamma^2)} \left(-A_1 + \frac{1}{\gamma} A_2\right). \quad (2.33)$$

The double-spin cross section asymmetries A_{\parallel} and A_{\perp} , measured by the polarised DIS experiments, are related to the virtual photon asymmetries A_1 and A_2 as follows:

$$A_{\parallel} = D(A_1 + \eta A_2), \quad A_{\perp} = d(A_2 - \xi A_1). \quad (2.34)$$

The depolarisation factor D and kinematic factors d , η and ξ , determined up to terms m_l^2/E^2 , with m_l the lepton mass, are given by:

$$D = \frac{y[(1 + \gamma^2 y/2)(2 - y) - 2y^2 m_l^2/Q^2]}{y^2(1 - 2m_l^2/Q^2)(1 + \gamma^2) + 2(1 - y - \gamma^2 y^2/4)(1 + \gamma^2)F_2/(2xF_1)}, \quad (2.35)$$

$$d = \frac{\sqrt{1 - y - \gamma^2 y^2/4}(1 + \gamma^2 y/2)}{(1 - y/2)(1 + \gamma^2 y/2) - y^2 m_l^2/Q^2} D, \quad (2.36)$$

$$\eta = \frac{\gamma(1 - y - \gamma^2 y^2/4 - y^2 m_l^2/Q^2)}{(1 + \gamma^2 y/2)(1 - y/2) - y^2 m_l^2/Q^2}, \quad (2.37)$$

$$\xi = \frac{\gamma(1 - y/2 - y^2 m_l^2/Q^2)}{1 + \gamma^2 y/2}. \quad (2.38)$$

The neglected terms are very small. For example, m_l^2/E^2 is of the order of 10^{-7} for the muon beams used at SMC and COMPASS experiments. The ratio of the polarisation averaged structure functions F_1 and F_2 can be replaced by the function R in the denominator of the factor D in Eq. (2.35) according to the relation $(1 + \gamma^2)F_2/(2xF_1) = 1 + R$, which is exact for a spin-1/2 target. It is also a very good approximation for a deuteron spin-1 target.

Relations (2.32) and (2.34) allow one to determine the polarisation dependent structure functions g_1 and g_2 from the measured longitudinal and transverse asymmetries A_{\parallel} and A_{\perp} if the polarisation averaged structure function F_1 , or equivalently F_2 and R , cf Eq. (2.27),

is known. Very precise data on the F_2 structure function are available thanks to a series of fixed-target experiments and excellent data collected by the ZEUS and H1 experiments at HERA. The function R can be also parameterized in a good accuracy. For small x and small Q^2 regime some models are needed to parameterize R , see [65]. In the kinematic region of the SMC and COMPASS measurements the factor γ is of the order of 10^{-3} and η is of order 10^{-4} . Moreover the asymmetries A_2 were measured and found to be significantly smaller than the positivity limit \sqrt{R} both for the proton and deuteron targets [69, 70]. The small values of A_2 , γ and η allow one to neglect the term ηA_2 in Eq. (2.34) and γA_2 in Eq. (2.33). In this case the measurement of A_{\parallel} directly determines A_1 and hence g_1 :

$$A_{\parallel} \simeq D A_1, \quad g_1 \simeq A_1 F_1. \quad (2.39)$$

The above simplified equation for A_{\parallel} gives a clear interpretation of the depolarisation factor D . The virtual photons emitted by the polarised leptons are depolarised by the factor D so that the spin asymmetry in the virtual photon–nucleon system is D times smaller than the asymmetry in the lepton–nucleon system. Note, that neglecting the factor γ is not justified in most of the JLAB experiments and the full relation: $g_1 = \frac{F_1}{(1+\gamma^2)} A_1$ should be used to determine g_1 .

The double-spin longitudinal asymmetry A_1 has been measured by many spin-dependent DIS experiments. One of the most precise data sets has been collected by the COMPASS experiment on deuteron and proton targets. The proton [68] and deuteron results [8] are presented in Fig. 2.4 in comparison with previous experimental results. In Fig. 2.5 the very precise deuteron COMPASS result for the asymmetry A_1^d for low Q^2 events [65] is presented. Since the Q^2 and x kinematical variables are strongly correlated for the fixed-target experiments, the small Q^2 results are very difficult to interpret in terms of QCD or in Regge-type approaches. The general consistency between data sets is seen from the Figs. 2.4 and 2.5.

The COMPASS A_1^d asymmetry results indicate that an "averaged" nucleon in the deuteron target is not polarised for small- x region. The asymmetry A_1 is the basis of the determination of the g_1 structure function which is discussed in the next section.

2.1.3 The polarisation dependent structure function g_1

The structure functions $F_{1,2}$ and $g_{1,2}$ have been considered so far as general functions needed to parameterize the DIS hadronic tensor or equivalently the virtual photon forward Compton amplitude. In a general Quantum Field Theory like QCD their scale dependence can be calculated via OPE Wilson coefficients. This method in principle allows one to get full

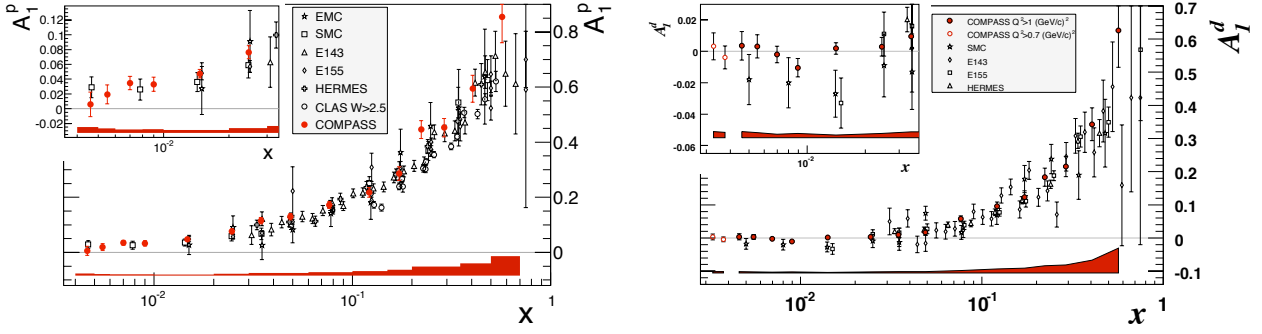


Figure 2.4: The asymmetry $A_1^p(x)$ (left) and $A_1^d(x)$ (right) as measured by COMPASS [68, 8] and previous results from EMC [2, 73], SMC [7], HERMES [6, 71], SLAC E143 [70], E155 [74, 9] and CLAS [10] at $Q^2 > 1 \text{ GeV}^2$. The cut $W > 2.5 \text{ GeV}$ has been applied to select DIS events in the CLAS data. The SLAC values of g_1/F_1 have been converted to A_1 and the E155 data corresponding to the same x have been averaged over Q^2 . Only statistical errors are shown with the data points. Only statistical errors are shown within data points. The shadowed areas shows the size of the COMPASS systematic errors.

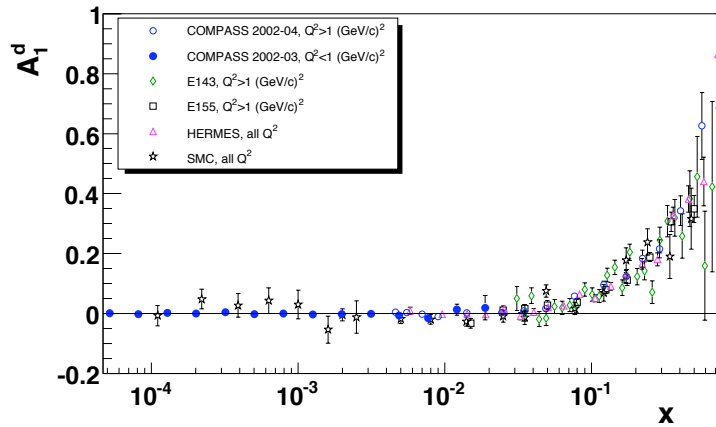


Figure 2.5: The asymmetry $A_1^d(x)$ as a function of x at the measured value of Q^2 : the results from COMPASS [65] for $Q^2 < 1 \text{ GeV}^2$ are compared with previous results at different values of Q^2 from COMPASS [8], SMC [7, 72], HERMES [71], SLAC E143 [70] and E155 [9]. The E155 data corresponding to the same x have been averaged over Q^2 . The indicated uncertainties are statistical.

information about the nucleon structure if all matrix elements between nucleon states of the local operators used in the OPE are measured. The matrix elements of the local operators used in the OPE are related to the structure functions by their moments in x . The lowest moments determine the small- x dependence of the structure functions while the higher ones

(due to the higher power of x in the moment definition) - large x behavior. Unfortunately measurements of the higher moments of the structure functions are impractical.

The QPM describes the nucleon as an object composed of almost noninteracting, massless partons identified with quarks and gluons. This model is defined in the infinite momentum frame, where the nucleon is moving with $P \rightarrow \infty$. The partons are moving collinear with nucleon and their transverse momenta are bound and neglected in the first approximation. Anti-collinear parton configurations are forbidden in the infinite momentum frame. In strict sense the life-time of such configurations approaching to zero while the life-time of the collinear ones is going to infinity. The so-called "impulse approximation" is assumed: during the virtual photon-parton interaction the partons are assumed not to interact and therefore a "frozen" parton configuration is seen by the photon probe. The cross section of the DIS process can then be calculated as an incoherent sum of the cross sections for virtual photon-parton scattering. The partons are assumed to be on shell. Under these assumptions the calculations of the DIS cross section are straightforward. The famous Bjorken scaling results, the structure functions depend only on one scaling variable, Bjorken x [76]. The structure functions are interpreted in terms of PDFs - that quantifies the probabilities of finding a parton with a given momentum fraction x in the nucleon. QCD interactions between partons modify this simple and physically intuitive picture and lead to scaling violation. The structure functions depend not only on x variable but also on the scale Q^2 . The scale dependence is strictly predicted by QCD while the x dependence requires models or fits to the data. The foundations of the QPM can be found in the original papers [53, 75, 76] and in many textbooks e.g. [77, 78, 79]. The strength and beauty of the QPM is that in many cases, however complicated, the QCD corrections can be absorbed in effective, universal PDFs and therefore the description of hadrons as collections of weakly interacting collinear partons is still valid. This possibility is strictly related to the factorization problem and is a very non-trivial consequence of the QCD infrared structure. The universality of the PDFs means that once measured in one reaction, they can be used to describe other reactions, e.g. proton-proton scattering.

The separation into "hard" (finite) and "soft" (divergent) parts of the QCD interactions is not unique and depends on the choice of a factorization scheme and factorization scale. The universality of the PDFs holds if the same factorization scheme is used in description of the QCD matrix elements of the considered partonic subprocess and in the procedure of PDFs determination. The schemes differ in how the non-divergent pieces are assimilated in the PDFs. A simple example of a factorization scheme is the choice of cut-off transverse momenta that allow one to separate hard and soft parts. It allows then one to incorporate the divergent part to the effective definition of the PDFs. The choice of factorization scale

is arbitrary and can be different from the perturbative scale (Q^2) in DIS.

A third scale that appears as a consequence of QCD parton interactions is the renormalization scale, needed to regularize the ultra-violet singularity of the theory. This regularization and the procedure to effectively remove the ultra-violet divergences is called renormalization scheme and also is not unique. Very often the renormalization scale is chosen to be equal to the factorization scale for simplicity. It is also common to take renormalization scale as Q^2 in DIS. Since the all physical quantities should not depend on the renormalization scale the so-called Renormalization Group Equation (RGE) can be formulated. The RGE guarantees that all renormalization scale dependent coefficients evolve with the change of this scale in such a way that all observed quantities are renormalization scale independent. In practice it means that RGE describes the QCD scale evolution as the renormalization scale can be chosen equal to Q^2 . Therefore, the RGE describes Q^2 evolution as well. Discussion of different factorization schemes for the structure functions and PDFs can be found in the original papers e.g. [81] -[86] and in e.g [15].

The DIS asymptotic regime $Q^2 \rightarrow \infty$ corresponds to the light-cone limit dominated by local twist-2 QCD operators in the OPE. The scale dependence is calculated with the RGE for the Wilson coefficients while the internal nucleon structure is "hidden" in the matrix elements of the operators related to the moments of the structure functions. In the framework of the QCD improved QPM the all information about nucleon structure is contained in PDFs. The DGLAP (Dokshitzer-Gribov-Lipatov-Altarelli-Parisi) set of the QCD evolution equations for PDFs describe their scale dependence [80, 87, 88]. Both approaches (QPM and the QCD evolution equations for PDFs and OPE with the RGE) are equivalent in describing inclusive DIS reactions.

In the naive QPM the spin independent F_1 and spin dependent g_1 structure functions are expressed in terms of the quark helicity distributions $q^+(x)$ and $q^-(x)$ as follows:

$$F_1(x) = \frac{1}{2} \sum_q e_q^2 [q^+(x) + q^-(x)] \equiv \frac{1}{2} \sum_q e_q^2 q(x), \quad (2.40)$$

$$g_1(x) = \frac{1}{2} \sum_q e_q^2 [q^+(x) - q^-(x)] \equiv \frac{1}{2} \sum_q e_q^2 \Delta q(x). \quad (2.41)$$

The $(+)(-)$ sign in $q^+(x)$ and $q^-(x)$ refers to a quark with its spin projection parallel (antiparallel) to that of the target nucleon. For longitudinally polarised target the $(+)(-)$ sign defines the quark helicity. $q(x)$ is the spin-averaged quark distribution (probability of finding quark q with a nucleon momentum fraction x) in the nucleon. The electric charge of a quark of flavour q is denoted by e_q .

The spin independent structure functions F_1 and F_2 for spin-1/2 satisfy the Callan-Gross relation [89]:

$$F_2(x) = 2xF_1(x). \quad (2.42)$$

In the QCD improved QPM the interactions between partons lead to scaling violations and the decomposition of the structure function g_1 is:

$$\begin{aligned} g_1(x, Q^2) &= \frac{1}{2} \sum_q e_q^2 \int_x^1 \frac{dy}{y} [\Delta q(y, Q^2) + \Delta \bar{q}(y, Q^2)] C_q(x/y, \alpha_s(Q^2)) \\ &+ \frac{\langle e_q^2 \rangle}{2} n_f \int_x^1 \frac{dy}{y} \Delta G(y, Q^2) C_G(x/y, \alpha_s(Q^2)) \\ &= \frac{1}{2} \sum_q e_q^2 C_q(\alpha_s(Q^2)) \otimes [\Delta q(Q^2) + \Delta \bar{q}(Q^2)] + \frac{\langle e_q^2 \rangle}{2} n_f C_G(\alpha_s(Q^2)) \otimes \Delta G(Q^2). \end{aligned} \quad (2.43)$$

where \otimes denotes a convolution integral. As a consequence of the QCD interactions between partons, in particular gluon decay, a so-called "sea" of quark pairs appears in the nucleon. Hence anti-quarks as well as gluons are part of the decomposition of g_1 . Here $\Delta q = q^+ - q^-$ and $\Delta \bar{q} = \bar{q}^+ - \bar{q}^-$. The number of flavours n_f is assumed to be 3 since the contribution of charm and heavier quarks is negligible at the energies of past and present polarised DIS experiments [90]. The QCD evolution (scale dependence) for g_1 is described by the DGLAP equations:

$$\begin{aligned} Q^2 \frac{d}{dQ^2} \begin{pmatrix} \Delta q \\ \Delta G \end{pmatrix} (x, Q^2) &= \frac{\alpha_s(Q^2)}{2\pi} \int_x^1 \frac{dy}{y} \begin{pmatrix} \Delta P_{qq} & \Delta P_{qG} \\ \sum_q \Delta P_{Gq} & \Delta P_{GG} \end{pmatrix} (x/y, \alpha_s(Q^2)) \begin{pmatrix} \Delta q \\ \Delta G \end{pmatrix} (y, Q^2) \\ &= \frac{\alpha_s(Q^2)}{2\pi} \begin{pmatrix} \Delta P_{qq} & \Delta P_{qG} \\ \sum_q \Delta P_{Gq} & \Delta P_{GG} \end{pmatrix} (\alpha_s(Q^2)) \otimes \begin{pmatrix} \Delta q \\ \Delta G \end{pmatrix} (Q^2), \end{aligned} \quad (2.44)$$

where $\alpha_s(Q^2)$ is the QCD running strong coupling constant. The coefficient functions C_i in Eq. (2.44) and splitting functions ΔP_{ij} in Eq. (2.44), can be calculated in a QCD perturbation series in α_s . The indices i and j running over quarks (antiquarks) q and gluons G , The procedure is analogous to the polarisation independent case (see e.g. [88, 91, 92]). The splitting functions P_{ij} have the nice physical interpretation that they are the probability of finding a parton i in a parton j at a scale Q^2 (at LO). The equivalence of the DIS description in the frame of RGE and OPE and in QCD improved QPM and DGLAP equations is clear after taking the Mellin transform of the DGLAP splitting functions. They correspond to the anomalous dimension of the QCD operators used in OPE for DIS reactions.

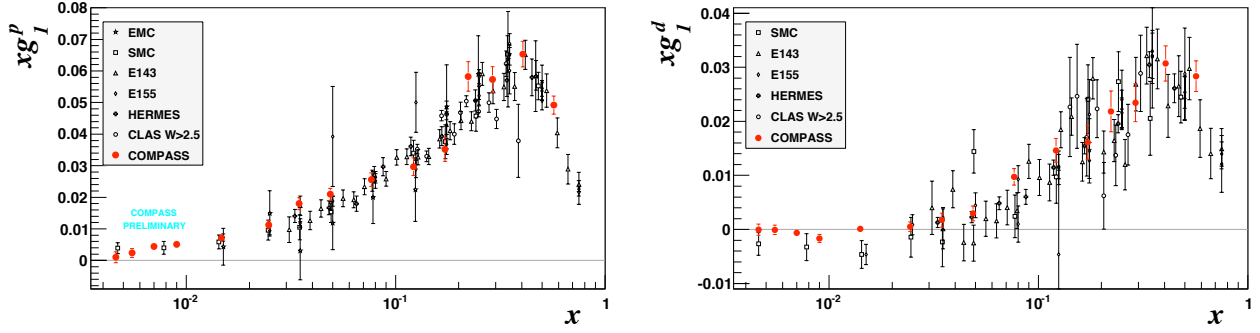


Figure 2.6: The spin dependent structure function $g_1(x)$ of the proton (left) and the deuteron (right) measured by EMC [2, 73], SMC [7], HERMES [6, 71], SLAC E143 [70], E155 [74, 9], CLAS [10] and COMPASS [8, 68] experiments. For comparison all points have been evolved to $Q^2 = 3 \text{ GeV}^2$.

A consistent description of the structure functions requires both the coefficient functions C_i and the splitting functions ΔP_{ij} to be calculated up to the same order in perturbative QCD. The calculations of C_i and ΔP_{ij} in Next-to-Leading-Order (NLO) can be found in [93, 94] (C_i^1 and ΔP_{ij}^1):

$$C_i(z, \alpha_s(Q^2)) = C_i^0(z) + \frac{\alpha_s(Q^2)}{2\pi} C_i^1(z) + \mathcal{O}(\alpha_s^2), \quad (2.45)$$

$$\Delta P_{ij}(z, \alpha_s(Q^2)) = \Delta P_{ij}^0(z) + \frac{\alpha_s(Q^2)}{2\pi} \Delta P_{ij}^1(z) + \mathcal{O}(\alpha_s^2). \quad (2.46)$$

At the LO the gluon distribution does not contribute to the spin dependent g_1 structure function directly because $C_q^0(z) = \delta(1-z)$ and $C_G^0(z) = 0$. The simple parton model expression for g_1 given by Eq. (2.41) is then recovered. The gluons contribute indirectly to the g_1 via the evolution equation (2.44) since $\Delta P_{qG}^0(z) \neq 0$. At NLO $C_i^1(z) \neq 0$ so the gluon helicity distribution $\Delta G(x)$ directly enters g_1 .

The x -dependence of the structure functions cannot be predicted by QCD. The exception is a low- x regime. Regge theory [96, 97] predicts the power-like increase of g_1 at small x with fixed Q^2 scale: $g_1 \sim x^{-\alpha}$ or $g_1 \sim \log(x)$. The importance of the $\log(x)$ terms has been pointed out and the BFKL evolution equations was postulated [95]. The combinations of these two types of the evolution (in Q^2 and x) as a Double Leading Logarithm Approximation (DLA) was also considered [98, 84]. It has been also checked that the single $\log(x)$ summation is not enough for polarisation dependent g_1 structure functions and double logarithms $(\log(x))^2$ terms should be also summed [99, 100]. This approach is beyond the DGLAP formalism. The Regge-type models are not applicable in the small Q^2 and low x region, where Q^2 and x are correlated (as in SMC and COMPASS experiments) and others approach based

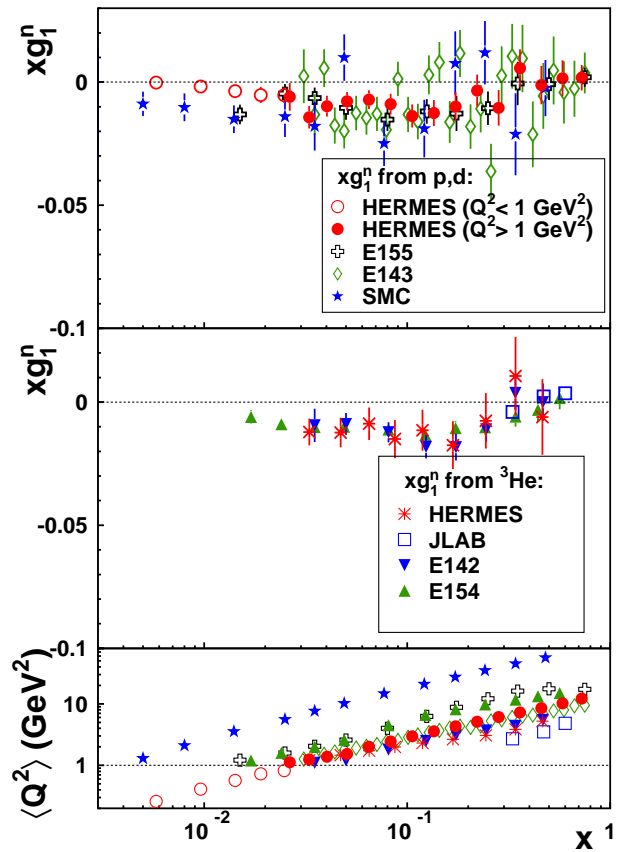


Figure 2.7: Top panel: The spin dependent structure function $g_1^n(x)$ of the neutron obtained from HERMES data on g_1^p and g_1^d , compared with similar data from SMC [7, 72, 113], E143 [70] and E155 [9, 74] in the HERMES x range. Middle panel from the top: $g_1^n(x)$ as obtained from ^3He target by JLAB [110], HERMES [111], E142 [109] and E154 [112]. (Figure from [6]).

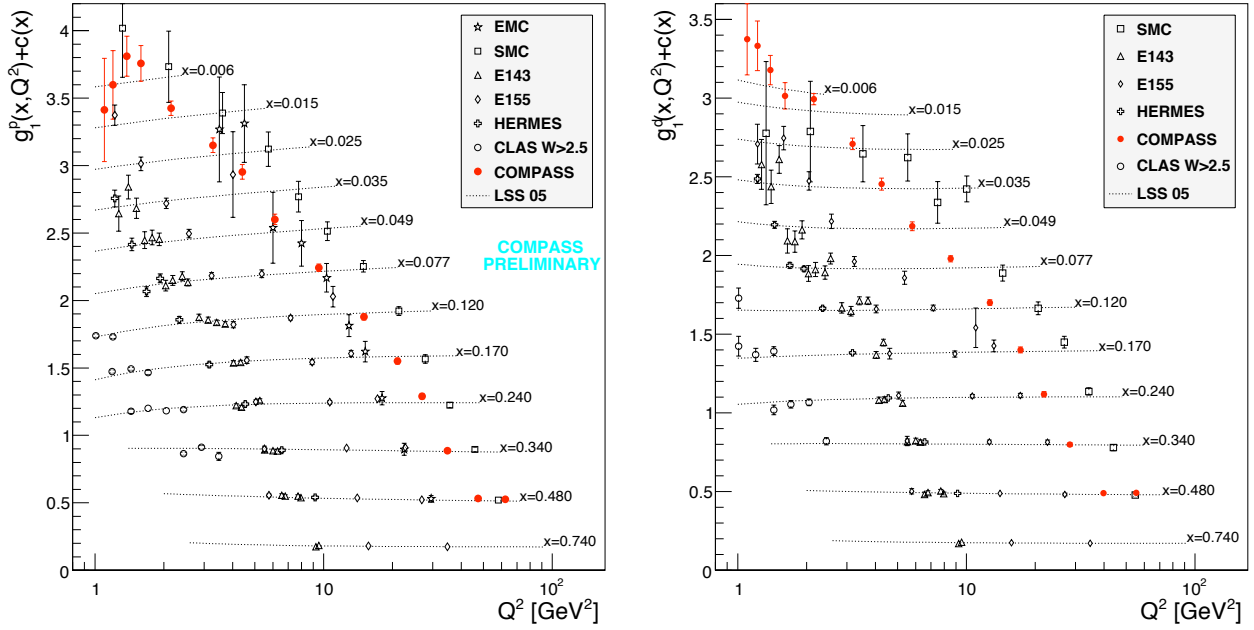


Figure 2.8: The spin-dependent structure function $g_1(x)$ measured in deep-inelastic scattering of leptons off proton (left) and deuteron (right) targets. Only the statistical errors are shown. The LSS05 parameterizations [104] have been used to align curves corresponding to a fixed x . Slight shifts have been applied to the data. A constant $c(x) = 0.28(11.6 - i_x)$ is added to g_1 values, where i_x is the number of the x bin ranging from $i_x = 0$ ($x = 0.006$) to $i_x = 11$ ($x = 0.74$).

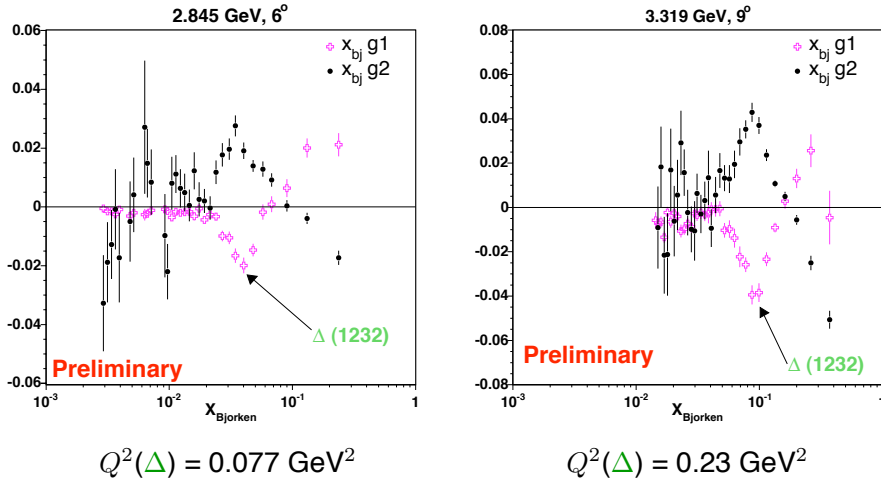


Figure 2.9: Neutron polarized structure functions xg_1^n and xg_2^n as a function of x from E97-110 experiment at Hall A at JLAB.

on QCD re-summations and on Vector Meson Dominance (VMD) models have been used [101, 102, 103].

There are also some theoretical constrains which can limit quark and gluon distributions for large x [79, 105, 106]. The gluon helicity is constrained by positivity of the fragmentation function and by the gauge theory requirements [107]. At the large x the g_1 structure function is dominated by the valence quarks and some predictions from static models, for example those based on the $SU(6)$ nucleon wave function, can be made. A review with references can be found in [15]. The confrontation of these predictions with data is possible in JLAB experiments.

The precise g_1 structure function data collected by various DIS experiments are shown in Figs 2.6 and 2.7. Very good agreement between the experimental data is seen. The Q^2 dependence in x bins (scalling violation) is illustrated In Fig. 2.8.

As an example of the g_2 structure function measurement the data of the "effective neutron" structure functions g_1^n and g_2^n performed on ^3He target in JLAB by [108] are presented in Fig. 2.9. Note that these measurements are in the resonance and small Q^2 kinematic domain, and are thus not DIS.

2.2 Decomposition of the nucleon spin

2.2.1 The Bjorken and Ellis-Jaffe sum rules

The first moment, Γ_1 , of the structure function, $g_1(x)$ contains information about the total quark helicity contribution to the nucleon spin. In the naive QPM:

$$\Gamma_1 = \int_0^1 g_1(x) dx = \frac{1}{2} \sum_q e_q^2 \int_0^1 [\Delta q(x) + \Delta \bar{q}(x)] dx. \quad (2.47)$$

By defining $\Delta q = \int_0^1 [\Delta q(x) + \Delta \bar{q}(x)] dx$, one can rewrite Γ_1^p for the proton can be rewritten as follows:

$$\begin{aligned} \Gamma_1^p &= \frac{1}{2} \left(\frac{4}{9} \Delta u + \frac{1}{9} \Delta d + \frac{1}{9} \Delta s \right) \\ &= \frac{1}{12} (\Delta u - \Delta d) + \frac{1}{36} (\Delta u + \Delta d - 2\Delta s) + \frac{1}{9} (\Delta u + \Delta d + \Delta s). \end{aligned} \quad (2.48)$$

Γ_1^n for neutron is obtained from isospin symmetry and the final Γ_1 decomposition for the proton (p) and the neutron (n) respectively, is thus:

$$\Gamma_1^{p(n)} = \pm \frac{1}{12} a_3 + \frac{1}{36} a_8 + \frac{1}{9} a_0, \quad (2.49)$$

with:

$$\begin{aligned}
a_3 &= \Delta u - \Delta d, \\
a_8 &= \Delta u + \Delta d - 2\Delta s, \\
a_0 &= \Delta u + \Delta d + \Delta s.
\end{aligned}
\tag{2.50}$$

In the naive QPM, $\Delta\Sigma = \Delta u + \Delta d + \Delta s$ is the total fraction of the spin of the nucleon carried by the quark spins and $\Delta\Sigma = a_0$. The axial charges a_3 and a_8 in Eqs (2.49) are related to the expectation values of the proton matrix elements of the $SU(3)_f$ flavour nonet of quark axial-vector currents: $2\langle P, S | A_{5\mu}^3 | P, S \rangle = a_3 S_\mu$, $2\sqrt{3}\langle P, S | A_{5\mu}^8 | P, S \rangle = a_8 S_\mu$. The axial currents are defined as $A_{5\mu}^j = \bar{\Psi} \gamma_\mu \gamma_5 \frac{\lambda_j}{2} \Psi$, where λ_j are the Gell-Mann matrices and Ψ is a column vector in flavour space. The axial charge a_0 corresponds to the flavour singlet operator; $A_{5\mu}^0 = \bar{\Psi} \gamma_\mu \gamma_5 \Psi$ and $\langle P, S | A_{5\mu}^0 | P, S \rangle = a_0 S_\mu$ ²

From isospin invariance it follows that $a_3 = F + D = g_A/g_V$ [114], where g_A/g_V is the ratio of axial vector and vector coupling constants measured in neutron β decay. F and D are the symmetric and antisymmetric couplings obtained from hyperon decay. If $SU(3)_f$ is a good symmetry to describe β decay for the octet of hyperons then $a_8 = 3F - D$. The octet currents are conserved and therefore a_3 and a_8 are independent of Q^2 . The singlet current a_0 is not conserved and in general depends on Q^2 . This is consequence of the axial anomaly [5] and will be discussed in the next section.

The values of the coupling constants F and D and consequently the values of two matrix elements a_3 and a_8 , can be determined from weak β decay of the neutron and spin-1/2 hyperons (*e.g.* $\Lambda \rightarrow p$, $\Sigma \rightarrow n$, $\Xi \rightarrow \Lambda$) in the SU_3 baryon octet. Thus knowledge of a_3 and a_8 allows for the extraction of a_0 from the measurement of Γ_1 . The following values for a_3 and a_8 [52, 115, 116, 117]:

$$a_3 = F + D = 1.2694 \pm 0.0028 \quad a_8 = 3F - D = 0.585 \pm 0.025,
\tag{2.51}$$

have been used in a_0 determination at the COMPASS experiment.

QCD corrections (QCD improved QPM) modify also the first moment of the g_1 structure function. Eq. (2.49) for g_1 integrals can be now expressed as follows:

$$\Gamma_1^{p(n)} = \frac{1}{12} \left\{ \left(\pm(a_3 + \frac{1}{3}a_8) E_{NS}(Q^2) + \frac{4}{3}a_0 E_S(Q^2) \right) \right\},
\tag{2.52}$$

²The relations between a_i and matrix elements are a matter of convention. Here the convention from [4] is used. Another convention $\langle P, S | A_{5\mu}^i | P, S \rangle = 2M a_i S_\mu$, ($i = 1 \dots 8$) is often used *e.g.* [15] but this convention introduces a $\sqrt{3}$ factor in a_8 . Factor M is only normalization in OPE.

with

$$E_{NS}(Q^2) = 1 - \frac{\alpha_s}{\pi} - (3.5833) \left(\frac{\alpha_s}{\pi}\right)^2 - (20.2153) \left(\frac{\alpha_s}{\pi}\right)^3 - (130) \left(\frac{\alpha_s}{\pi}\right)^4 \dots, \quad (2.53)$$

$$E_S(Q^2) = 1 - \frac{\alpha_s}{\pi} - (1.0959) \left(\frac{\alpha_s}{\pi}\right)^2 - (6) \left(\frac{\alpha_s}{\pi}\right)^3 \dots, \quad (2.54)$$

where \pm stands for proton and neutron, respectively. The coefficients $E_{NS}(Q^2)$ and $E_S(Q^2)$ are taken from [4, 118]. The calculations have been done in the Modified Minimal Subtraction (\overline{MS}) renormalisation and factorization scheme [119]. The renormalization scale has been chosen as $\mu^2 = Q^2$. This simplifies the relation Eq.(2.52) but introduces an explicit dependence of a_0 on Q^2 in³

A scale independent \hat{a}_0 can be defined taking a_0 in the limit $Q^2 \rightarrow \infty$. The singlet coefficient, $E_S(Q^2)$, is then modified so that all scale dependence is now explicitly "hidden" in a modified $\hat{E}_S(Q^2)$ [120]:

$$\Gamma_1^{p(n)} = \frac{1}{12} \left\{ \left(\pm(a_3 + \frac{1}{3}a_8) \right) E_{NS}(Q^2) + \frac{4}{3} \hat{a}_0 \hat{E}_S(Q^2) \right\}, \quad (2.55)$$

with

$$\hat{E}_S(Q^2) = 1 - (0.33333) \frac{\alpha_s}{\pi} - (0.54959) \left(\frac{\alpha_s}{\pi}\right)^2 - (4.44725) \left(\frac{\alpha_s}{\pi}\right)^3 \dots \quad (2.56)$$

The difference between Γ_1 for the proton and neutron gives the Bjorken sum [114] :

$$\Gamma_1^p - \Gamma_1^n = \frac{1}{6} a_3 E_{NS} \equiv \frac{1}{6} \left| \frac{g_A}{g_V} \right| E_{NS}. \quad (2.57)$$

This is a fundamental sum rule because it relies only on isospin invariance, *i.e.* on the $SU(2)$ symmetry between up and down quarks. As discussed, beyond leading order, E_{NS} depends on the number of flavours and the renormalisation scheme.

COMPASS has measured Γ_1^p and Γ_1^n and finds [68]:

$$|g_A/g_V| = 1.28 \pm 0.07(\text{stat.}) \pm 0.10(\text{syst.}), \quad (2.58)$$

to be compared with value 1.2694 ± 0.0028 derived from neutron β decay[117]. The Bjorken sum rule is confirmed by data to within 5% of its value. The result is in good agreement with the results from the previous experiments [7, 6]. The result is insensitive to the choice

³The scale dependence appears in the coefficient functions and in an anomalous dimension term. a_0 depends on the renormalization scale μ . For renormalization scale $\mu^2 = Q^2$ the anomalous dimension term simplifies to 1 and a_0 explicitly depends on Q^2 . The scale independent a_3 and a_8 do not renormalize and their anomalous dimensions are equal to 0.

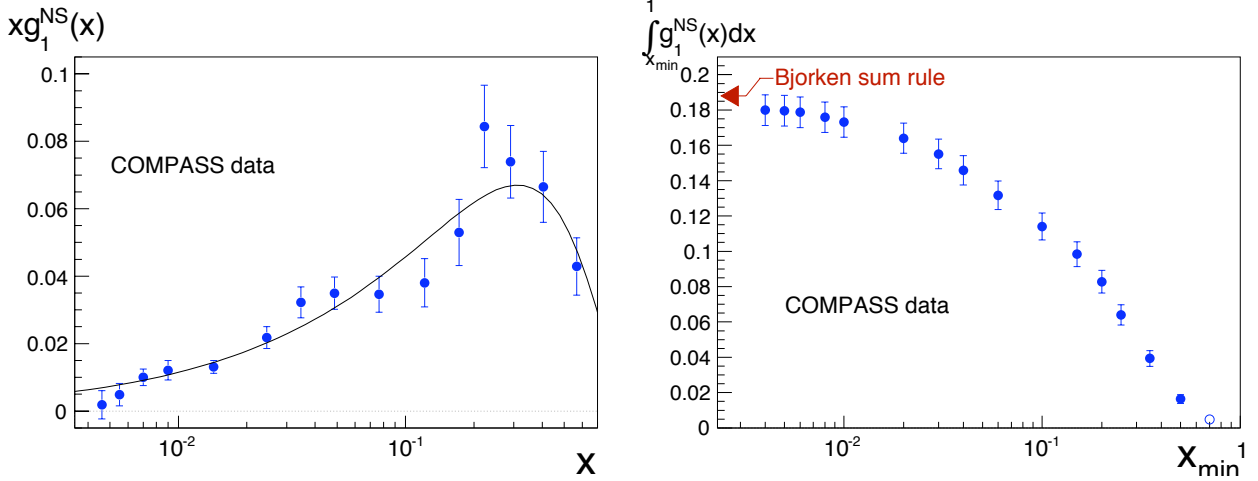


Figure 2.10: Left: Values of $g_1^{NS}(x)$ at $Q^2 = 3 \text{ GeV}^2$, derived from the COMPASS measurements [68] of A_1^p and A_1^d and the result of a three parameter QCD fit at NLO to the data. The errors are statistical only. Right: $\int_{x_{min}}^1 g_1^{NS} dx$ as a function of x_{min} as obtained from the COMPASS data. The open circle at $x = 0.7$ is obtained from the fit. The arrow on the left side shows the value expected for the full range $0 < x < 1$ with $|g_A/g_V| = 1.269$ [117].

of Q^2 [68]. In the Fig. 2.10 the Bjorken sum rule integral as a function of x_{min} is shown as obtained from COMPASS data together with non-singlet spin structure function defined as:

$$g_1^{NS}(x, Q^2) = g_1^p(x, Q^2) - g_1^n(x, Q^2). \quad (2.59)$$

This function has been obtained from deuteron and proton data as follows:

$$g_1^{NS}(x, Q^2) = 2 \left[g_1^p(x, Q^2) - \frac{g_1^d(x, Q^2)}{1 - \omega_D} \right], \quad (2.60)$$

where $\omega_D = 0.05 \pm 0.01$ is a correction for the D-wave state probability in the deuteron [121]. The non-singlet spin structure function is of special interest because its Q^2 dependence is decoupled from the singlet and the gluon spin densities.

Predictions for the values of the first moment of g_1^p and g_1^n can be obtained under the assumption $\Delta s + \Delta \bar{s} = 0$ taking the values of a_3 and a_8 from weak decays (F and D) and relating a_0 to a_8 . This is the Ellis-Jaffe sum rule [3]. The value of the a_8 suggests that the total fraction of spin carried by quark spins is 0.6, in good agreement with the expectation from the QPM with relativistic corrections. $\Delta \Sigma = a_0 = 1$ is a naive prediction from the QPM but the relativistic corrections reduce this value to roughly 0.65. The $SU(6)$ static model with relativistic corrections or the MIT bag model, in which quarks are confined in a sphere with the finite radius, are good examples (see e.g.[15]). The measured

value of the first moment of g_1 contradicts the Ellis-Jaffe sum rule. Eq. (2.52) allows one to determine a_0 from the measured value of Γ_1 , a_3 and a_8 used as an input. The obtained result indicates that only 1/3 of the nucleon spin is carried by quark spins. The first results from the EMC experiment for proton target suggested an even smaller value (even compatible with zero) however with large uncertainty [2]. One of the most accurate measurements of the first moment of g_1 structure function has been reported by the COMPASS experiment [8] for deuteron targets. The isoscalar deuteron target allows one to measure an "averaged nucleon" structure:

$$g_1^N(x, Q^2) = (g_1^p + g_1^n)/2 = g_1^d(x, Q^2)/(1 - 1.5\omega_D). \quad (2.61)$$

The isoscalarity allows one to express the first moment of the g_1^N only by a_8 and a_0 as follows:

$$\Gamma_1^N = \frac{1}{36}a_8E_{NS}(Q^2) + \frac{1}{9}a_0E_S(Q^2). \quad (2.62)$$

or, in terms \hat{a}_0 (a_0 at $Q^2 \rightarrow \infty$ limit) and \hat{E}_S :

$$\Gamma_1^N = \frac{1}{36}a_8E_{NS}(Q^2) + \frac{1}{9}\hat{a}_0\hat{E}_S(Q^2). \quad (2.63)$$

The value for a_0 obtained by COMPASS is:

$$a_0(Q^2 = 3\text{GeV}^2) = 0.35 \pm 0.03 \text{ (stat.)} \pm 0.05 \text{ (syst.)}, \quad (2.64)$$

in QCD NLO approximation with the value of α_s evolved from the PDG value $\alpha_s(m_Z^2) = 0.1187 \pm 0.005$ and assuming three active quark flavours. The data have been evolved to the reference $Q^2 = 3 \text{ GeV}^2$ and two independent QCD NLO fits have been used, see [8]. The quoted systematic error accounts for the error from the evolution and for the experimental systematic error, combined in quadrature. To obtain the scale independent \hat{a}_0 the 3-loop results for the coefficients E_{NS} and \hat{E}_S have been used [120] (beyond NLO) but the experimental data have been evolved to a common Q^2 using NLO fit only. The choice of a value close to the average Q^2 of the data is expected to minimize the effect of the evolution on the \hat{a}_0 result:

$$\hat{a}_0 = 0.33 \pm 0.03 \text{ (stat.)} \pm 0.05 \text{ (syst.)}. \quad (2.65)$$

The first moment of the strange quark spin distribution in the limit $Q^2 \rightarrow \infty$ is found to be:

$$(\Delta s + \Delta \bar{s})_{Q^2 \rightarrow \infty} = \frac{1}{3}(\hat{a}_0 - a_8) = -0.08 \pm 0.01 \text{ (stat.)} \pm 0.02 \text{ (syst.)}. \quad (2.66)$$

As stated before, this result relies on $SU(3)_f$ flavour symmetry. Symmetry breaking, at the level up to 20% [116], would shift the value of $\Delta s + \Delta \bar{s}$ by ± 0.04 .

2.2.2 The triangle anomaly and the role of gluons

In the OPE there is no twist-2, gauge invariant, spin-1 local gluonic operator and therefore gluons don't contribute to the first moment of g_1 . On the other hand, the explicit gluon contribution is written in the decomposition of structure function g_1 , Eq. (2.44), The singlet axial vector current $A_{5\mu}^0 = \bar{\Psi}\gamma_\mu\gamma_5\Psi$ is not conserved (even for massless quarks) because of the presence of the axial anomaly [5] :

$$\partial^\mu A_{5\mu}^0 = 2i \sum_{i=1}^f m_i \bar{q}_i \gamma_5 q_i + 2n_f \partial^\mu K_\mu, \quad (2.67)$$

where

$$K_\mu = \frac{\alpha_s}{4\pi} \epsilon^{\mu\nu\rho\sigma} \left[A_a^\nu \left(\partial^\rho A_a^\sigma - \frac{1}{3} g f_{abc} A_b^\rho A_c^\sigma \right) \right], \quad (2.68)$$

is a gluonic Chern-Simons current, A_a^μ is a gluon field and $\partial^\mu K_\mu = \frac{\alpha_s}{4\pi} G_{\mu\nu} G^{\mu\nu}$ is a topological charge density. The symbols f_{abc} are $SU(3)_{color}$ group constants and q_i stands for different quark flavours "i" (Ψ field is defined in flavour space). Finally $\alpha_s = g^2/4\pi$. With the help of Eq. (2.67) the singlet axial vector current can be then re-defined to obtain a partially conserved current:

$$A_{5\mu}^{0,con} = A_{5\mu}^0 - 2n_f K_\mu. \quad (2.69)$$

As discussed in [122, 123] the problem with non-existence of the twist-2, gauge invariant, local gluonic operators in OPE causes troubles with a definition of the gluon helicity distribution. Fortunately the QPM is formulated in the light-cone gauge ($A_+ = 0$) where the forward matrix elements of K_+ are invariant and in addition the non-abelian part of K_+ vanishes. In this gauge the matrix elements of K_+ are related to the gluon helicity distribution in the nucleon. Therefore the gluon helicity distribution ΔG can be measured in polarised DIS experiment if it is interpreted in the framework of the QPM and QCD. Explicit calculations of the gluon contribution to the first moment of the g_1 structure function via the PGF process have two contributions: hard and soft ones. The soft term is a contact term with a triangle anomaly [124, 125, 126, 127]. The procedure to manage the soft and hard parts of the partonic cross section in the first moment of the g_1 structure function is a matter of choice of factorization scheme. In the gauge invariant \overline{MS} scheme [119] the first moment of C_G in the decomposition of structure function g_1 , Eq. (2.44), vanishes and $\Delta G(x, Q^2)$ does not contribute directly to Γ_1 . Note, that this does not mean that $\Delta G(Q^2)$ vanishes. In other words the axial anomaly contact term in this scheme is a soft part of the partonic process (PGF) and therefore it is not present explicitly in Γ_1 . In the Adler-Bardeen (AB) scheme [84] which conserves chirality, the first moment of C_G is non zero and Γ_1 depends directly

on $\Delta G(x, Q^2)$. The axial anomaly term is a part of the hard process. The first moments of the singlet quark distribution $\Delta\Sigma(Q^2)$ in these two schemes are related by

$$\Delta\Sigma_{\overline{MS}}(Q^2) = \Delta\Sigma_{AB} - n_f \frac{\alpha_s(Q^2)}{2\pi} \Delta G(Q^2), \quad (2.70)$$

where ΔG is the first moment of the gluons helicity distribution. In the \overline{MS} scheme $\Delta\Sigma = a_0$ depends on Q^2 while in the AB scheme:

$$a_0 = \Delta\Sigma - n_f \frac{\alpha_s}{2\pi} \Delta G. \quad (2.71)$$

The scale independent $\Delta\Sigma$ (related to the matrix element of the conserved singlet axial vector $A_{5\mu}^{0,con}$ current) and the anomaly term $n_f \frac{\alpha_s}{2\pi} \Delta G$ (related to the K_+ operator matrix element) appears in AB scheme in the Eq.(2.71). The AB scheme simplifies the discussion of the quark helicity content of the nucleon. In the (\overline{MS}) scheme the g_1 structure function is composed only of quark helicity distributions.

Eq.(2.71) relates gluon helicity ΔG and a_0 . According to Eq.(2.71), a sufficiently large gluon contribution could restore Ellis-Jaffe sum rule prediction for $\Delta\Sigma$. The measured a_0 around 1/3 can be in agreement with the Ellis-Jaffe sum rule prediction ($\Delta\Sigma \simeq 0.65$) if the $\alpha_s \Delta G \simeq 0.7$ what corresponds $\Delta G > 2$ at the several GeV scale. The expectation that the gluon polarisation is large was a "driving force" for generation of the polarised DIS experiments, that aim to precisely measure the gluon polarisation. The restoration of the Ellis-Jaffe sum rule prediction does not mean that the nucleon's spin structure is again a simple consequence of the naive QPM, with or without relativistic corrections, where spin of the nucleon is carried by the valence quarks only. First of all the existence of a confining space for the quarks (as in e.g. the MIT bag model) implies the existence of OAM of the confined quarks. The large gluon polarisation needed to restore the Ellis-Jaffe sum rule implies that the OAM contribution should be large so as to obey:

$$\frac{1}{2} = \frac{1}{2} \Delta\Sigma + \Delta G + L, \quad (2.72)$$

where L refers to the OAM of the quarks and gluons. The decomposition of the total angular momentum for helicity and orbital momentum part is a complicated matter and depends on the definition of the total/orbital angular momentum [14]. Therefore the above spin decomposition for the longitudinally polarised nucleon should be considered "qualitative". The problem of the precise definition of the OAM will be discussed in the chapter 7. Here $\Delta\Sigma$ and ΔG are well defined helicity distributions in the framework of the QCD improved QPM an L simple carries the remainder of the nucleon spin.

The contribution of the gluon helicity to the nucleon spin can be estimated by using the DGLAP evolution equations in QCD fits to the measured g_1 . The procedure is analogous

to the QCD fits made for the polarisation averaged structure functions. Perturbative QCD predicts the change of the parton distribution functions with the scale Q^2 , given a functional form in x for the quark and gluon helicities at a given reference Q_0^2 . It is then possible to evaluate Δq and ΔG at any value of Q^2 . For each measured value of $g_1(x, Q^2)$ the corresponding predicted $g_1(x, Q^2)$ is evaluated and a χ^2 minimization is performed using the body of measurements. The parameters of the assumed x -dependence of $\Delta q(x, Q_0^2)$ and $\Delta G(x, Q_0^2)$ are fitted by χ^2 minimisation. Several QCD fits have been made by different groups using inclusive as well as semi-inclusive data available. The LSS05 fit [104] is shown in Fig. 2.8. Another QCD analysis applied to the polarised data can be found in [128]. The functional form of the parton distributions in x , not predicted by QCD, is chosen to be smooth and flexible enough to ensure that the fit converges with a reasonable χ^2 . The functional form is rarely motivated by rigorous Physics principles. Instead standard polynomial type parameterizations in terms of Regge inspired low- x behavior connected to high- x counting rules by ad-hoc ansatz for intermediate x behaviour is used. An interesting exception is the quantum statistical approach proposed in [129] where parton helicity distribution functions for quarks are given by Fermi-Dirac functions while the gluon helicity distribution is described by a black body inspired Bose-Einstein function. This approach allows one to consider simultaneously the polarisation dependent and polarisation independent PDFs with Physics motivated functional forms. The agreement with present data is also good.

Another example is given in Fig. 2.11 which shows the QCD fits for quark and gluon helicity distribution from the global analysis fit from DSSV group [46, 47]. In this fit not only inclusive DIS process but also semi-inclusive (SIDIS process) data and RHIC collider hadroproduction data are taken into account. The most important problem in the procedure is the treatment of uncertainties. For details the reader is referred to [47]. The value of the first moment of the gluon helicity distribution was found to be $\Delta G(Q^2 = 4 \text{ GeV}^2) = -0.096$. Since the uncertainties due to extrapolation over the unmeasured x range are hard to be estimated the error on this value is not quoted but the error bands seen in Fig. 2.11 are large. The truncated first moment of $\Delta G(x, Q^2)$ in the range $0.001 < x < 1$ was found to be $\Delta G^{[0.001 \rightarrow 1]} = 0.13 \pm 0.18$.

The COMPASS collaboration has also performed a QCD analysis of all available data on g_1 structure function, including new COMPASS measurements [8]. Two solutions for $\Delta G(x, Q^2)$ have been found: one with a positive and one with a negative value for ΔG . The absolute value of the first moment of the gluon helicity distribution was found to be in both cases $|\Delta G| \approx 0.2-0.3$. The stability of these results with respect to a change in $\alpha_s(m_Z^2)$: when $\alpha_s(m_Z^2)$ is varied by ± 0.005 was checked and the results are not changed by more than half a standard deviation. The first moment of the singlet quark distribution derived from

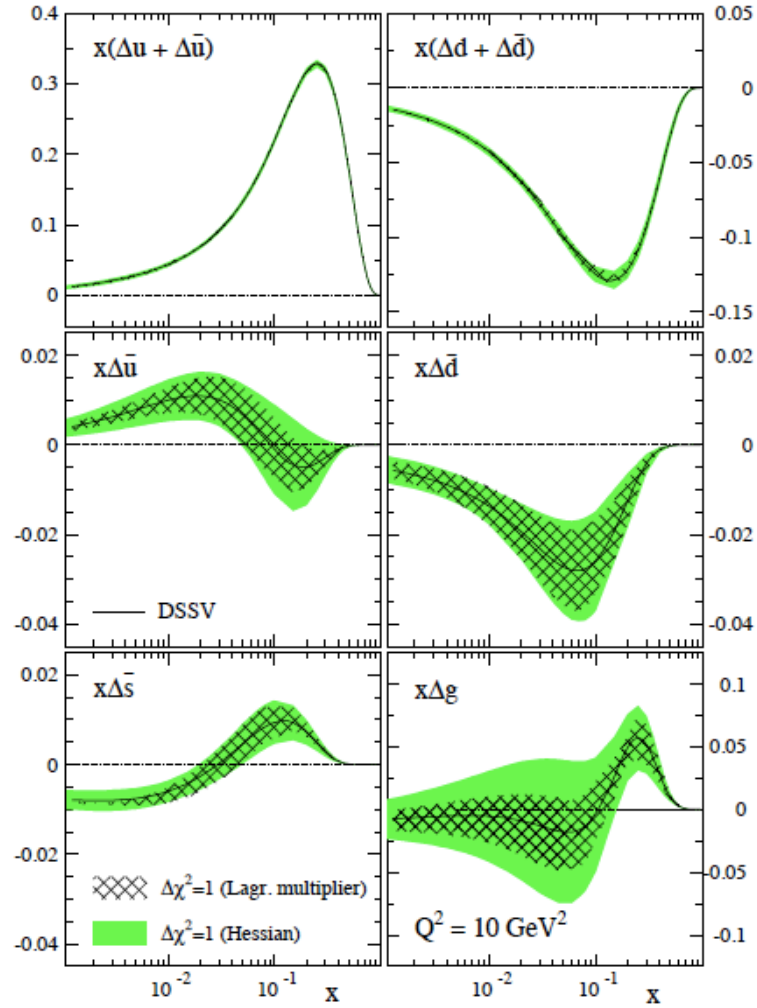


Figure 2.11: The polarised PDFs of the proton at $Q^2 = 10 \text{ GeV}^2$ in the (\overline{MS}) scheme along with their $\Delta\chi^2 = 1$ uncertainty bands computed with Lagrange multipliers and the improved Hessian approach [47].

the fits to the g_1 data was found to be:

$$\Delta\Sigma(Q^2 = 3 \text{ GeV}^2) = 0.30 \pm 0.01(\text{stat.}) \pm 0.02(\text{evol.}). \quad (2.73)$$

From these two examples one can conclude that the central value of ΔG is likely small and that the uncertainty remains sizable.

To achieve better precision of the polarised gluon distribution, the g_1 structure function has to be measured over in a wider kinematic range. At present this range is rather limited compared to the range covered by measurements of the unpolarised structure function F_2 . Such an increase will be possible only at a future polarised electron-ion collider [42]

Since the gluon polarisation determined from QCD fits has large uncertainties even if all data (including SIDIS and RHIC ones) are used, additional direct measurements of the gluon polarisation are needed. This is a one of the main goals of the COMPASS experiment and this is the main topic of this thesis.

2.3 The Gerasimov-Drell-Hearn sum rule

The very interesting sum rule has been obtained by Gerasimov [130], Drell and Hearn [131], the GDH sum rule:

$$\int_{\text{threshold}}^{\infty} \frac{d\nu}{\nu} (\sigma_{1/2} - \sigma_{3/2}) = \frac{2\pi^2\alpha}{M^2} \kappa^2, \quad (2.74)$$

where κ is an anomalous magnetic moment of the target nucleon, $\sigma_{1/2,3/2}$ are the cross sections for the absorption of the real photons with energy ν and with spin anti-parallel and parallel, respectively. M is a mass of the target particle. This sum rule was obtained from the very general principles like causalities, unitarity, Lorentz invariance, gauge invariance. The unsubtracted dispersion relation is only assumed for g_1 structure function. The GDH sum rule can be rewritten defining first the integral $I(Q^2)$ in the following way:

$$I(Q^2) = \frac{2M^2}{Q^2} \int_0^1 dx g_1(x, Q^2) = \frac{2M^2}{Q^2} \Gamma_1(Q^2). \quad (2.75)$$

Then the GDH sum rule corresponds to the relation $I(0) = -\frac{1}{4}\kappa^2$. Investigating Q^2 dependence of the integral $I(Q^2)$ gives a chance to understand the "bridge" between the perturbative regime dominated by QCD and QPM and the non-perturbative effective models (chiral approximation, vector-meson dominance etc.) In this intermediate region the important role plays Δ resonance. The very accurate data of the GDH sum rule measurement have been collected by experiments at ELSA and MAMI accelerators [132, 133]. The interesting generalization of the GDH sum rule for parity violation case (parity violation GDH sum rule) have been discussed in [134, 135].

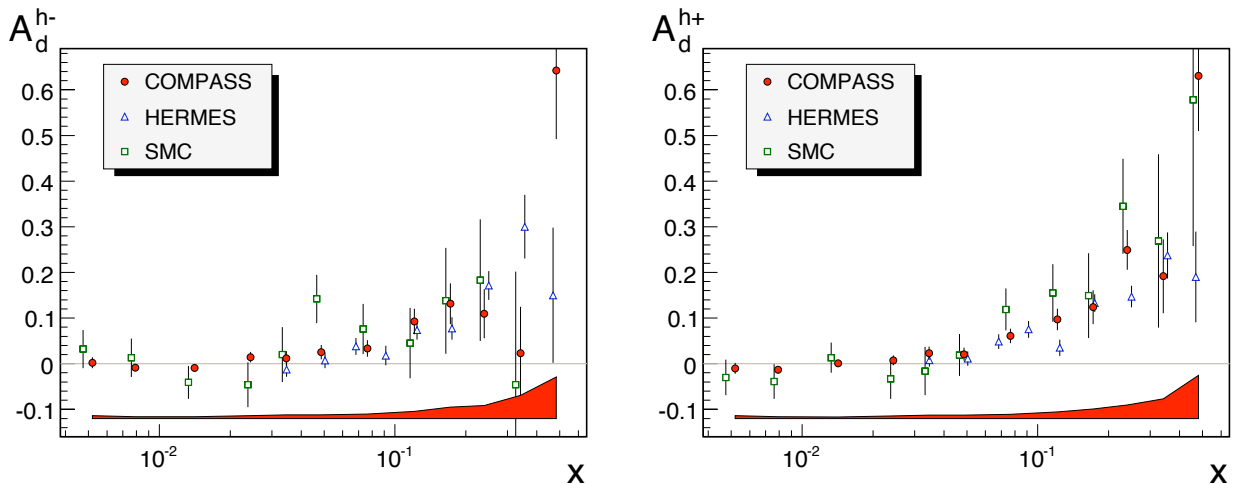


Figure 2.12: Hadron asymmetries $A_d^{h^+}$ (left) and $A_d^{h^-}$ (right) measured by COMPASS [140] SMC [141] and HERMES [71] experiments. The bands at the bottom of the figures show the systematic errors of the COMPASS measurements.

2.4 Semi-inclusive asymmetries and the flavour separation

The asymmetry measured in the inclusive DIS process requires observation of the scattered lepton only. Additional information about the nucleon structure can be obtained if in addition to the lepton one or more hadrons in the final state are measured. The interpretation of such data in general requires knowledge of the fragmentation functions (FF). There is however a special combination of the semi-inclusive asymmetries (SIDIS) called difference asymmetry which is independent of the fragmentation functions in the first approximation (LO QCD). The difference asymmetry approach for the extraction of helicity distributions was introduced in [136]. It has been used in the SMC analysis [137] and has been discussed further in [138, 139]. The COMPASS result has been reported in [140]. The semi-inclusive spin asymmetries for positive and negative hadrons h^+ and h^- are defined similarly to the inclusive cross section asymmetry by:

$$A^{h^+} = \frac{\sigma^{\overleftrightarrow{\leftarrow}, h^+} - \sigma^{\overleftrightarrow{\rightarrow}, h^+}}{\sigma^{\overleftrightarrow{\leftarrow}, h^+} + \sigma^{\overleftrightarrow{\rightarrow}, h^+}}, \quad A^{h^-} = \frac{\sigma^{\overleftrightarrow{\leftarrow}, h^-} - \sigma^{\overleftrightarrow{\rightarrow}, h^-}}{\sigma^{\overleftrightarrow{\leftarrow}, h^-} + \sigma^{\overleftrightarrow{\rightarrow}, h^-}}, \quad (2.76)$$

where the arrows indicate the relative beam and target spin orientations. Data on these asymmetries from COMPASS [140], HERMES [71] and SMC [141] are shown in Fig. 2.12.

Under the assumption that hadrons in the current fragmentation region are produced by independent quark fragmentation, the semi-inclusive asymmetries A^{h^+} and A^{h^-} can be

written:

$$A^h(x, z, Q^2) = \frac{\sum_q e_q^2 \Delta q(x, Q^2) D_q^h(z, Q^2)}{\sum_q e_q^2 q(x, Q^2) D_q^h(z, Q^2)}, \quad (2.77)$$

in LO QCD. Here $\Delta q(x, Q^2)$ and $q(x, Q^2)$ are the polarisation dependent and polarised independent parton PDFs, respectively, and $D_q^h(z, Q^2)$ is the fragmentation function of a parton q into a hadron h .⁴

The difference asymmetry is defined as the spin asymmetry for the difference of the cross sections for positive and negative hadrons:

$$A^{h^+-h^-} = \frac{(\sigma^{\vec{\epsilon}, h^+} - \sigma^{\vec{\epsilon}, h^-}) - (\sigma^{\vec{\epsilon}, h^+} - \sigma^{\vec{\epsilon}, h^-})}{(\sigma^{\vec{\epsilon}, h^+} - \sigma^{\vec{\epsilon}, h^-}) + (\sigma^{\vec{\epsilon}, h^+} - \sigma^{\vec{\epsilon}, h^-})}. \quad (2.78)$$

In LO QCD and under the assumption that isospin and charge conjugation are good symmetries, the fragmentation functions D_q^h cancel in $A^{\pi^+-\pi^-}$. In addition, in the case of an isoscalar target (deuteron) and with the assumption $\Delta s = \Delta \bar{s}$, the difference asymmetries for pions and kaons are both equal to the valence quark polarisation

$$A_N^{\pi^+-\pi^-} = A_N^{K^+-K^-} = \frac{\Delta u_v + \Delta d_v}{u_v + d_v}. \quad (2.79)$$

The valence quark distributions q_v are defined here as $q_v = q - \bar{q}$. Since kaons contribute to the asymmetry in the same way as pions, their identification is not needed, allowing one to improve the statistical errors of the measurements. At higher order in QCD the difference asymmetries still determine the valence quark polarisation without any assumption on the sea and gluon densities [138] but the fragmentation functions no longer cancel out. Their effect is expected to be small [139] compared to LO expression.

The relation between the difference asymmetries of Eq. (2.78) and the single hadron asymmetries of Eq. (2.76) is:

$$A^{h^+-h^-} = \frac{1}{1-r} (A^{h^+} - r A^{h^-}), \quad \text{with } r = \frac{\sigma^{h^-}}{\sigma^{h^+}}, \quad (2.80)$$

where ratio r is a subject to acceptance corrections because positive and negative hadrons, produced at identical angles, normally transverse different regions of the spectrometer. The polarised valence quark distribution $\Delta u_v + \Delta d_v$ can be obtained by multiplying $A_d^{h^+-h^-}$ by the unpolarised valence distribution. The sea contribution to the unpolarised structure

⁴The above formula does not account for the full complexity of the hadronisation process like described in e.g. Lund string fragmentation model [142] and its validity in low energy fixed target experiments has been questioned [143]. It has nevertheless been shown to hold as a good approximation at the energy of COMPASS [144].

function F_2 decreases rapidly with increasing x and becomes smaller than 0.1 for $x > 0.3$. Due to the positivity conditions $|\Delta q| \leq q$ and $|\Delta \bar{q}| \leq \bar{q}$, the polarised sea contribution to the nucleon spin also becomes negligible in this region. In view of this, the evaluation of the valence spin distribution for large x can be replaced by a more accurate one obtained from the inclusive interactions (LO):

$$\Delta u_v + \Delta d_v = \frac{36}{5} \frac{g_1^d}{(1 - 1.5\omega_D)} - \left[2(\Delta \bar{u} + \Delta \bar{d}) + \frac{2}{5}(\Delta s + \Delta \bar{s}) \right]. \quad (2.81)$$

The first moment of the polarised valence distribution, Γ_v has been estimated at the reference $Q^2 = 10 \text{ GeV}^2$ point as [140]:

$$\Gamma_v(0 < x < 1) = 0.41 \pm 0.07 \text{ (stat.)} \pm 0.06 \text{ (syst.)}. \quad (2.82)$$

The assumption of a fully flavour symmetric sea $\Delta \bar{u} = \Delta \bar{d} = \Delta s = \Delta \bar{s}$ leads to $\Gamma_v(0 < x < 1) = a_8$. As shown in Fig. 2.13 (right), the experimental value is two standard deviations below the value of $a_8 = 0.58 \pm 0.03$ derived from neutron and hyperon β decays. It has been suggested that a value of the valence contribution Γ_v smaller than a_8 (as expected from the constituent quark models) could be a hint that a so far unmeasured part of the nucleon's spin resides at $x = 0$ [145].

An estimate of the light sea quark contribution to the nucleon spin can be obtained by combining the values of Γ_v , Γ_1^N and a_8 :

$$\Delta \bar{u} + \Delta \bar{d} = 3\Gamma_1^N - \frac{1}{2}\Gamma_v + \frac{1}{12}a_8. \quad (2.83)$$

The result is found to be zero in contrast to the non-zero result for $\Delta s + \Delta \bar{s}$. At LO in QCD the strange quark polarisation is given by

$$\Delta s + \Delta \bar{s} = 3\Gamma_1^N - \frac{5}{12}a_8 = -0.09 \pm 0.01 \text{ (stat.)} \pm 0.02 \text{ (syst.)} \quad (2.84)$$

at $Q^2 = 10 \text{ GeV}^2$ [140]. The zero result for the sea $\Delta \bar{u} + \Delta \bar{d}$ suggests that if $\Delta \bar{u}$ and $\Delta \bar{d}$ are different from zero, they must be of opposite sign. Opposite signs of $\Delta \bar{u}$ and $\Delta \bar{d}$ are predicted in several models, among them in the quantum statistical approach of Refs [129, 146] (see also [147] and references therein).

Semi-inclusive DIS cross-section asymmetries, where in addition to the scattered lepton, identified pions and kaons are detected, are sensitive to the individual quark and antiquark flavours. With Inclusive A_1 measurements and the knowledge of unpolarised PDFs and fragmentation functions the flavour separation can be performed into the helicity distributions for every quark flavours. To do the complete decomposition data from the proton and

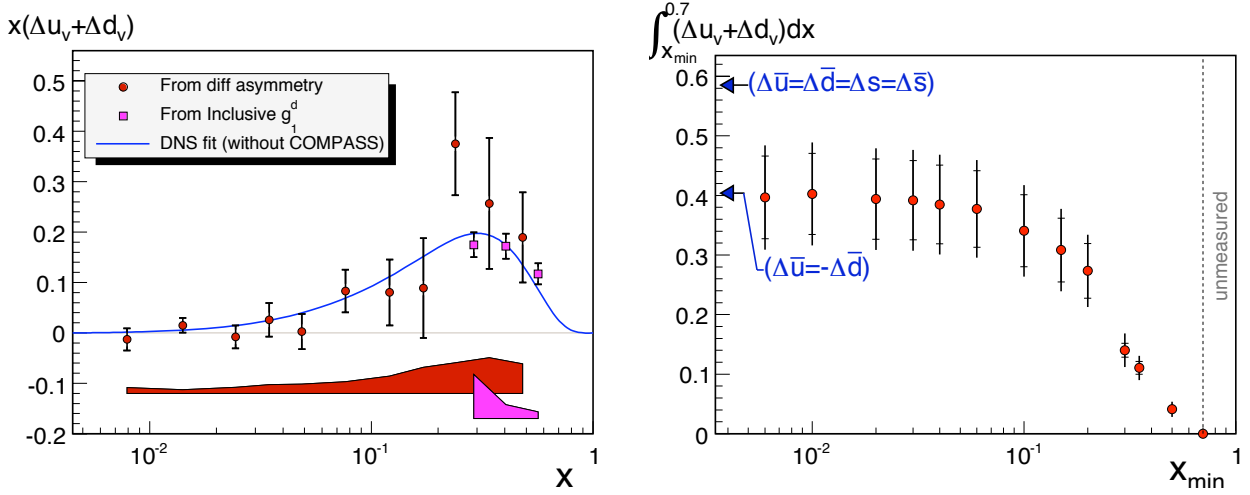


Figure 2.13: Left: Polarised valence quark distribution $x(\Delta u_v(x) + \Delta d_v(x))$ from COMPASS [140] evolved to $Q^2 = 10 \text{ GeV}^2$ according to the DNS fit at LO [148] (line). Three additional points at high x are obtained from g_1^d [8]. The two shaded bands show the systematic errors for the two sets of values. Right: The integral of $\Delta u_v(x) + \Delta d_v(x)$ over the range $0.006 < x < 0.7$ as the function of the low x limit, evaluated at $Q^2 = 10 \text{ (GeV}/c)^2$.

deuteron/neutron targets are needed. The first measurements of SIDIS asymmetries were performed by the EMC Collaboration [73]. More recently, the SMC Collaboration has measured SIDIS asymmetries for unidentified charged hadrons [141] as presented in Fig. 2.12. The HERMES Collaboration has reported SIDIS asymmetries for charged pion production on a proton target and for charged pion and kaon production on a deuteron target [71]. These asymmetries were used for a flavour decomposition into five helicity distributions. However these data do not permit the extraction of $\Delta \bar{s}$. The LO QCD evaluation of the isoscalar polarised valence, sea and strange distributions, $\Delta u_v + \Delta d_v$, $\Delta \bar{u} + \Delta \bar{d}$ and $(\Delta s + \Delta \bar{s})/2$, all derived from DIS and SIDIS asymmetries on a polarised deuteron target only, have been presented in [149]. New semi-inclusive asymmetries for scattering of high-energy muons off a polarised proton target for production of identified charged pions ($A_{1,p}^{\pi^+}$, $A_{1,p}^{\pi^-}$) and of identified charged kaons ($A_{1,p}^{K^+}$, $A_{1,p}^{K^-}$) measured by COMPASS have been published in [150]. These measurements include the previous COMPASS results on ($A_{1,d}^{\pi^+}$, $A_{1,d}^{\pi^-}$) and ($A_{1,d}^{K^+}$, $A_{1,d}^{K^-}$) SIDIS deuteron data as well as inclusive double-spin asymmetries $A_{1,p}$ [68] and $A_{1,d}$ [149]. Using these measurements a full flavour decomposition in LO has been performed, thus accessing all up, down and strange quark and antiquark helicity distributions separately.

The inclusive and SIDIS asymmetries obtained by COMPASS [68, 149, 150] and HERMES [6, 71] are shown in Figs. 2.14 and 2.15.

Based on the measured SIDIS asymmetries, there is no evidence for a significant difference

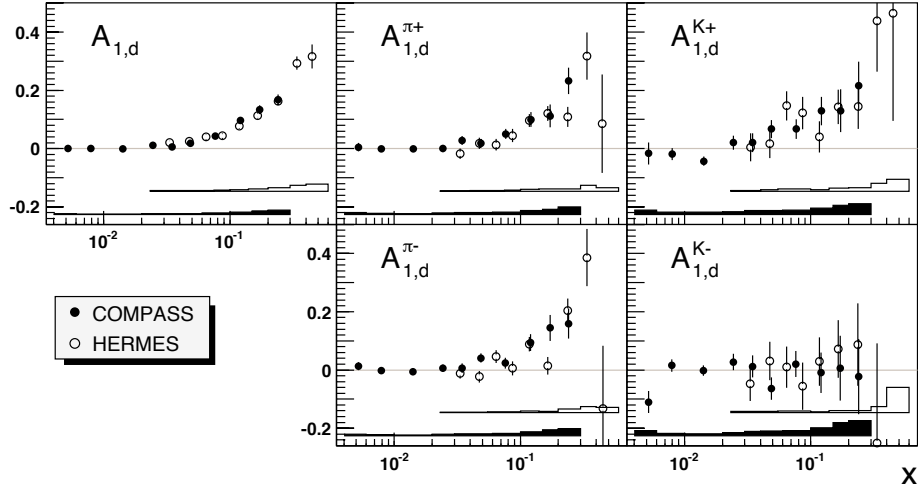


Figure 2.14: Comparison of final deuteron target asymmetries of COMPASS [149] as a function of x with results of HERMES [71]. The bands at bottom of the graphs represent the size of the systematic uncertainties. The filled symbols markers and bands correspond to the COMPASS data whereas the open markers and bands are those by HERMES.

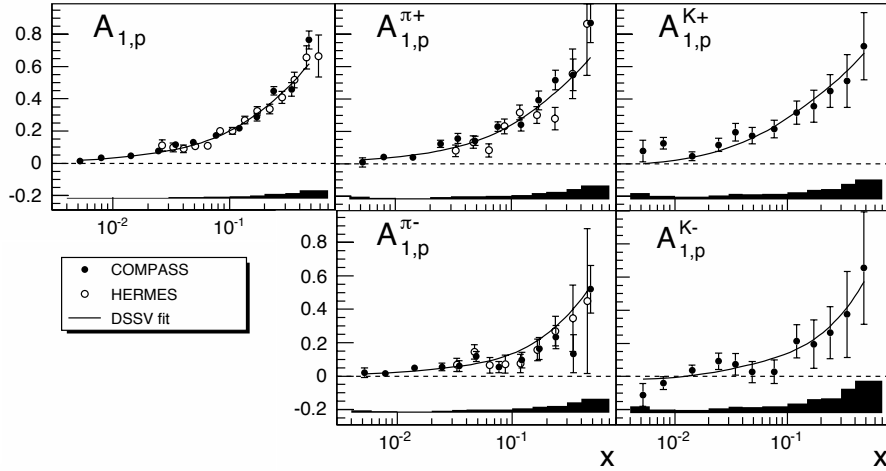


Figure 2.15: The inclusive asymmetry $A_{1,p}$ [68] and the semi-inclusive asymmetries $A_{1,p}^{\pi^+}$, $A_{1,p}^{K^+}$, $A_{1,p}^{\pi^-}$, $A_{1,p}^{K^-}$ [150] measurements by COMPASS (closed circles). The bands at the bottom of each plot show the size of the systematic errors. The $A_{1,p}$, $A_{1,p}^{\pi^+}$ and $A_{1,p}^{\pi^-}$ data by HERMES [6, 71] (open circles) are shown for comparison. The curves show the predictions of the DSSV fit [46, 47].

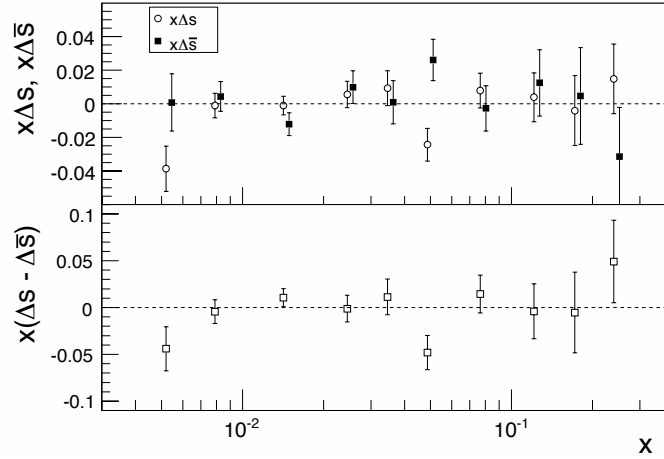


Figure 2.16: Comparison of $x\Delta s$ (open circles) and $x\Delta\bar{s}$ (squares) at $Q_0^2 = 3 \text{ GeV}^2$ (top) and the corresponding values of the difference $x(\Delta s - \Delta\bar{s})$ (bottom). The MRST parameterisation of the unpolarised PDFs [154] has been used in the analysis [150].

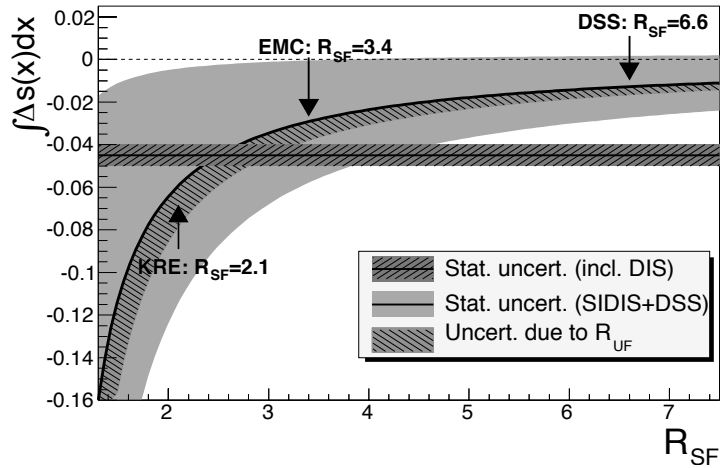


Figure 2.17: Integral of Δs over the COMPASS measured range of x , as a function of the ratio R_{SF} for R_{UF} fixed at the DSS value of 0.13 (thick solid curve). The light-grey area shows the statistical uncertainty and the hatched band inside of it shows the effect of increasing R_{UF} to 0.35 (EMC value). The horizontal band represents the full moment of Δs derived from the COMPASS value of the first moment of $g_1^d(x)$. The values of R_{SF} corresponding to the DSS [155], EMC[151] and KRE[158] parameterisations of FFs are indicated by the arrows.

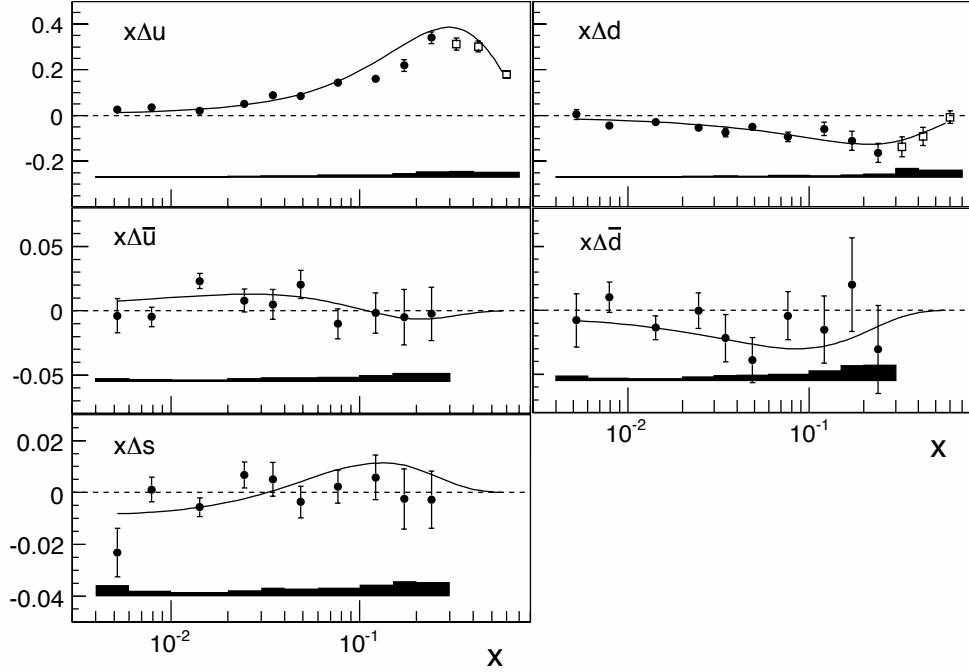


Figure 2.18: The quark helicity distributions $x \Delta u$, $x \Delta d$, $x \Delta \bar{u}$, $x \Delta \bar{d}$ and $x \Delta s$ at $Q_0^2 = 3 \text{ GeV}^2$ as a function of x . The values for $x < 0.3$ (black dots) are derived at LO from the COMPASS spin asymmetries using the DSS fragmentation functions [155]. Those at $x > 0.3$ (open squares) are derived from the values of the polarised structure function $g_1(x)$ quoted in [8, 68] assuming $\Delta \bar{q} = 0$. The bands at the bottom of each plot show the systematic errors. The curves show the predictions of the DSSV fit calculated at NLO[46, 47].

between $\Delta s(x)$ and $\Delta \bar{s}(x)$ in the x -range covered by the COMPASS data, see Fig. 2.16. This remains valid when instead of the DSS fragmentation functions the older fragmentation functions by the EMC [151] are used. The results on $\Delta s(x)$ and $\Delta \bar{s}(x)$ are at variance with the $SU(3)$ Chiral Quark-Soliton model prediction that $|\Delta s(x)| \gg |\Delta \bar{s}(x)|$ [153] and are compatible with quantum statistical models prediction that $\Delta s(x) - \Delta \bar{s}(x)$ is zero [152] or small [129].

Under the assumption that the distributions of Δs and $\Delta \bar{s}$ are equal (at least in the measured region) better precision can be obtained for the other helicity distributions. The results for the quark helicity distributions Δu , Δd , $\Delta \bar{u}$, $\Delta \bar{d}$ and Δs with the assumption that $\Delta s = \Delta \bar{s}$, are shown in Fig. 2.18.

The COMPASS helicity distributions are in good qualitative agreement with the results from HERMES [6]⁵. As the DSSV fit results, shown in Fig. 2.18), have been obtained at

⁵A quantitative comparison has not been made since the HERMES helicity distributions are extracted under different assumptions for the fragmentation functions and for the unpolarised flavour distributions.

NLO approximation, the comparison with the experimental results derived at LO is thus only qualitative. Nevertheless, the curves reproduce fairly well the shape of the data, confirming a previous observation that a direct extraction at LO forms a reasonable estimate of the shape of the helicity distributions [156].

The values of the strange quark helicity distribution confirm the results obtained by COMPASS from the deuteron data alone [149]. This distribution is of particular interest in view of the apparent contradiction between the SIDIS results and the negative first moment obtained from the spin structure function $g_1(x)$ [8]. The evaluation of the first moment of $\Delta s(x)$ from inclusive measurements relies on the value of the octet axial charge a_8 , which is derived from hyperon weak decays under the assumption of $SU(3)_f$ symmetry. Recent model calculations suggest that a_8 may be substantially smaller than the $SU(3)_f$ value and become close to the singlet axial charge a_0 extracted from the polarised DIS data [157]. If confirmed in experiment, the inclusive data would no longer imply a negative value of Δs .

On the other hand the semi-inclusive results on the quark helicity distribution $\Delta q(x)$ strongly depend on the choice of fragmentation functions and $\Delta s(x)$ is particularly sensitive. The relation between the semi-inclusive asymmetries and the quark helicity distributions depends on the ratios of fragmentation functions, integrated over the range of z that is measured by the experiment. In the case of COMPASS this is ($0.2 < z < 0.85$) [150]. Relevant for the kaon asymmetries and hence $\Delta s(x)$ are the unfavoured-to-favoured FF ratio, R_{UF} , and strange-to-favoured FF ratio, R_{SF} :

$$R_{UF} = \frac{\int D_d^{K^+}(z)dz}{\int D_u^{K^+}(z)dz}, \quad R_{SF} = \frac{\int D_s^{K^+}(z)dz}{\int D_u^{K^+}(z)dz}. \quad (2.85)$$

The Fig. 2.17 shows the variation of the integral of $\Delta s(x)$ over the measured region as a function of R_{SF} with R_{UF} fixed at DSS value of 0.13 [155]. The resulting values for Δs are close to zero and are larger than the negative full moment derived from the inclusive analysis.

Due to the crucial dependence on the FF ratios in the determination of Δs , the precise determination of these ratios is important. Although of key interest from a flavour symmetry and model calculation point of view, the values of the strange quark distribution $\Delta s(x)$ and the value of its first moment appear small. Therefore, the strange quark spin contribution to the nucleon spin budget is less important.

The sum of all quark and antiquark contributions $\Delta\Sigma = 0.32 \pm 0.03(stat.)$, obtained from the SIDIS asymmetries [150] is nearly identical to the value of $a_0 = 0.33 \pm 0.03(stat.)$ derived from the first moment of $g_1^d(x)$ using the value for the octet axial charge a_8 [8]. The sum of the valence quark contributions $\Delta u_v + \Delta d_v = 0.39 \pm 0.03(stat.)$ is also consistent with

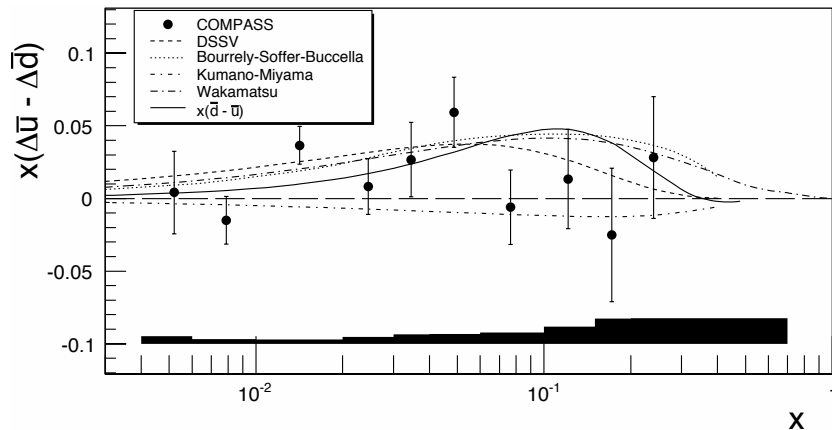


Figure 2.19: The flavour asymmetry of the helicity distribution of the sea $x(\Delta\bar{u} - \Delta\bar{d})$ at $Q_0^2 = 3 \text{ GeV}^2$. The shaded area displays the size of the systematic error. The dashed curve is the result of the DSSV fit at NLO. The other curves are model predictions by Wakamatsu[153] (long dash-dotted line), Kumano and Miyama [160] (short dash-dotted line) and Bourrely, Soffer and Buccella [159] (dotted line). The solid curve shows the MRST parameterisation for the unpolarised difference $x(\bar{d} - \bar{u})$ at NLO.

the determination based on the difference asymmetry of positive and negative hadrons in a subsample of the deuteron data ($0.41 \pm 0.07(\text{stat.})$ at $Q^2 = 10 \text{ GeV}^2$).

The flavour asymmetry of the helicity distribution of the sea, $\Delta\bar{u} - \Delta\bar{d}$, is shown in Fig. 2.19. Although compatible with zero, the values indicate a slightly positive distribution. The DSSV fit at NLO [46] and the unpolarised asymmetry $\bar{d} - \bar{u}$ are shown for comparison. The first moment $\Delta\bar{u} - \Delta\bar{d}$ truncated to the range $0.004 < x < 0.3$ is $0.06 \pm 0.04(\text{stat.}) \pm 0.02(\text{syst.})$. It is worth noting that the polarised first moment is about one standard deviation smaller than the unpolarised one truncated to the same range (≈ 0.10 for the MRST parameterisation[154]). The data thus disfavour models predicting $\Delta\bar{u} - \Delta\bar{d} \gg \bar{d} - \bar{u}$ (see [147, 49] and references therein). Three model predictions are shown in Fig. 2.19. The quantum statistical approach model [159] and the $SU(3)$ version of the Chiral Quark-Soliton model of [153] both predict positive distributions, while the Meson Cloud model of [160] predicts a slightly negative distribution. Very recently [161] the predictions for antiquarks polarisation have been obtained combining information from COMPASS Γ_v result, integrated magnetic moments distributions of quarks, β decays of baryons and finally taking into account the orbital angular momenta of valence quarks from Lattice QCD calculations (see chapter 7). The approach is based on the model for magnetic moments of $SU(6)$ octet baryons [162]. The obtained results for difference between u and d antiquarks polarisations are consistent with COMPASS and HERMES measurement.

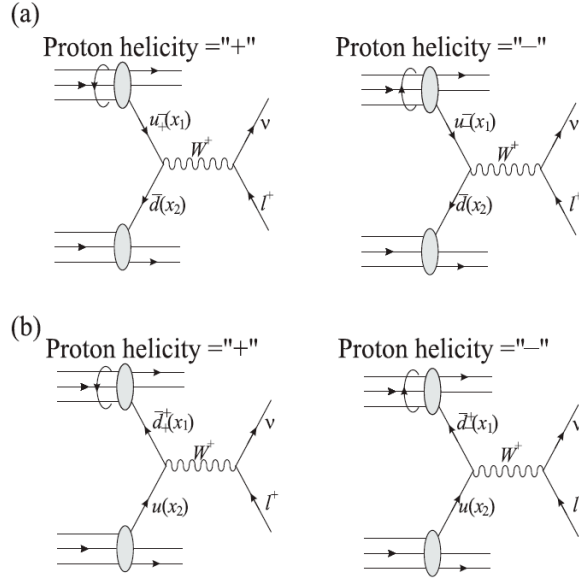


Figure 2.20: Production of the W^+ boson in $p \rightarrow p$ collision (lowest order). (a) Δu is probed in polarised proton, (b) $\Delta \bar{d}$ is probed (Fig. from [163]).

Within statistical errors, the COMPASS data are compatible with all three predictions shown in Fig. 2.19. The sum of the light quark helicity distributions, $\Delta \bar{u} + \Delta \bar{d}$, is mainly constrained by the deuteron data and nearly identical to the result published in [149]. The first moment truncated to the range of the data is found to be $-0.03 \pm 0.03(\text{stat.}) \pm 0.01(\text{syst.})$.

An interesting possibility to study the flavour decomposition is being pursued with W boson production in polarised proton-proton interactions of RHIC [163]) Within the Standard Model the W boson is produced via pure $V - A$ weak interactions and the helicity combination of the quarks is fixed in the reaction. In addition the W couples to a weak charge that correlates directly to flavours. Therefore the W boson production seems to be an ideal tool to study spin structure of the proton.

The limitations are: an energy, high enough in Tevatron [164, 165, 166] and RHIC, and small cross section which limits the precision of the measurements. The production of W bosons in proton-proton collision is dominated by u , d , \bar{u} and \bar{d} , as shown in Fig. 2.20.⁶ At RHIC different spin configurations are probed in successive beam bunches. The parity violation single-spin asymmetry is the difference of left-handed and right-handed W production divided by the sum and normalized by the beam polarisation and luminosity

⁶there is a small contamination of s , c , \bar{s} and \bar{c} due to quark mixing.

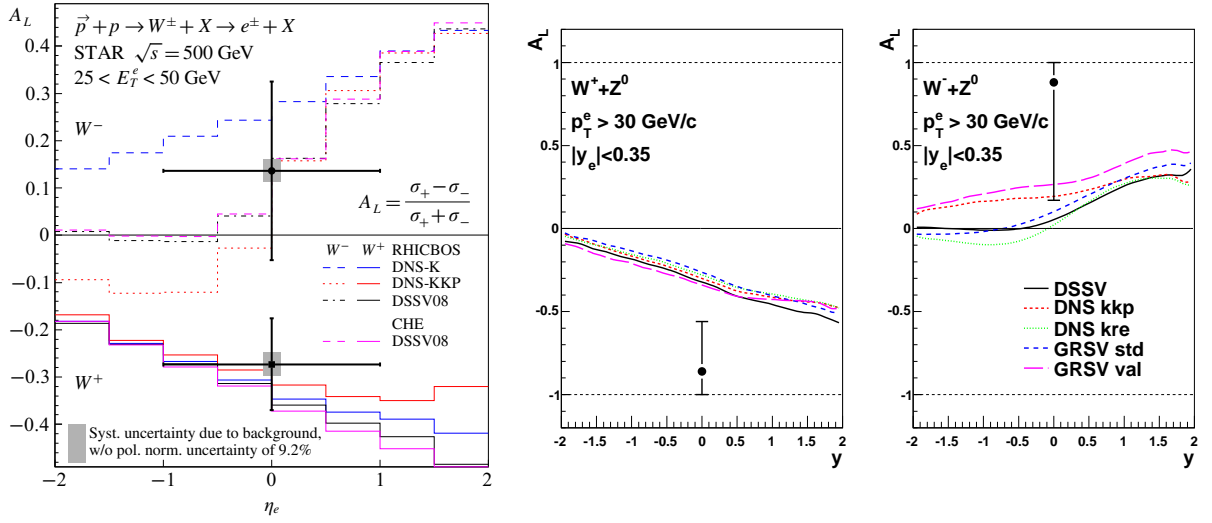


Figure 2.21: Left: Longitudinal single-spin asymmetry, A_L for W^\pm events from STAR [169] as a function of the leptonic pseudorapidity, η_e , for $25 < E_T^e < 50$ GeV in comparison to theory prediction. Right: Longitudinal single-spin asymmetry for electrons and positrons for A_L for W^\pm and Z decays measured by PHENIX [170]. The error bars represent 65% CL. The theoretical curves are from [171].

[163]. The observed asymmetry is expressed in terms of the helicity distributions of quarks as follows:

$$A_L^{W^+} = \frac{\Delta u(x_1)\bar{d}(x_2) - \Delta\bar{d}(x_1)u(x_2)}{u(x_1)\bar{d}(x_2) + \bar{d}(x_1)u(x_2)}, \quad (2.86)$$

and the similar expression for $A_L^{W^-}$ can be obtained by interchanging u and d . For large x_1 (rapidity $y_W \gg 0$) the $A_L^{W^+} \rightarrow \Delta u/u$ while for large x_2 ($y_W \ll 0$) the $A_L^{W^-} \rightarrow \Delta\bar{d}/\bar{d}$ and the flavour can be separated. The effect survives the higher order corrections to the W production [167, 168] and the predicted asymmetry is large. The experimental difficulty is that the W is observed via its leptonic decay and only charged lepton is observed. Therefore it is not known if quark or antiquark is provided by polarised proton. The first results of the measurement of the single-spin parity violation asymmetry A_L^W have been reported very recently by the STAR [169] and PHENIX [170] collaborations. The measured large asymmetries probe the polarised PDFs at much larger scales than in polarised DIS experiments. The results shown in Fig. 2.21 agree well with NLO and resummed calculations [46, 47, 171]. The reported results have poor precision so far and more data are needed.

2.5 Summary of the nucleon's longitudinal spin structure

The results presented in this chapter can be summarized as follows:

- It is confirmed that quark spin content of the nucleon spin is only around 1/3. This is a direct conclusion from the Ellis-Jaffe sum rule, which relates the first moment of the polarisation dependent g_1 structure function to β decay of the spin 1/2 hyperons octet. This result is also confirmed by SIDIS data which make it possible to determine the helicity distributions of quarks using additional information in the form of FFs. The different QCD fits obtain similar results. A global analysis QCD fit that takes into account SIDIS and RHIC data suggests even smaller value of about 1/4 for the quark spin contribution to the nucleon spin [46].
- The original Ellis-Jaffe sum rule is violated unless the gluon polarisation is large. A large value of the gluon polarisation would require a large, compensating angular momentum contribution so as to satisfy the total value of 1/2 in the nucleon spin sum rule. Present data provide no evidence for such a large ΔG . The Bjorken sum rule is confirmed.
- Inclusive measurements allow one to conclude that the strange (anti)quark polarisation is compatible with zero while $\Delta\bar{u}$ and $\Delta\bar{d}$, if different from zero, must be of opposite sign. The SIDIS flavour decomposition confirms that the polarisation of the "sea" quarks is very small and that the "asymmetric" scenario, $\Delta\bar{u} = -\Delta\bar{d}$, is preferred.
- The valence u and d quarks are highly polarised with opposite signs (u along the nucleon spin orientation) while the gluon polarisation determined indirectly from the QCD fits seems to be small. Present data don't allow to constrain polarised gluons and the uncertainties of these results are large. Therefore the scenario, where gluons are enough polarised to satisfy the 1/2 nucleon sum rule is still not excluded. The large polarised or the unpolarised gluons require the important extension of the QPM: the contribution from the angular momentum of quarks and gluons.

The precise data show that there is the deficit between the spin of the nucleon and the total spin carried by quark spins. Various theories have been put forward to explain this observation. One of them proposes that the spin dependent structure function g_1 is divergent for very small x [97]. The SMC and COMPASS precision data on g_1 for small x provide no evidence for this hypothesis. Nevertheless, one of the uncertainties in the determination

of the moment of g_1 remains the small x behavior in the unmeasured region at small x . Another possibility could be that the strange quarks are polarised. An experiment at MIT-Bates [172] reported a non-zero strange quark magnetic form factor for the proton. However the measured effect is opposite to what would be expected from DIS measurements. Again DIS and SIDIS data provide no evidence for this possibility as the measured Δs is close to zero. Therefore the interpretation of the results is still unclear.

A large value for the gluon polarisation and the role of the anomaly is a natural solution in the QCD improved QPM. Indirect gluon polarisation measurements based on QCD evolution suggest a rather small value of ΔG . Direct gluon polarisation measurements lead to the conclusion that gluons are not largely polarised, as will be discussed in the next chapters in this thesis.

Skyrme based models, e.g. [173] in the chiral limit and in leading order $1/N$ expansion predict that a large fraction of the nucleon spin should originate from OAM. This possibility seems to be a most interesting and - in the light of the present data - probable scenario. The decomposition of the nucleon spin into angular momentum part is a non trivial issue and it remains an open question if OAM is Skyrme-like.

The OAM contribution to the spin of the nucleon complicates the simple picture of the nucleon in the QPM and even in QCD improved QPM. The first step is to go beyond the collinear approximation used in the naive QPM.

In the next chapter the transverse spin structure of the nucleon is briefly discussed.

Chapter 3

Transverse spin structure of the nucleon

Collins and Sivers asymmetries, measured by the COMPASS and HERMES experiments, are presented in this chapter. The transversity distribution of quarks is briefly discussed. The leading Transverse Momentum Dependent PDFs (TMDs) are defined. Their complementarity to the Generalized Parton Distribution functions (GPDs) is discussed in the context of the three-dimensional description of the nucleon structure. The basic features of the leading TMDs are presented.

3.1 Transversity PDF, Collins and Sivers asymmetries

There are three types of twist-2 parton distributions which describe nucleon internal structure in the QPM and perturbative QCD in the collinear approximation: the polarisation averaged quark (anti-quark) and gluon distributions $q(x, Q^2)$ and $G(x, Q^2)$, determined from the measured spin averaged structure functions $F_2(x, Q^2)$ and $F_1(x, Q^2)$ (or $R(x, Q^2)$), the helicity distributions of the quarks (anti-quarks) and gluons, $\Delta q(x, Q^2)$ and $\Delta G(x, Q^2)$, determined in the polarisation dependent longitudinal structure function $g_1(x, Q^2)$ and in the longitudinal double spin asymmetries for semi-inclusive processes and the transversity quark distribution, $\Delta q_\perp(x, Q^2)$. The transversity distribution describes the transversely polarised quarks inside the transversely polarised nucleon [174, 175, 176, 177]. Transversity probes the relativistic nature of the quarks inside the nucleon (for non-relativistic quarks the transversity is equivalent to the helicity distribution). In the helicity basis it corresponds to a spin-flip object. It is C-odd and chiral-odd and therefore transversity cannot be measured in inclusive polarisation dependent DIS processes. Transversity would not decouple from DIS if

some electro-weak vertex would flip chirality but γ , W^\pm and Z^0 couplings preserve chirality. Mass effects leads to chirality flip but the light quark masses are too small to come an observable effect. Therefore a "quark polarimeter" is needed. The "golden" observable is the transverse double-spin asymmetry for both polarised (anti)proton-proton collision producing lepton pair e.g. via production of J/Ψ : $\bar{p}^\uparrow p^\uparrow \rightarrow l^+ l^- X$, $p^\uparrow p^\uparrow \rightarrow l^+ l^- X$. These processes could be measured in future experiments at RHIC, GSI, JINR (Dubna) and J-Parc (Tokai). The asymmetry predicted for the GSI-HESR future experiment (PAX Collaboration) has been estimated to be up to 30% [178, 179, 180]. Factorization also holds for lepton pair production.

The non-zero Collins fragmentation function [16] allows one to measure the transversity in semi-inclusive DIS processes, where at least one hadron is observed in addition to the scattered lepton. The Collins fragmentation function is not the only twist-2 chiral-odd fragmentation function; there are several others including two-pion interference fragmentation functions [181]. Other possibilities are to study exclusive processes with vector mesons produced in the final state as discussed in [182, 183] and to exploit hyperon polarisation (Λ production). There is no gluon transversity distribution because of angular momentum conservation¹. Therefore the QCD evolution of the transversity PDFs is more similar to the evolution of the non-singlet longitudinal structure function - there is no mixing with the gluons. From this point of view transversity should be more sensitive to the quark model than to QCD effects. However, the integral of the transversity (tensor charge) as well as the axial charge is scale dependent. The spin sum rule in the transversity case is the following:

$$\frac{1}{2} = \frac{1}{2} \int_0^1 \Delta q_\perp(x) dx + L, \quad (3.1)$$

where the sum is over all quarks (antiquarks) and L stands for the OAM of quarks and gluons, projected on the direction transverse to the nucleon momentum in the infinite momentum frame. In leading order QCD the transversity distribution is upper bound by Soffers's inequality [185]:

$$|\Delta q_\perp(x, Q^2)| \leq \frac{1}{2} (q(x, Q^2) + \Delta q(x, Q^2)). \quad (3.2)$$

In SIDIS reactions off transversely polarised nucleons the transversity distribution can be accessed by measuring transverse single spin asymmetries; for proton-proton collision the double transverse spin asymmetry is measured in Drell-Yan production. Another possibility is to study azimuthal distributions within jets produced in singly polarised reactions. STAR

¹There is no chirality-flip object for gluons because chirality is defined only for fermions. Instead of the 2 units helicity-flip of structure function F_3^γ can be defined and related to gluons, see [184].

experiment is performing such an analysis. The measured asymmetries are input to global fits [186, 187] and allow one to determine the transversity PDFs from the data.

The Collins fragmentation function leads to a left-right asymmetry in the distribution of the hadron produced in the fragmentation of the transversely polarised quarks. Thus a transverse spin dependence in the azimuthal distributions of the final state hadrons can be generated in SIDIS off transversely polarised nucleons. This so-called Collins asymmetry, A_{Coll} , is proportional to the convolution of the transversity PDF and Collins FF, defined as part of the \vec{p}_T^h -dependent fragmentation function. The general \vec{p}_T^h -dependent fragmentation function is expected to be of the form

$$D_{Tq}^h(z, \vec{p}_T^h) = D_q^h(z, p_T^h) + \Delta_T^0 D_q^h(z, p_T^h) \cdot \sin(\Phi_C), \quad (3.3)$$

where $\Delta_T^0 D_q^h(z, p_T^h)$ is the T -odd Collins fragmentation function, responsible for the left-right asymmetry in the fragmentation of a transversely polarised quark. The ‘‘Collins angle’’ Φ_C was originally defined in [16] as the angle between the transverse momentum of the outgoing hadron and the transverse spin vector of the fragmenting quark, i.e.,

$$\sin \Phi_C = \frac{(\vec{p}_T^h \times \vec{q}) \cdot \vec{s}'}{|\vec{p}_T^h \times \vec{q}| |\vec{s}'|}, \quad (3.4)$$

or

$$\Phi_C = \phi_h - \phi_{s'}. \quad (3.5)$$

Since the directions of the final and initial quark spins are related to each other by $\phi_{s'} = \pi - \phi_s$, equation (3.5) becomes

$$\Phi_C = \phi_h + \phi_s - \pi. \quad (3.6)$$

As shown in Fig. 3.1, ϕ_h and $\phi_{s'}$ are the azimuthal angles of the hadron and of the struck quark spin in the coordinate system in which the z-axis is the virtual photon direction, and the x-z plane is the lepton scattering plane with positive x-direction along the scattered lepton transverse momentum. \vec{S}_\perp is the target spin normal to the virtual photon direction and ϕ_s is its azimuthal angle with respect to the lepton scattering plane.

Beyond the collinear approximation and with a finite transverse momentum of the partons inside the nucleon, \vec{k}_\perp , eight transverse momentum dependent PDFs are needed to fully describe the cross section at leading twist and order in α_S [188]-[190]. They will be discussed in the next section in detail. All these functions lead to azimuthal asymmetries in the distribution of hadrons produced in SIDIS processes and can be disentangled measuring the different angular modulations.

The T -odd Sivers function is of particular interest. This function arises from a correlation between the transverse momentum \vec{k}_\perp of an unpolarised quark in a transversely polarised

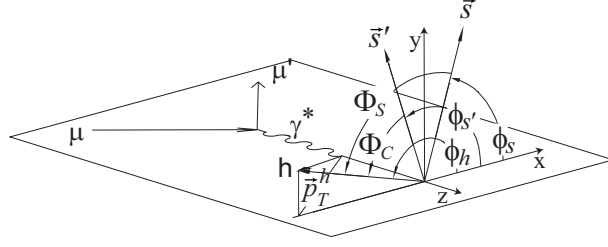


Figure 3.1: Definition of the Collins and Sivers angles. The vectors \vec{p}_T^h , \vec{s} and \vec{s}' are the hadron transverse momentum and spin of the initial and struck quarks respectively.

nucleon and the nucleon spin vector, \vec{S}_T . That is,

$$q_{\perp}(x, \vec{k}_{\perp}) = q(x, \vec{k}_{\perp}) + |\vec{S}_T| \cdot \Delta_0^{\perp} q(x, k_{\perp}) \cdot \sin \varphi', \quad (3.7)$$

where φ' is the difference of the azimuthal angle of the transverse spin of the nucleon \vec{S}_{\perp} and of the quark transverse momentum relative to the nucleon direction, \vec{k}_T . In SIDIS off transversely polarised nucleons the Sivers mechanism results in a modulation in the azimuthal distribution of the produced hadrons with the so-called ‘‘Sivers angle’’

$$\Phi_S = \phi_h - \phi_s, \quad (3.8)$$

The Sivers angle is the relative azimuthal angle between the transverse momentum of the hadron p_T^h and the nucleon target spin in the photon-nucleon reference system. Under the assumption that the hadron produced in the fragmentation and the fragmenting quark are collinear, i.e. that all the hadron transverse momentum originates from the intrinsic transverse momentum of the quark in the nucleon, the Sivers angle is equal to φ' in Eq. (3.7). A more detailed discussion of the Sivers effect and its relation to the OAM will be presented in Chapter 7.

Transverse spin effects in SIDIS have been measured at different beam energies, by the HERMES [24] and COMPASS [25, 26, 191] experiments. An experiment to measure transversity using a transversely polarised ^3He target has recently been performed also at JLab (Experiment E-06-10/E-06-11 in HALL A).

The transverse single spin SIDIS asymmetry is given by

$$\begin{aligned} A_T^h &\sim \frac{d\sigma(\vec{S}_{\perp}) - d\sigma(-\vec{S}_{\perp})}{d\sigma(\vec{S}_{\perp}) + d\sigma(-\vec{S}_{\perp})} \\ &= |\vec{S}_{\perp}| \cdot D_{NN} A_{Coll} \cdot \sin \Phi_C + |\vec{S}_{\perp}| \cdot A_{Siv} \cdot \sin \Phi_S, \end{aligned} \quad (3.9)$$

where the Collins asymmetry is defined as follows:

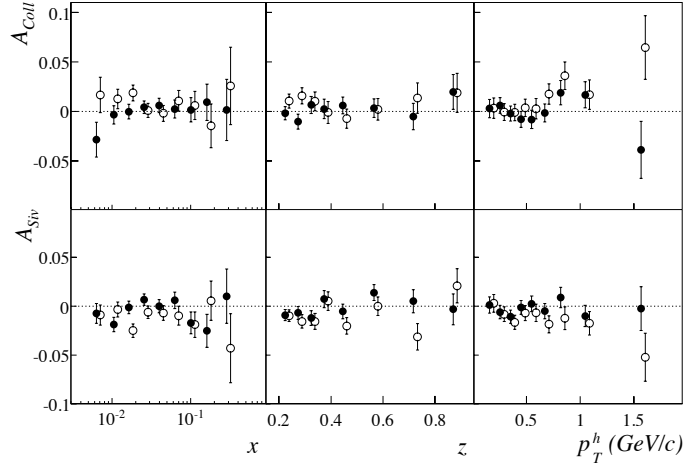


Figure 3.2: The Collins asymmetry (top) and the Sivers asymmetry (bottom) versus x , z and p_T^h for positive (filled circles) and negative hadrons (open circles) from 2002-2004 COMPASS deuteron data. (Fig. from [25]). The bars indicate the size of the statistical uncertainties. The open circles are slightly shifted along the horizontal axis for clarity.

$$A_{Coll} = \frac{\sum_q e_q^2 \cdot \Delta_{\perp} q(x) \otimes \Delta_T^0 D_q^h(z, p_T^h)}{\sum_q e_q^2 \cdot q(x) \otimes D_q^h(z, p_T^h)}, \quad (3.10)$$

and

$$D_{NN} = \frac{1 - y}{1 - y + y^2/2}, \quad (3.11)$$

is the transverse spin transfer coefficient from the initial to the struck quark². The Sivers asymmetry

$$A_{Siv} = \frac{\sum_q e_q^2 \cdot \Delta_0^{\perp} q(x, p_T^h/z) \otimes D_q^h(z)}{\sum_q e_q^2 \cdot q(x, p_T^h/z) \otimes D_q^h(z)}, \quad (3.12)$$

could be revealed as a $\sin \Phi_S$ modulations in the number of produced hadrons. here $\Delta_0^{\perp} q(x, p_T^h/z)$ is the Sivers function.

Since the Collins and Sivers terms in the transverse spin asymmetry depend on the two independent angles Φ_C and Φ_S , SIDIS measurement with a transversely polarised target allow one to disentangle the Collins and the Sivers effects and asymmetries.

The SIDIS cross-section at leading order QCD contains other terms related to different single and double spin azimuthal asymmetries. They will be considered in the next section.

The size of the effects is illustrated with the COMPASS data for the Collins and Sivers asymmetries in Figs 3.2, 3.3, 3.4 and 3.5 The corresponding results for identified hadrons

²The γ kinematical factor $\gamma = 2Mx/Q$ and lepton mass corrections are neglected.

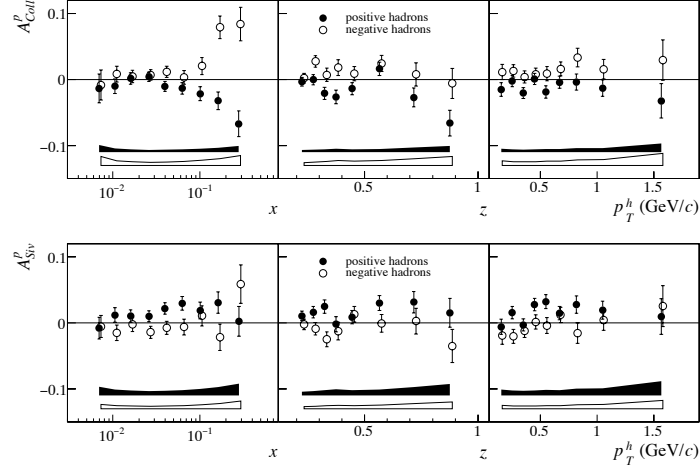


Figure 3.3: The Collins asymmetry (top) and the Sivers asymmetry (bottom) as a function of x , z , and p_T^h , for positive (filled points) and negative (open points) hadrons for 2007 COMPASS proton data. (Fig. from [26]). The bars show the statistical errors. The point to point systematic uncertainties have been estimated to be $0.5 \sigma_{stat}$ for positive and $0.6 \sigma_{stat}$ for negative hadrons and are given by the bands.

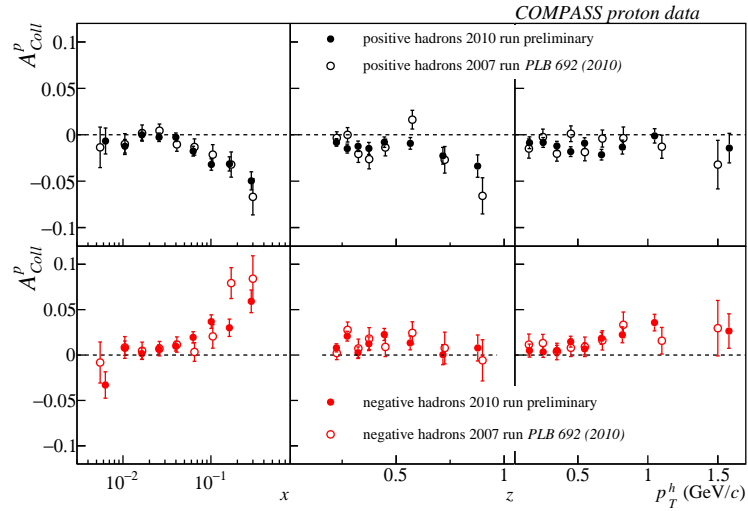


Figure 3.4: The Collins asymmetry as a function of x , z , and p_T^h , for positive (top) and negative (bottom) hadrons for 2007 and 2010 COMPASS proton data. The comparison illustrates a very good consistency between 2007 and 2010 COMPASS data sets. The bars show the statistical errors.

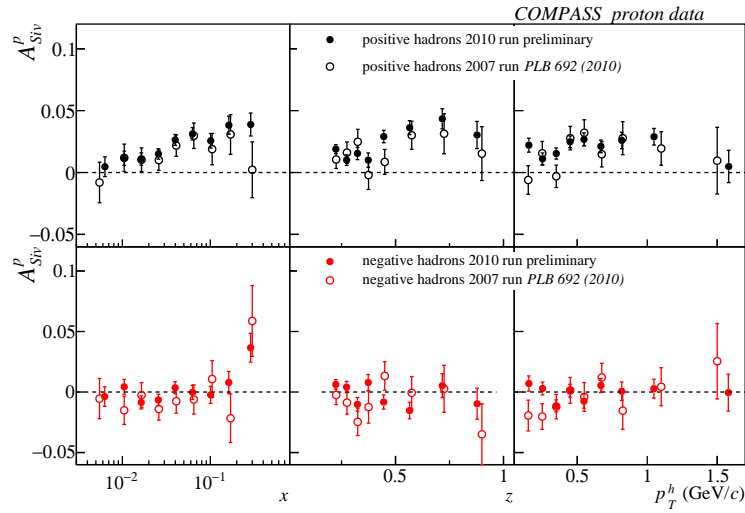


Figure 3.5: The Siverts asymmetry as a function of x , z , and p_T^h , for positive (top) and negative (bottom) hadrons for 2007 and 2010 COMPASS proton data. The comparison illustrates a very good consistency between 2007 and 2010 COMPASS data sets. The bars show the statistical errors.

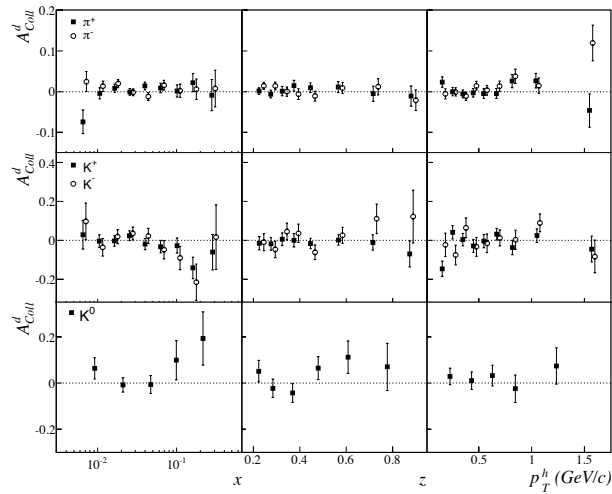


Figure 3.6: COMPASS results for the Collins asymmetry versus x , z and p_T^h for the charged pions and kaons samples from the 2003–2004 deuteron data, and K_S^0 's sample from the 2002–2004 deuteron data. (Fig. from [191]).

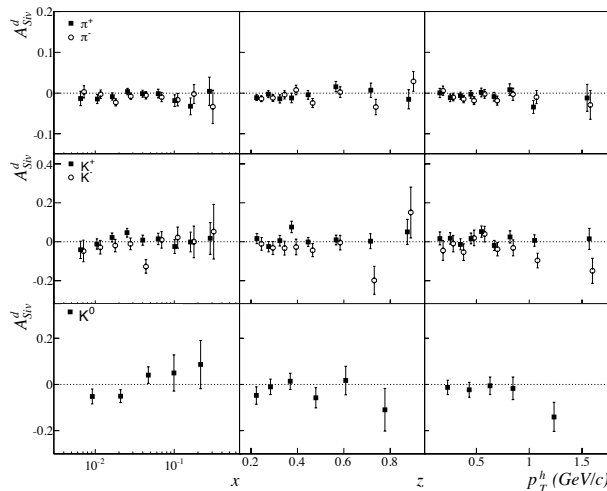


Figure 3.7: COMPASS results for Sivers asymmetry versus x , z and p_T^h for the charged pions and kaons samples from the 2003–2004 deuteron data, and K_S^0 's sample from the 2002–2004 deuteron data. (Fig. from [191]).

are shown In Figs.3.6 and 3.7 All deuteron asymmetries are measured to be small. The trend which was already observed in the data for the non-identified hadrons is confirmed by identified hadron data. The smallness of the asymmetries is not a surprise, in view of the predicted cancellations between the u- and d-quark distributions in the isoscalar deuteron, as in the helicity case.

The COMPASS proton data show that the Collins asymmetry has a strong x dependence. It is compatible with zero at small x within the small statistical errors and increases in absolute value up to about 0.1 for $x > 0.1$. The values agree in the region of kinematic overlap both in magnitude and in sign with the measurements of HERMES [24] and [193],(Figs 3.8 and 3.9) which were performed at the considerably lower electron beam energy of 27.5 GeV, compared to the 160 GeV muon beam energy used at COMPASS.

The COMPASS results agree with evaluations based on the global analysis of ref. [186, 187] (which does not include COMPASS data). The underlying interpretation of the Collins asymmetry in terms of a convolution of the twist-2 transversity PDF and FF of a transversely polarised quark is used in the global analysis. An important issue is the Q^2 dependence of these functions. The COMPASS results are compatible with the HERMES data in the x region of overlap despite the 2 to 3 times higher Q^2 values [26]. The Q^2 dependence is then presumably not dramatic in the present energy ranges.

The COMPASS proton results for the Sivers asymmetry for negative hadrons exhibit values compatible with zero to within the statistical precision of the measurement. For

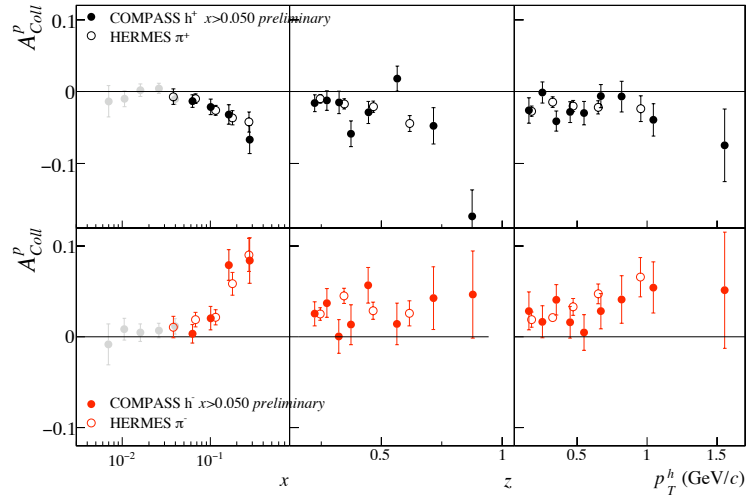


Figure 3.8: Comparison between COMPASS [26] and HERMES [24] proton Collins asymmetry data versus x , z and p_T^h .

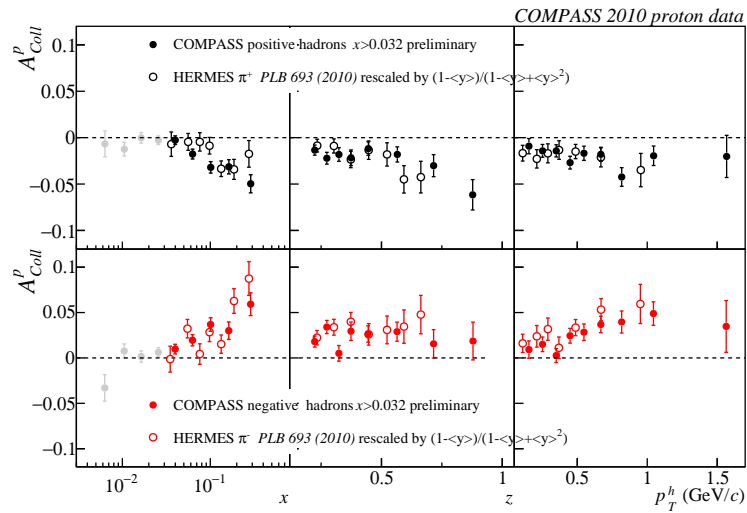


Figure 3.9: Comparison between COMPASS (2010 data) and HERMES [193] proton Collins asymmetry data versus x , z and p_T^h .

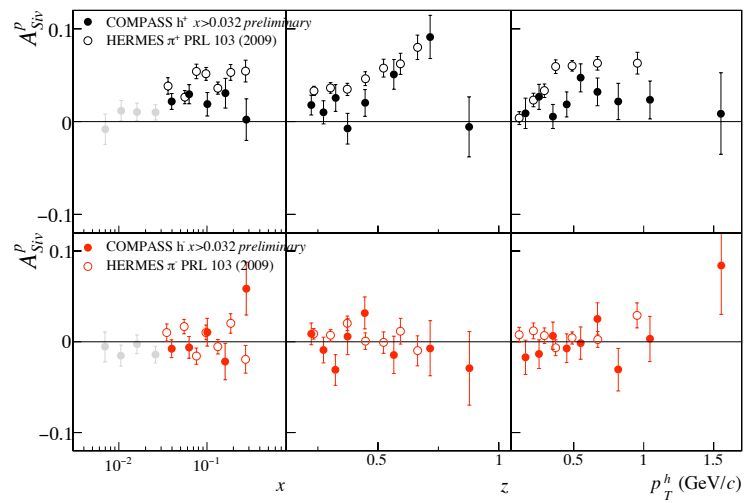


Figure 3.10: Comparison between COMPASS [26] and HERMES [192] proton Sivers asymmetry data versus x , z and p_T^h .

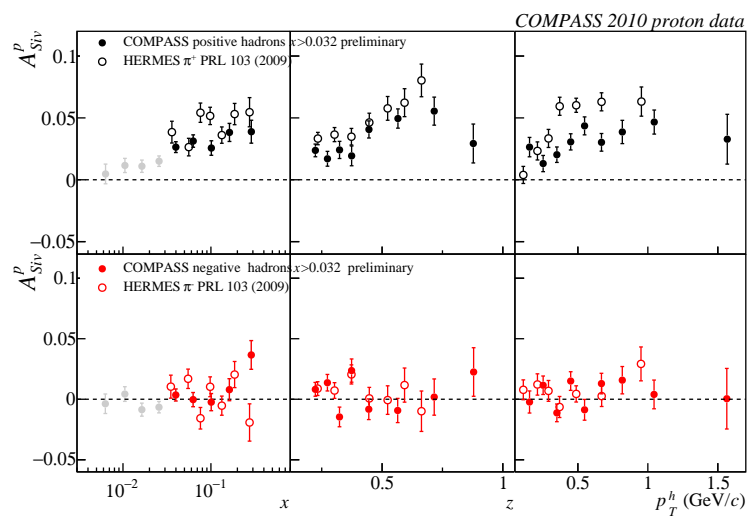


Figure 3.11: Comparison between COMPASS (2010 data) and HERMES [192] proton Sivers asymmetry data versus x , z and p_T^h .

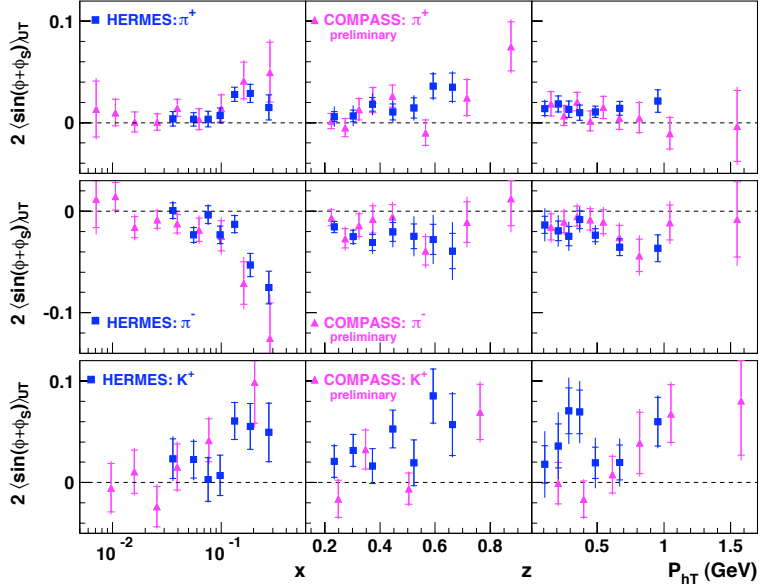


Figure 3.12: COMPASS and HERMES proton data for the Collins asymmetry versus x , z and p_T^h . The data are reproduced from [205]. The error bars indicate the size of the statistical uncertainties. Notice a different sign convention used at HERMES.

positive hadrons, the data are positive and reach up to about 3% in the valence region. These values tend to be somewhat smaller than the ones measured by HERMES [192] at smaller Q^2 (Figs 3.10 and 3.11), but still compatible. A difference may originate from a possible W dependence. However definite conclusions will be possible only when new more precise data at high energy will become available.

Very recently new detailed data comparison separately for positive and negative pions and positive kaons for Collins asymmetry (Fig 3.12) and for positive pions and kaons for Sivers asymmetry (Fig 3.13) has been showed by HERMES [205].

In addition the difference between positive and negative pions observed for Sivers effect are shown in the lower row of Fig. 3.13. Note that the sign convention used in HERMES analysis of Collins effect is opposite to the COMPASS one. The "UT" notation used in description of the axis in Figs 3.12 and 3.13 is discussed in the next section.

The very preliminary results of the Sivers asymmetry from JLAB HALL A Collaboration measured on the neutron target have been recently reported [194]. New precise data are anticipated from JLAB also after the 12 GeV upgrade, see e.g. [195].

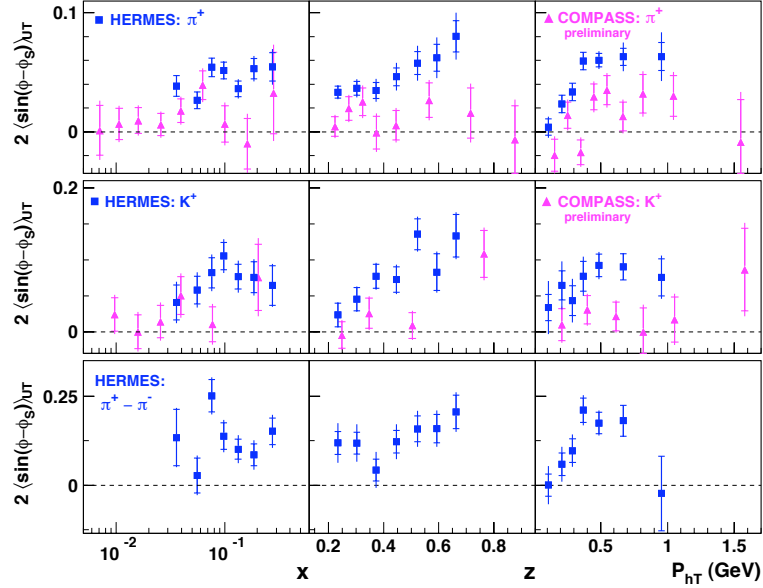


Figure 3.13: COMPASS and HERMES proton data for the Sivers asymmetry versus x , z and p_{T}^h . The plot are taken from [205]. The error bars indicate the size of the statistical uncertainties.

3.2 Catalogue of twist-2 parton distribution functions

The description of the nucleon structure in terms of number, helicity and transversity PDFs gives a one-dimensional characteristic of the nucleon - the longitudinal motion of the partons or equivalent - the parton's momentum distributions along the light-cone direction singled out by hard scale momentum flow in the process, e.g. the virtual photon in DIS. A fast moving nucleon is Lorentz-contracted but its transverse size is still large (1 fm) compared with the strong interaction scale. The questions how quarks/gluons are spatially distributed or more importantly for the study of nucleon spin study - do they orbit and carry orbital momentum cannot be answered within an one-dimensional description. Nucleon tomography or 3D-imaging of the nucleon is possible beyond the collinear approximation. The spatial distributions of the partons in the transverse plane are included in GPDs (Generalized Parton Distributions) while TMD PDFs (Transverse Momentum Dependent PDFs) incorporate the momentum distributions in the transverse plane in the description. Complementary information from TMDs and GPDs leads to a full 3D description of the nucleon internal structure. The GPDs precise measurement is still a question of future (see e.g. [42, 40] however first results from study Deeply Virtual Compton Scattering (DVCS) have been already published, e.g.[33]-[39]. The Sivers function, presented in the previous section, is an example of a TMD distribution. To situate the TMDs in a general scheme which allows to

describe nucleon internal structure it is convenient to come back to the so-called Wigner function, originally introduced by E. Wigner in 1933 on the ground of Quantum Mechanics. The Wigner function defined as follows:

$$W(x, p) = \int \Psi^*(x - \eta/2) \Psi(x + \eta/2) e^{ip\eta} d\eta, \quad (3.13)$$

when integrated over $x(p)$ describes the momentum (probability) distribution. The Wigner function contains all information and any dynamical variable can be calculated as follows

$$\langle O(x, p) \rangle = \int O(x, p) W(x, p) dx dp. \quad (3.14)$$

The Wigner function is in general not necessarily positive, although it is well-defined in the classical limit. A similar concept has been introduced in [196] where the Wigner distribution operator for quarks is defined in QCD as:

$$\hat{W}_\Gamma(\vec{r}, k) = \int \bar{\Psi}(r - \eta/2) \Gamma \Psi(r + \eta/2) e^{ik\eta} d^4\eta, \quad (3.15)$$

where \vec{r} is the quark phase-space position and k the phase-space four-momentum. Γ is the Dirac matrix defining the types of quark densities and Ψ is a gauge-invariant quark field (with gauge link, see [196]). The \hat{W}_Γ is a gauge invariant but depends on the choice of gauge vector η . The Wigner distribution can then be defined as the expectation value of \hat{W}_Γ in the hadron states. Wigner distribution following this definition leads to TMDs after integrating over r . After integrating over k one gets the Fourier transform of GPDs.

A more general Wigner-type distribution, obeying also off-diagonal (non-forward) matrix elements has been considered recently in [27]. The Generalized Parton Correlation Function (GPCF) parameterizes the fully unintegrated off-diagonal quark-quark correlator. The GPCF depends on the four-momentum k of the quark and on the four-momentum Δ (skewness parameter) which is transferred by the probe to the hadron. The classification of Wigner-type distributions is also discussed in [197, 198]. After integrating the GPCF over light-cone energy of the quark one obtains the Generalized Transverse Momentum Parton Distributions (GTMDs) which contain the most general one-body information of partons, corresponding to the full one-quark density matrix in momentum space [27]. As presented in Fig. 3.14 the GTMDs reduce to different parton distributions and form factors. The different arrows in this figure represent particular projections in hadron and quark momentum space and give the links between the matrix elements of different reduced density matrices. At leading twist there are sixteen complex GTMDs. In the forward limit $\Delta = 0$ they reduce to the eight TMDs depending on the longitudinal momentum fraction \vec{k}_\perp of quarks. They therefore give access to the three-dimensional picture of the nucleon in momentum

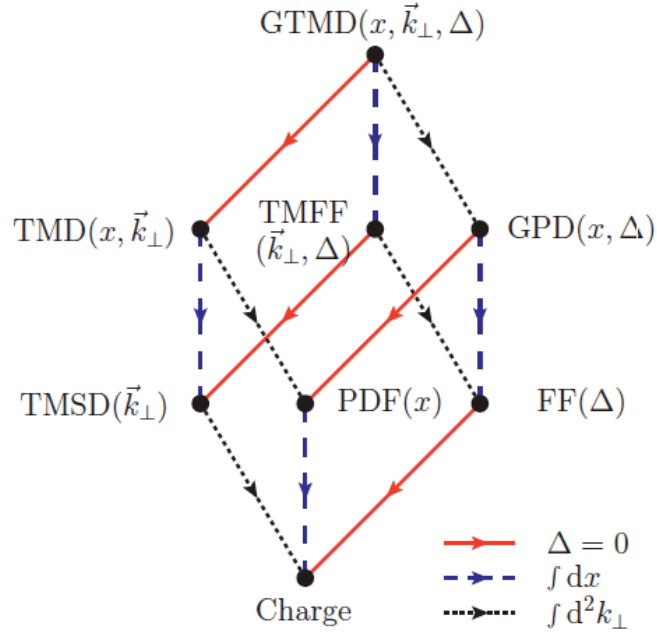


Figure 3.14: Representation of the projections of the GTMDs into parton distributions and form factors. The arrows correspond to different reductions in hadron and quark momentum space: the solid (red) arrows give the forward limit in the hadron momentum; the dotted (black) arrows correspond to the integration over the quark transverse momenta and the dashed (blue) arrows project out the longitudinal momentum of quarks. The figure is reproduced from [27]. Here FF denotes form factors, TMFF - transverse momentum dependent form factor, TMSD - transverse momentum spin densities, PDF - parton distribution functions, GPD - generalized parton distributions.

space. Integration of the GTMDs over \vec{k}_\perp leads to eight GPDs taken at zero limit in the skewness parameter. After Fourier Transformation of $\vec{\Delta}_\perp$ to impact parameter space they provide a three-dimensional picture of the nucleon in the mixed coordinate-momentum space [199, 30, 200]. There is also another reduction of GTMDs which leads to the third three-dimensional distribution defined in the mixed coordinate-momentum space. It depends on e.g. the longitudinal momentum in z , transverse momentum in x and impact parameter in y directions, respectively. Since x and y coordinates commutes the measurement of these coordinates is not restricted by the Heisenberg principle. Due to the Wilson gauge links in the gauge-independent definitions of the TMDs and GPDs there is no direct connection (e.g. via Fourier transforms) between TMDs and GPDS [27].

The eight leading-twist TMDs for the nucleon can be defined in terms of the unintegrated quark-quark correlator, similar to the Wigner distribution Eq. (3.15):

$$\hat{W}(x, \vec{k}_\perp, \vec{S})_\eta = \int e^{ikz} \langle \vec{P}, \vec{S} | \bar{\Psi}(0) W_\eta(0, z) \Psi(z) | \vec{P}, \vec{S} \rangle \Big|_{z^+=0} \frac{dz^- d^2 z_\perp}{(2\pi)^3}. \quad (3.16)$$

The gauge link operator $W_\eta(0, z)$ ("hidden" in definition of Ψ in Eq. (3.15) ensures color gauge-invariance of the matrix element and depends on the path. The factorization theorem gives the prescription along which path the position of 0 and z of the quark field have to be connected and the η dependence reflects the dependence on the process. The light-cone coordinates are defined by $a^\mu = (a^-, a^+, \vec{a}_\perp)$ with $a^\pm = \frac{1}{\sqrt{2}}(a^0 \pm a^3)$. The leading-twist TMDs are related to the large + component of the nucleon momentum and parameterize the following Dirac structures:

$$\frac{1}{2} Tr(\gamma^+ \hat{W}(x, \vec{k}_\perp, \vec{S})) = f_1(x, \vec{k}_\perp) - \frac{\varepsilon^{jk} k_\perp^j S_T^k}{M} f_{1T}^\perp(x, \vec{k}_\perp), \quad (3.17)$$

$$\frac{1}{2} Tr(\gamma^+ \gamma_5 \hat{W}(x, \vec{k}_\perp, \vec{S})) = S_L g_{1L}(x, \vec{k}_\perp) + \frac{\vec{k}_\perp \vec{S}_T}{M} g_{1T}(x, \vec{k}_\perp), \quad (3.18)$$

$$\frac{1}{2} Tr(i\sigma^{j+} \gamma_5 \hat{W}(x, \vec{k}_\perp, \vec{S})) = S_T^j h_1(x, \vec{k}_\perp) + S_L \frac{k_\perp^j}{M} h_{1L}^\perp(x, \vec{k}_\perp) \quad (3.19)$$

$$+ \frac{(k_\perp^j k_\perp^k - \frac{1}{2} \vec{k}_\perp^2) S_T^k}{M^2} h_{1T}^\perp(x, \vec{k}_\perp) + \frac{\varepsilon^{jk} k_\perp^k}{M} h_1^\perp(x, \vec{k}_\perp). \quad (3.20)$$

Here, the η dependence is omitted for notational simplicity. The TMDs of antiquarks and gluons are defined analogously and the notation used follows so-called "Amsterdam" notation [189, 201]. This notation is slightly different from the notation used in the previous section and in the COMPASS publications [25, 26, 191]. The Sivers function $\Delta_0^\perp q(x, p_T^h/z)$ discussed in Eqs 3.12 and 3.7 is equal to:

$$\Delta_0^\perp q(x, p_T^h/z) = -2 \frac{k_\perp^j}{M} f_{1T}^\perp(x, \vec{k}_\perp). \quad (3.21)$$

Also $q(x, \vec{k}_\perp)$ introduced for quarks is here replaced by more general notation for parton distribution $f_1(x, \vec{k}_\perp)$. A detailed review of the different notations can be found in [202]. The Dirac γ^+ structure describes unpolarised quarks inside an unpolarised nucleon ($f_1(x, \vec{k}_\perp)$) and unpolarised quarks inside a transversely polarised nucleon (Sivers function f_{1T}^\perp). The Dirac $\gamma^+\gamma^+$ structure singles out longitudinally polarised quarks in a longitudinally polarised nucleon ($g_{1L}(x, \vec{k}_\perp)$) or in a transversely polarised nucleon ($g_{1T}(x, \vec{k}_\perp)$, first worm-gear function). The structure $\sigma^{j+}\gamma_5$ selects transversely polarised quarks inside a transversely polarised nucleon ($h_1(x, \vec{k}_\perp)$ and h_{1T}^\perp pretzelosity function), or in a longitudinally polarised nucleon (h_{1L}^\perp , second worm gear function) and inside an unpolarised nucleon (h_1^\perp , Boer-Mulders function). Integration of $f_1(x, \vec{k}_\perp)$ over \vec{k}_\perp leads to the usual unpolarised PDF measured in DIS for quarks and gluons. The unintegrated helicity distribution $g_{1L}(x, \vec{k}_\perp)$ of quarks and gluons after integrating over \vec{k}_\perp leads to the helicity distributions $\Delta q(\Delta G)$ determined from the measurement of double spin longitudinal asymmetry. The analog of the helicity distribution for transversely polarised target is denoted as $h_1(x, \vec{k}_\perp)$. After integration over \vec{k}_\perp one gets transversity Δq_\perp . The only three independent PDFs, f_1 , g_{1L} and h_1 , survive in the collinear limit, $\vec{k}_\perp \rightarrow 0$ and transverse momentum integration.

The Sivers asymmetry has been discussed in the previous section. Since the Sivers function f_{1T}^\perp plays a crucial role in the understanding of the nucleon structure and its non-zero value is a clear indication of parton orbital motion it will be again discussed in chapter 7, where OAM is discussed. The Sivers function together with the Boer-Mulders function h_1^\perp can be related to the deformation of the parton (quark) distribution in the transverse plane as predicted by some models and Lattice QCD calculations. This very interesting concept and its consequences in the nucleon description is also discussed in the chapter 7. Both functions are not strictly universal - they depend on the process. The Sivers and Boer-Mulders functions measured in SIDIS should change sign if they are measured in Drell-Yann (DY) process [201]. QCD interactions play a very nontrivial role in both effects (chromodynamic lensing) and they differ in different processes (final state interactions in SIDIS and initial state interactions in DY case). The concept of chromodynamic lensing is also presented in chapter 7. Future DY experiments aim to the QCD prediction of a sign change for the Sivers and Boer-Mulders function [40, 42, 203]. This test requires also better precision of the corresponding measurements in SIDIS.

The remaining TMDs: $g_{1T}(x, \vec{k}_\perp)$, $h_{1L}^\perp(x, \vec{k}_\perp)$ and $h_{1T}^\perp(x, \vec{k}_\perp)$ are related to double spin correlations in the PDFs. Neglecting higher-twist terms approximate relationships with other TMDs can be obtained [204]. A similar correlation between spin and transverse motion can appear in the fragmentation process of a transversely polarised quark. The Collins fragmentation function was shortly discussed in the previous section. The effect is well-

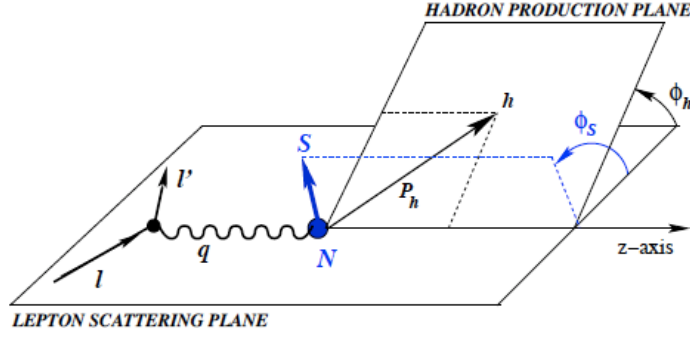


Figure 3.15: Azimuthal angles for SIDIS in the target rest frame [190].

establish and its chiral-odd nature allows one to measure the transversity distribution and the Boer-Mulders function in SIDIS processes.

The main source of information about TMDs are SIDIS experiments where at least one hadron is registered in addition to the scattered lepton. In this case the observed hadron preserves part of the original motion of scattered quark, including the transverse one. In the one-photon exchange approximation the unintegrated SIDIS cross section for unpolarised hadron production can be decomposed as follows:

$$\begin{aligned}
\frac{d\sigma}{dx dy dd\phi_S d\phi_h dz_h dP_{hT}^2} &= \frac{e^4}{32\pi^2 x Q^2} \frac{y}{1-\varepsilon} \left(1 + \frac{\gamma^2}{2x}\right) \left\{ F_{UU,T} + \varepsilon F_{UU,L} + \varepsilon \cos(2\phi_h) F_{UU}^{\cos 2\phi_h} \right. \\
&+ \sqrt{2\varepsilon(1-\varepsilon)} (\cos\phi_h F_{UU}^{\cos\phi_h} + h_l \sin\phi_h F_{LU}^{\sin\phi_h}) \\
&+ S_{\parallel} \left[\sqrt{2\varepsilon(1+\varepsilon)} \sin\phi_h F_{UL}^{\sin\phi_h} + \varepsilon \sin(2\phi_h) F_{UL}^{\sin 2\phi_h} \right] \\
&+ S_{\parallel} h_l \left[\sqrt{1-\varepsilon^2} F_{LL} + \sqrt{2\varepsilon(1-\varepsilon)} \cos\phi_h F_{LL}^{\cos\phi_h} \right] \\
&+ |S_{\perp}| \left[\sin(\phi_h - \phi_S) (F_{UT,T}^{\sin(\phi_h - \phi_S)} + \varepsilon F_{UT,L}^{\sin(\phi_h - \phi_S)}) \right. \\
&\quad + \varepsilon \sin(3\phi_h - \phi_S) F_{UT}^{\sin(3\phi_h - \phi_S)} + \varepsilon \sin(\phi_h + \phi_S) F_{UT}^{\sin(\phi_h + \phi_S)} \\
&\quad \left. + \sqrt{2\varepsilon(1+\varepsilon)} (\sin\phi_S F_{UT}^{\sin\phi_S} + \sin(2\phi_h - \phi_S) F_{UT}^{\sin(2\phi_h - \phi_S)}) \right] \\
&+ |S_{\perp}| h_l \left[\sqrt{1-\varepsilon^2} \cos(\phi_h - \phi_S) F_{LT}^{\cos(\phi_h - \phi_S)} \right. \\
&\quad \left. + \sqrt{2\varepsilon(1-\varepsilon)} (\cos\phi_S F_{LT}^{\cos\phi_S} + \cos(2\phi_h - \phi_S) F_{LT}^{\cos(2\phi_h - \phi_S)}) \right] \left. \right\}, \tag{3.22}
\end{aligned}$$

following the notation of Ref. [190], where ε is a ratio of longitudinal and transverse photon

flux:

$$\varepsilon = D_{NN} = \frac{1 - y - \frac{1}{4}y^2\gamma^2}{1 - y - \frac{1}{2}y^2 + \frac{1}{4}y^2\gamma^2}, \quad (3.23)$$

with $\gamma = \frac{2Mx}{Q}$ and $\sqrt{1 - \varepsilon^2}$ is equal to the longitudinal depolarization factor D (up to correction for F_L , and R), c.f. Eq. (2.35). All lepton mass corrections are neglected in Eqs (3.22) and (3.23). The first and second subscripts of the above structure functions F indicate the respective polarisation of beam and target, whereas the third subscript in $F_{UU,T}$, $F_{UU,L}$, $F_{UT,T}^{\sin(\phi_h - \phi_S)}$ and $F_{UT,L}^{\sin(\phi_h - \phi_S)}$ specifies the polarisation of the virtual photon. S_{\parallel} denotes longitudinal target polarisation and h_l is the lepton helicity. Definitions of angles are given in Fig. 3.15. It is a matter of simple algebra to obtain the Collins and Sivers asymmetries given in Eq. (3.9), from the Eq. (3.22) by selecting transverse polarisation and neglecting all terms except $F_{UU,T}$, $F_{UT,T}^{\sin(\phi_h - \phi_S)}$ and $F_{UT}^{\sin(\phi_h + \phi_S)}$.

Measuring the structure functions F 's in Eq. (3.22) allows one to obtain the information on all eight leading TMDs:

$$F_{UU,T} \sim \sum_q e_q^2 \cdot f_1^q \otimes D_q^h, \quad F_{LT}^{\cos(\phi_h - \phi_S)} \sim \sum_q e_q^2 \cdot g_{1T}^q \otimes D_q^h, \quad (3.24)$$

$$F_{LL} \sim \sum_q e_q^2 \cdot g_{1L}^q \otimes D_q^h, \quad F_{UT,T}^{\sin(\phi_h - \phi_S)} \sim \sum_q e_q^2 \cdot f_{1T}^{\perp q} \otimes D_q^h, \quad (3.25)$$

$$F_{UU}^{\cos 2\phi_h} \sim \sum_q e_q^2 \cdot h_1^{\perp q} \otimes H_1^{\perp q}, \quad F_{UT}^{\sin(\phi_h + \phi_S)} \sim \sum_q e_q^2 \cdot h_1^q \otimes H_1^{\perp q}, \quad (3.26)$$

$$F_{UL}^{\sin 2\phi_h} \sim \sum_q e_q^2 \cdot h_{1L}^{\perp q} \otimes H_1^{\perp q}, \quad F_{UT}^{\sin(3\phi_h - \phi_S)} \sim \sum_q e_q^2 \cdot h_{1T}^{\perp q} \otimes H_1^{\perp q}. \quad (3.27)$$

$H_1^{\perp q}$ denotes Collins T -odd fragmentation function.³ Integration of Eq. (3.22) over the transverse momentum \vec{P}_{hT} of the outgoing hadron gives the SIDIS cross section in terms of kinematic factors and five structure functions: $F_{UU,T}$, $F_{UU,L}$, F_{LL} , $F_{LT}^{\cos\phi_S}$ and $F_{UT}^{\sin\phi_S}$ now integrated over \vec{P}_{hT} . The next integration over the energy of the hadron z_h leads - after the summation over all hadrons in the final state - to the inclusive DIS cross section, parameterized by four structure functions: $\mathcal{F}_{UU,T}$, $\mathcal{F}_{UU,L}$, \mathcal{F}_{LL} and $\mathcal{F}_{LT}^{\cos\phi_S}$ [190]:

$$\begin{aligned} \frac{d\sigma}{dx dy d\phi_S} = & \frac{e^4}{32\pi^2 x Q^2} \frac{y}{1 - \varepsilon} \left\{ \mathcal{F}_{UU,T} + \varepsilon \mathcal{F}_{UU,L} \right. \\ & \left. + S_{\parallel} h_l \sqrt{1 - \varepsilon^2} \mathcal{F}_{LL} + |S_{\perp}| h_l \sqrt{2\varepsilon(1 - \varepsilon)} \cos\phi_S \mathcal{F}_{LT}^{\cos\phi_S}, \right\}, \end{aligned} \quad (3.28)$$

³Collins T -odd fragmentation function was previously denoted as $\Delta_T^0 D_q^h(z, p_T^h)$ in Eq. (3.3), where the notation from COMPASS publications are used.

The functions $\mathcal{F}_{UU,T}$, $\mathcal{F}_{UU,L}$, \mathcal{F}_{LL} and $\mathcal{F}_{LT}^{\cos\phi_S}$ are expressed in terms of the standard inclusive structure functions F_1 , F_2 , g_1 and g_2 , (c.f. chapter 2):

$$\begin{aligned}
\mathcal{F}_{UU,T} &= \sum_h \int dz_h dP_{hT}^2 z F_{UU,T} = 2x F_1(x, Q^2), \\
\mathcal{F}_{UU,L} &= \sum_h \int dz_h dP_{hT}^2 z F_{UU,L} = (1 + \gamma^2) F_2(x, Q^2) - 2x F_1(x, Q^2) \equiv F_L(x, Q^2), \\
\mathcal{F}_{LL} &= \sum_h \int dz_h dP_{hT}^2 z F_{LL} = 2x(g_1(x, Q^2) - \gamma^2 g_2(x, Q^2)), \\
\mathcal{F}_{LT}^{\cos\phi_S} &= \sum_h \int dz_h dP_{hT}^2 z F_{LT}^{\cos\phi_S} = -2x\gamma(g_1(x, Q^2) + g_2(x, Q^2)), \\
&\sum_h \int dz_h dP_{hT}^2 z F_{UT}^{\sin\phi_S} = 0.
\end{aligned} \tag{3.29}$$

Eq. (3.28) corresponds to Eq. (2.16) and Eqs (2.18) and (2.19) (up to lepton mass corrections, $\phi_S \approx \phi$) however the g_1 and g_2 structure functions used to parameterize \mathcal{F}_{LL} and $\mathcal{F}_{LT}^{\cos\phi_S}$ in Eq. (3.29) (following [190]) differ from the ones introduced in Eq (2.14). In the DIS limit, $\gamma \rightarrow 0$, g_1 is the same while g_2 is differently defined. The function $F_{UT}^{\sin\phi_S}$ vanishes when integrated because of time-reversal invariance, c.f. Eq. (3.29).

3.3 Summary of the TMDs and transverse spin structure of the nucleon

The eight leading TMD parton distribution functions are given in Table 3.1. U, L and T correspond to Unpolarised, Longitudinally polarised and Transversely polarised quarks (rows) and nucleons (columns). As it was mentioned earlier to have a gauge invariant definition

Table 3.1: Leading twist TMDs.

	U_q	L_q	T_q
U_N	f_1		h_1^\perp
L_N		g_{1L}	h_{1L}^\perp
T_N	f_{1T}^\perp	g_{1T}	h_1, h_{1T}^\perp

of TMD the gauge link (Wilson line) has to be inserted between quark fields. This is not specific for TMDs only but two features are unique in the case of TMDs: some of the TMDs

are non-zero only because of the presence of the Wilson line (e.g. Sivers and Boer-Mulders) and the Wilson line depends on the process which leads to non-trivial universality (Sivers versus Boer-Mulders TMDs). TMDs are potentially related to the OAM, L_z , which may play an important role in the nucleon spin decomposition. Model calculations have shown that the leading TMDs $f_{1T}^{\perp q}$, g_{1T}^q , $h_1^{\perp q}$, $h_{1L}^{\perp q}$, $h_{1T}^{\perp q}$ and many sub-leading ones would vanish if they were not different components in the nucleon wave function with $\Delta L_z \neq 0$. Unfortunately a rigorous connection between TMDs and the OAM contribution to the nucleon spin has not been established so far.

Factorization is an important aspect of the TMDs ([205] and references therein). For SIDIS (with one hadron observed in the final state) and for DY processes as well as back-to-back hadron or jet production in e^+e^- annihilation the factorization seems to hold. For hadro-production of back-to-back hadrons or jets factorization has been shown to fail [206]-[210]. Since for many TMDs the leading part is small or zero and the sub-leading terms can potentially be important measurement of TMDs gives an opportunity to test factorization and very non-trivial QCD predictions. From an experimental point of view their measurement is still a challenge.

The experimental results presented in section 3.1 can be summarize as follows:

- The Collins asymmetry measured on proton targets is sizable for both positive and negative hadrons. The COMPASS and HERMES results agree well.
- A non-zero Sivers asymmetry is seen for positive hadrons, which persists to rather small x values.
- A possible W dependence of this asymmetry might be suggested by data, but the present statistical and systematic uncertainties do not allow definite conclusions.
- The Collins and Sivers results on deuteron targets are compatible with zero. This combined with non-zero proton results suggests a cancellation between u and d quarks.

The observation of the non-zero Sivers asymmetry suggests the presence of the OAM. As the non-zero OAM is generated by QCD evolution the important role of the OAM is expected in the nucleon spin decomposition.

Most of the transverse polarisation dependent asymmetries and TMDs are very small or compatible with zero. Therefore the understanding of the large (up to 40%) transverse Single-Spin Asymmetry (SSA) for polarised (anti)proton - proton collision observed by Fermilab experiment [18] and confirmed by RHIC experiments STAR [19], PHENIX [20] and BRAHMS [21] is still difficult on the QCD ground [211].

Chapter 4

COMPASS experimental set-up

The next two chapters of this thesis are dedicated to the direct measurement of the gluon polarisation at COMPASS experiment. Therefore a short description of the COMPASS beam line, spectrometer and polarised target is given in the present chapter.

The COMPASS spectrometer is a fixed target set-up situated at the M2 beam line of the CERN SPS using muon or hadron beams. For the measurements discussed in this thesis a longitudinally polarised positive muons of 160 GeV momentum were scattered off a large polarised solid state target. A detailed description of the set-up can be found in Ref. [56].

The muons originate from the weak decay of 175 GeV pions and kaons produced by the 400 GeV SPS proton beam impinging on a primary beryllium target and are thus naturally polarised. The beam polarisation, P_μ , is about 0.8 at 160 GeV with a relative uncertainty of 5% [212]. In Fig. 4.1 the muon beam polarisation is presented as a function of its momentum. A beam intensity of about $4 \cdot 10^7$ muons/s was used, with the spill length between 4.8 s and 9.6 s for SPS cycles between 16.8 s and 48 s, respectively. The beam is focused onto the target centre with a spread of 7 mm (r.m.s.) and a momentum spread of 5% for the Gaussian core. The momentum of each incoming muon is measured with a precision better than 1% upstream of the experimental hall using a beam momentum station. Before the target the trajectory of each beam particle is determined using a set of scintillating fibres and silicon detectors with an angular precision of $30 \mu\text{rad}$. The solid state target is housed in a large superconducting solenoid providing a field of 2.5 Tm with a field uniformity, $\delta B/B$, better than 10^{-4} . From 2002 to 2004 the angular acceptance was ± 69 mrad at the upstream edge and ± 170 mrad at the downstream edge of the target material. From 2006 onwards an upgraded target magnet with a new large aperture solenoid was used. It yields an angular acceptance of ± 180 mrad for the upstream target edge resulting in a much improved hadron acceptance and matching the ± 180 mrad acceptance of the spectrometer.

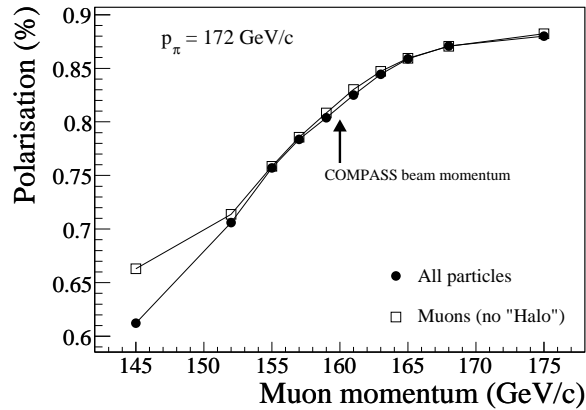


Figure 4.1: The muon beam polarisation (absolute value) as a function of the central muon momentum, assuming a central pion momentum 172 GeV.

The target material consisted of ${}^6\text{LiD}$ beads in 2002 to 2006 and NH_3 beads in 2007, in a bath of ${}^3\text{He}/{}^4\text{He}$. The target was cooled down to a temperature below 100 mK by a ${}^3\text{He}$ - ${}^4\text{He}$ dilution refrigerator. The target polarisation was accomplished using the method of dynamical nuclear polarisation (DNP) and was measured continuously by a set of NMR coils surrounding the target material. The achieved polarisation, P_t , was about 0.5 for deuterons (${}^6\text{LiD}$) and 0.9 for protons (NH_3) with a relative uncertainty of 5% and 2%, respectively. Corrections are applied to account for the polarisation of the ${}^6\text{Li}$ nucleus in ${}^6\text{LiD}$ and of the ${}^{14}\text{N}$ nucleus in NH_3 .

In 2002 to 2004 the target material was contained into two 60 cm long cells and polarised in opposite directions. The polarisation was reversed 3 times a day by rotating the field of the target magnet. From 2006 onwards a three cell target set-up was used with a central 60 cm long cell placed between two 30 cm long ones. The central cell was polarised oppositely to the outer ones. The use of this new target arrangement allows a further reduction of the systematic uncertainty due to the variation of the spectrometer acceptance along the target; thus only one field rotation per day had to be performed. In order to minimise possible acceptance effects related to the orientation of the solenoid field, the sign of the polarisation in each target cell was also reversed several times per year by changing the DNP microwave frequencies.

As not all nucleons in the target material are polarised the so-called dilution factor, f , is introduced. It is expressed in terms of the number n_A of nuclei with mass number A and the corresponding total (*i.e.* including radiative effects) spin-independent cross sections, σ_A^{tot} ,

per nucleon for all the elements involved:

$$f_{\text{H,D}} = \frac{n_{\text{H,D}} \cdot \sigma_{\text{H,D}}^{\text{tot}}}{\sum_{\text{A}} n_{\text{A}} \cdot \sigma_{\text{A}}^{\text{tot}}}. \quad (4.1)$$

The dilution factor is modified by a correction factor $\rho = \sigma_{\text{p,d}}^{1\gamma} / \sigma_{\text{p,d}}^{\text{tot}}$ accounting for the dilution due to radiative events on unpolarised protons (deuterons) [213]. Two more corrections are applied for the ${}^6\text{LiD}$ target: first accounting for the relative polarisation of deuterons bound in ${}^6\text{Li}$ compared to free deuterons, second a correction factor $(1 - 3/2\omega_{\text{D}})$ where ω_{D} is the probability for a deuteron to be in a D-state ($\omega_{\text{D}} = 0.05 \pm 0.01$) [121] are applied. For the ${}^{14}\text{NH}_3$ material the dilution factor contains a correction for the polarisation of the admixture of ${}^{15}\text{N}$ to ${}^{14}\text{N}$.

The dilution factor depends on Bjorken x . At low x it is higher for events containing hadrons in the final state due to the absence of radiative elastic tails. Its values at medium x for ${}^6\text{LiD}$ and NH_3 are about 0.37 and 0.14, respectively, with relative uncertainties of 2% and 1% for those two materials.

The two stages of the COMPASS set-up are open dipole spectrometers for large and small angle tracks, respectively. The schematic view of the COMPASS spectrometers is shown in Fig. 4.2 for 2004 configuration. Each dipole is surrounded by tracking detectors. COMPASS uses various types of them in order to match the expected particle flux at various locations in the spectrometer. In high-flux regions close to the beam, tracking is provided by arrays of scintillating fibers, silicon detectors, micromesh gaseous chambers and gas electron multiplier chambers. Further away from the beam, larger-area tracking devices as multiwire proportional chambers, drift chambers and straw detectors are used. In 2006 the tracking system in the first stage of the spectrometer was adapted to match the increased aperture of the superconducting solenoid. Muons are identified in large area tracking detectors and scintillators downstream of concrete or iron muon filters. Hadrons are detected by two scintillator-iron sandwich calorimeters installed in front of the muon filters. Electromagnetic lead glass calorimeters are placed in front of the hadron ones. The data recording system is activated by triggers indicating the presence of a scattered muon and/or energy deposited by hadrons in the calorimeters. Both inclusive and semi-inclusive triggers were used. In the former the scattered muon is identified by coincident signals in the trigger hodoscopes and in the latter, the energy deposited in calorimeters was demanded in addition. Moreover a calorimetric trigger with a high energy threshold is implemented to extend the acceptance. To suppress triggers due to halo muons, veto counters upstream of the target are used. COMPASS trigger system covers a wide range of Q^2 , from quasi-real photoproduction to deep inelastic region.

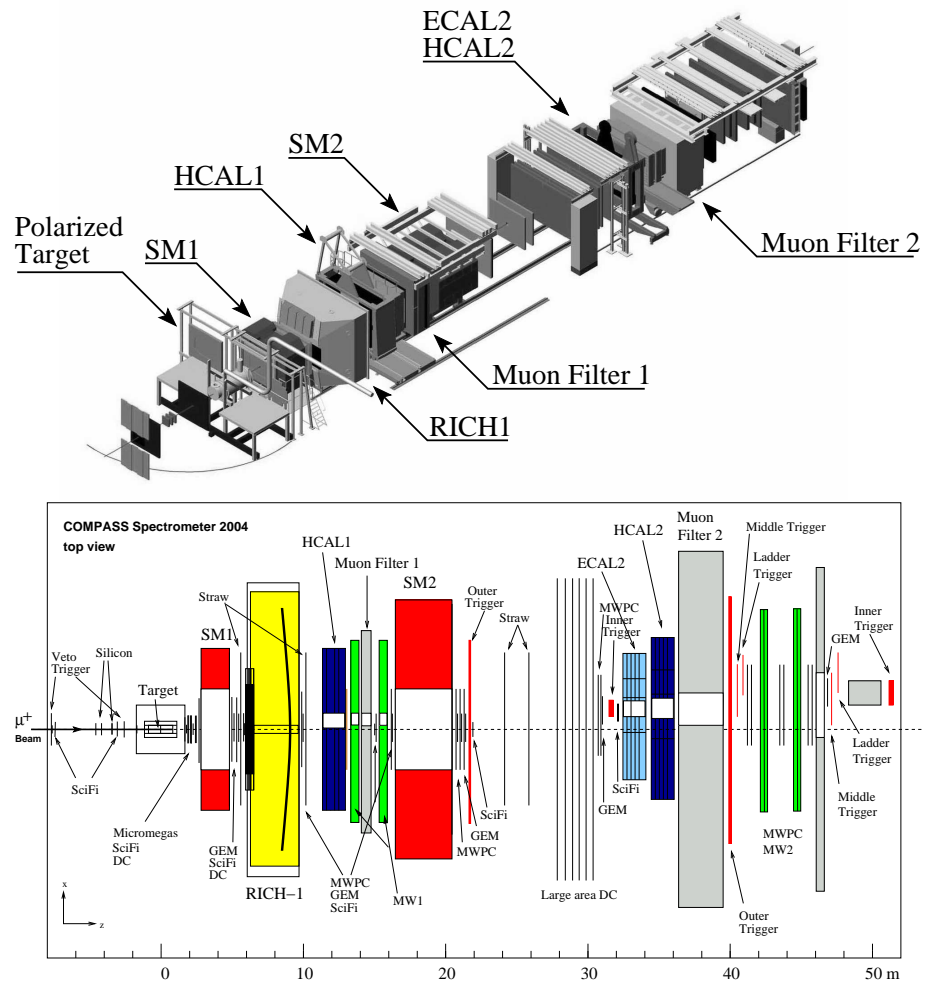


Figure 4.2: Compass 2004 muon setup (top) artistic view, (bottom) top view (for detector names, see [56]).

For charged particle identification in the first stage of the set-up a Ring Imaging Cherenkov detector (RICH) is installed [214]. It is a gas RICH with a 3 m long C_4F_{10} radiator. Two spherical mirror surfaces reflect and focus the Cherenkov photons on two sets of detectors above and below the acceptance of the tracking detectors respectively. The photon detection utilises MWPCs with segmented CsI photocathodes which detect photons in the UV region. In 2006 the central part of the RICH was upgraded replacing the MWPCs by multianode photomultiplier tubes yielding a considerably higher number of detected photons and a much faster response. For the outer parts the readout electronics was refurbished allowing a significant reduction of the background.

The particle identification procedure relies on a likelihood function constructed with the photons detected in the RICH and associated with a charged particle trajectory. The likelihood function uses the photons of the signal and a theoretical expectation of their distribution, taking into account possible signal losses due to dead zones in the detector. The description of the background photons, is taken from the photon detectors occupancy in the data. For each track the likelihood value is computed for different mass and the background hypotheses. Identification of a pion (kaon) is possible for their momenta between 2.5 GeV (9 GeV) and 50 GeV.

The performance of the detectors as well as the stability of the reconstructed data was carefully monitored and all spills not fulfilling stability requirements were excluded from the further analysis. Time intervals used for asymmetry measurements correspond to periods of stable spectrometer performance. The data taking amounted in total to 48 weeks in 2002 to 2007.

Chapter 5

Open-charm analysis with an Artificial Neural Network

Precision DIS data show that there is the deficit between the spin of the nucleon and the total spin carried by quark spins. By now, the contribution of the quark helicities to the nucleon spin is known to be about 30%, significantly smaller than the value of 60% expected from the Ellis–Jaffe sum rule. A large value for the gluon polarisation and the role of the anomaly is a natural solution of this problem in the QCD improved QPM. As discussed in [122, 123] the lack of twist-2, gauge invariant, local gluonic operators in OPE causes problem in defining the gluon helicity distribution. This problem was discussed in chapter 2 in section 2.2.2 in detail. In spite of the ongoing theoretical debate on how to correctly decompose of the nucleon spin in gauge-invariant way [64], agreement exists that besides the quark helicities also the gluon helicity contribution ΔG is a measurable, gauge-invariant observable.

Indirect gluon polarisation measurements based on QCD evolution suggest a rather small value of ΔG [46]. Direct determinations of the average gluon polarisation in a limited range of x , were performed in a model-dependent way using the PGF process by SMC [215], HERMES [216, 217] and COMPASS [218]. These analyses used events containing hadrons or hadron pairs with high transverse momenta, p_T (typically 1 to 2 GeV), defined with respect to the virtual photon direction. This method provides good statistical precision but strongly relies on Monte Carlo generators simulating QCD processes.

Chapter 6 details the COMPASS high- p_T analysis for $Q^2 > 1 \text{ GeV}^2$ events to determine the gluon polarisation. All these measurements indicate a small value of the gluon polarisation at $x \approx 0.1$. This is consistent with recent results from PHENIX [12] and STAR [11] at RHIC where the production of inclusive π^0 or high transverse momentum jets constrain ΔG (e.g. in QCD fits [46]).

In this chapter a new result on ΔG obtained from charm production, tagged by D meson decays in 160 GeV polarised muon-nucleon scattering is presented. The data were collected by the COMPASS Collaboration at CERN in the 2002–2004 and 2006–2007 running periods.

This result supersedes the one given in [219] since it is based on the full data sample and an improved analysis method that make use of Artificial Neural Network (ANN). Compared to the data sample used in [219], additional final state channels have been used. The gluon polarisation is determined assuming that open-charm production is dominated by the PGF mechanism, $\gamma^*g \rightarrow c\bar{c}$, shown in Fig. 5.1. The subsequent fragmentation of the $c\bar{c}$ pair, mainly into D mesons, is assumed to be spin-independent¹.

The dominance of the PGF mechanism in the COMPASS kinematic region is supported by the EMC results on $F_2^{c\bar{c}}$ [220], further discussed in [221], and by a COMPASS study of charm meson production [222]. The gluon polarisation determined with this assumption has the advantage that, in lowest order of the strong coupling constant, there are no other contributions to the cross-section. However, it is statistically limited. Next-to-leading order QCD calculations for determination of the gluon polarisation have been employed for the first time in this analysis.

The corrections to the PGF processes account at NLO precision. There is also a new class of the processes originating from light quarks. These processes contribute to the observed signal (D meson production) but they do not probe gluons. Therefore the determination of the gluon polarisation in NLO analysis requires to correct for these unwanted processes. Fortunately, the contribution from light-quark production processes is small. The PGF-like mechanism of open-charm production dominates in the COMPASS kinematic region, even in NLO approximation.

Since the PGF process is dominated by quasi-real photoproduction ($Q^2 \rightarrow 0$), the perturbative scale for the selected events, μ^2 , cannot be taken to be Q^2 , as is done in the QCD analyses of the inclusive data. It is chosen to be the transverse mass of the charmed quarks, $\mu^2 \equiv 4M_T^2 = 4(m_c^2 + p_T^2)$, where p_T , the D meson transverse momentum, is defined with respect to the virtual photon.

In the present analysis only one charmed meson is required in every event. This meson is selected through its decay into one of the following channels: $D^*(2010)^+ \rightarrow D^0\pi_{\text{slow}}^+ \rightarrow (K^-\pi^+/K^-\pi^+\pi^0/K^-\pi^+\pi^+\pi^-)\pi_{\text{slow}}^+$ and $D^0 \rightarrow K^-\pi^+$ as well as their charge conjugates. The former sample is called the tagged one while the latter is the untagged. Virtual photon cross section asymmetries, $A^{\gamma^*N \rightarrow D^0X}$, and the average gluon polarisation $\Delta G/G$ are extracted from these open charm events.

¹The potential dependence on spin in the fragmentation process is discussed in section 5.5 in the context of the observed asymmetry between D^0 and \bar{D}^0 meson production.

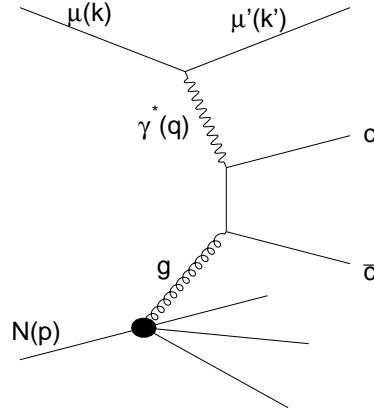


Figure 5.1: Photon–Gluon Fusion into a pair of charm quarks, $c\bar{c}$. Symbols in parentheses are four–vectors.

This chapter is organized as follows. In section 5.1 the double-spin asymmetry for D meson production events is defined and expressed in terms of the gluon polarisation and analysing power in LO QCD approximation. In section 5.2 the data selection is reported in detail. This is followed by the description of the analysis method, section 5.3. In this section the experimental asymmetry determination, the ANN method of the parameterization of the signal purity and the calculations and parameterization with ANN of the analysing power are discussed. Results for the gluon polarisation at LO accuracy and the asymmetry measurement are presented in sections: 5.4.1 and 5.4.2. The NLO corrections and their application to the COMPASS analysis and the result of the gluon polarisation at NLO accuracy are discussed in section 5.4.3. The potential influence of the observed asymmetry between D^0 and \bar{D}^0 meson production on the gluon polarisation determination is discussed in section 5.5.

5.1 Spin cross section asymmetry for D meson production

The longitudinal double-spin cross section asymmetry for D^0 (\bar{D}^0) meson production events is defined as:

$$A^{\mu N \rightarrow \mu' D^0 X} \equiv \frac{\Delta d\sigma}{2d\bar{\sigma}} = \frac{d\sigma^{\uparrow\uparrow} - d\sigma^{\uparrow\downarrow}}{d\sigma^{\uparrow\uparrow} + d\sigma^{\uparrow\downarrow}}, \quad (5.1)$$

where the arrows indicate the relative beam (\rightarrow) and target (\Rightarrow) spin orientations. As shown below, information on the gluon polarisation, $\Delta G/G$ is contained in this asymmetry.

The differential cross section for D^0 meson production, $d\sigma$, can be decomposed (see appendix 9.1) as ²:

$$d\sigma = G \otimes d\hat{\sigma} \otimes H, \quad (5.2)$$

and similarly for the spin-dependent part of the cross section, $d\Delta\sigma$:

$$d\Delta\sigma = \Delta G \otimes d\Delta\hat{\sigma} \otimes H, \quad (5.3)$$

where for simplicity all kinematic variable dependencies are omitted in the notation and \otimes denotes the convolution integrals as in Eq. (2.44).

In LO $d\hat{\sigma}$ and $d\Delta\hat{\sigma}$ are spin averaged and spin dependent partonic cross sections for $\mu g \rightarrow \mu' c\bar{c}$ reaction. The polarisation averaged and polarisation dependent gluon PDFs are denoted as G and ΔG , respectively. The $c\bar{c}$ quark pair produced in the PGF process fragments into charmed hadrons (mainly D mesons). The fragmentation function H is assumed to be spin-independent. The assumption of single-hadron independent fragmentation is not needed. H describes fragmentation of one of the charm quarks into a D meson and any number of unobserved hadrons (including second charmed meson). In particular the Lund string hadronization model [223], used in many Monte-Carlo generators, is described by H .

The spin-dependent cross section $d\Delta\sigma$ is equal to:

$$d\Delta\sigma = \frac{\Delta G}{G} G \otimes a_{LL} d\hat{\sigma} \otimes H. \quad (5.4)$$

The analysing power, a_{LL} , is defined as a partonic level asymmetry of the differential cross sections (polarisation dependent and polarisation averaged) for the $\mu g \rightarrow \mu' c\bar{c}$ reaction is given:

$$a_{LL} = \frac{d\Delta\hat{\sigma}}{d\hat{\sigma}}. \quad (5.5)$$

With the help of Eqs (5.2) and (5.4) the asymmetry $A^{\mu N \rightarrow \mu' D^0 X}$ can be decomposed as:

$$A^{\mu N \rightarrow \mu' D^0 X} = \left\langle \frac{\Delta G}{G} a_{LL} \right\rangle = \left\langle \frac{\Delta G}{G} \right\rangle_{a_{LL}} \langle a_{LL} \rangle, \quad (5.6)$$

where the averaging procedure is defined as follows:

$$\langle a_{LL} \rangle \equiv \frac{a_{LL} G \otimes d\hat{\sigma} \otimes H}{G \otimes d\hat{\sigma} \otimes H}, \quad \left\langle \frac{\Delta G}{G} \right\rangle_{a_{LL}} = \frac{\Delta G/G a_{LL} G \otimes d\hat{\sigma} \otimes H}{a_{LL} G \otimes d\hat{\sigma} \otimes H}. \quad (5.7)$$

²The cross sections for D^0 and \bar{D}^0 meson production are identical since PGF processes are symmetric in c and \bar{c} .

The formulae for LO cross sections corresponding to $\mu g \rightarrow \mu' c \bar{c}$ process can be found in [224] and [225]. These cross sections, $d\hat{\sigma}$ and $d\Delta\hat{\sigma}$, expressed in terms of Mandelstam kinematical variables \hat{s}, \hat{t} and \hat{u} are ³.

$$d\hat{\sigma} = \frac{\alpha^2 e_q^2 \alpha_s}{x Q^2 (\hat{s} + Q^2)^2} \left\{ \left[2(1-y) + y^2 \left(1 - \frac{2m_l^2}{Q^2} \right) \right] \left[\frac{Q^4 + \hat{s}^2}{(\hat{s} + Q^2)^2} \frac{\tilde{u}^2 + \tilde{t}^2}{2 \tilde{u} \tilde{t}} + \frac{2m^2}{\tilde{u} \tilde{t}} \left(\hat{s} - Q^2 + \frac{Q^2(\hat{s} + Q^2)^2}{2 \tilde{u} \tilde{t}} \right) - \frac{2m^4(\hat{s} + Q^2)^2}{\tilde{u}^2 \tilde{t}^2} \right] + 8(1-y) Q^2 \left[\frac{\hat{s}}{(\hat{s} + Q^2)^2} - \frac{m^2}{\tilde{u} \tilde{t}} \right] \right\}, \quad (5.8)$$

and

$$d\Delta\hat{\sigma} = \frac{\alpha^2 e_q^2 \alpha_s}{x Q^2 (\hat{s} + Q^2)^2} y \left(2 - y - \frac{2y^2 m_l^2}{Q^2} \right) \frac{\tilde{u}^2 + \tilde{t}^2}{2 \tilde{u} \tilde{t}} \left[\frac{Q^2 - \hat{s}}{\hat{s} + Q^2} + \frac{2m^2(\hat{s} + Q^2)}{\tilde{u} \tilde{t}} \right], \quad (5.9)$$

where: $\tilde{t} = m^2 - \hat{t}$, $\tilde{u} = m^2 - \hat{u}$, m is a mass of charm quark, m_l stands for the lepton (muon) mass, α and α_s are electromagnetic and strong coupling constants, and e_q is the quark charge (2/3 for charm quarks). Terms proportional to the muon mass and the ratio of Q and the incident muon beam energy were neglected in Eqs (5.9) and (5.9) in view of their size.

The analysing power of the $\mu g \rightarrow \mu' c \bar{c}$ process includes the depolarisation factor D , (comp. Eq. (2.35)), accounting for the polarisation transfer from the lepton to the virtual photon:

$$D = \frac{y \left(2 - y - \frac{2y^2 m_l^2}{Q^2} \right)}{y^2 \left(1 - \frac{2m_l^2}{Q^2} \right) + 2(1-y)}, \quad (5.10)$$

Strictly speaking the factorization of the D from a_{LL} is possible only in the photo-production limit, $Q^2 = 0$. The analysing power for virtual PGF, $\gamma^* g \rightarrow c \bar{c}$, can be defined as $\hat{a}_{LL} = \frac{a_{LL}}{D}$.

The muon-gluon analysing power a_{LL} , depends on the partonic kinematics \hat{s} and \hat{t} . This partonic asymmetry is not accessible experimentally on an event by event basis ⁴. It is obtained using a Monte Carlo generator. In order to use the generated values of a_{LL} in real data, an ANN is used to parameterise it in terms of measured kinematic variables, here

³The partonic cross sections presented here are integrated over azimuthal angles of the quarks; the non-integrated formulae can be found in [225]. In the open-charm analysis the azimuthal angle dependent parts of the cross section are small and they are averaged to zero thanks to the symmetric acceptance.

⁴The only one D meson is reconstructed in COMPASS data analysis. The reconstruction of both charmed particles in the final state could help to reconstruct the partonic kinematics, but even in this case this reconstruction is only approximate.

denotes with X . The resulting average $a_{LL}(X)$ is evaluated even-by-event for real data. For small Q^2 (the COMPASS kinematic domain, as discussed in the next section), \hat{a}_{LL} is very weakly y -dependent. Therefore it is more convenient to parameterize \hat{a}_{LL} while D can be determined directly from data. It is discussed in section 5.3.2. With the help of analysing power the gluon polarisation can be determined from the D meson cross section asymmetry, observed in the data. The result depends on the QCD approximation used in the calculations of a_{LL} .

The signal asymmetry $A^{\mu N \rightarrow \mu' D^0}$ discussed in this section is determined from data after the subtraction of large combinatorial background. The experimentally measured asymmetry A_{meas} is a combination of two asymmetries: the signal asymmetry $A^{\mu N \rightarrow \mu' D^0}$ and background asymmetry A_B . The statistical weight technique which allows one to extract the signal and the background asymmetry from data is described in section 5.3.

5.2 Data selection

In order to extract information about the gluon polarisation, events with D mesons have to be selected from the data. To this aim, events containing an incoming and outgoing muon, together with at least two outgoing charged tracks were considered. Further, only events with a beam track potentially crossing the entire target and with an interaction point (or ‘vertex’) within the target were retained.

The direction of the tracks reconstructed at the vertex is determined with a precision better than 0.2 mrad and the momentum resolution for charged tracks detected in the first stage of the spectrometer is about 1.2% whereas it is about 0.5% in the second stage. The longitudinal vertex resolution varies from 5 mm to 25 mm along the target and permits the assignment of each event to either target spin direction. The distributions of the reconstructed vertex position z_{vtx} along the beam axis for events remaining after the aforementioned selection criteria are shown in Fig. 5.2. The relative increase of the number of events in the upstream target cell in 2006 compare to 2004 is due to the upgrade of the target magnet.

The spatial resolution of the vertex reconstruction is not sufficient to separate the production and decay points of charmed mesons, especially due to multiple Coulomb scattering in the solid state target, As a result, these mesons can only be reconstructed using the invariant mass of their decay products. The decay modes considered in this analysis are listed in Table 5.1. The D^0 decays that involve the same set of final state particles cannot be distinguished event by event. Therefore five independent data samples with different final states are defined for this analysis, see Table 5.2. In the four tagged samples, *i.e.* $D_{K\pi}^*$, $D_{K_{\text{sub}}\pi}^*$, $D_{K\pi\pi^0}^*$ and $D_{K\pi\pi\pi}^*$, the D^0 meson originates from a D^* decay into a D^0 meson and a

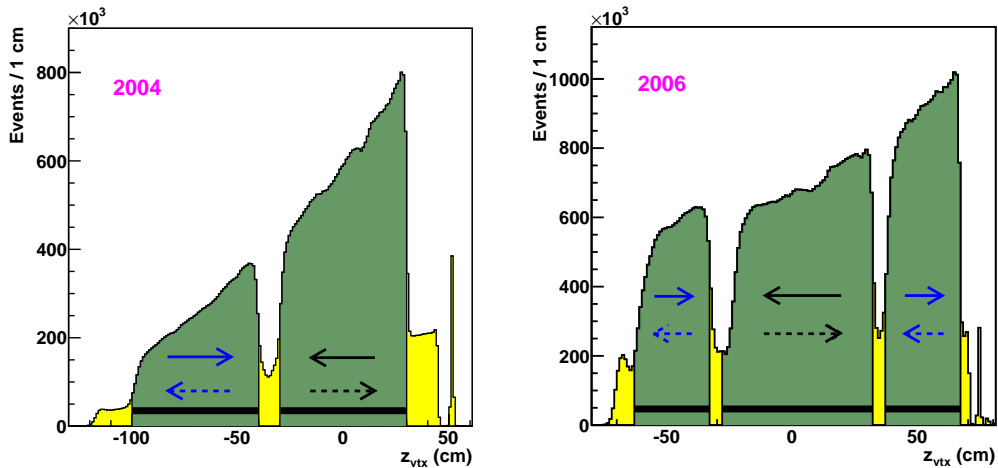


Figure 5.2: Distribution of the reconstructed vertex positions z_{vtx} along the beam axis for target with two (left) and three (right) cells. Dark horizontal bars at the bottom mark the target cells, arrows denote the target polarisation directions.

Category	D^0 decay mode
1	$D^0 \xrightarrow{3.89\%} K^- \pi^+ + \text{c.c.}$
2	$D^0 \xrightarrow{13.9\%} K^- \pi^+ \pi^0 + \text{c.c.}$
3	$D^0 \xrightarrow{10.8\%} K^- \rho^+ \xrightarrow{\approx 100\%} K^- (\pi^+ \pi^0) + \text{c.c.}$
4	$D^0 \xrightarrow{2.22\%} K^{*-} \pi^+ \xrightarrow{\approx 100\%} (K^- \pi^0) \pi^+ + \text{c.c.}$
5	$D^0 \xrightarrow{1.88\%} \bar{K}^{*0} \pi^0 \xrightarrow{\approx 100\%} (K^- \pi^+) \pi^0 + \text{c.c.}$
6	$D^0 \xrightarrow{8.09\%} K^- \pi^+ \pi^+ \pi^- + \text{c.c.}$
7	$D^0 \xrightarrow{6.76\%} K^- \pi^+ \rho^0 \xrightarrow{\approx 100\%} K^- \pi^+ (\pi^+ \pi^-) + \text{c.c.}$

Table 5.1: The charmed D^0 meson decay modes, together with their branching ratios, considered in this analysis. The charge conjugate (c.c.) final states from the \bar{D}^0 decays were also included.

slow pion, $D^* \xrightarrow{67.7\%} D^0 \pi_s$. The kinematic selection criteria, tuned to reduce the combinatorial background without affecting the D^0 meson signal are listed in Table 5.3.

Particles are identified using the RICH detector. Using the measured momentum of a charged particle and the distributions of Cherenkov photons, likelihood values for different

	Untagged sample	Tagged samples			
Sample	$D_{K\pi}^0$	$D_{K\pi}^*$	$D_{K_{\text{sub}}\pi}^*$	$D_{K\pi\pi^0}^*$	$D_{K\pi\pi\pi}^*$
Category	1	1	1	2, 3, 4, 5	6, 7

Table 5.2: Samples in the analysis. For the tagged events, the D^0 originates from the decay of D^* . The final state of the D^0 decay is indicated by the subscripts.

	Kinematic cut intervals				
	$D_{K\pi}^0$	$D_{K\pi}^*$	$D_{K_{\text{sub}}\pi}^*$	$D_{K\pi\pi^0}^*$	$D_{K\pi\pi\pi}^*$
$(M_{K\pi}^{\text{rec}} - M_{D^0})$ [MeV]	[-400, +400]	[-600, +600]	[-400, +400]		
$ \cos \theta^* $	< 0.65	< 0.90		< 0.85	
z_{D^0}	[0.20, 0.85]	[0.20, 0.85]	[0.25, 0.85]	[0.30, 0.85]	
p_K [GeV]	[9.5, 50]	[9.5, 50]	[2.5, 9.5]	[9.5, 50]	
p_π [GeV]	[7, 50]	[2.5, 50]			
ΔM [MeV]	—	[3.2, 8.9]			[4.0, 7.5]
p_{π_s} [GeV]	—	< 8			

Table 5.3: List of all kinematic cuts used in this analysis. For every sample, a D^0 candidate is accepted if it fulfills all the conditions. Here $\Delta M = M_{K\pi\pi_s}^{\text{rec}} - M_{K\pi}^{\text{rec}} - M_\pi$, where the superscript ‘rec’ denotes the reconstructed mass.

mass hypotheses and for a background hypothesis are computed. A particle is identified as a kaon or a pion if the likelihood value is larger than that for any other hypothesis. This procedure is very efficient in reducing the combinatorial background of two particles other than π and K . A full description of the identification procedure is given in [226].

The following selection criteria have been applied to obtain the final event samples. The untagged $D_{K\pi}^0$ sample contains events with $K\pi$ pairs that do not stem from decays of reconstructed D^* mesons and have the reconstructed invariant mass given in Table 5.3. Due to its large combinatorial background this sample requires more restrictive cuts for the identification of pion and kaon: a pion momentum above 7 GeV is required to suppress contamination from electrons. For the four tagged samples, a D^* meson is selected by requiring the presence of a slow pion, $p_{\pi_s} < 8$ GeV, in addition to a D^0 candidate. The presence of the slow pions permits the application of two additional cuts. The first one uses the RICH detector to reject electrons that mimic slow pion candidates and reduces the combinatorial background by a factor of two. The second one is a cut on the mass difference,

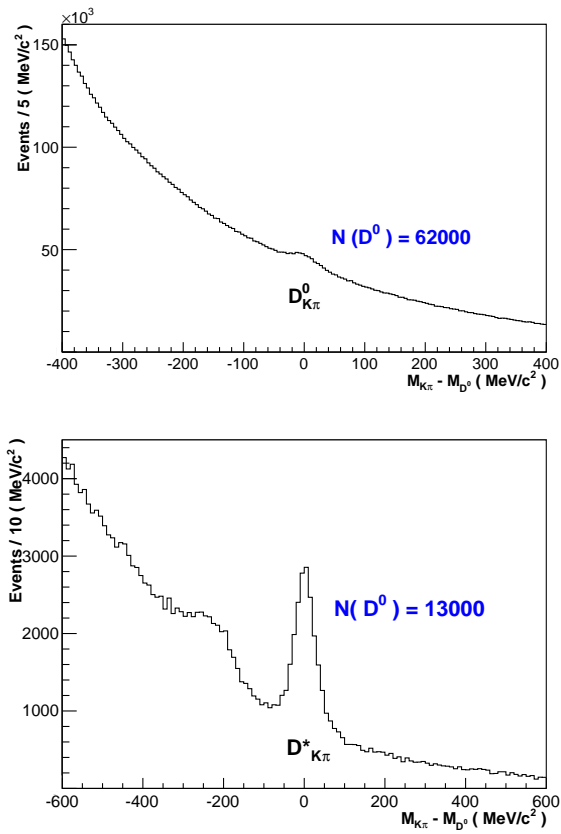


Figure 5.3: Invariant mass spectra for the $D^0_{K\pi}$ and $D^{*0}_{K\pi}$ samples. The approximate number of D^0 mesons above background is given.

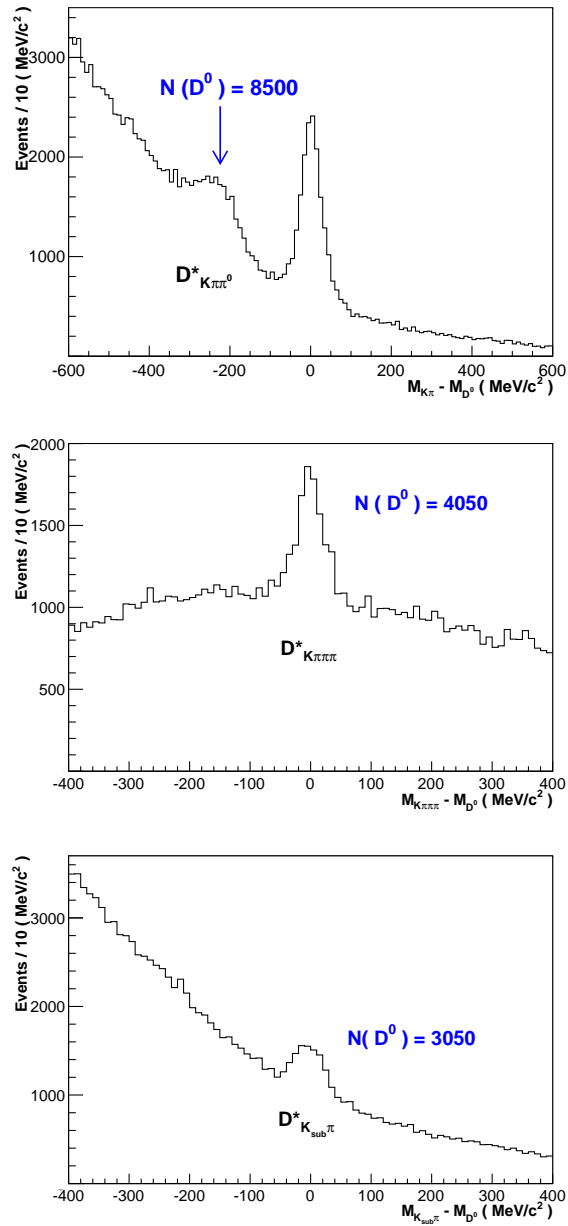


Figure 5.4: Invariant mass spectra for the $D^*_{K\pi\pi^0}$, $D^*_{K\pi\pi\pi}$ and $D^*_{K_{sub}\pi\pi}$ samples. The purity of the samples was optimized using the ANN. The approximate number of D^0 mesons above background is given.

$\Delta M = M_{K\pi\pi_s}^{\text{rec}} - M_{K\pi}^{\text{rec}} - M_\pi$, where $M_{K\pi\pi_s}^{\text{rec}}$ and $M_{K\pi}^{\text{rec}}$ are the reconstructed masses of the D^* and the D^0 candidates, respectively. This mass difference can be measured with very good precision and thus the cut on ΔM results in a significant reduction of the combinatorial background in the tagged samples.

Other kinematic cuts were applied to all samples in addition to the cuts described above. It was demanded that $|\cos\theta^*| < 0.9$ for the tagged samples, $|\cos\theta^*| < 0.65$ for the sample of $D_{K\pi}^0$ and $|\cos\theta^*| < 0.85$ for the remaining samples. This cut suppresses mainly background events and improves the figure of merit. Finally, all events were required to satisfy a cut on $z_{D^0} = E_{D^0}/E_{\gamma^*}$. Since a pair of charmed quarks is produced in the c.m. of the γ^*g system, each one of them receives on average a half of the virtual photon energy. Indeed, the measured z_{D^0} distribution and the one simulated assuming a pure PGF are very similar and have a most probable value close to 0.5, Fig. 5.5. This strongly supports the assumption of PGF dominance in charm production.

The final mass spectra for the untagged sample selected according to Table 5.3 are shown in Fig. 5.3(top). For tagged events selected according to the $D_{K\pi}^*$ cuts the resulting mass spectrum is shown in Fig. 5.3(bottom) and the D^0 mass resolution of about 27 MeV was obtained.

In this mass spectrum also a second structure at about $-250 \text{ MeV}/c^2$ is visible. It is due to events with $D^0 \rightarrow K^-\pi^+\pi^0$ decays where the neutral pion is not reconstructed in the analysis. Thus the $K\pi$ spectrum is shifted to a lower mass with respect to the $D^0 \rightarrow K^-\pi^+$ decays. The purity of this signal is much worse due to the not observed neutral pion.

Further improvement of the significance of the signal is accomplished by applying the ANN method described in section 5.3.3. The resulting mass spectrum for $D_{K\pi\pi^0}^*$ is shown in Fig. 5.4(top) with a clear improvement of the signal to background ratio for $D_{K\pi\pi^0}^*$. For the $D^0 \rightarrow K^-\pi^+$, the signal and the background are reduced in a similar way so that the figure of merit stays unchanged. Therefore the selection criteria from Table 5.3 are only used for the final $D_{K\pi}^*$ sample (Fig. 5.3(bottom)).

The considerable reduction of the combinatorial background in the tagged samples permits us also to study other channels with a weaker D^0 signal like $D_{K_{\text{sub}}\pi}^*$ and $D_{K\pi\pi\pi}^*$, shown in Fig. 5.4(middle and bottom). The sample $D_{K_{\text{sub}}\pi}^*$ contains events where the momentum of the kaon candidate is below the limit of 9 GeV for kaon identification with the RICH detector. Simulations using the AROMA [227] Monte Carlo generator for heavy flavours, and a full spectrometer description based on GEANT, show that about 30% of kaons originating from D^0 decays have their momenta below this RICH threshold. Therefore, the analysis required that those particles, K_{sub} , were not identified as pions or electrons.

Finally, in case of two D^0 candidates in the same event, only one of them, chosen ran-

domly, is considered in the analysis. In case of two channels contributing with a D^0 candidate to the same event, only one of them is accepted according to the following priority rule: $D_{K\pi\pi\pi}^*$, $D_{K\pi}^*$ or $D_{K\pi\pi^0}^*$, $D_{K\pi}^0$, $D_{K_{\text{sub}}\pi}^*$, see [226].

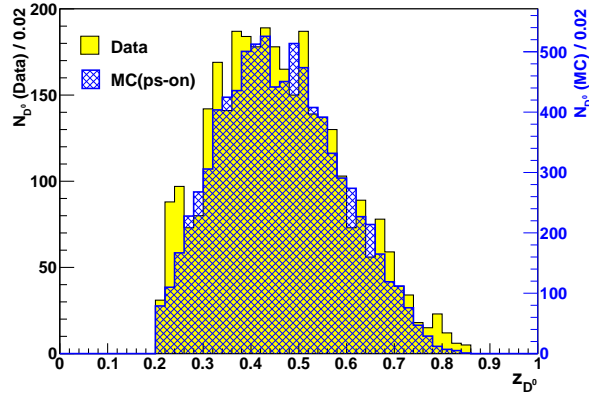


Figure 5.5: Distribution of the z_{D^0} for the $D_{K\pi}^*$ data sample after background subtraction and corresponding Monte Carlo events. The signal was selected by requiring for the ± 80 MeV mass window around the nominal D^0 mass.

Distributions of Bjorken x , Q^2 and y variables for the $D_{K\pi}^*$ candidates from 2006, and from the D^0 signal region, are presented in Fig. 5.6. The x values range from about 10^{-5} to 0.1 with $\langle x \rangle = 0.004$, the Q^2 values from 10^{-3} to 30 GeV^2 with $\langle Q^2 \rangle = 0.6 \text{ GeV}^2$, and the y values range from 0.1 to 1 with $\langle y \rangle = 0.63$.

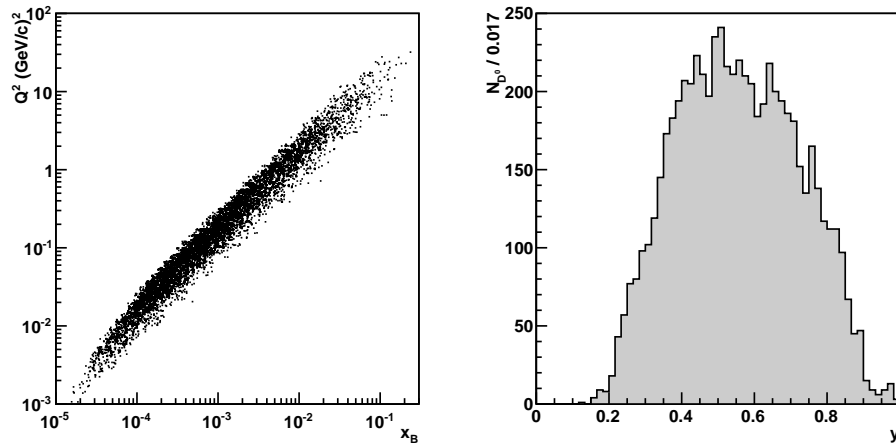


Figure 5.6: Distributions of x and y for the 2006 $D_{K\pi}^*$ sample selected as in Fig. 5.5 before background subtraction.

5.3 The weighted analysis

In this section we describe the determination of the gluon polarisation from the event samples defined in Table 5.2.

5.3.1 Asymmetry determination

The number of events collected in a given target cell and time interval is given by:

$$\frac{dN}{dm dX} = a\phi n(s+b) \left[1 + P_t P_\mu f \left(\frac{s}{s+b} A^{\mu N \rightarrow \mu' D^0 X} + \frac{b}{s+b} A_B \right) \right]. \quad (5.11)$$

Here $A^{\mu N \rightarrow \mu' D^0 X}$ is the longitudinal double spin differential cross-section asymmetry of events with a D^0 or \bar{D}^0 in the final state and A_B is the corresponding asymmetry originating from the background events in the mass spectra. Furthermore, $m \equiv M_{K\pi}$, and X denotes a set of kinematic variables describing an event (Q^2, y, z, \dots) while a, ϕ and n are the spectrometer acceptance, the incident muon flux integrated over the time interval and the number of target nucleons, respectively. The differential unpolarised cross-sections for signal and background folded with the experimental resolution as a function of m and X are represented by $s = s(m, X)$ and $b = b(m, X)$, respectively. The ratio $s/(s+b)$ defines signal purity. The background asymmetry $A_B = DA_B^{\gamma^* N}$ can be written as the product of the virtual photon asymmetry and the depolarisation factor and is assumed to be independent of m .

A straightforward way to extract the gluon polarisation is the following: First, Eq. (5.11) is integrated over the variables X to obtain the number of events in both spin configurations as a function of the invariant mass m . Next the event rate asymmetry in the D^0 signal region is extracted and a possible background asymmetry, determined from the asymmetries in side-bands to the left and right from the signal region, is subtracted. The asymmetry obtained in this way is proportional to the weighted average value of gluon polarisation, $\langle \Delta G/G \rangle_\beta$, where the averaged value of the weight $\beta = P_t P_\mu f a_{LL}$, $\langle \beta \rangle$, is a proportionality coefficient, compare Eqs (5.6, 5.7).

There are however more efficient ways to analyse the data in terms of statistical precision. One possibility would be to perform the analysis in bins of β , but this method causes problems in the asymmetry extraction due to low number of events in some bins. Therefore the method of event weighting is applied.

Every event gets a weight factor which is β/P_t . The target polarisation is not included in the weight, because its time dependence would lead to an increase in systematic error. One can show [228] that the statistical error in this method is smaller by a factor $\sqrt{\langle \beta^2 \rangle / \langle \beta \rangle^2}$ compared to the method where simply the event rates are used. In this analysis the gain is particularly large since β includes a_{LL} , which can be positive or negative, depending on the event kinematics. Close to the threshold a_{LL} is positive while at higher \hat{s} it becomes negative [225]. This is in contrast to the a_{LL} for light quarks. The distribution of β for the sample $D_{K\pi}^*$ is given in Fig. 5.7.

The weighting procedure can even be extended to determine the background asymmetry A_B simultaneously with the weighted averaged gluon polarisation, [229]. Every event is weighted once with a signal weight, w_S , and once with a background weight, w_B :

$$w_S = P_\mu f a_{LL} \frac{s}{s+b}, \quad (5.12)$$

$$w_B = P_\mu f D \frac{b}{s+b}. \quad (5.13)$$

Thus the signal purity, $s/(s+b)$, and the ‘background purity’, $b/(s+b)$, are both included in the weight. This procedure leads to the lowest possible statistical error which would also be obtained in an unbinned maximum likelihood method [229]. Note however that the latter cannot be applied here because the acceptance and flux factors $a\phi n(s+b)$ in Eq. (5.11) are not known with sufficient precision. Only their ratios between different spin states and target cells are known. These ratios will be used for the extraction of $\langle \Delta G/G \rangle$ and $\langle A_B^{\gamma^*N} \rangle$.

Eq. (5.11) can be rewritten as follows:

$$\frac{dN}{dm dX} = a\phi n(s+b) \left(1 + \beta_S \frac{\Delta G}{G} + \beta_B A_B^{\gamma^*N} \right), \quad (5.14)$$

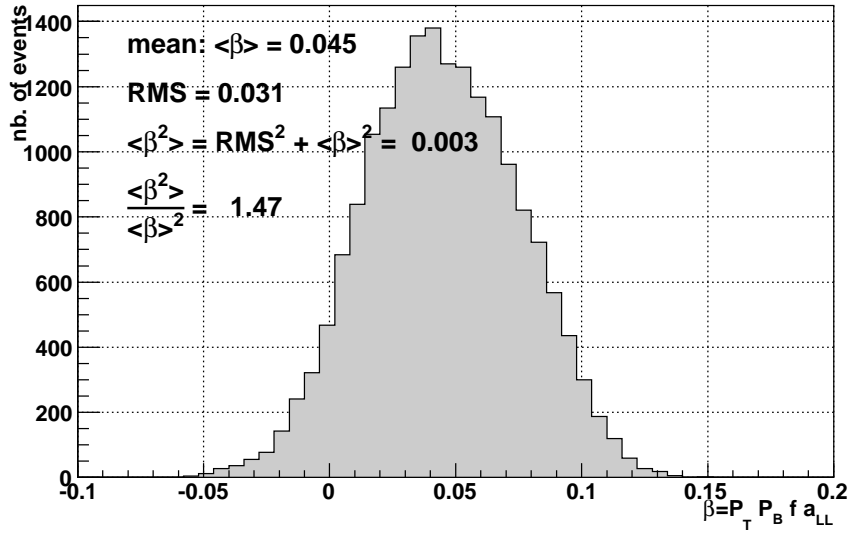


Figure 5.7: Distribution of the weighting factors, $P_\mu f a_{LL}$, for the $D_{K\pi}^*$ sample.

where:

$$\beta_S = P_t w_S \quad \beta_B = P_t w_B \quad (5.15)$$

Note, that Eqs (5.11) and (5.14) are not integrated yet over X . This integration corresponds to convolution integrals, symbolically denoted as \otimes in section 5.1. Therefore the D meson asymmetry, $A^{\mu N \rightarrow \mu' D^0 X}$, has been substituted by the product of a_{LL} and $\Delta G/G$ instead of the averaged values as present in Eq. (5.6).

The expectation value of the sum of weights $\left\langle \sum_{i=1}^{N_t} w_{S,i} \right\rangle$ can be obtained by multiplying Eq. (5.14) by w_S and integrating over X and m :

$$\begin{aligned} \left\langle \sum_{i=1}^{N_t} w_{S,i} \right\rangle &= \int w_S(X, m) \frac{d^k N_t}{dm dX} dX dm \\ &= \tilde{\alpha}_{S,t} \left[1 + \langle \beta_S \rangle_{w_S} \left\langle \frac{\Delta G}{G} \right\rangle_{\beta_S w_S} + \langle \beta_B \rangle_{w_S} \left\langle A_B^{\gamma^* N} \right\rangle_{\beta_B w_S} \right] \end{aligned} \quad (5.16)$$

with the following definitions:

$$\alpha_t = a_t \phi_t n_t (s + b), \quad (5.17)$$

$$\tilde{\alpha}_{S,t} = \int w_S \alpha_t dm dX, \quad (5.18)$$

$$\langle \eta \rangle_w = \frac{\int \eta w \alpha_t dm dX}{\int w \alpha_t dm dX}, \quad (5.19)$$

where $\eta = \beta_S, \beta_B, \frac{\Delta G}{G}$ and $A_B^{\gamma^* N}$, and $w = w_S, w_B, w_S \beta_S, w_S \beta_B$. The index t denotes the target cell before ($t = u, d$) and after ($t = u', d'$) the spin rotation. N_t is the number of events observed in one target cell⁵. An equation analogous to Eq. (5.16) holds for the sum of background weights, $\left\langle \sum_{i=1}^{N_t} w_{B,i} \right\rangle$:

$$\begin{aligned} \left\langle \sum_{i=1}^{N_t} w_{B,i} \right\rangle &= \int w_B(X, m) \frac{d^k N_t}{dm dX} dX dm \\ &= \tilde{\alpha}_{B,t} \left[1 + \langle \beta_S \rangle_{w_B} \left\langle \frac{\Delta G}{G} \right\rangle_{\beta_S w_B} + \langle \beta_B \rangle_{w_B} \left\langle A_B^{\gamma^* N} \right\rangle_{\beta_B w_B} \right] \end{aligned} \quad (5.20)$$

In total 8 equations similar to Eq. (5.16) and Eq. (5.20) are obtained for the signal and background weights in the two target cells and for the two spin configurations. These equations contain 12 unknowns: $\langle \frac{\Delta G}{G} \rangle_{\beta_S w_S}, \langle \frac{\Delta G}{G} \rangle_{\beta_S w_B}, \langle A_B^{\gamma^* N} \rangle_{\beta_B w_S}, \langle A_B^{\gamma^* N} \rangle_{\beta_B w_B}$ and eight acceptance factors: $\tilde{\alpha}_{S,t}$ and $\tilde{\alpha}_{B,t}$.

The expectation values of the sum of weights on the left hand side of Eq. (5.16) are equated with the measured sums of weights. In order to extract $\Delta G/G$ and $A_B^{\gamma^* N}$ from the measured sums of weights one proceeds as follows. The factors $\langle \beta_{S,B} \rangle_{w_{S,B}}$ are evaluated from the data. For example for $\langle \beta_S \rangle_{w_S}$:

$$\langle \beta_S \rangle_{w_S} \approx \frac{\sum_{i=1}^{N_t} \beta_S w_S}{\sum_{i=1}^{N_t} w_S}. \quad (5.21)$$

The expectation values appearing in Eqs (5.19) should be evaluated from an unpolarised sample. The sum of events concerns a polarised sample. This has a negligible effect on the results, because the raw asymmetry, $P_t P_{\mu} f a_{LL} \Delta G/G$, is very small.

The acceptance factors $\tilde{\alpha}_{S,t}$ and $\tilde{\alpha}_{B,t}$ cannot be determined with sufficient precision to be able to extract $\Delta G/G$ and $A_B^{\gamma^* N}$ directly from Eq. (5.16) and Eq. (5.20).

⁵In 2002–2004 the target consisted of two cells: upstream u and downstream d , with opposite polarisation. In 2006–2007, it consisted of three volumes, with the central piece being in one polarisation state and the pair of outer pieces being in the opposite state. For the sake of simplicity, these two sets of volumes (central one and two outer ones), are named by term "cell" and are denoted by u and d .

Assuming that the background asymmetry, $A_B^{\gamma^*N}$, and the gluon polarisation, $\Delta G/G$, are constant in the kinematic domain covered by the measurement:

$$\left\langle \frac{\Delta G}{G} \right\rangle_{\beta_S w_S} = \left\langle \frac{\Delta G}{G} \right\rangle_{\beta_S w_B} \equiv \left\langle \frac{\Delta G}{G} \right\rangle, \quad (5.22)$$

$$\left\langle A_B^{\gamma^*N} \right\rangle_{\beta_B w_S} = \left\langle A_B^{\gamma^*N} \right\rangle_{\beta_B w_B} \equiv \left\langle A_B^{\gamma^*N} \right\rangle, \quad (5.23)$$

and assuming that possible acceptance variations affect the upstream and downstream cells in the same way, i.e. $\tilde{\alpha}_C^u/\tilde{\alpha}_C^d = \tilde{\alpha}_C^{u'}/\tilde{\alpha}_C^{d'}$, ($C = S, B$). This reduces the number of unknowns to eight. With an extra assumption that signal and background events from the same target cell are affected in the same way by the acceptance variations, one arrives at a system of eight equations with seven unknowns. Possible deviations from the above assumptions may generate false asymmetries which are included in the systematic uncertainty and will be discussed in section 5.4.1. Using the set of eight equations, the gluon polarisation $\Delta G/G$ at LO accuracy, and the background asymmetry A_B are determined simultaneously with a standard least square minimisation procedure taking into account the statistical correlation between $\sum w_S$ and $\sum w_B$ in the same target cell. The correlation factor $\text{cov}(\sum w_S, \sum w_B)$ is given in ref. [228]. The analysis is performed independently for all the D meson decay channels.

The weighted analysis discussed in this section allows one to obtain a result with the highest precision allowed by the data. However the assumption that $\Delta G/G$ is constant is a strong assumption. It is in general justified only if the range of x_G covered by the measurement is very narrow. It is much more reasonable to assume a linear dependence in x_G , $\Delta G/G(x_G) = a(x_G - \langle x_G \rangle) + \Delta G/G(\langle x_G \rangle)$. Under this assumption, Eq. (5.22) holds if $\langle x_G \rangle_{\beta_S w_S} \approx \langle x_G \rangle_{\beta_S w_B} \equiv \langle x_G \rangle$ and $\Delta G/G \equiv \Delta G/G(\langle x_G \rangle)$.

The linear dependence in x_G is assumed in the determination of the gluon polarisation from the weighted asymmetry for signal and background measured in several kinematic bins, as discussed in section 5.4.2. In this case it is sufficient to assume that the asymmetries are constant in small bins. The approximation $\langle x_G \rangle_{\beta_S w_S} \approx \langle x_G \rangle_{\beta_S w_B}$ is not needed but the uncertainty in the gluon polarisation determined from the asymmetries in bins is about 5% larger than in the fully weighted method.

5.3.2 Parameterization of the analysing power

The muon-gluon analysing power a_{LL} for charm production depends on the partonic kinematics. The partonic asymmetry is not accessible experimentally on an event-by-event basis.

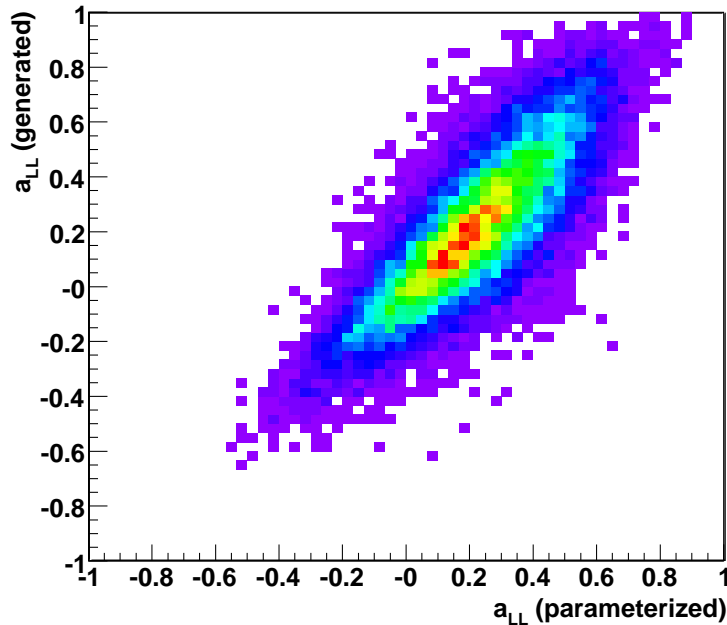


Figure 5.8: Example of the correlation between the generated analysing power and the analysing power parameterised by a Neural Network for the $D_{K\pi}^*$ channel and for the 2006 experimental acceptance.

It is obtained from the Monte Carlo generator AROMA [227] in LO QCD approximation, *i.e.* with parton showers switched off. The generated events are passed through a GEANT package [230] to simulate the full response of the COMPASS spectrometer. They are then reconstructed with the same analysis chain as real data. In order to use the values of a_{LL} obtained from generated MC events for the real data, an Artificial Neural Networks, (ANN), [231] is used to parameterise obtained a_{LL} in terms of measured kinematic variables, X . The resulting $a_{LL}(X)$ is evaluated for real data on an event-by-event basis. The Neural Network used in the analysis is briefly described in appendix 9.2.

The input layer of neurons contains the following set of kinematic observables: Q^2 , y , z_D , $p_T^{D^0}$ and x . There are two hidden layers in the Network and the number of neurons in them varies during the training process (dynamic Network). The supervised training technique is used in this work [231]. For each generated event, the Network tunes the strength of each variable-neuron and neuron-neuron connection. The strengths are obtained by minimising the squared deviation between the expected output and the actual Neural Network prediction, *i.e.* between the generated a_{LL} and the parameterised $a_{LL}(X)$. This training process is stopped when the deviation reaches a stable minimum [231]. A unipolar sigmoid activation

function (see appendix 9.2) was used in this analysis except for the output layer where a linear neuron activation function of is used to ensure that the output is proportional to the input signal. ⁶

The correlation achieved between the generated and the parametrised analysing powers is 77% for the $D_{K\pi\pi^0}^*$ channel and 82% for the remaining channels (see Fig. 5.8). Six separate $a_{LL}(X)$ parameterisations were built: one of each of the three D meson decay channels ($K\pi$, $K\pi\pi^0$, $K\pi\pi\pi$) and each of the two experimental setups (2002–2004 and 2006–2007). The trained networks is applied to real data. The results from the ANN, corresponds to the analysing power a_{LL} , which was subsequently used for the extraction of the gluon polarisation.

5.3.3 The signal purity

The signal purity $s/(s+b)$ can be extracted from a fit to the invariant mass distribution of D^0 candidates. It depends on the kinematical parameters of the event. In order to implement the kinematic dependence of the signal purity on the kinematics in the weights given by Eqs (5.12,5.13), one would naively proceed by performing fits to the corresponding invariant mass distributions in bins of the kinematical variables. This procedure is not feasible in COMPASS case because of two conflicting constraints present in the data. Firstly, the statistics is limited, which restricts the number of bins one can consider. Secondly anti-correlations exist between the signal purity and the parameterized analysing power, $a_{LL}(X)$. In kinematical domains where the signal purity is high, the analysing power is low and vice versa as shown in Fig. 5.9.

The observed anticorrelation between signal purity and analysing power parameterized by $a_{LL}(X)$ at LO describes the hidden correlation between the signal purity and the event characteristic described by the kinematic vector X . To avoid bias in the result this correlation should be taken into account in $s/(s+b)$.

The method presented here employs a parameterization based on an ANN. For that purpose the same network model and adjustment algorithm was used as described in section 5.3.2 and appendix 9.2.

The aim of the ANN is to distinguish signal from background events using only data. For each analysed sample (see Table 5.2) two data sets are used as inputs to the Neural Network. The first one contains the D^0 signal These events are called "good" charge combination, gcc , referring to the charges of particles from the D^0 decays and are selected as described in section 5.2. The second set, the "wrong" charge combination events, wcc , is selected in a similar

⁶Note, that a_{LL} changes sign while the sigmoid function is always positive.

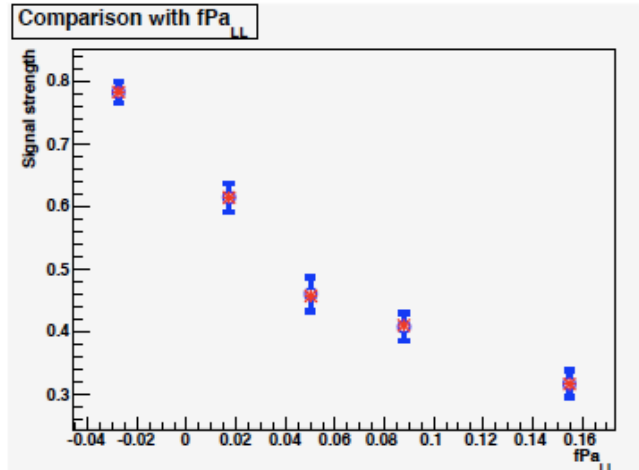


Figure 5.9: The signal strength versus analysing power from the fit (blue open symbols) and from Ref. [219] (red star) for different bins in $fP_{\mu}a_{LL}$. The signal strength and analysing power are visibly anti-correlated. Fig. taken from [232].

way except that the sum of charges of the corresponding particles should be different from zero. It contains only background events as seen in Fig. 5.10 and it is used as a background model. The ANN performs a multi-dimensional comparison of events in a ± 40 MeV/ c^2 mass window around the D^0 mass ⁷. Within the gcc set, the signal events are distinguished from combinatorial background by exploiting differences between gcc and wcc sets in the shapes of distributions of kinematic variables as well as multi-dimensional correlations between them. An example of a properly chosen variable is $\cos \theta^*$, whose distributions are shown in Fig. 5.11. The reconstructed mass cannot be used because it would artificially enhance the probability that a background event is a true D meson event in the signal region.

The ANN classifies all the gcc events according to their dissimilarity in kinematics with respect to the wcc ones, and to each event it assigns a probability of being a signal. A probability 0.5 is assigned to undistinguished events. If the ANN is trained with proper input samples (*i.e.* a correct background model and a sufficiently strong signal), the Network output, $[s/(s+b)]_{NN}$, could be directly interpreted as the signal purity in the corresponding mass window. This is the so called “pure” Neural Network method, applicable for the $D_{K\pi\pi^0}^*$, $D_{K\pi}^*$ and $D_{K\pi\pi\pi}^*$ samples, collected in 2004–2007 where event statistics and purities are large.

The mass dependence of signal and background, $s(m)$ and $b(m)$, which cannot be obtained from ANN, is determined from a fit to the mass spectra in bins of $[s/(s+b)]_{NN}$. In order to to

⁷A mass window ± 30 MeV/ c^2 is used for the sample $D_{K\pi}^0$ and ± 40 MeV/ c^2 around -250 MeV/ c^2 for the sample $D_{K\pi\pi^0}^*$.

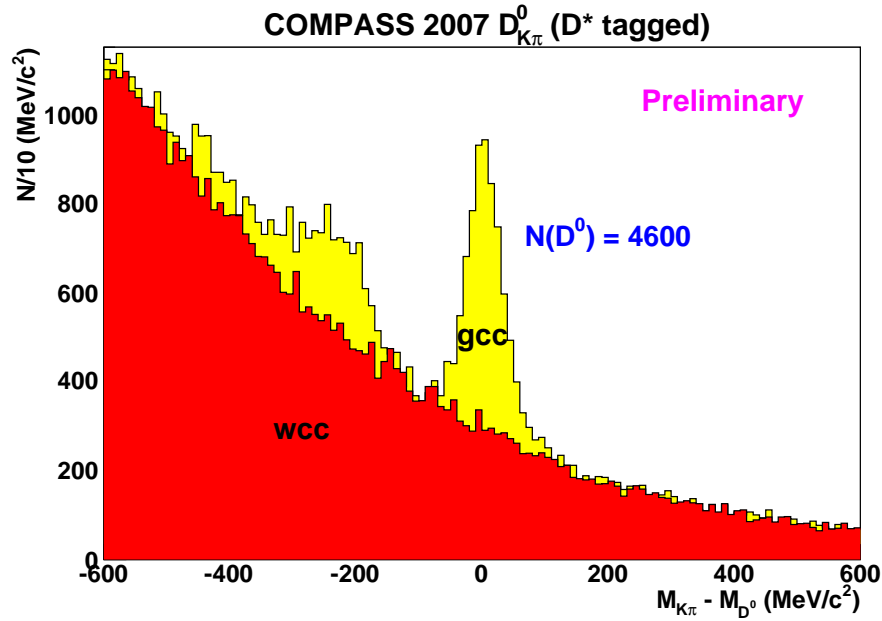


Figure 5.10: The $K\pi$ invariant mass spectrum for the $D_{K\pi}^*$ sample with the good (gcc) and wrong (wcc) combination of pion and kaon charge signs. The data were collected in 2007 with the proton target.

describe the signal a Gaussian distribution is used for all samples while for the background the following fitting functions are employed: two exponential distributions for the $D_{K\pi}^0$ channel and one exponential for the remaining D^* tagged channels. An exception is the $D_{K\pi\pi\pi}^*$ sample for which a second degree polynomial is used to properly fit the combinatorial background. From those fits corrections λ to the signal purity are obtained in the mass windows defined above:

$$\lambda = \frac{1}{\langle [s/(s+b)]_{NN} \rangle} \frac{\int s(m) dm}{\int [s(m) + b(m)] dm}. \quad (5.24)$$

The signal purity, $s/(s+b)$ is:

$$\frac{s}{s+b} = \frac{s(m)}{s(m) + \lambda b(m)}. \quad (5.25)$$

The fit of the invariant mass spectra in bins of the ANN signal purity can also be used to validate the classification obtained by the ANN. For each bin, the signal purity is determined from an integration of the signal and background fits over the used mass windows. Good agreement between the signal purities from ANN and the fit is found for all samples. This

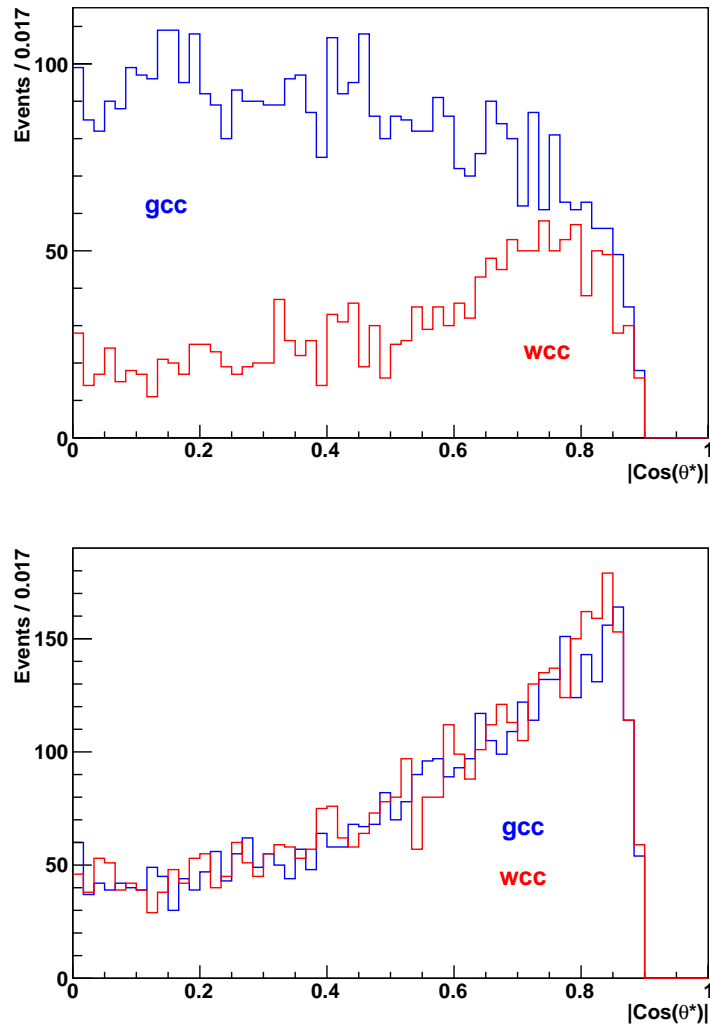


Figure 5.11: Example of the distribution of $|\cos\theta^*|$ in the D^0 meson rest frame for the gcc and wcc events ($D_{K\pi}^*$ sample, 2006 data). Top: region of D^0 signal (events from the mass window around D^0) bottom: outside the D^0 signal.

confirms that the ANN does not introduce bias in the analysis. As an illustration the mass spectra in bins of the ANN signal purity together with a comparison of the two signal purities are shown for the $D_{K\pi}^*$ sample in Fig. 5.12. The signal purity clearly increases with the increasing $[s/(s+b)]_{\text{NN}}$.

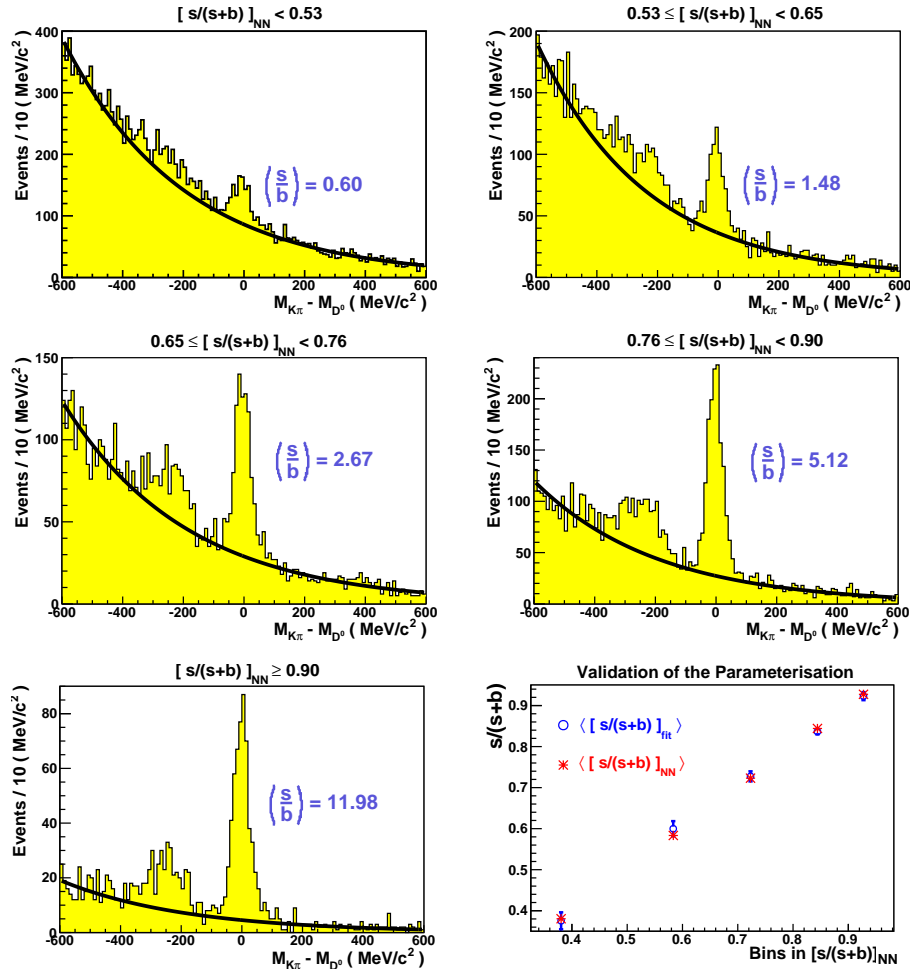


Figure 5.12: The $K\pi$ invariant mass spectra in bins of $[s/(s+b)]_{\text{NN}}$ for the $D_{K\pi}^*$ sample. The signal purity is seen to increase with increasing probability, $[s/(s+b)]_{\text{NN}}$. The last panel shows a comparison of purities determined from the fit and from the Neural Network approach.

The signal purity can be parameterized in various ways provided it correctly reproduces the data. Several possible parameterizations were used to check that indeed yield asymmetries and gluon polarisation consistent within statistical uncertainties. To achieve the statistically most precise and unbiased result on the gluon polarisation a parameterization of a_{LL} was additionally included in the training of ANN to take into account the anticorrelation.

lation between $a_{LL}(X)$ and $[s/(s+b)]_{NN}$.

For the low purity sample of $D_{K\pi}^0$ collected in 2002–2007, and for all samples collected in 2002 and 2003, the extraction of D^0 probabilities from the ANN output is more complicated since the weak signals preclude accounting for anti-correlation. Therefore a ‘hybrid’ method was employed. Similar to the method used in [219, 233], this approach uses fits to the mass spectra which are sampled in bins of two variables: The ANN signal purity and $fP_\mu a_{LL}$. The former sorts the events according to their similar kinematic dependencies, while the latter is used to ensure the anticorrelation between $a_{LL}(X)$ and $[s/(s+b)]_{NN}$. The signal and background distributions belonging to the mass spectra sampled in those bins are fitted by the same functions as defined above to describe the mass dependence of signal and background. Integrating the fits within the same mass windows used for the ANN training procedure yields the signal purities extracted from the fit. For each of the two variables, a function is built using linear interpolation between the fit results. An iterative procedure is used to obtain a stable result on these two functions simultaneously. Finally the correction λ , Eq.(5.24), is applied. Due to the statistical limitations of the analysis, only one parameterisation was built for each decay channel and year.

Since the hybrid method can be used for both, the low purity and the high purity channels it was decided to use it for all channel parameterisations of the signal purities.

5.4 Results

In this section the results of the measurement of gluon polarisation from the open-charm D meson production are presented.

First, in the section 5.4.1, the results from the weighted method of $\langle\Delta G/G\rangle$ extraction at LO accuracy are presented for all five event samples. Also, the average values of the corresponding background asymmetries $\langle A_B^{\gamma^*N}\rangle$ are given. Next, in the section 5.4.2, the virtual photon asymmetries for D^0 production, $A^{\gamma^*N\rightarrow D^0X}$, are presented in bins of D^0 transverse momentum and energy for each D^0 decay channel, together with average values of the kinematic variables. Finally the QCD calculations at NLO accuracy for the signal asymmetry and the gluon polarisation are discussed in section 5.4.3. A value of 1.5 GeV^2 for the mass of the charm quark has been used in the analysis. The uncertainty related to the charm quark mass is taken into account in the systematics. This analysis neglects possible contribution from ‘intrinsic charm’, nonperturbative charm quark or charmed hadron components of the nucleon wave function. Such components, estimated to be $\approx 1\%$, [234, 235], are different from the perturbative splitting of a gluon into a $c\bar{c}$ pair; the latter decrease strongly with Bjorken x , x_{Bjk} . In the EMC measurement of the charm component in the nucleon structure

function $F_2^{c\bar{c}}$ [220], a possible intrinsic charm contribution of about 1% at $x_{Bjk} \sim 0.4$ could not be excluded [220, 221]. Up to now, the estimates of refs [234, 235] cannot be experimentally verified due to the poor statistics of the EMC measurement at large x_{Bjk} , the low values of x_{Bjk} in HERA $F_2^{c\bar{c}}$ measurements [236] and because the COMPASS kinematic acceptance is limited to the region $x_{Bjk} \approx 0.1$ for open charm production. Finally, it should be mentioned that the contribution from resolved photon interactions was estimated using the RAPGAP generator [237] and found to be negligible in the COMPASS kinematic domain.

5.4.1 Leading Order results for the gluon polarisation

Values for $\langle \Delta G/G \rangle$ and the background asymmetry $\langle A_B^{\gamma^*N} \rangle$ are obtained for each of the 48 weeks of data taking and separately for each of the five event samples. The results shown in Table 5.4 are the weighted means of the weekly values. The background asymmetries are consistent with zero.

Table 5.4: Results for $\langle \Delta G/G \rangle$ and $\langle A_B^{\gamma^*N} \rangle$ for each data sample. The uncertainties are statistical.

	$D_{K\pi}^*$	$D_{K\pi\pi^0}^*$	$D_{K\pi\pi\pi}^*$	$D_{K_{\text{sub}}\pi}^*$	$D_{K\pi}^0$
$\langle \Delta G/G \rangle$	-0.192 ± 0.305	-0.414 ± 0.575	0.628 ± 0.833	0.497 ± 0.995	0.020 ± 0.415
$\langle A_B^{\gamma^*N} \rangle$	$+0.019 \pm 0.029$	$+0.051 \pm 0.035$	$+0.002 \pm 0.037$	$+0.004 \pm 0.047$	-0.005 ± 0.004

The final value of the gluon polarisation was obtained as the weighted mean of the five results shown in Table 5.4 and amounts to $\langle \Delta G/G \rangle = -0.08 \pm 0.21$. Assuming that $\Delta G/G(x_G)$ is approximately a linear function of x_G in the range covered by the present data, the above result is the gluon polarisation $\Delta G/G$ at $\langle x_G \rangle$, where $\langle x_G \rangle$ is the weighted average calculated using the signal weights.

The major sources of systematic uncertainty in the $\Delta G/G$ measurement are listed in Table 5.4.1. The contributions from P_μ , P_t and f , which have uncertainties of 5%, 5% and 2%, respectively, are discussed in [68] while the remaining ones are reviewed below. The signal purity $s/(s+b)$ and the partonic asymmetry a_{LL} relate the muon-nucleon asymmetry and $\Delta G/G$. Their uncertainties will not result in false asymmetries, which are additive terms, but in an error which is a fraction of $\Delta G/G$. The uncertainty of $\Delta G/G$ is obtained from the spread of weighting factors w , Eq. (5.12). To this aim the default analysis with weight w_0 is compared to other analyses with different weights, w . The spread of $\langle ww_0 \rangle / \langle w_0^2 \rangle$ was then propagated to a relative systematic uncertainty of $\Delta G/G$.

Source	$\delta(\langle \frac{\Delta G}{G} \rangle)$	Source	$\delta(\langle \frac{\Delta G}{G} \rangle)$
Beam polarisation P_μ	0.015	$s/(s+b)$	0.022
Target polarisation P_t	0.015	a_{LL}	0.025
Dilution factor f	0.006	False asymmetry	0.080
Reduction of number of unknowns	0.025		
Total uncertainty		0.094	

Table 5.5: Contributions to the systematic uncertainty in $\langle \Delta G/G \rangle$.

In order to study the contribution of $s/(s+b)$ to the systematic error, three different effects were considered. The alternative fitting functions were used, different mass windows were considered for the ANN parameterisation and the impact of a different binning in the mass spectra was analysed. The resulting spread of weights was computed for every of these effects for each sample and each year of data taking. The three averages of all spreads was determined. The final error is a fraction of the $\langle \Delta G/G \rangle$ value, obtained from those three averages added in quadrature. A final systematic error of 7% was obtained for $s/(s+b)$. More details can be found in [226].

To estimate the influence of the simulation parameters, Monte Carlo samples with different parameter sets were generated and a_{LL} was recalculated. The parameter set included the mass of the charm quark (varied from 1.3 GeV² to 1.6 GeV²), the parton distribution functions (MRST, GRV and CTEQ groups) and the factorisation scales (defined via charm quark mass). The results are shown in Fig. 5.13. The resulting uncertainty of a_{LL} is 9%.

The uncertainty introduced by the assumption of $\langle A^{\gamma^*N} \rangle_{w_S\beta_B} = \langle A^{\gamma^*N} \rangle_{w_B\beta_S} = A^{\gamma^*N}$ and $\langle A_B^{\gamma^*N} \rangle_{w_S\beta_B} = \langle A_B^{\gamma^*N} \rangle_{w_B\beta_S} = A_B^{\gamma^*N}$ (reduction of 9 to 7 unknowns) is estimated as follows. Values of $\Delta G/G$ are taken from the COMPASS fit [8] with $\Delta G > 0$ at 1σ of the measured x_G . This fit is chosen to maximize the potential bias of the above assumption. The difference between the two values obtained from the fit is added as a bias to the system of equations. The resulting $\Delta G/G$ gives the relative systematic uncertainty for this contribution. Possible variations of $A_B^{\gamma^*N}$ are studied in a similar way through the use of a parameterisation of A_1 .

To study the influence of false asymmetries, the final $D_{K\pi}^*$ sample was subdivided into two samples using criteria related to the experimental apparatus, *e.g.* the slow pion going to the left or to the right side of the incoming muon. The resulting asymmetries were found to be compatible within their statistical accuracy. An upper limit of the contribution of time dependent acceptance effects to the systematic uncertainty was derived from the dispersion of $\langle \Delta G/G \rangle$ and $\langle A_B^{\gamma^*N} \rangle$ in the 48 weeks of data taking. The study was performed using

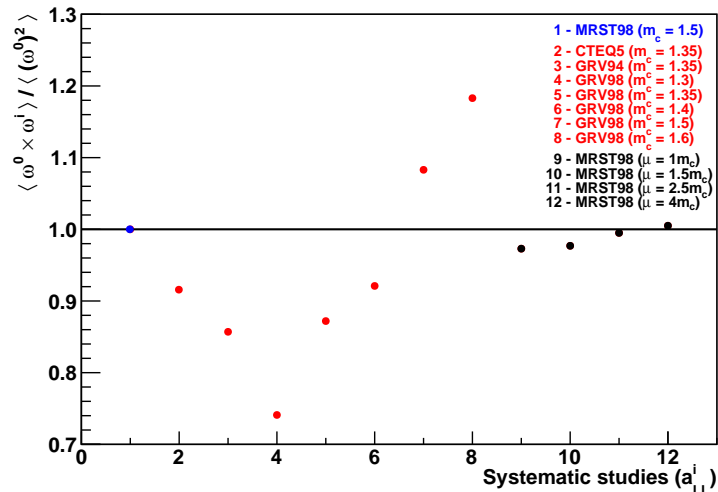


Figure 5.13: The spreads introduced in the signal weights by all the systematic studies considered for a_{LL} . All data is included. The default analysis is given by the first point (blue). An average spread of 9% is obtained. The PDFs sets are taken from HEPDATA [238].

the background asymmetry due to the high statistics. Thereafter the obtained results were translated to $\langle \Delta G/G \rangle$ using the method described in [226]. A systematic error of 0.024 was obtained assuming that possible detector instabilities are similar for background and signal events. To avoid this assumption a second, more conservative approach has been taken: the double ratio of acceptances, $\tilde{\alpha}_C^u \cdot \tilde{\alpha}_C^d / \tilde{\alpha}_C^d \cdot \tilde{\alpha}_C^u$ ($C = S, B$), for the signal is considered to be uncorrelated with the one for the background events. The combination of these two cases leads to an upper limit of 0.081 for the false asymmetries.

The final value of the gluon polarisation amounts to

$$\left\langle \frac{\Delta G}{G} \right\rangle = -0.08 \pm 0.21 \text{ (stat.)} \pm 0.09 \text{ (syst.)} \quad (5.26)$$

in the range of $0.06 < x_G < 0.22$ with $\langle x_G \rangle \approx 0.11$, and a scale $\langle \mu^2 \rangle \approx 13 \text{ (GeV}/c)^2$. As discussed in section 5.3 the fully weighted method allows one to obtain the best statistical precision from the data but the method requires the assumption that $\Delta G/G$ is constant in the measured domain. The more realistic assumption of a linear x_G dependence of the gluon polarisation can be used if the condition $\langle x_G \rangle_{\beta_S w_S} \approx \langle x_G \rangle_{\beta_S w_B}$ is satisfied. The values 0.08 and 0.11 have been estimated for $\langle x_G \rangle_{\beta_S w_B}$ and $\langle x_G \rangle_{\beta_S w_S}$, respectively. The differences in $\langle x_G \rangle$: between $\langle x_G \rangle_{\beta_S w_B}$ and $\langle x_G \rangle_{\beta_S w_S}$, is small compared to the x_G range covered by the measurement and hence it can be concluded that the approximation about the linear

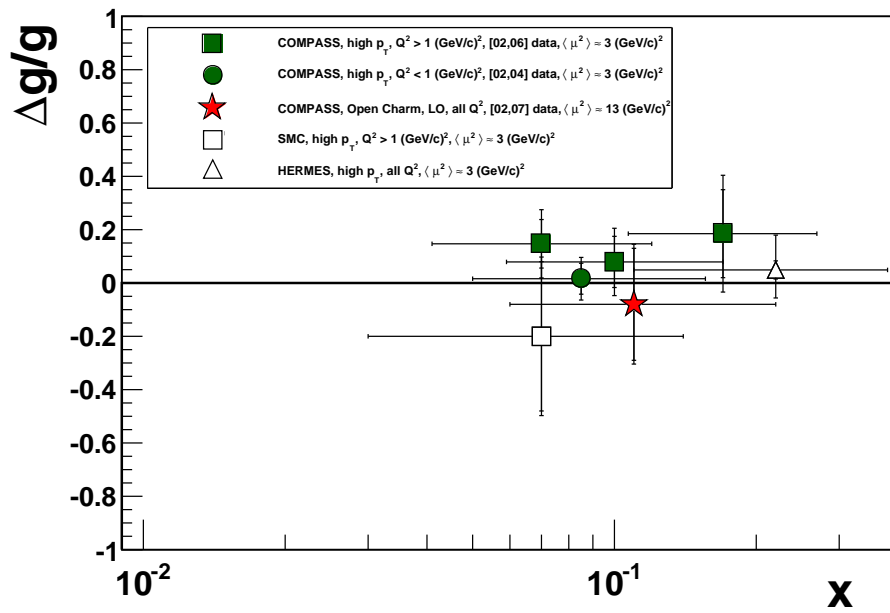


Figure 5.14: Compilation of the $\Delta G/G$ measurements from open charm and high- p_T hadron pair production by COMPASS [218, 239, 240], SMC [215] and HERMES [217] as a function of x_G . The horizontal bars mark the range in x_G for each measurement, the vertical ones give the statistical precision and the total errors (if available). The open charm measurement is at a scale of about 13 GeV 2 and the other measurements at about 3 GeV 2 .

x_G dependence in the gluon polarisation can be justified and the measured averaged gluon polarisation can be interpreted as

$$\left\langle \frac{\Delta G}{G} \right\rangle = \frac{\Delta G}{G}(\langle x_G \rangle), \quad (5.27)$$

with $\langle x_G \rangle \equiv \langle x_G \rangle_{\beta_S w_S}$.

In Fig. 5.14 the above result is displayed together with other results. The obtained result is consistent with these measurements favouring small values of $\Delta G/G$. Note that scales of the measurements differ. The scales are defined as proportional to p_T^2 of the observed hadrons for COMPASS low Q^2 high- p_T hadron pairs analysis, Q^2 is the scale for the high- p_T hadron pairs analysis of the SMC [215] measurement and for COMPASS high- p_T hadron pairs analysis for $Q^2 > 1 \text{ GeV}^2$. The latter is discussed in detail in the next chapter. The scale of the present open-charm result is given by the transverse mass of the charmed quarks $\mu^2 = 4M_T^2 \approx 13 \text{ GeV}^2$. The other experimental points in Fig. 5.14 are given at $\mu^2 \approx 3 \text{ GeV}^2$.

5.4.2 Open-charm asymmetry in kinematic bins

The data analysis described in section 5.2 also allows for the determination of the virtual photon asymmetry for D^0 meson production, $A^{\gamma^*N \rightarrow D^0 X} = A^{\mu N \rightarrow \mu' D^0 X}/D$. It can be used in global NLO QCD fits to constrain the values of ΔG . In contrast to $\Delta G/G$ this asymmetry should not depend on any QCD approximations. Averaging over the full kinematic range would largely dilute the asymmetry due to the large dispersion of a_{LL} , see Fig. 5.8. However calculated at LO accuracy, the dispersion of a_{LL} reflects the possible effect on an asymmetry. Therefore the asymmetry $A^{\gamma^*N \rightarrow D^0 X}$ is extracted in bins of the transverse momentum of the D^0 with respect to the virtual photon, $p_T^{D^0}$, and the energy of the D^0 in the laboratory system, E_{D^0} . The bins were chosen such that the variation of a_{LL}/D within each bin is small compared to the variation over the whole sample and also such that the dependence on the acceptance is minimized.

The asymmetry $A^{\gamma^*N \rightarrow D^0 X}$ is obtained in every kinematic bin in exactly the same way as $\Delta G/G$, with the weighting method, except that the factor a_{LL} is replaced by the factor D in the definition of the signal weight in Eq. (5.12). This provides $A^{\gamma^*N \rightarrow D^0 X}(\langle p_T^{D^0} \rangle, \langle E_{D^0} \rangle)$. As is shown below, the above binning allows to reproduce the LO $\langle \Delta G/G \rangle$ obtained with the method described in section 5.3 with at most 5% loss of precision. The asymmetry obtained in bins are weighted with w_S^2 according to Eqs (5.19). This asymmetry is equivalent to a counting rate asymmetry between upstream and downstream target cells: $(\sum w_S - \sum' w_S)/(\sum w_S^2 + \sum' w_S^2)$, for every bin:

$$\left\langle A^{\gamma^*N \rightarrow D^0X} \right\rangle_{\beta_S w_S} = \left\langle A^{\gamma^*N \rightarrow D^0X} \right\rangle_{w_S^2} \equiv \frac{\sum w_S - \sum' w_S}{\sum w_S^2 + \sum' w_S^2} \quad (5.28)$$

with the weight $w_S = P_\mu f D s / (s + b)$.

The asymmetry $A^{\gamma^*N \rightarrow D^0X}$ was extracted simultaneously with the background asymmetry, $A_B^{\gamma^*N}$ for each bin, channel and year of data taking except for low purity channels where some data taking periods with identical target setups were merged. The final results for every D^0 decay mode are given in Tables 5.6 - 5.8 where $A^{\gamma^*N \rightarrow D^0X}$ in each $(p_T^{D^0}, E_{D^0})$ bin, together with the averages of kinematic variables. All averages are calculated with the weight w_S^2 .

The systematic uncertainties in the measurement of A^{γ^*N} are discussed below. Again the contribution from P_μ , P_t and f , which amounts to 5%, 5% and 2% respectively are taken from [68]. In order to study the contribution from $s/(s + b)$ to the systematic uncertainty, different fitting functions were used for the functional form of the background, different mass windows were investigated for the ANN parameterization and the impact introduced in the analysis by the choice of the binning used in the reconstruction of the D^0 meson spectra were investigated. These tests lead new $s/(s + b)$ and, consequently, new weights were obtained. The resulting spread of weights was computed for each year of data taking, each sample and each bin to estimate the error. The obtained value is 7% of the measured asymmetries. Note that the later corresponds to an average value over all bins.

The contribution of a depolarisation factor D to the uncertainty of $A^{\gamma^*N \rightarrow D^0X}$ was obtained as follows.

A relative experimental uncertainty of 1% was assigned to the momentum measurement of the scattered muon. Then y was re-evaluated for every event and new values of D were computed to obtain new weight. Again the resulting spread of the weights is taken to be the systematic uncertainty of depolarisation factor D . The obtained value is 1.6%. The false asymmetries were estimated as before in the fully weighted method and then translated to $A^{\gamma^*N \rightarrow D^0X}$. The absolute value of this contribution averaged over all bins is 0.022. The maximum value is 0.061.

Finally, the reduction of number of unknowns from 8 to 7, which is the assumption of $\langle A^{\gamma^*N} \rangle_{w_S \beta_B} = \langle A^{\gamma^*N} \rangle_{w_B \beta_S} = A^{\gamma^*N}$ and $\langle A_B^{\gamma^*N} \rangle_{w_S \beta_B} = \langle A_B^{\gamma^*N} \rangle_{w_B \beta_S} = A_B^{\gamma^*N}$ introduces an uncertainty in the measured asymmetries of 0.007. This absolute value corresponds to the weighted average over all bins. The maximum value for this contribution is 0.016. As for the study of false asymmetries, this contribution is determined for $\Delta G/G$ and then translated to A^{γ^*N} in bins of $p_T^{D^0}$ and E_{D^0} .

Bin limits		$A^{\gamma^*N \rightarrow D^0 X}$	$\langle y \rangle$	$\langle Q^2 \rangle$ (GeV) ²	$\langle p_T^{D^0} \rangle$ (GeV)	$\langle E_{D^0} \rangle$ (GeV)	$\langle D \rangle$
$p_T^{D^0}$ (GeV)	E_{D^0} (GeV)						
0–0.3	0–30	$-0.90 \pm 0.63 \pm 0.20$	0.50	0.46	0.19	24.3	0.62
0–0.3	30–50	$-0.19 \pm 0.48 \pm 0.10$	0.60	0.69	0.20	39.1	0.74
0–0.3	> 50	$+0.07 \pm 0.68 \pm 0.11$	0.69	1.17	0.20	59.2	0.84
0.3–0.7	0–30	$-0.18 \pm 0.37 \pm 0.13$	0.51	0.47	0.51	24.6	0.63
0.3–0.7	30–50	$+0.10 \pm 0.26 \pm 0.06$	0.60	0.62	0.51	39.5	0.75
0.3–0.7	> 50	$-0.04 \pm 0.36 \pm 0.07$	0.69	0.73	0.51	59.0	0.83
0.7–1	0–30	$-0.42 \pm 0.44 \pm 0.11$	0.50	0.45	0.85	24.7	0.62
0.7–1	30–50	$-0.36 \pm 0.29 \pm 0.07$	0.61	0.60	0.85	39.2	0.75
0.7–1	> 50	$+1.49 \pm 0.42 \pm 0.22$	0.69	0.76	0.84	58.6	0.83
1–1.5	0–30	$-0.30 \pm 0.35 \pm 0.06$	0.54	0.41	1.23	25.3	0.66
1–1.5	30–50	$+0.13 \pm 0.23 \pm 0.03$	0.64	0.55	1.24	39.2	0.77
1–1.5	> 50	$-0.20 \pm 0.33 \pm 0.04$	0.71	0.73	1.24	58.3	0.85
> 1.5	0–30	$+0.38 \pm 0.49 \pm 0.08$	0.56	0.47	1.84	25.6	0.69
> 1.5	30–50	$0.00 \pm 0.25 \pm 0.03$	0.65	0.70	1.92	39.9	0.79
> 1.5	> 50	$+0.36 \pm 0.33 \pm 0.06$	0.69	0.60	1.95	59.9	0.86

Table 5.6: Combined asymmetries $A^{\gamma^*N \rightarrow D^0 X}$ for the $D_{K\pi}^0$, $D_{K\pi}^*$ and $D_{K_{\text{sub}}\pi}^*$ samples in bins of $(p_T^{D^0}, E_{D^0})$, together with the w_{ξ}^2 - weighted averages of several kinematic variables.

Bin limits		$A^{\gamma^*N \rightarrow D^0 X}$	$\langle y \rangle$	$\langle Q^2 \rangle$ (GeV) ²	$\langle p_T^{D^0} \rangle$ (GeV)	$\langle E_{D^0} \rangle$ (GeV)	$\langle D \rangle$
$p_T^{D^0}$ (GeV)	E_{D^0} (GeV)						
0–0.3	0–30	$-0.63 \pm 1.29 \pm 0.17$	0.52	0.75	0.19	24.4	0.65
0–0.3	30–50	$+0.27 \pm 1.17 \pm 0.15$	0.67	0.65	0.20	38.8	0.81
0–0.3	> 50	$-2.55 \pm 2.00 \pm 0.73$	0.72	1.12	0.19	59.3	0.86
0.3–0.7	0–30	$-0.24 \pm 0.80 \pm 0.10$	0.53	0.51	0.52	24.3	0.65
0.3–0.7	30–50	$+0.49 \pm 0.69 \pm 0.10$	0.65	0.65	0.51	39.0	0.79
0.3–0.7	> 50	$-1.28 \pm 1.03 \pm 0.20$	0.72	0.77	0.51	59.1	0.86
0.7–1	0–30	$+0.55 \pm 0.95 \pm 0.15$	0.53	0.41	0.84	24.6	0.65
0.7–1	30–50	$-0.53 \pm 0.76 \pm 0.11$	0.63	0.53	0.86	39.4	0.77
0.7–1	> 50	$-0.17 \pm 1.00 \pm 0.09$	0.73	0.80	0.85	58.2	0.88
1–1.5	0–30	$+1.35 \pm 0.86 \pm 0.22$	0.54	0.38	1.24	25.4	0.67
1–1.5	30–50	$-0.11 \pm 0.51 \pm 0.06$	0.64	0.59	1.25	39.6	0.78
1–1.5	> 50	$-0.05 \pm 0.78 \pm 0.07$	0.74	0.62	1.25	58.3	0.88
> 1.5	0–30	$-0.19 \pm 1.14 \pm 0.13$	0.56	0.52	1.80	25.7	0.70
> 1.5	30–50	$-0.23 \pm 0.51 \pm 0.07$	0.66	0.66	1.88	40.0	0.80
> 1.5	> 50	$+0.26 \pm 0.90 \pm 0.10$	0.74	0.88	1.92	57.3	0.88

Table 5.7: Asymmetries $A^{\gamma^*N \rightarrow D^0 X}$ for the $D_{K\pi\pi^0}^*$ sample in bins of $(p_T^{D^0}, E_{D^0})$ together with the w_{ξ}^2 - weighted averages of several kinematic variables.

Bin limits		$A^{\gamma^*N \rightarrow D^0 X}$	$\langle y \rangle$	$\langle Q^2 \rangle$ (GeV) ²	$\langle p_T^{D^0} \rangle$ (GeV)	$\langle E_{D^0} \rangle$ (GeV)	$\langle D \rangle$
$p_T^{D^0}$ (GeV)	E_{D^0} (GeV)						
0–0.3	0–30	$+7.03 \pm 4.74 \pm 2.65$	0.46	0.38	0.22	27.7	0.58
0–0.3	30–50	$-2.05 \pm 1.10 \pm 0.66$	0.60	0.72	0.20	40.6	0.74
0–0.3	> 50	$+0.17 \pm 1.83 \pm 0.65$	0.69	0.88	0.20	59.1	0.84
0.3–0.7	0–30	$-0.59 \pm 1.74 \pm 0.63$	0.52	0.31	0.53	27.8	0.71
0.3–0.7	30–50	$+1.00 \pm 0.54 \pm 0.32$	0.61	0.44	0.52	39.7	0.80
0.3–0.7	> 50	$-1.75 \pm 0.84 \pm 0.50$	0.68	0.70	0.51	60.2	0.84
0.7–1	0–30	$+2.91 \pm 2.61 \pm 0.78$	0.45	0.26	0.84	27.7	0.61
0.7–1	30–50	$+1.42 \pm 0.57 \pm 0.36$	0.64	0.57	0.85	40.9	0.81
0.7–1	> 50	$+1.69 \pm 0.81 \pm 0.39$	0.69	0.58	0.86	60.9	0.84
1–1.5	0–30	$-1.89 \pm 2.64 \pm 0.68$	0.46	0.31	1.22	27.7	0.64
1–1.5	30–50	$-0.45 \pm 0.51 \pm 0.14$	0.63	0.58	1.23	41.1	0.79
1–1.5	> 50	$+1.06 \pm 0.66 \pm 0.20$	0.71	0.77	1.24	61.8	0.86
> 1.5	0–30	$+1.64 \pm 3.52 \pm 0.91$	0.46	0.40	1.84	28.1	0.72
> 1.5	30–50	$+0.44 \pm 0.68 \pm 0.15$	0.65	0.75	1.95	42.2	0.78
> 1.5	> 50	$+0.08 \pm 0.63 \pm 0.08$	0.74	0.77	2.03	64.4	0.88

Table 5.8: Asymmetries $A^{\gamma^*N \rightarrow D^0 X}$ for the $D_{K\pi\pi\pi}^*$ sample in bins of $(p_T^{D^0}, E_{D^0})$ together with the w_S^2 - weighted averages of several kinematic variables.

Source	$\delta(\langle \frac{\Delta G}{G} \rangle)$	Source	$\delta(\langle \frac{\Delta G}{G} \rangle)$
Beam polarisation P_μ	0.017	$s/(s+b)$	0.024
Target polarisation P_t	0.017	D	0.005
Dilution factor f	0.007	False asymmetry	0.001
Reduction of number of unknowns	0.025	a_{LL}/D	0.050
Total uncertainty		0.103	

Table 5.9: Contributions to the systematic uncertainty of $\langle \Delta G/G \rangle$ from asymmetries $A^{\gamma^*N \rightarrow D^0 X}$.

Bin limits		Photon-gluon asymmetry								
		D _{Kπ} ⁰ , D _{Kπ} [*] and D _{Ksubπ} [*] samples combined			D _{Kππ⁰} [*] sample			D _{Kπππ} [*] sample		
p _T ^{D⁰} (GeV)	E _{D⁰} (GeV)	LO	NLO		LO	NLO		LO	NLO	
		$\langle \frac{a_{LL}}{D} \rangle$	$\langle \frac{a_{LL}}{D} \rangle$	$\langle A_{\text{corr}} \rangle$	$\langle \frac{a_{LL}}{D} \rangle$	$\langle \frac{a_{LL}}{D} \rangle$	$\langle A_{\text{corr}} \rangle$	$\langle \frac{a_{LL}}{D} \rangle$	$\langle \frac{a_{LL}}{D} \rangle$	$\langle A_{\text{corr}} \rangle$
0–0.3	0–30	0.65	0.00	0.01	0.62	-0.11	0.01	0.37	-0.09	0.01
0–0.3	30–50	0.68	-0.06	0.01	0.65	-0.08	0.01	0.47	-0.08	0.01
0–0.3	> 50	0.76	-0.12	0.02	0.74	-0.11	0.02	0.62	-0.09	0.01
0.3–0.7	0–30	0.46	-0.08	0.01	0.42	-0.17	0.01	0.27	-0.10	0.02
0.3–0.7	30–50	0.50	-0.19	0.02	0.46	-0.23	0.02	0.33	-0.20	0.02
0.3–0.7	> 50	0.56	-0.22	0.02	0.53	-0.18	0.02	0.44	-0.21	0.02
0.7–1	0–30	0.26	-0.26	0.01	0.19	-0.29	0.02	0.15	-0.19	0.02
0.7–1	30–50	0.26	-0.29	0.01	0.21	-0.32	0.02	0.20	-0.31	0.02
0.7–1	> 50	0.29	-0.33	0.03	0.26	-0.36	0.03	0.25	-0.32	0.03
1–1.5	0–30	0.00	-0.35	0.01	-0.06	-0.40	0.02	0.01	-0.36	0.02
1–1.5	30–50	0.01	-0.40	0.02	-0.05	-0.44	0.03	0.03	-0.41	0.02
1–1.5	> 50	0.05	-0.43	0.03	-0.02	-0.42	0.04	0.07	-0.45	0.03
> 1.5	0–30	-0.23	-0.49	0.02	-0.29	-0.52	0.02	-0.19	-0.49	0.03
> 1.5	30–50	-0.26	-0.53	0.03	-0.31	-0.50	0.04	-0.18	-0.54	0.03
> 1.5	> 50	-0.27	-0.53	0.04	-0.31	-0.49	0.05	-0.19	-0.54	0.05

Table 5.10: The photon-gluon asymmetries, a_{LL}/D , in bins of $(p_T^{D^0}, E_{D^0})$ for each D^0 decay mode studied in the analysis. The LO averages use a_{LL}^{LO}/D from data events, obtained from the Neural Network parameterisation; they are weighted with w_S^2 . The NLO averages are obtained from the full Monte Carlo simulation of the pure signal and therefore they are weighted only with the factor D^2 . The NLO asymmetries, a_{LL} and A_{corr} , are discussed in section 5.4.3.

The ratio $\Delta G/G$ is related to the asymmetry by:

$$\left\langle A^{\gamma^*N \rightarrow D^0 X} \right\rangle_{w_S^2} = \left\langle \frac{a_{LL}}{D} \frac{\Delta G}{G} \right\rangle_{w_S^2} = \left\langle \frac{\Delta G}{G} \right\rangle_{\frac{a_{LL}}{D} w_S^2} \left\langle \frac{a_{LL}}{D} \right\rangle_{w_S^2}, \quad (5.29)$$

in every kinematical bin. The results in bins can be combined to give the final result on $\Delta G/G$. As discussed in section 5.3, the weighted method requires that the asymmetry is constant in a given kinematic bin. This is not necessarily the case for the combined result, in particular for combined result on gluon polarisation $\Delta G/G$. Instead, a linear dependence on the gluon polarisation $\Delta G/G(x_G) = a(x_G - \langle x_G \rangle) + \Delta G/G(\langle x_G \rangle)$ can be assumed. Under this

assumption the averaged value of the gluon polarisation, $\langle \Delta G/G \rangle_{\frac{a_{LL}}{D} w_S^2}$ can be interpreted as the gluon polarisation taken at averaged $\langle x_G \rangle$:

$$\left\langle \frac{\Delta G}{G} \right\rangle \equiv \left\langle \frac{\Delta G}{G} \right\rangle_{\frac{a_{LL}}{D} w_S^2} = \frac{\Delta G}{G}(\langle x_G \rangle), \quad (5.30)$$

where $\langle x_G \rangle = \langle x_G \rangle_{\frac{a_{LL}}{D} w_S^2}$.

The gluon polarisation at LO accuracy, obtained from $A^{\gamma^*N \rightarrow D^0X}$ amounts to

$$\left\langle \frac{\Delta G}{G} \right\rangle = -0.11 \pm 0.23 \text{ (stat.)} \pm 0.1 \text{ (syst.)} \quad (5.31)$$

The major sources of systematic uncertainties in the determination of $\Delta G/G$ from $A^{\gamma^*N \rightarrow D^0X}$ are listed in Table 5.9

The muon-nucleon asymmetry $A^{\mu N \rightarrow \mu' D^0X}$ can be obtained from $A^{\gamma^*N \rightarrow D^0X}$ by multiplying it by $\langle D \rangle$ which depends on average values of all the kinematic variables.

The signal asymmetry obtained in kinematic bins contains experimental information that does not rely on the QCD approximation. To obtain the gluon polarisation from this asymmetry the weighted analysing power $\langle \frac{a_{LL}}{D} \rangle_{w_S^2}$ (c.f. Eq. (5.29)) has to be calculated in a specific order of QCD. The calculation of a_{LL} at NLO is discussed in the next section. The weight w_S^2 contains the signal purity, $s/(s+b)$, which is available only for real COMPASS data. The correlation between the calculated and parameterized a_{LL} at NLO is significantly smaller than in LO because the same information (event vector X) is used in ANN to parameterize the more complex NLO kinematics. Therefore the averaged a_{LL} in kinematic bins evaluated on MC events is used instead of parameterization of a_{LL} on real data ($a_{LL}(X)$) in the gluon polarisation determination at NLO accuracy.

5.4.3 NLO QCD corrections for spin-dependent charm muoproduction

The gluon polarisation extraction described in section 5.3 has been performed at LO accuracy where the only process leading to open-charm production is PGF. Extraction of the gluon polarisation requires knowledge of the analysing power a_{LL} and of the signal purity on an event-by-event basis. Only combinatorial background has been considered in the LO analysis as described in section 5.3.

Apart from the NLO corrections to the PGF mechanism, there exists yet another NLO contribution to muoproduction of open-charm, where a gluon originating from light quark processes produces the $c\bar{c}$ pair. Such processes do not probe the gluons inside the nucleon, however they contribute to the D meson signal. Hence the signal asymmetry extracted at

NLO contains a correction term. Examples of NLO processes that produce charm are shown in Fig.5.15.

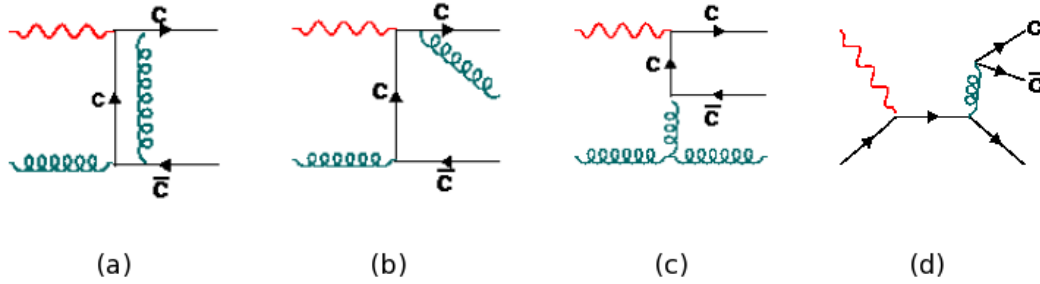


Figure 5.15: NLO contributions to charm production: a) virtual correction b), c) gluon bremsstrahlung d) light quark background process. The complete set of NLO diagrams can be found in [241, 242].

The differential cross section for D meson production in NLO accuracy can be decomposed as:

$$d\sigma = (G \otimes d\hat{\sigma}^{PGF} + \sum_q e_q^2 q \otimes d\hat{\sigma}^q + \sum_q q \otimes d\hat{\sigma}^c) \otimes H. \quad (5.32)$$

Here, gluon and light quark PDFs are denoted G and q , respectively. As in LO case all kinematic variable dependencies are omitted in the notation and \otimes denotes convolution integrals. $d\hat{\sigma}^{PGF}$ is the PGF cross section with NLO corrections as illustrated in Fig.5.15, a) -c). The light quark cross section contains two types of contributions: $d\hat{\sigma}^q$, where the photon couples to light quarks (e.g. diagram d) in Fig. 5.15) and $d\hat{\sigma}^c$, where the photon couples to a heavy (charm) quark, (not shown in Fig. 5.15). After integration over one charm quark from the $c\bar{c}$ pair the interference term between these two contributions vanishes. The fragmentation process from charm quarks to observed D mesons is noted as H . The spin-dependent part of the cross section can be decomposed in a similar way.

COMPASS data have been collected on an isoscalar deuteron target and on a proton target. Taking this into account the cross section from Eq. (5.32) is:

$$d\sigma = (G \otimes d\hat{\sigma}^{PGF} + \beta^d \sum_q q \otimes d\hat{\sigma}^d + \beta^p \sum_q e_q^2 q \otimes d\hat{\sigma}^q) \otimes H, \quad (5.33)$$

where:

$$d\hat{\sigma}^d = d\hat{\sigma}^c + \beta^d \frac{5}{18} d\hat{\sigma}^q \quad (5.34)$$

and the weights $\beta^{p,d}$ are fractions of data collected on proton and deuteron, respectively.⁸

⁸Strictly speaking the weights are defined as a figure of merit, $s^2/(s+b)$.

The signal asymmetry $A^{\mu N \rightarrow \mu' D^0 X}$ in NLO approximation is equal to:

$$A^{\mu N \rightarrow \mu' D^0 X} = \left\langle \frac{\Delta G}{G} \right\rangle_{a_{LL}} \langle a_{LL} \rangle + \langle A_{\text{corr}} \rangle, \quad (5.35)$$

where:

$$A_{\text{corr}} \equiv A_1^d a_{LL}^d + A_1^p a_{LL}^p, \quad a_{LL} = \frac{G d \Delta \hat{\sigma}^{PGF}}{d \hat{\sigma}}, \quad a_{LL}^d = \frac{\sum_q q d \Delta \hat{\sigma}^d}{d \hat{\sigma}}, \quad a_{LL}^p = \frac{\sum_q e_q^2 q d \Delta \hat{\sigma}^q}{d \hat{\sigma}}, \quad (5.36)$$

and

$$d \hat{\sigma} = (G d \hat{\sigma}^{PGF} + \beta^d \sum_q q \hat{\sigma}^d + \beta^p \sum_q e_q^2 q d \hat{\sigma}^q) \quad (5.37)$$

The $A_1^{p,d}$ asymmetries are parameterized directly from the measured data and contain information about light quark polarisation in the proton and the deuteron, respectively. The weights $\beta^{p,d}$ used in the computations were 0.225 and 0.775, respectively. The analysing powers, a_{LL} , for the PGF process as well as for the light quark corrections A_{corr} , depend on the gluon and quark spin independent PDFs, G and q . The light quark corrections, A_{corr} , are very small (c.f. in Tables 5.10) and the dependence on the polarisation averaged PDFs is very weak. Therefore, the main difference between the NLO and LO analysis is a_{LL} , which now contains NLO corrections to the PGF process. The light quark NLO corrections have been included in the COMPASS analysis according to the formula Eq. (5.35) even though these corrections are very small. QCD calculations at NLO accuracy for spin averaged [241] as well as polarisation dependent cross-sections for open charm production [242] are available only in the photoproduction limit⁹. These calculations were used in the analysis to estimate the value of the NLO corrections to a_{LL} and in the light quark contribution. The average value of Q^2 in the kinematic region of the COMPASS measurement is about 0.6 GeV². It was confirmed by a direct check at the LO accuracy that the $Q^2 \rightarrow 0$ limit used in the calculation is a very good approximation in the COMPASS kinematic domain. The NLO calculations for a_{LL} and the light quark background are performed in the photoproduction limit. To obtain event-by-event the a_{LL} in NLO accuracy the same MC generator was used as at LO. The phase space needed for the NLO real gluon emission processes, $\gamma^* g \rightarrow c \bar{c} g$, was simulated through parton showers included in the standard AROMA generator. In Fig.5.16 the comparison of the differential cross sections between COMPASS data and AROMA simulated data with parton showers simulations are shown. As at LO analysis the acceptance

⁹The unpublished, finite part of the NLO partonic cross sections can be obtained directly from authors of [242]. The *Mathematica* code for calculating the polarised and polarisation averaged partonic NLO cross sections is also available on the request from author of this thesis.

effects can be simulated with GEANT package. Good agreement between simulations and data is found.

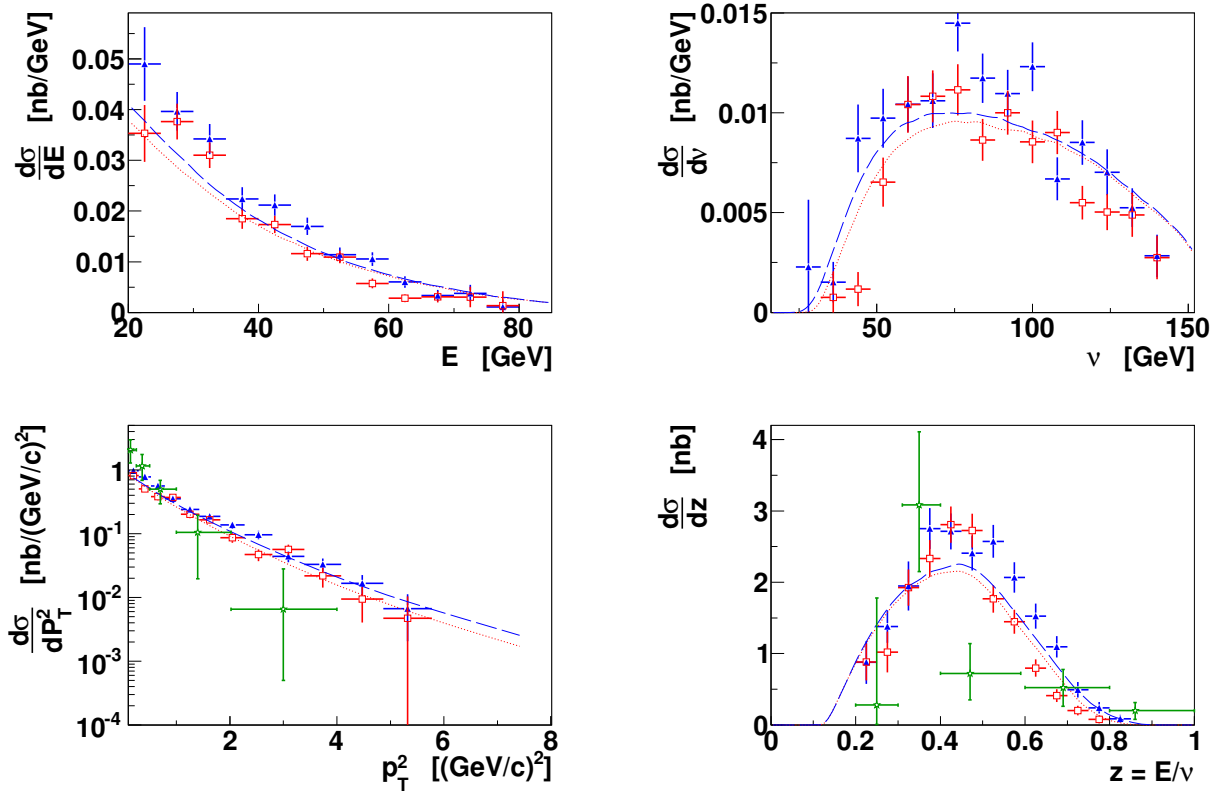


Figure 5.16: Semi-inclusive differential cross sections for D^{*+} (red squares) and D^{*-} (blue triangles) production as a function of D^0 energy, virtual photon energy ν , p_T^2 and energy fraction z . The data are from the year 2004 only and concerns the D^* sample. The green circles are from the EMC experiment [243]. The solid red and dashed blue curves are AROMA predictions (with PS switched on, normalization is not absolute).

Note that only one D meson is observed in the COMPASS data. The second charmed particle is not reconstructed. The NLO calculations from [241] and [242] also represent integrated cross sections for only one charmed quark/meson observed in the final state. The second charm quark as well as emitted gluon (present in a hard gluon emission NLO processes) are integrated out. In any finite bin of p_T and E_D the observed D mesons can be produced by LO process and by NLO processes with different energy emitted due to radiated gluons. These gluons are also not observed and therefore the summation over all configurations is applied. The limits of the integrations over an energy of the non-observed particles are defined by the available phase space.

The MC event contains partonic kinematic information. The observed D meson together with the photon and initial gluon allow one to define the partonic kinematics at LO. The second charmed particle is unambiguously "fixed" at LO due to energy-momentum conservation. For PS events the available energy is shared between unobserved final gluons and unobserved second charm particle. Therefore different configurations lead to the same observed D meson produced from the same initial photon and gluon. For every p_T and E_D bin all corresponding MC events differ only in the energy of the emitted hard gluon and in the energy of second charm particle, both unobserved. Therefore the partonic cross section in the bin can be approximated by the sum of the LO cross section (no emission), virtual and soft part of the NLO cross section and hard part of the NLO cross section, integrated over emitted gluon energy from zero to the maximum gluon energy simulated in MC events within the bin. Note that the distribution of the events inside the bin are not essential because all events in the bin lead to the same observed D meson and the distributions of D mesons nicely agree with the data as shown in Fig.5.16.

The procedure of calculating analysing power a_{LL} at NLO is then the following. For every simulated PS event, the energy of PS defines the upper limit of the integration over the energy of the unobserved gluon in the hard NLO emission process. This integration reduces the differential cross section for a three-body final state ($c\bar{c}g$) (hard NLO part) into a two-body one ($c\bar{c}$) which can be combined with the LO cross-section ($c\bar{c}$, PGF) and the two-body virtual and soft NLO corrections. The latter part is due to the interference between LO and higher order virtual loop corrections amplitudes. The procedure ensures cancellation of infra-red divergencies [242]. In this way the total partonic cross-section at NLO accuracy is calculated on an event-by-event basis for the spin averaged as well as spin dependent case. Consequently the a_{LL} at NLO QCD precision is obtained. The same procedure is applied for the correction originating from light quarks.

The procedure uses MC events as a phase space simulation for theoretical NLO calculations. The part of information (e.g. distributions of the unobserved particles) is not used. The similar situation exists with the azimuthal angle dependence. The LO partonic cross section formulas, Eqs (5.9) and (5.9), used in the LO a_{LL} calculation, are integrated over azimuthal angles while the MC events explicitly depend on them. The obtained results for LO a_{LL} coincide with the ones calculated with the help of the fully azimuthal angle dependent formulas, see [225]¹⁰.

In addition, the MC with PS is an effective model for simulating higher-order QCD effects at the tree-level approximation. The virtual loops are not simulated and the PS are

¹⁰Strictly speaking it is true if the spectrometer acceptance is symmetric in the azimuthal angle; this has been carefully checked at COMPASS analysis.

regularized by the cut-offs MC parameters. Therefore MC with PS is not equivalent to the MC in the NLO QCD approximation. There is still a big discussion how to use LO MC with PS to simulate NLO processes but the subject is difficult and the satisfactory solutions exist only in some cases [245]¹¹.

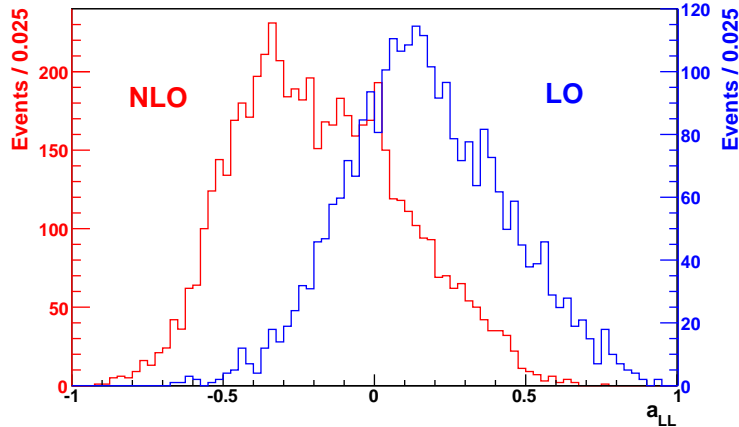


Figure 5.17: Distributions of the analysing power a_{LL} in LO and NLO QCD approximations. Note the different normalisations of the LO and NLO samples.

The analysing power a_{LL} at NLO calculated for every AROMA event may be parameterised by the ANN as was done for the LO extraction of the gluon polarisation. The correlation between generated and parameterized a_{LL} in NLO turned out to be smaller than in the LO case. This is obvious since the partonic kinematics is more complicated in NLO (*e.g.* there are 3 particles in the final state for real gluon emissions) while the input vector used for the Neural Network training is the same as in LO. The expected gain in the precision of the gluon polarisation determination for the weighted method is thus lower at NLO as compared to the LO analysis. The approach of section 5.4.2 is then followed and the asymmetries in bins of p_T and E_D are used. In each $(p_T^{D^0}, E_{D^0})$ bin, the weighted averages of a_{LL}/D : $\langle a_{LL}/D \rangle_{w_S^2}$ and the weighted A_{corr} : $\langle A_{\text{corr}} \rangle_{w_S^2}$ are calculated and the gluon polarisation is evaluated from the asymmetries given in Tables 5.6 – 5.8. The NLO light quark contribution to the D meson asymmetry A_{corr} is very small compared to the measured asymmetries as seen from the results in Table 5.10. The a_{LL} distributions calculated in LO and NLO QCD approximation are presented in Fig. 5.17.

Two-dimensional distributions of a_{LL} and of AROMA events as a function of $p_T^{D^0}$ and

¹¹Recently a full NLO MC tool for heavy flavour photoproduction, based on HERWIG MC generator has been developed [246].

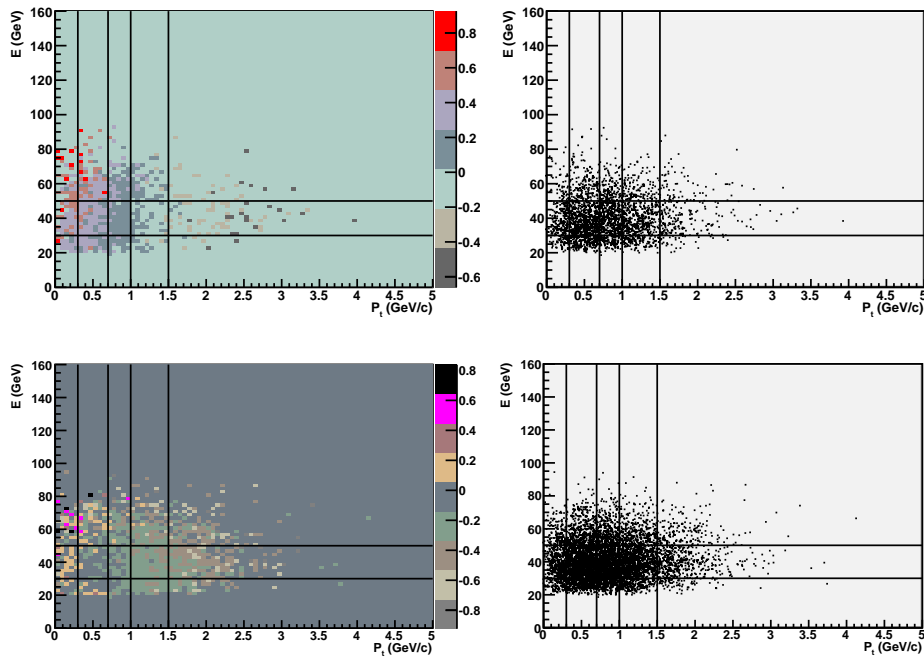


Figure 5.18: Distributions of a_{LL} in bins of $p_T^{D^0}$ and E_{D^0} (left column) and of the corresponding AROMA events (right column) in the LO (upper) and the NLO (lower) analysis. The lines indicate bin boundaries.

E_{D^0} for both LO and NLO are shown in Fig. 5.18. Clearly the $p_T^{D^0}$ distribution is wider at NLO than at LO.

As it was mentioned LO Monte Carlo generator AROMA with parton showers cannot properly describe the full phase space for NLO processes due to the approximations used when simulating the parton showers. In particular a very hard gluon emissions are not generated in parton showers. This is a reason why integration over energy emitted due to gluon radiation is limited to energy present in the PS event instead of maximum energy allowed by phase space. Also, the normalisation of the generated event distributions is based on the LO cross section. In order to estimate the potential effect on a_{LL} related to the approximations used in the parton shower concept, a second "toy" Monte Carlo generator was employed. The events with and without real gluon emissions are generated using uniformly distributed partonic kinematic variables. Afterwards the events are reweighted according to the correct unpolarised NLO cross-section, containing all the corrections: virtual, soft, and hard gluon emissions. Such a procedure ensured proper NLO normalisation. This Monte Carlo uses an independent fragmentation model and the D meson fragmentation function is taken from the world most precise BELLE e^+e^- annihilation measurement [244]. The

gluon polarisation determined from the asymmetries in bins of $p_T^{D^0}$ and E_{D^0} with a_{LL}/D calculated in AROMA with parton showers is well approximated by that using the "toy" Monte Carlo ¹².

The final result on the gluon polarisation is obtained from all bins and is equal to

$$\left\langle \frac{\Delta G}{G} \right\rangle^{\text{NLO}} = -0.20 \pm 0.21 \text{ (stat.)}, \quad (5.38)$$

in the interval $0.18 < x_G < 0.47$ with $\langle x_G \rangle \approx 0.28$ and at a scale $\langle \mu^2 \rangle \approx 13 \text{ GeV}^2$.

The systematic uncertainties are still under investigation. The experimental systematic error is similar to LO analysis. Theoretical uncertainties related to the scale dependence are discussed in [242]. This uncertainty is smaller than in LO analysis. The uncertainties related to the method used in the NLO analysis are not estimated yet. The total errors of the LO as well as NLO results are dominated by large statistical errors. The NLO result on the

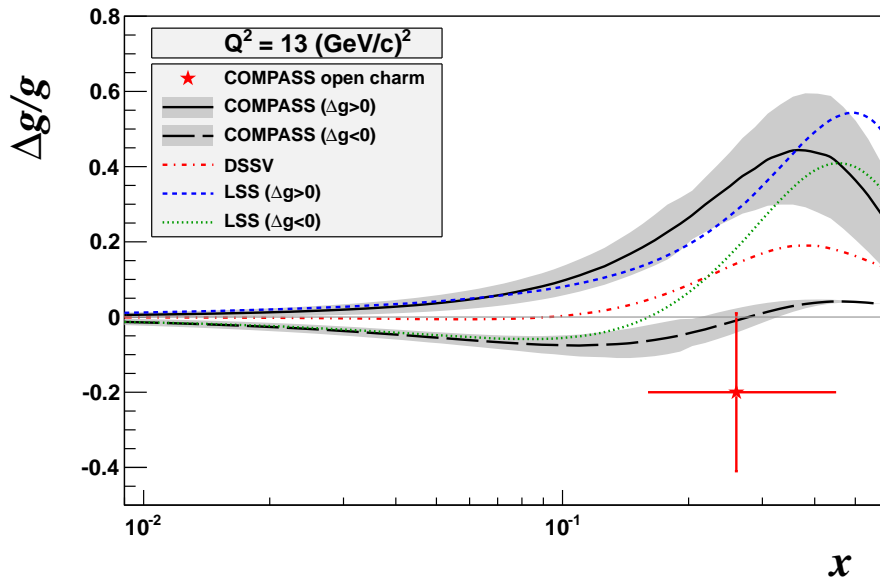


Figure 5.19: The present NLO measurement of the gluon polarisation $\langle \Delta G/G \rangle$ at $\mu^2 = 13 \text{ GeV}^2$, compared to the NLO QCD fits of COMPASS with $\Delta G > 0$ (continuous line) and $\Delta G < 0$ (long-dashed), of LSS [247] (dashed and dotted curves respectively) and of DSSV [47] (dashed-dotted curve), all at the same value of $Q^2 = 13 \text{ GeV}^2$. The measurement error and the error bands are statistical, horizontal bar marks an interval of x_G in which $\langle \Delta G/G \rangle$ is determined.

gluon polarisation is shown in Fig. 5.19. The results of two global fits, DSSV [47] and LSS

¹²Here the comparison was made without simulating the detector acceptance. This simplification is not crucial for the test because the asymmetry bins were chosen to minimize acceptance effect.

[247], which employ both DIS and SIDIS asymmetries are also shown together with the new COMPASS NLO QCD fits of polarised parton distributions. The latter include the result on $\langle \Delta G/G \rangle^{\text{NLO}}$, Eq.(5.38), obtained at a scale $\langle \mu^2 \rangle \approx 13 \text{ GeV}^2$. A more detailed discussion of the effect of open-charm NLO result on QCD NLO fits of PDFs is presented in Appendix 9.3.

The range of x_G is determined by fitting a gaussian distribution in $\text{Log}_{10}(x_G)$ and using it's RMS wide, c.f. [226] for details. The weighted average value of x_G : $\langle x_G \rangle_{\frac{a_{LL}}{B} w_S^2}$, at which the gluon polarisation is probed, depends on the analysing power and consequently, on the QCD approximation used in the analysis. Moreover, due to the real gluon emissions in NLO processes, the energy in the photon-gluon centre-of-mass system required to produce a given D^0 meson is higher than in LO where only the two-body PGF subprocess contributes. These two effects lead to a higher average value of x_G at which the gluon polarisation is determined at NLO, $\langle x_G \rangle \approx 0.28$, in contrast to $\langle x_G \rangle \approx 0.11$ in the LO approximation.

The gluon helicity, ΔG , can be obtained by multiplying the gluon polarisation by the $G(x_G, Q^2)$ value corresponding to the x_G of the $\Delta G/G$ measurement. Using MRST 98 PDF set [248] for the gluon parameterisation (which was used in MC for the estimation of a_{LL}), it was found that $\langle \Delta G \rangle$ are:

$$\langle \Delta G \rangle^{LO} = -0.83 \pm 2.30 \quad x_G = 0.11_{-0.05}^{0.11}, \quad (5.39)$$

$$\langle \Delta G \rangle^{NLO} = -0.20 \pm 0.23 \quad x_G = 0.28_{-0.10}^{0.19}. \quad (5.40)$$

The uncertainties contain the statistical and systematic errors added in quadrature and multiplied by $G(x_G, Q^2)$. An additional error related to the choice of gluon PDF should be also assigned but it is negligible comparing to the values in Eqs (5.39) and (5.40). The results for $\langle x_G \Delta G \rangle$ are shown in Fig. 5.20.

5.5 The D^0 and \bar{D}^0 meson production asymmetry

The general agreement between the shapes of measured distributions and corresponding AROMA MC generator predictions with the parton shower is rather good as shown in Fig. 5.16. However, significant deviations have been observed between AROMA predictions and the measured data with respect to the differences between D^{*+} and D^{*-} production. Fig. 5.21 shows particle-antiparticle asymmetries of the semi-inclusive cross sections:

$$A^{D^0, \bar{D}^0}(X) = \frac{d\sigma^{D^{*+}} - d\sigma^{D^{*-}}}{d\sigma^{D^{*+}} + d\sigma^{D^{*-}}} = \frac{d\sigma^{D^0} - d\sigma^{\bar{D}^0}}{d\sigma^{D^0} + d\sigma^{\bar{D}^0}}, \quad (5.41)$$

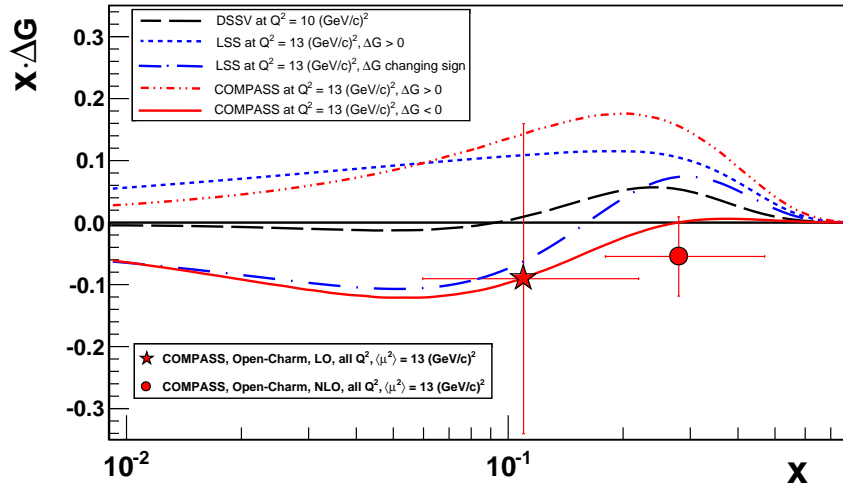


Figure 5.20: Different NLO QCD fits for $x_G \Delta G$ together with the LO and NLO results obtained from the open-charm analysis. For references and description of the fits see Fig.5.19. Figure is taken from [226].

for the D^* tagged sample and for AROMA, as a function of $X = \nu, E_{D^0}, z_{D^0}$ and $p_{T2}^{D^0}$ variables. In the simple LO approach, assuming the PGF with independent fragmentation of charm and anticharm quarks to be the relevant production mechanism, no differences should be observed between D^{*+} and D^{*-} production. However, for processes where the quark content of the target remnant enters differences may occur. Only D^{*-} has a valence quark in common with target nucleon. Furthermore the c quark instead of fragmenting into D^{*+} can hadronize into a charm baryon together with a diquark of the target nucleon, leading to the so-called associated production of, for instance $D^{*-} \Lambda_c$. If the parton shower and LUND fragmentation model is used in AROMA, part of these effects are taken into account in the simulations and therefore the asymmetry in the D^{*+} and D^{*-} production is seen also in the MC, see Fig. 5.21. A significant discrepancy is seen in z_{D^0} dependence for large z but not in the other kinematic dependencies. The data at large z were therefore discarded from the analysis of gluon polarisation. Asymmetries between production of D^0 and \bar{D}^0 or D^{*+} and D^{*-} were already observed in numerous earlier experiments, [249, 250, 251, 252, 253, 254] The reported observations support the existence of the production mechanism others than PGF for large z_{D^0} . More details about the COMPASS results on the production of charm mesons can be found in [222] and [255].

Spin-independent fragmentation has been assumed in the determination of the gluon po-

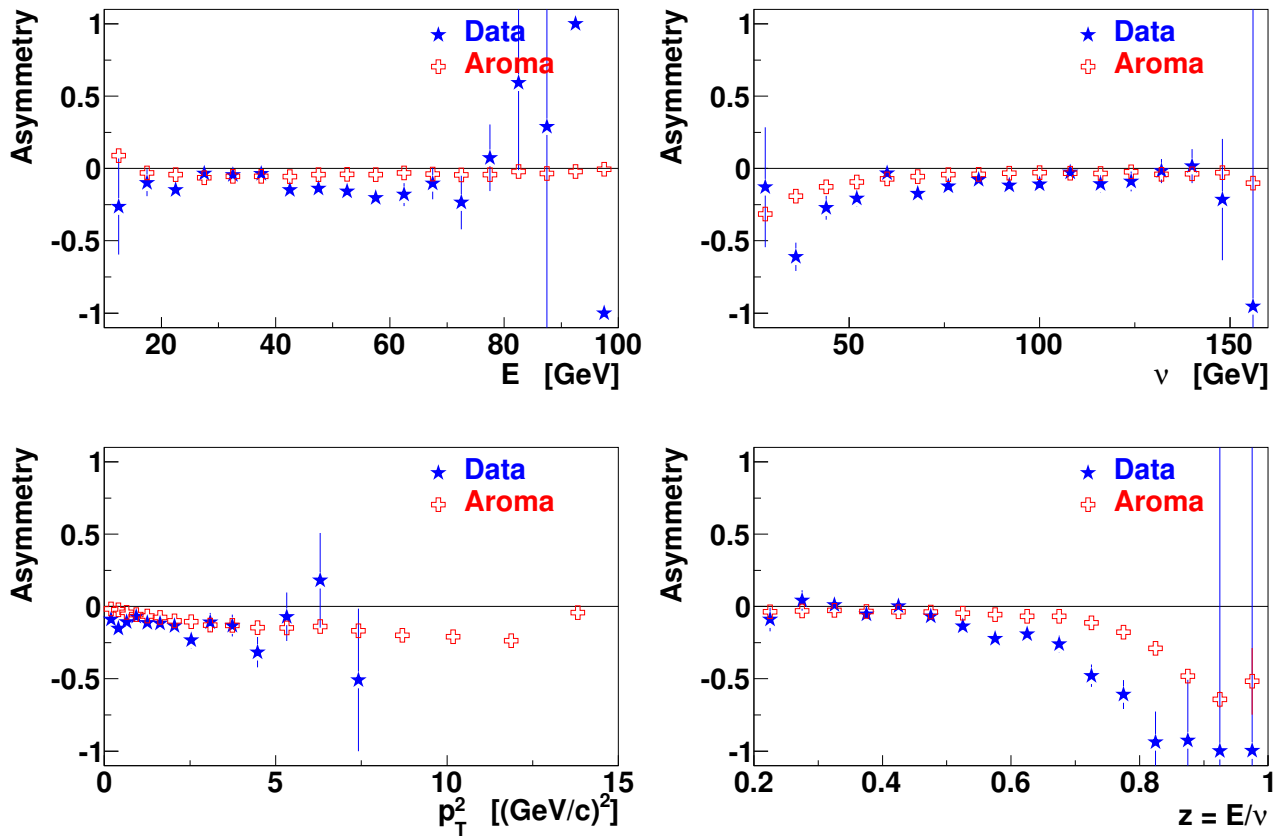


Figure 5.21: The measured asymmetries $A(X)$ for D^* data (blue stars) and AROMA MC (red crosses) events as a function of $X = \nu, E_{D^0}, z_{D^0}$ and $p_T^{D^0}$. The data were obtained in 2002-2006 years. This figure is reproduced from [222].

larisation from the open-charm D meson production data. The non-zero asymmetry A^{D^0, \bar{D}^0} from Eq. (5.41) may imply that the hadronization process can depend on the spin states of the active parton and the target remnants. This hypothesis and its potential consequences for the gluon polarisation determination is discussed below in the framework of a simple model to obtain an upper limit on the possible effect. According to the formulae Eq.9.3 from Appendix 9.1 the potential spin-dependent part of fragmentation function, ΔH , appears in the polarisation averaged as well as in the spin dependent parts of the cross section for D meson production. A simple mechanism which that leads to spin dependence in the fragmentation function could be the following. The fragmenting anti-charm quark from PGF can form a \bar{D}^0 meson together with a u valence quark from the polarised target remnant within the string-type LUND fragmentation model. Information about the initial polarisation state of the nucleon is then transferred to the fragmentation process and in principle the

fragmentation can depend on the polarisation of the u quark. This mechanism is negligible for D^0 mesons which are produced from anti- u quark from the target remnant since the sea quarks are practically unpolarised. Therefore, asymmetry in the fragmentation process can occur between anti- D^0 and D^0 meson production. The dependence of the polarisation in the fragmentation of the \bar{D}^0 meson can affect also the double-spin asymmetry, used in the gluon polarisation determination. Simple calculations lead to the following expressions for the muon-nucleon double-spin signal asymmetry $A^{\mu N \rightarrow \mu' D^0 X}$ and the D^0 and \bar{D}^0 meson production asymmetry A^{D^0, \bar{D}^0} :

$$A^{D^0, \bar{D}^0} = -\frac{1}{2} \frac{\Delta G \otimes d\hat{\sigma} \otimes \Delta H^{\bar{D}^0}}{G \otimes d\hat{\sigma} \otimes H}, \quad (5.42)$$

$$A^{\mu N \rightarrow \mu' D^0 X} = \frac{\Delta G \otimes d\Delta\hat{\sigma} \otimes H + \frac{1}{2} G \otimes d\Delta\hat{\sigma} \otimes \Delta H^{\bar{D}^0}}{G \otimes d\hat{\sigma} \otimes H}, \quad (5.43)$$

where $H = 1/2H^{\bar{D}^0} = 1/2H^{D^0}$ is a fragmentation function and $\Delta H^{\bar{D}^0}$ describes the polarisation dependent part of fragmentation process. $\Delta H^{D^0} = 0$ and the Eqs (5.42) and (5.43) are written in LO approximation. Generalization to NLO is straightforward. The production asymmetry A^{D^0, \bar{D}^0} can be estimated in the same kinematic bins as the double-spin asymmetry used in the gluon polarisation analysis. Solving Eqs (5.43) bin-by-bin allows one to estimate the potential spin-dependent fragmentation effect (on the determination of the gluon polarisation). LO calculations show that it is not possible to explain the whole effect of the asymmetry A^{D^0, \bar{D}^0} only by spin-dependent fragmentation. Assuming, that only part of the effect of the asymmetry A^{D^0, \bar{D}^0} can be related to spin-dependent fragmentation process the solution of the Eqs (5.43) allowed to find the potential effect on gluon polarisation to be very small (up to 5%). This estimate should be an upper limit on the effect. One can then conclude that the observed asymmetry in the production of D^0 and \bar{D}^0 mesons has, at most, small impact on the gluon polarisation measurement from double-spin asymmetries in D meson production. It is also clear that the production asymmetry A^{D^0, \bar{D}^0} is indication of a mechanism different from PGF charm production. Associated production is a probably candidate. Due to the cut on z_D the determination of the gluon polarisation is not affected.

5.6 Summary of the gluon polarisation measurement from open-charm D meson production

Detailed analysis of the open-charm data from the COMPASS experiment, performed at LO and NLO QCD accuracy has been discussed. The gluon polarisation results have been

obtained at a scale $\langle\mu^2\rangle \approx 13 \text{ GeV}^2$. The LO result is: $\langle\frac{\Delta G}{G}\rangle^{\text{LO}} = -0.08 \pm 0.21 \text{ (stat.)} \pm 0.09 \text{ (syst.)}$ for x_G range : 0.06, 0.22. The gluon polarisation result at NLO accuracy has been found: $\langle\frac{\Delta G}{G}\rangle^{\text{NLO}} = -0.20 \pm 0.21 \text{ (stat.)}$ in the x_G range : 0.18, 0.47. The obtained gluon polarisation is small, well below the values needed to restore the Ellis-Jaffe sum rule due to the gluon anomaly term.

Chapter 6

Determination of the gluon polarization from DIS events with high- p_T hadron pairs

In DIS, virtual photo-absorption is the dominant process. It does not provide direct access to the gluon distribution since the virtual photon does not couple directly to the gluon. Measurement of events from higher order photon-gluon fusion (PGF) processes is a way to extract the gluon distribution and the gluon polarisation. The Feynman diagram of the PGF Born process is presented in Fig. 6.1c together with the dominant DIS process (Fig. 6.1a) and Compton gluon radiation (Fig. 6.1b).

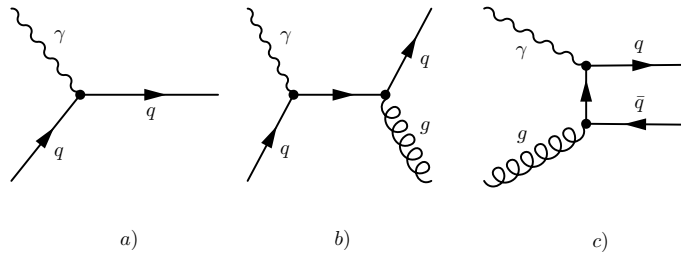


Figure 6.1: DIS diagrams for γ^*N scattering: a) virtual photo-absorption (LP), b) gluon radiation (QCD Compton diagram), c) photon-gluon fusion (PGF).

Both PGF and QCD Compton (QCDC) processes are of first order in the strong coupling constant α_S , so their contributions to the DIS cross section are lower than the Born virtual photon absorption contribution. The cleanest way to tag the PGF process is via the open charm-production, *i.e.* by selecting charmed mesons in the final state. Here the contribution

from the dominant diagram is very small, because the charm quark contents in the nucleon is negligible. Due to the large mass of the charm quark, the contribution from the fragmentation processes is also low. However, for the same reason, charm pair production via PGF is suppressed, so that the statistical precision on the gluon helicity distribution obtained in this way is relatively low. In the previous chapter the determination of the gluon polarisation from open-charm D meson production at COMPASS was discussed in detail. A way to overcome the statistical limitation is to tag the PGF process for light quark pairs production by detecting final state hadrons with large transverse momentum (p_T) with respect to the virtual photon direction. In the dominant process, the hadron p_T is due to the intrinsic k_T of quarks in the nucleon [256] and due to the fragmentation process, resulting in small transverse momenta.

For QCDC and PGF processes hadrons mainly acquire transverse momentum from primary produced partons. The requirement of observing two hadrons with large transverse momentum is expected to enhance the contribution of the PGF process in the selected sample. This method of selecting PGF events has been proposed in [125], revised in [257] and applied in SMC ([215]), HERMES ([216, 217]) and also in COMPASS ([218]) experiments.

As the method requires selection of hadrons with large p_T to enhance the fraction of PGF events, the final sample is reduced. Therefore it is important to optimize the kinematic cuts to find an optimal trade off between the PGF fraction in the data sample and the statistical precision. This is especially important for DIS, where in addition $Q^2 > 1 \text{ GeV}^2$ is required¹. Such an optimization was done in the SMC analysis [215] where for the first time a neural networks approach was used in this type of analysis. In this chapter the determination of the gluon polarisation from DIS events with high- p_T hadron pairs observed in the final state with the COMPASS experiment is presented. A new approach based on a statistical weighting method and the ANN approach are discussed. For the first time the gluon polarisation result is extracted in three bins of x_G . The detailed description of this analysis can be also found in [239, 258]. The analysis is performed in LO QCD approximation where the physical model of the DIS interaction is composed of the three partonic level processes: the dominant DIS process, QCDC and PGF, see Fig. 6.1. The potential contribution from resolved photons is discussed and is estimated to be negligible in the COMPASS kinematic regime. The unwanted contributions from the dominant DIS and QCDC processes are estimated with a MC generator. Good agreement between the data and the MC sample is a crucial point in this analysis. The NLO corrections for high- p_T hadron pair production are only available in the photoproduction limit [259, 260] and cannot be applied in this analysis. Some of the NLO effects are taken into account in the systematics studies via parton showers in the MC.

¹About 90% of the high- p_T events collected in COMPASS are events in the $Q^2 < 1 \text{ GeV}^2$ region.

The chapter is organized as follows. In section 6.1 the decomposition of the asymmetry and the relation to obtain the gluon polarisation from the measured asymmetries is discussed. The data sample and the event selections are discussed in section 6.2. In section 6.3 the weighting method is presented while the Monte-Carlo simulations and ANN training is discussed in section 6.4. The gluon polarisation results are shown in section 6.6, followed by a short summary of the gluon polarisation results in section 6.7.

6.1 Spin cross section asymmetry for high- p_T hadron pairs

The differential cross section for the production of two high- p_T hadrons in the DIS regime, $Q^2 > 1 \text{ GeV}^2$, can be written as:

$$d\sigma = (G \otimes d\hat{\sigma}^{PGF} + \sum_q e_q^2 q \otimes d\hat{\sigma}^{LP} + \sum_q e_q^2 q \otimes d\hat{\sigma}^{QCDDC}) \otimes H. \quad (6.1)$$

A similar decomposition can be made for the spin-dependent part of the cross section. As defined in the previous chapters, G and q denote PDFs for gluons and quarks respectively, and H is a fragmentation function. Here for simplicity all kinematic variable dependencies are omitted in the notation and \otimes denotes a convolution integral.

The helicity asymmetry for the production of two high- p_T hadrons in the DIS regime, $Q^2 > 1 \text{ GeV}^2$, can be expressed as a function of the Bjorken scaling variable x as follows:

$$\begin{aligned} A_{LL}^{2h}(x) &= \left\langle \frac{\Delta G}{G}(x_G) \right\rangle_{a_{LL}^{PGF} R_{PGF}} \langle a_{LL}^{PGF} R_{PGF} \rangle + \langle A_1^{LO}(x) \rangle_{DR_{LP}} \langle DR_{LP} \rangle \\ &+ \langle A_1^{LO}(x_C) \rangle_{a_{LL}^{QCDC} R_{QCDC}} \langle a_{LL}^{QCDC} R_{QCDC} \rangle, \end{aligned} \quad (6.2)$$

where

$$A_1^{LO} \equiv \frac{\sum_i e_i^2 \Delta q_i}{\sum_i e_i^2 q_i}, \quad (6.3)$$

and all other variables are integrated in the experimental kinematic domain. R_{LP} , R_{PGF} and R_{QCDC} are the process fractions, presented in Fig. 6.1. The corresponding partonic cross sections needed for the analysing powers a_{LL}^{PGF} and a_{LL}^{QCDC} (*i.e.*, the partonic cross section asymmetry) have been calculated in [225]. For the PGF process, the partonic cross sections are given in Eqs (5.9) and (5.9), with the quark mass m equal to 0. The partonic cross

sections for the QCDC process are ².

$$d\hat{\sigma} = \frac{8\alpha^2 e_q^2 \alpha_s}{3x(\hat{s} + Q^2)^2} \left[\frac{2(1-y) + y^2 \left(1 - \frac{2m_l^2}{Q^2}\right)}{2Q^2} \left(2 - \frac{2\hat{u}Q^2}{(\hat{s} + Q^2)^2} - \frac{Q^4 + \hat{u}^2}{\hat{s}\hat{t}}\right) - \frac{4(1-y)\hat{u}}{(\hat{s} + Q^2)^2} \right], \quad (6.4)$$

and

$$d\Delta\hat{\sigma} = \frac{8\alpha^2 e_q^2 \alpha_s}{3x(\hat{s} + Q^2)^2} \frac{y(2-y - \frac{2y^2 m_l^2}{Q^2})}{2Q^2} \left[\frac{2(Q^2 - \hat{u})}{\hat{s} + Q^2} - \frac{Q^4 + \hat{u}^2}{\hat{s}\hat{t}} \right] \quad (6.5)$$

The depolarisation factor D , the fraction of the muon beam polarization transferred to the virtual photon, depends mainly on y , as see from Eq.(5.10), and is equal to the analysing power for the dominant DIS process. The quark momentum fractions are equal to Bjorken x for the LP and to x_C for the QCDC process. In the PGF events x_G denotes the gluon momentum fraction. The averaged values are defined in an analogous way to Eq. (5.7), as follows:

$$\langle a_{LL}^{PGF} R_{PGF} \rangle \equiv \frac{a_{LL}^{PGF} G \otimes d\hat{\sigma}^{PGF} \otimes H}{d\sigma}, \quad \left\langle \frac{\Delta G}{G} \right\rangle_{a_{LL}^{PGF} R_{PGF}} \equiv \frac{\Delta G/G a_{LL}^{PGF} G \otimes d\hat{\sigma}^{PGF} \otimes H}{a_{LL}^{PGF} G \otimes d\hat{\sigma}^{PGF} \otimes H}, \quad (6.6)$$

for PGF.

The spin independent cross section $d\sigma$ is given in Eq.(6.1). Similar definitions hold for the LP and for QCD Compton processes.

The asymmetry A_1^{LO} depends on x (x_C) and very weakly on Q^2 . Therefore instead of the weighted averaged values: $\langle A_1^{LO}(x) \rangle_{DR_{LP}}$ and $\langle A_1^{LO}(x_C) \rangle_{a_{LL}^{QCDC} R_{QCDC}}$ a parameterization of A_1^{LO} as a function of x can be used. The asymmetry in Eq.(6.2) then simplifies to:

$$A_{LL}^{2h}(x) = \left\langle \frac{\Delta G}{G}(x_G) \right\rangle_{a_{LL}^{PGF} R_{PGF}} \langle a_{LL}^{PGF} R_{PGF} \rangle + A_1^{LO}(x) \langle DR_{LP} \rangle + A_1^{LO}(x_C) \langle a_{LL}^{QCDC} R_{QCDC} \rangle. \quad (6.7)$$

The evaluation of $\Delta G/G$ from the experimental asymmetry A_{LL}^{2h} using expression (6.7) is possible only when the contribution from background processes (LP, QCDC) can be computed and subtracted. Therefore the analysis requires a precise Monte Carlo description of

²The partonic cross sections presented here are integrated over azimuthal angles of the partons. The unintegrated formulae taken into account the the azimuthal angles dependences were used in the analysis, see [225].

the data, so that the fractions R and the analysing powers a_{LL} can be reliably determined. The LO asymmetry A_1^{LO} can be evaluated from the PDFs (polarised and unpolarised quarks distribution functions extracted e.g. from global fits), or by using directly the measured A_1^d inclusive asymmetries³. In this analysis the measured asymmetry A_1^d has been used which is less dependent on QCD analysis and related assumptions.

Expression (6.7) is valid at LO accuracy. The possible spin dependence of the fragmentation functions (see Appendix 9.1) is neglected. The latter effect was estimated in a MC study performed with LEPTO [261] generator. A string-type mechanism to describe the fragmentation process in LEPTO is used [142]. The probability for a diquark to be in a scalar state based on the SU(6) proton wave function was introduced [144]. This method allows one to set an upper limit on the effect related to the potential spin dependence in the fragmentation process. The effect was found to be negligible in the COMPASS kinematical regime while it can be more significant for HERMES kinematics.

The inclusive asymmetry A_{LL}^{incl} can be decomposed analogously to A_{LL}^{2h} in Eq. (6.7):

$$\begin{aligned}
 A_{LL}^{incl}(x) &= \left\langle \frac{\Delta G}{G}(x_G) \right\rangle_{a_{LL}^{incl,PGF} R_{PGF}^{incl}} \left\langle a_{LL}^{incl,PGF} R_{PGF}^{incl} \right\rangle + A_1^{LO}(x) \langle DR_{LP}^{incl} \rangle \\
 &+ A_1^{LO}(x_C) \left\langle a_{LL}^{incl,QCDC} R_{QCDC}^{incl} \right\rangle.
 \end{aligned} \tag{6.8}$$

Note that y , x , x_G and x_C , and consequently D and a_{LL} , can be different in the inclusive and high- p_T samples. It was, however, checked in MC simulation that the averaged x_G and x_C in the two samples are very similar and they will be thus the same below.

The combination of Eqs (6.7) and (6.8) and neglect small terms (note that the fractions R_{PGF} and R_{QCDC} are much smaller for the inclusive sample than for the high- p_T sample) leads to:

³The COMPASS high- p_T data used in the present analysis were collected with a deuteron target.

$$\begin{aligned}
A_{LL}^{2h}(x) &= \left\langle \frac{\Delta G}{G}(x_G) \right\rangle_{a_{LL}^{PGF} R_{PGF}} \langle a_{LL}^{PGF} R_{PGF} \rangle \\
&- \frac{\langle DR_{LP} \rangle}{\langle DR_{LP}^{incl} \rangle} \left\langle \frac{\Delta G}{G}(x_G) \right\rangle_{a_{LL}^{incl,PGF} R_{PGF}^{incl}} \langle a_{LL}^{incl,PGF} R_{PGF}^{incl} \rangle \\
&- \frac{\langle a_{LL}^{QCDC} R_{QCDC} \rangle}{\langle DR_{LP}^{incl} \rangle} \left\langle \frac{\Delta G}{G}(x'_G) \right\rangle_{a_{LL}^{incl,PGF} R_{PGF}^{incl}} \langle a_{LL}^{incl,PGF} R_{PGF}^{incl} \rangle \\
&+ \frac{\langle DR_{LP} \rangle}{\langle DR_{LP}^{incl} \rangle} \left[A_{LL}^{incl}(x) - A_{LL}^{incl}(x_C) \frac{\langle a_{LL}^{incl,QCDC} R_{QCDC}^{incl} \rangle}{\langle DR_{LP}^{incl} \rangle} \right] \\
&+ \frac{\langle a_{LL}^{QCDC} R_{QCDC} \rangle}{\langle DR_{LP}^{incl} \rangle} \left[A_{LL}^{incl}(x_C) - A_{LL}^{incl}(x'_C) \frac{\langle a_{LL}^{incl,QCDC} R_{QCDC}^{incl} \rangle}{\langle DR_{LP}^{incl} \rangle} \right]. \quad (6.9)
\end{aligned}$$

The averages in Eq.(6.9) are evaluated over all events that have the same x (or are within the same bin in x). In the weighing method the statistical weight is determined for every event-by-event. The corresponding formula for $A_{LL}^{2h}(x)$ written formally for a single event reads:

$$\begin{aligned}
A_{LL}^{2h}(x) &= \frac{\Delta G}{G}(x_G) \left[a_{LL}^{PGF} R_{PGF} - \frac{R_{LP}}{R_{LP}^{incl}} a_{LL}^{incl,PGF} R_{PGF}^{incl} \right] \\
&- \frac{a_{LL}^{QCDC} R_{QCDC}}{DR_{LP}^{incl}} \frac{\Delta G}{G}(x'_G) a_{LL}^{incl,PGF} R_{PGF}^{incl} \\
&+ \frac{DR_{LP}}{R_{LP}^{incl}} \left[A_1(x) - A_1(x_C) \frac{a_{LL}^{incl,QCDC} R_{QCDC}^{incl}}{DR_{LP}^{incl}} \right] \\
&+ \frac{a_{LL}^{QCDC} R_{QCDC}}{R_{LP}^{incl}} \left[A_1(x_C) - A_1(x'_C) \frac{a_{LL}^{incl,QCDC} R_{QCDC}^{incl}}{DR_{LP}^{incl}} \right], \quad (6.10)
\end{aligned}$$

where $A_1 = A_{LL}^{incl}/D$.

Since $\Delta G/G$ appears in Eq. (6.10) at x_G and x'_G , the determination of the gluon polarisation requires the definition of an effective x_G value that is probed in the measurement. This relies on the assumption of a linear dependence of $\Delta G/G$ on x_G :

$$x_G^{av} = \frac{\alpha_1 x_G - \alpha_2 x'_G}{\alpha} \quad (6.11)$$

where:

$$\alpha_1 = a_{LL}^{PGF} R_{PGF} - a_{LL}^{incl,PGF} R_{LP} \frac{R_{PGF}^{incl}}{R_{LP}^{incl}}, \quad (6.12)$$

$$\alpha_2 = a_{LL}^{incl,PGF} R_{QCDC} \frac{R_{PGF}^{incl}}{R_{LP}^{incl}} \frac{a_{LL}^{QCDC}}{D}. \quad (6.13)$$

Although the shape of the gluon polarisation is not known, the assumption of a linear dependence in x_G can be fulfilled for an appropriate choice of the x_G binning.

The final relation between the gluon polarisation and the measured asymmetry A_{LL}^{2h} can be written as follows:

$$\Delta G/G(x_G^{av}) = \frac{A_{LL}^{2h}(x) - A^{corr}}{\alpha_1 - \alpha_2}, \quad (6.14)$$

where

$$\begin{aligned} A^{corr} &= A_1(x) D \frac{R_{LP}}{R_{LP}^{incl}} + A_1(x_C) \frac{1}{R_{LP}^{incl}} (a_{LL}^{QCDC} R_{QCDC} - a_{LL}^{incl,QCDC} R_{QCDC}^{incl} \frac{R_{LP}}{R_{LP}^{incl}}) \\ &- A_1(x'_C) a_{LL}^{incl,QCDC} \frac{R_{QCDC}^{incl}}{R_{LP}^{incl}} \frac{R_{QCDC}}{R_{LP}^{incl}} \frac{a_{LL}^{QCDC}}{D}. \end{aligned} \quad (6.15)$$

6.2 Data sample and event selection

The data were collected during the years: 2002 - 2004 and 2006. Events retained for the further analysis were required to have an interaction vertex located in the target fiducial volume, a beam muon (μ) and a scattered muon (μ'). The DIS region is selected by the usual $Q^2 > 1 \text{ GeV}^2$ and by a selection depending on the energy fraction y carried by the exchanged virtual photon; events with $y < 0.1$ are rejected because their depolarisation factor is rather low, while events with $y > 0.9$ are rejected because they are strongly affected by radiative effects. The above cuts define the inclusive sample. The high- p_T sample requires at least two additional charged hadrons associated with the vertex. The two with the highest p_T are considered to in the analysis. The following selection criteria are applied to hadron candidates: $p_{T_1} > 0.7 \text{ GeV}$ for the leading hadron and $p_{T_2} > 0.4 \text{ GeV}$ for the sub-leading one; the Feynman variable $x_F > 0$ for both hadrons and $z_1 + z_2 < 0.95$, where z is the hadron energy divided by the virtual photon energy, in order to remove events originating from exclusive processes. After all cuts, a sample of about 7.3 million events is used in the present analysis.

6.3 The analysis method

A method similar to the one used in the inclusive asymmetry measurement at COMPASS [262] is used in this analysis ⁴. This method is similar also to the weighting method used in the determination of the gluon polarisation from open-charm D meson production, discussed in the previous chapter. In this approach data from different cells $j = u, d, u', d'$ are combined so that the beam fluxes, the apparatus acceptances and the unpolarised cross sections cancel out. The gluon polarisation can be estimated by solving the following second order equation:

$$\frac{p_u p_{d'}}{p_{u'} p_d} = \frac{(1 + \langle C_u \rangle_w + \langle \beta_u \rangle_w \Delta G/G(x_G^{av}))(1 + \langle C_{d'} \rangle_w + \langle \beta_{d'} \rangle_w \Delta G/G(x_G^{av}))}{(1 + \langle C_{u'} \rangle_w + \langle \beta_{u'} \rangle_w \Delta G/G(x_G^{av}))(1 + \langle C_d \rangle_w + \langle \beta_d \rangle_w \Delta G/G(x_G^{av}))}, \quad (6.16)$$

where p_j is a sum of event weights w in the sample j and $\langle C_j \rangle_w$ and $\langle \beta_j \rangle_w$ are weighted means of $fP_b P_t A^{corr}$ and $fP_b P_t (\alpha_1 - \alpha_2)$, respectively. The weight w in the current analysis is defined as $w = fP_b (\alpha_1 - \alpha_2)$. Eq.(6.16) is obtained from a set of equations similar to Eqs (5.16) and (5.20). In the original SMC ([215]) high- p_T analysis only mean values of the fractions R and analysing powers a_{LL} for the three processes were used. The contribution of the leading process (LP) was suppressed by requiring the presence of two hadrons with very high transverse momenta. This requirement leads to a severe loss of statistics. In the present analysis, a Bayesian driven ANN approach for the extraction of $\Delta G/G$ is used. It allows the use of less restrictive p_T cuts by dealing simultaneously with the three processes. The ANN, trained on a MC sample, assigns to each event a probability of originating from one of the three processes. The weight w , constructed for each individual event, includes these probabilities. Events which most likely are not PGF are kept with a weight which reduces their contribution to the gluon polarisation. For a given event different ANNs provide not only the probabilities of the various processes but also their analysing powers as well as the x_C and x_G variables. As in the open-charm analysis the weighting approach based on the ANN makes optimal use of the statistical power of the data and allows to avoid biases which may result from correlations between the analysing power and the kinematic quantities used to evaluate asymmetries.

⁴The formulae for a first-order and for a second-order as well as for a weighted method applied to the high- p_T analysis in COMPASS are discussed in [239].

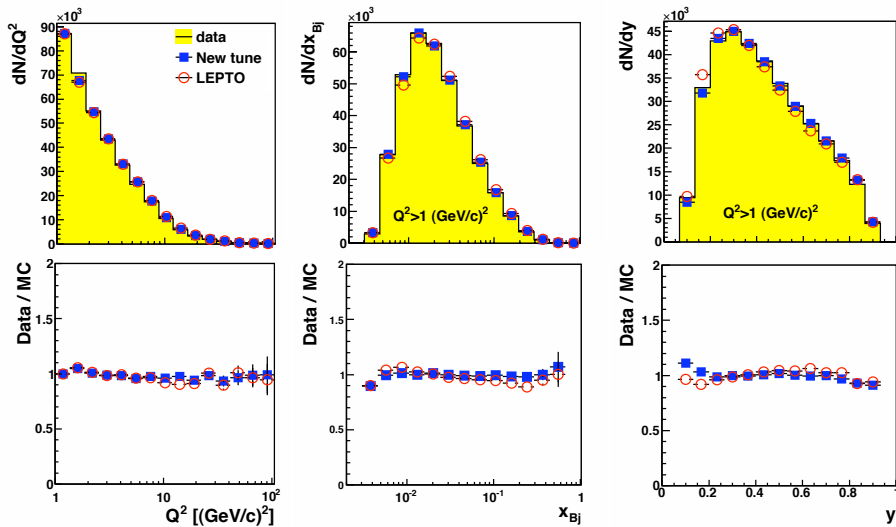


Figure 6.2: Comparison between data (histogram) and MC LEPTO simulations using COMPASS tuning (full squares) and default LEPTO tuning (open circles). The distributions of the inclusive variables Q^2 , x and y are shown in top figures whereas the data/MC ratios are shown in the bottom. Normalized to the number of events.

6.4 Monte-Carlo simulations and ANN training

In the high- p_T analysis the same ANN package is used as in the open-charm analysis [263]. Many results derived from the Neural Network approach strongly depend on the Monte Carlo sample on which the ANN is trained. Hence a precise description of the experimental data by MC is essential for the analysis.

The LEPTO event generator was used to generate both an inclusive DIS sample and a sample which already contains at least a two of high- p_T hadrons. The generated events were processed by the COMPASS detector simulation package COMGEANT and reconstructed in the same way as real events by the COMPASS reconstruction program CORAL. Finally, the same cuts used in the analysis of real data were also applied on the reconstructed MC samples. The MSTW08 PDF parametrization [264] has been used in the analysis as it gives reasonable agreement with F_2 measured in the COMPASS kinematic range and is valid down to $Q^2 = 1 \text{ GeV}^2$. The LEPTO "built in" F_L function (calculated inside the MC generator from the PGF and QCDC contributions) is used to improve data/MC agreement in the high y region. Finally, a correction for radiative effects, as described in [265], was introduced.

For the better description of the hadronic variables, the Parton Shower (PS) option in

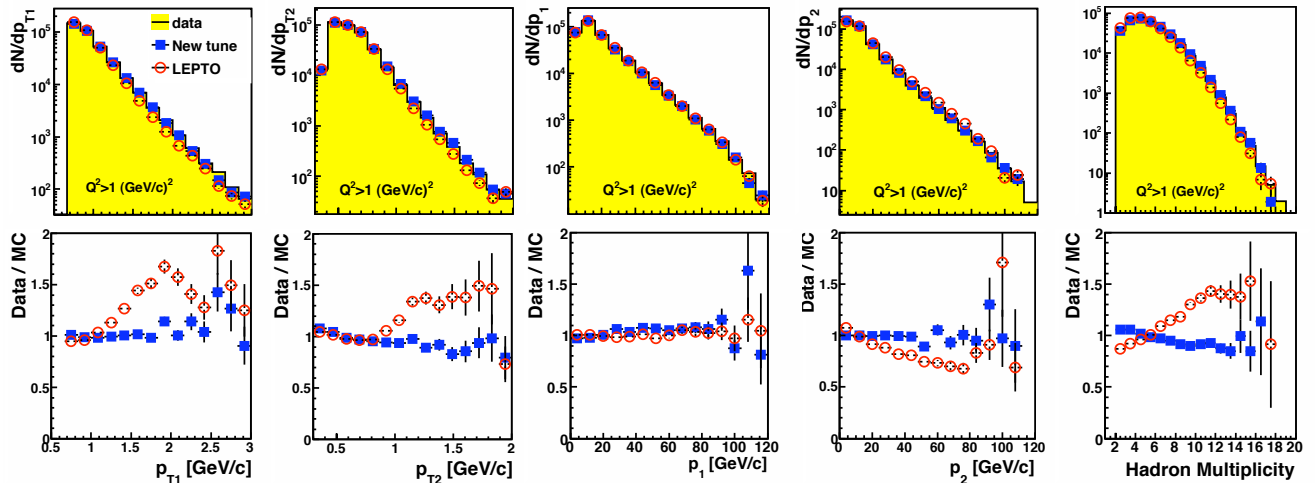


Figure 6.3: Comparison between data (histogram) and MC simulations using COMPASS tuning (full squares) and default LEPTO tuning (open circles), in terms of distributions and Data/MC ratios for the hadronic variables: p_{T1} , p_{T2} , p_1 , p_2 and the hadron multiplicity, normalized to the number of events.

LEPTO has to be enabled. However this procedure introduces some inconsistency, since PS simulates higher order effects while the gluon polarisation $\Delta G/G$ is determined at LO. The impact of this discordance is taken into account in the evaluation of systematic errors. To further improve the agreement with data for the hadronic variables, some parameters describing the fragmentation process in LEPTO have been tuned (Table 6.1). They correspond to the width of the gaussian p_T distribution (PARJ 21), the shape of the non-gaussian tail (PARJ 23-PARJ 24) and the symmetric Lund fragmentation function (PARJ 41-PARJ 42) [261, 142]:

	PARJ 21	PARJ 23	PARJ 24	PARJ 41	PARJ 42
Default	0.36	0.01	2.0	0.3	0.58
COMPASS	0.34	0.04	2.8	0.025	0.075

Table 6.1: LEPTO parameters with default and changed values used to tune the fragmentation function.

The comparison of the high- p_T data sample and MC with COMPASS and default LEPTO tuning is shown in Fig. 6.2 for the inclusive variables Q^2, x and y , and in Fig. 6.3 for the hadronic ones, the leading and sub-leading hadron momenta p_1 , p_2 , the correspond-

ing transverse momenta p_{T_1} , p_{T_2} , and the hadron multiplicity. One observes that, with COMPASS MC tuning, a satisfactory description is obtained for these distributions.

To parametrize processes fractions and analysing powers needed to determine the statistical weight w several ANN were used. The input vectors contain the reconstructed kinematical observables and the ANN are designed to provide a parametrization of a required quantity X . The ANN are trained to give as an output the expectation value of X for the considered values of the input parameters [239, 258]. For the inclusive sample the input parameters are x and Q^2 , while for the high- p_T sample the transverse and longitudinal momenta of the leading and sub-leading hadrons, p_{T_1} , p_{T_2} , p_{L_1} , and p_{L_2} , are used in addition. The trained ANN were then used on the real data to obtain statistical weights for every event.

Fig. 6.4 shows an example of ANN parameterization of three processes fractions R 's in two-dimensional plots as a function of all input variables used in the ANN training. As expected, the LP contribution decreases with increasing transverse momentum of the hadrons, while contribution of QCDC and PGF increase. The PGF fraction is very small at high x and the QCDC dominates at high y . LP is concentrated on the lower values of y . The fractions R 's are classified by two ANN output variables o_1 and o_2 in the following way:

$$R_{LP} = \frac{2}{\sqrt{3}}o_2, \quad R_{QCDC} = o_1 - \frac{1}{\sqrt{3}}o_2, \quad R_{PGF} = 1 - o_1 - \frac{1}{\sqrt{3}}o_2. \quad (6.17)$$

The two-dimensional plots of MC events as a functions of o_1 and o_2 are shown in Fig. 6.5. MC events distributions for three different sets of p_T cuts, $p_{T_1} > 0.7$ GeV and $p_{T_2} > 0.4$ GeV, $p_{T_1} > 0.7$ GeV and $p_{T_2} > 0.7$ GeV and $p_{T_1} > 1.2$ GeV and $p_{T_2} > 0.7$ GeV are shown to illustrate the increase of the PGF and QCDC fractions with these cuts.

An example of the quality of the ANN parametrization is given in Fig. 6.6. It shows the probability of the LP, QCDC and PGF processes as a function of $\sum p_T^2$ for the MC and for the parametrization given by the ANN. Good agreement is observed. While the LP probability reduces with p_T (p_{T_1} , p_{T_2} and $\sum p_T^2$), the QCDC and PGF become the more significant contributions.

The ANN parameterizations of the analysing powers and momenta fractions x_G and x_C have been obtained in a similar way as in the open-charm analysis, (c.f. section 5.3.2). The correlations between MC a_{LL} and the ANN parameterized ones are smaller than in the LO open-charm case because the high- p_T model used in this analysis contains three different processes while LO open-charm production is dominated only by PGF.

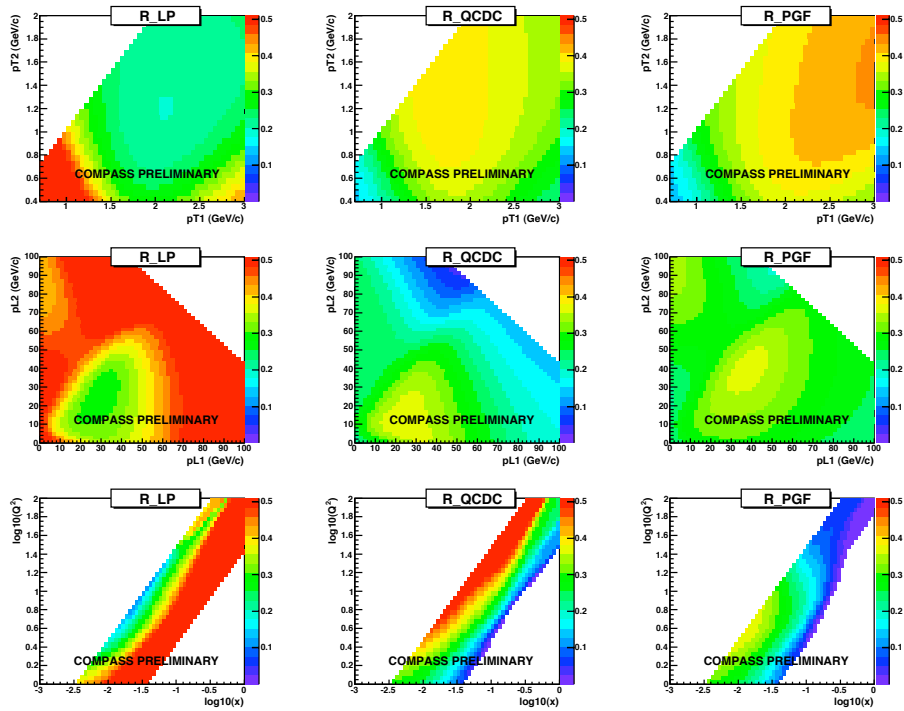


Figure 6.4: ANN parameterization of fractions R of three processes presented as a two-dimensional projections of six input variables: $(p_{T1}, p_{T2}), (p_{L1}, p_{L2}), (x, Q^2)$. Each time four out of these six variable in the ANN input vector are chosen as a weighted mean values of the high- p_T sample: $x = 0.012$, $Q^2 = 2.2 \text{ GeV}^2$, $p_{T1} = 1.4 \text{ GeV}$, $p_{T2} = 0.8 \text{ GeV}$, $p_{L1} = 30 \text{ GeV}$ and finally $p_{L2} = 18 \text{ GeV}$.

6.5 Systematic studies

The main contribution to the systematic error comes from the MC dependence in the analysis. In total, seven MC samples were generated with different combinations of fragmentation tuning. They consisted in default LEPTO or COMPASS tuning, parton shower (PS) on and off options, different choices of the PDFs (MSTW08, CTEQ5L [266]) and with different F_L functions (LEPTO "built in" and from the $R = \sigma_L/\sigma_T$ parametrization of [267]). In addition different s0-called cut-off parameters schemes (*cf.* [261]) for PS on and PS off MC options were used. They do not affect the data/MC comparison but they change the fraction *e.g.* PGF events and are therefore important for systematics studies. So, while keeping the cut-offs default parameters [261], a various cut-off parameters schemes were tested. The RMS value of the obtained $\Delta G/G$ from these MC samples was found to be small, 0.02. However, it turned out that the asymmetry A_{LL}^{2h} is very small, and so the above RMS may

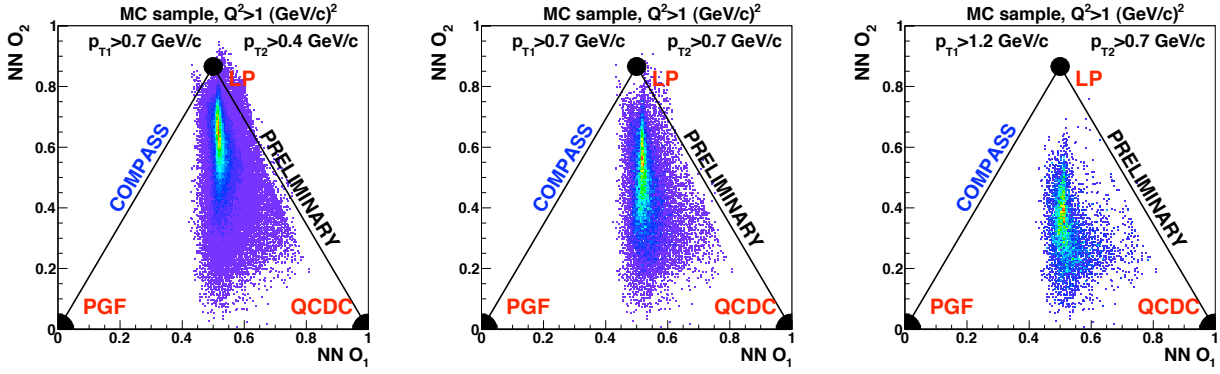


Figure 6.5: The MC events distributions as a function of the output variables: o_1 and o_2 of the ANN parameterization of fractions R' s. Three different sets of p_T cuts are shown: $p_{T_1} > 0.7$ GeV and $p_{T_2} > 0.4$ GeV (left), $p_{T_1} > 0.7$ GeV and $p_{T_2} > 0.7$ GeV (middle), and $p_{T_1} > 1.2$ GeV and $p_{T_2} > 0.7$ GeV (right). The plots illustrate the increase of the PGF and QCDC fractions in the samples with these p_T cuts.

underestimate the systematic uncertainty related to MC. To avoid this, it was considered in addition how the statistical error of $\Delta G/G$ changes for various MC tunings. This leads to an error contribution $\delta(\Delta G/G)_{MC} = 0.045$. The other uncertainty contributions are discussed below.

The uncertainty of $\Delta G/G$ due to choice of A_1^d parameterization and stability of the ANN results were found to be small, $\delta(\Delta G/G)_{A_1^d} = 0.015$ and $\delta(\Delta G/G)_{NN} = 0.010$ respectively. The uncertainties of f , P_b , and P_t have an even smaller impact on the final result: $\delta(\Delta G/G)_{f,P_b,P_t} = 0.004$.

The HERMES results [268] suggest that for heavier nuclei the dilution factor f depends on the transverse momentum of hadrons. In COMPASS, tests were performed to check this dependence. No such dependence is observed for the ${}^6\text{LiD}$ target as compared to He , the medium in which the target material is immersed.⁵

A possible spin dependence of the fragmentation functions is also neglected. Its effect was estimated in a MC study performed with LEPTO in which the probability for a diquark to be in a scalar state was introduced based on $SU(6)$ proton wave function [144] and it was found to be very small in our kinematic regime.

The experimental false asymmetries appear if the acceptance ratio of the neighbouring cells is different for the data taken before and after the field reversal. They were searched for

⁵This effect can be important for COMPASS proton target data. In this analysis only deuteron data, collected on ${}^6\text{LiD}$ target are analysed.

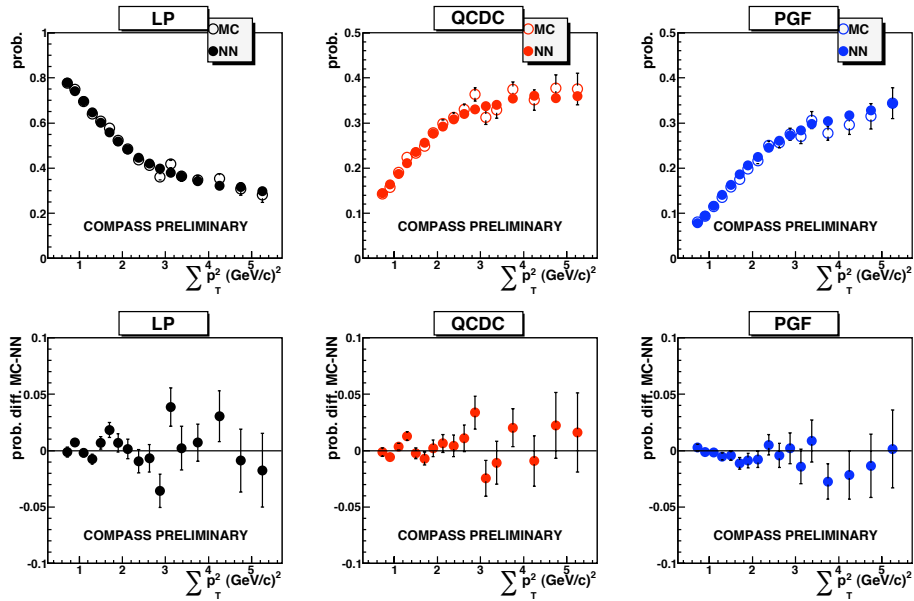


Figure 6.6: ANN parameterization and MC results comparison for fractions R_{PGF} , R_{QCDC} , R_{LP} in bins of $\sum p_T^2$.

in a sample in which cuts on transverse momenta of the hadrons were lowered to $p_{T_{1,2}} > 0.35$ GeV and $Q^2 > 0.7$ GeV². This led to a large increase in statistics and allowed more precise studies of the spectrometer stability. False asymmetries exceeding the statistical error were not found. Taking this error as a limit for the false asymmetries one obtains $\delta(\Delta G/G)_{false} = 0.019$.

The two different values x_C and x'_C appearing in Eq. (6.14) were assumed to be equal. Two tests were performed to check the systematic effect of this assumption. In the first one, $x_C = 1.6x'_C$ was assumed. The value 1.6 was found as an "educated guess" taken from MC. In the second one, the ANN parameterisation of x_C was used with the previously obtained x_C (instead of x) as an input parameter. This leads to $\delta(\Delta G/G)_{form} = 0.035$.

The expression used for the calculation of a_{LL} assumes that the quarks are massless. This assumption can be questioned for the strange quarks. Tests were performed excluding kaons from the data sample, or making a parametrization of the ANN using as an input events only with pions. The final results were found to be unchanged within the expected statistical fluctuations.

The impact of the resolved photon processes on the extracted value of $\Delta G/G$ was also studied. Using the RAPGAP generator [237] it was found that events originating from resolved photons are expected to have very different kinematic distributions with respect to

the event from high- p_T sample. It was checked whether adding an admixture of events from resolved photon processes can improve the MC description of the data. The results show that the contribution from resolved photons in the considered kinematic range is well below 1% and, hence, negligible. The more detailed discussion about resolved photon contribution to this analysis can be found in [239].

	total	bin 1	bin 2	bin 3
$\delta(\Delta G/G)_{MC}$	0.045	0.077	0.067	0.129
$\delta(\Delta G/G)_{A1^d}$	0.015	0.021	0.014	0.017
$\delta(\Delta G/G)_{NN}$	0.010	0.010	0.010	0.010
$\delta(\Delta G/G)_{f,P_b,P_t}$	0.004	0.007	0.007	0.010
$\delta(\Delta G/G)_{false}$	0.019	0.023	0.016	0.012
$\delta(\Delta G/G)_{form}$	0.035	0.026	0.039	0.057
TOTAL	0.063	0.088	0.081	0.143

Table 6.2: Summary of the systematic contributions.

The contributions to the systematic uncertainty and their quadratic sum are presented in Table 6.2. They were also evaluated in three x_G bins defined below (see Table 6.3). The total systematic uncertainty of the $\Delta G/G$ results is estimated to be 0.063, which is slightly larger than the statistical error.

6.6 The gluon polarisation results

$\Delta G/G$ has been extracted with Eq.(6.16) for every conguration separately ⁶ to reduce systematic uncertainties. The results have been corrected for the probability of the deuteron target to be in a D-wave state [121]. The mean values for each year of data taking are shown in the left-hand plot of Fig. 6.7. They are compatible within their statistical errors, with a global average:

$$\Delta G/G = 0.125 \pm 0.060(stat.) \pm 0.063(syst.), \tag{6.18}$$

at $x_G = 0.09$ and hard scale $\mu^2 = 3 \text{ GeV}^2$.

The data cover the range $0.04 < x_G < 0.27$ and have been divided into three statistically independent subsamples by cuts on the x_G variable parameterised by the ANN. . The correlation between the generated and the parameterised x_G is about 62% As a consequence, the division leads to three x_G bins which have different mean values but a large overlap. The

⁶One conguration usually corresponds to 16h (2 days) of data taking in 2002 - 2004 (2006).

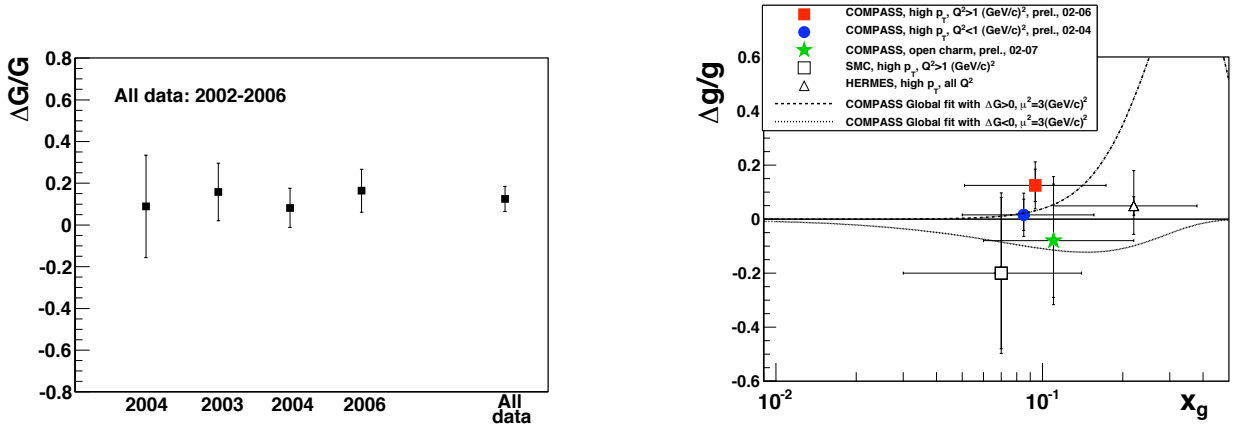


Figure 6.7: Left: $\Delta G/G$ for each year of data taking and the final average value. Right: comparison of the final $\Delta G/G$ as a function of x_G with the previous results. The QCD fit curves are from [8].

results, listed in Table 6.3, provide no evidence for any significant dependence of $\Delta G/G$ on x_G . These results are compared with previous LO evaluations of $\Delta G/G$ based on high- p_T hadronic events in Fig. 5.14. In the right-hand plot of Fig. 6.7 the global average $\Delta G/G$ result is shown together with previous LO results.

	total	bin 1	bin 2	bin 3
x_G mean	$\langle x_G \rangle = 0.09$	$\langle x_G \rangle = 0.07$	$\langle x_G \rangle = 0.10$	$\langle x_G \rangle = 0.17$
x_G range	$0.04 < x_G < 0.27$	$0.04 < x_G < 0.12$	$0.06 < x_G < 0.17$	$0.11 < x_G < 0.27$
$\Delta G/G$	0.125 ± 0.060	0.147 ± 0.091	0.079 ± 0.096	0.185 ± 0.165

Table 6.3: Summary of the $\Delta G/G$ results.

The $\Delta G/G$ results obtained in the quasi-real photoproduction regime ($Q^2 < 1 \text{ GeV}^2$) at COMPASS are also shown in Figs 5.14 and 6.7. The hard scale in this analysis is defined by $\sum p_T^2$ of the hadron transverse momenta instead of Q^2 . Therefore, in addition to the cuts on p_T of the leading and sub-leading hadrons, $\sum p_T^2 > 2.5 \text{ GeV}^2$ is required. The physical model used in the low- Q^2 high- p_T COMPASS analysis is based on PYTHIA MC generator [223], which include the resolved photon contribution as well as LP, PGF and QCDC. The resolved photon processes contribute significantly (50% according to PYTHIA MC) to the high- p_T hadron pairs production in photoproduction regime while they are negligible in the large Q^2 DIS domain. These contributions introduce an important uncertainty related to the so-called hadronic component of the photon structure. The polarised photon structure has not

been measured to data. On the other hand the DIS events used in the analysis presented here became only a small fraction of the collected events; about 90% of the COMPASS high- p_T hadron pair events originate from the photoproduction domain. More details of the determination of the gluon polarisation in the quasi-real photoproduction regime at COMPASS can be found in [218] and in [269, 270]. The hard scale and the range of gluon momentum are almost the same as in both COMPASS measurements and the two values of $\Delta G/G$ are compatible within their statistical error. The $\Delta G/G$ value obtained in the COMPASS open charm analysis at LO (see chapter 5) is also in a good agreement with the presented results. The SMC results from high- p_T , $Q^2 > 1 \text{ GeV}^2$ [215] and the HERMES results from high- p_T , all Q^2 analyses [217] are also compatible with the present ones.

In conclusion, a direct measurement of the gluon polarisation extracted in the LO approximation has been performed on all COMPASS data taken with longitudinal polarised ^6LiD target. $\Delta G/G$ is extracted from a large sample of DIS events with $Q^2 > 1 \text{ GeV}^2$, including a high- p_T hadron pair, by a method based on the Neural Networks. This approach increased the statistical precision of the result by almost a factor two with respect to the standard method in which a set of cuts is applied to $p_{T_{1,2}}$ to optimize $\delta(\Delta G/G)$. For the first time the gluon polarisation was evaluated in three intervals of the fractional gluon momentum.

6.7 Summary of the gluon polarisation measurement

The direct measurements of the gluon polarisation performed by SMC, COMPASS and HERMES Collaborations indicate that gluons are not polarised in the x_G range covered by the measurements. The collider experiments STAR [11] and PHENIX [12] at RHIC measured the gluon polarisation by observing helicity asymmetries for hadrons and jets in polarised proton-proton collisions. These measurements of the double spin longitudinal asymmetries have been used in a global QCD fits and the results also indicate that gluons are weakly polarised [46]. There is, however, also true that the precision of the gluon polarisation measurements is still not satisfactory. Therefore the better measurements with higher precision are needed.

The interesting question is if gluons are polarised in a very small x_G domain. To measure the gluon polarisation in this region one needs to wait for a new lepton-proton/ion collider, see e.g. [42] and [205]. From the other hand the gluon polarisation can be "washed out" by the gluon-gluon interactions dominated at small x_G . Therefore there are no strong arguments for highly polarised gluons concentrated at small x_G in the nucleon. The weak sea quarks polarisation observed in many experiments also can suggest that gluons are not strongly polarised. The gluons for large x_G region are also not precisely measured but they are

strongly suppressed.

If gluons are not polarised or in opposite, if they are strongly polarised, the OAM of partons should play an important role in the structure of the nucleon. This interesting subject is shortly discussed in the next chapter.

Chapter 7

The spin structure of the nucleon; GPDs and orbital motion

During four decades of DIS experiments of high energy leptons off nucleons, the knowledge of the nucleon structure has made impressive progress. The collinear (longitudinal) structure of the nucleon is encoded in PDFs. The successful prediction of the scale dependence of the PDFs is one of the great successes of QCD. The complementary aspect of the nucleon structure is the description of partons in the transverse plane in momentum space. On the quantum field theoretical ground TMDs are adequate to describe the transverse structure of the nucleon. The TMDs are discussed in detail in chapter 3. The TMDs depend on the intrinsic motion of partons inside the nucleon and allow reconstruction of the three-dimensional nucleon structure in momentum space. Most TMDs would vanish in the absence of parton OAM and therefore the TMDs offer the opportunity to learn about the OAM of quarks and gluons inside a nucleon. In addition most TMDs and related observables, azimuthal asymmetries, are due to couplings of the transverse momentum of quarks with the nucleon (or the quark) spin. This "spin-orbit" correlations, similar to those in the hydrogen atom, can therefore be studied. The relation between OAM and TMDs is, however, rather qualitative and model dependent.

To complete the three-dimensional imaging of the nucleon the information from TMDs is combined with the information on the parton spatial distribution from GPDs. The Fourier transform of the GPDs can be expressed in terms of Impact Parameter Distributions (IPDs). These IPDs provide a probabilistic interpretation of GPDs. Hard exclusive reactions such as deeply virtual Compton scattering (DVCS) and exclusive production of mesons can give an access to GPDs.

GPDs generalize the form factors, distribution amplitudes and standard PDFs and quan-

tify various correlations/distributions of quarks and gluons in terms of their momentum fractions and positions in the transverse plane (IPDs).

The GPDs as seen in DVCS depend on the photon virtuality Q^2 , the total four-momentum square t transferred between initial and final nucleon states and on x and ξ . The latter two variables represent respectively the average and half the difference between the initial and final longitudinal momentum fractions of the nucleon, carried by the parton throughout the process. Note that here x is not equal to Bjorken x_{Bj} in DIS and can be negative. Negative momentum fractions are identified with antiquarks. Note also that GPDs appear in the DVCS amplitude instead of the DIS cross section¹. Only Q^2 , t and $\xi = x_{Bj}/(2 - x_{Bj})$ (Bjorken limit) are accessible experimentally; x is a variable which is integrated over (due to the loop in the "handbag" diagram describing GPDs at LO accuracy).

To take into account the spin properties of hadrons and quarks, one needs four GPDs: H , \tilde{H} , E and \tilde{E} . The GPDs H^i and \tilde{H}^i ($i = u, d, s, G$), which describe nucleon-helicity conserved scattering processes, include as limiting cases ($t = 0, \xi = 0$) the standard polarised and unpolarised PDFs. The case of nucleon-helicity flip is described by the GPDs E^i and \tilde{E}^i for which there are no such limiting cases. GPDs with $\xi \neq 0$ describe the correlations. Taking only the point $t = 0$ (forward limit) corresponds to integration over impact parameters (IPDs, see section 7.1) and information about the transverse structure is lost.

The first moment (in x) of GPDs give the electromagnetic form factors. Form factors contain information about the distribution of partons in the transverse plane. As the form factor is a first moment of GPDs, they involve integration over the momentum fraction x . Information about longitudinal structure is thus lost.

The E functions are inaccessible in DIS as the DIS is described by forward limit. However the limit: $t = 0$ and $\xi = 0$ of E exists:

$$E^i(Q^2, x, 0, 0) = \kappa^i(x) \quad (7.1)$$

and its integral leads to the anomalous magnetic moment of the nucleon:

$$\sum_q e_q \int_0^1 (\kappa^q(x) - \kappa^{\bar{q}}(x)) dx = \kappa_N \quad (7.2)$$

The GPDs are related to TAM as defined in Ji's sum rule [31]:

$$J^q(Q^2) = \frac{1}{2} \sum_{i=q, \bar{q}} \int_{-1}^1 x (H^i(Q^2, x, \xi, 0) + E^i(Q^2, x, \xi, 0)) dx \quad (7.3)$$

$$J^G(Q^2) = \frac{1}{2} \int_{-1}^1 x (H^G(Q^2, x, \xi, 0) + E^G(Q^2, x, \xi, 0)) dx \quad (7.4)$$

¹They can be also defined in terms of so-called nonforward parton distributions, see [205].

and

$$\frac{1}{2} = J^q(Q^2) + J^G(Q^2) \quad (7.5)$$

The variable ξ can be arbitrary in Eqs: (7.4) and (7.4) but fixed. Fixing $\xi = 0$ the Ji's sum rule can be written as follows:

$$J^q(Q^2) = \frac{1}{2} \sum_q \int_0^1 x(q(x, Q^2) + \bar{q}(x, Q^2) + \kappa^q(x, Q^2) + \kappa^{\bar{q}}(x, Q^2))dx \quad (7.6)$$

$$J^G(Q^2) = \frac{1}{2} \int_0^1 x(G(x, Q^2) + \kappa^G(x, Q^2))dx \quad (7.7)$$

The momentum integral add up to 1 while the angular momenta to 1/2, Eq. (7.5) and the following interesting sum rule for GPD E is obtained:

$$\sum_q \int_0^1 x(\kappa^q(x, Q^2) + \kappa^{\bar{q}}(x, Q^2) + \kappa^G(x, Q^2))dx = 0 \quad (7.8)$$

Note, that only valence quarks contribute to κ_N , while J^q involves also sea quarks.

All these relations seem to be a good way to constrain the contributions from the total quark angular momenta to the nucleons spin budget.

In general, the GPDs contain much richer structural information on the nucleon than conventional form factors and structure functions. There are two possible approaches to model GPDs: calculations in specific dynamical models like the bag model or the chiral soliton model, or relations of the GPDs and the PDFs and form factors. In the latter case the key point is the interplay between the x, ξ and t dependencies of the GPDs. An example is given in Fig. 7.1, where one particular model [271, 272] for GPD H is shown as a function of x and ξ at $t = 0$. One can easily identify the standard quark density PDF at $\xi = 0$ including its typical rise around $x = 0$ corresponding to the diverging sea contribution. The negative x part is related to antiquarks.

The QCD evolution equations for GPDs are similar to those for the PDF and in principle allow one to fit the data using parameterizations of GPDs and to extract the less model dependent information on them. At the moment, our knowledge about GPDs is mostly limited to the valence quark GPDs (HERMES, COMPASS, Jefferson Lab 6 GeV and also Jefferson Lab 12 GeV in the near future) and rather low precision data from HERA, see [32]-[41]. A high-energy high-luminosity Electron-Ion Collider (EIC) will be a good machine for studies of hard exclusive reactions and sea quark and gluon GPDs. [42, 205]. Ref. [205] contains a recent review of the present knowledge of GPDs and future prospects for their measurement.

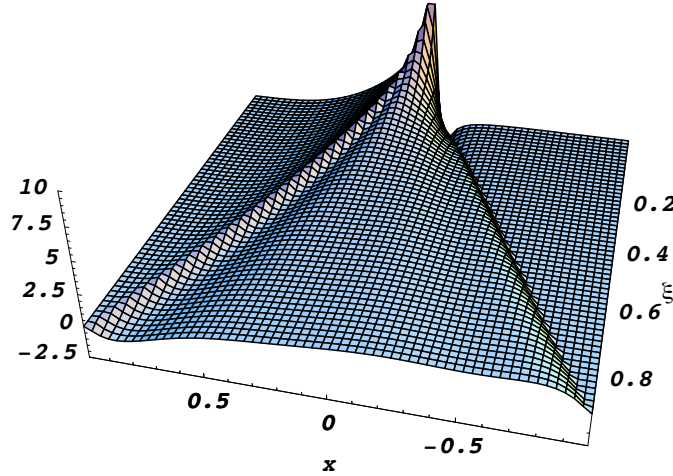


Figure 7.1: An example of the GPD H model [271, 272] as a function of x and ξ for $t = 0$. For $\xi = 0$ the typical shape of the standard quark PDF distribution is seen. The negative x part is interpreted as the antiquark contribution. The figure is taken from [271].

In next sections of this chapter selected topics related to orbital motion are discussed. In section 7.1 relations between TMDs and IPDs (Fourier transforms of GPDs) are discussed. The qualitative description of Sivers effect can be made in terms of distorted IPDs and so-called Chromodynamic lensing. Remarks related to the controversy on the definition of OAM/TAM are given in section 7.2. Results for OAM obtained from Lattice QCD calculations and on selected nonperturbative models are discussed in section 7.3.

7.1 Transverse distortion, QCD lensing and the Sivers effect

A particularly simple physical interpretation for the GPDs as probability densities exists in the limiting case $\xi = 0$ where the parton carries the same longitudinal momentum fraction x in initial and final state and hence the momentum transfer is purely transverse, $t = -\vec{\Delta}_\perp^2$. The Fourier transform of the GPDs with respect to $\vec{\Delta}_\perp$ defines the impact parameter representation, IPD. The IPDs provide a probabilistic interpretation of the GPDs. The impact parameter \vec{b}_\perp (the distance between the active quark and the center of longitudinal momentum $\vec{R}_\perp = \sum_i x_i \vec{r}_{i\perp}$) defines the position of the quark in the transverse plane. The

unpolarised IPD is defined as a Fourier transform of GPD H :

$$\mathcal{H}(x, \vec{b}_\perp) = \int \frac{d^2\Delta_\perp}{2\pi} e^{i\vec{\Delta}_\perp \cdot \vec{b}_\perp} H(x, 0, -\vec{\Delta}_\perp^2). \quad (7.9)$$

The helicity IPD $\tilde{\mathcal{H}}$ as well as helicity-flip IPD \mathcal{E} are defined in a similar way:

$$\tilde{\mathcal{H}}(x, \vec{b}_\perp) = \int \frac{d^2\Delta_\perp}{2\pi} e^{i\vec{\Delta}_\perp \cdot \vec{b}_\perp} \tilde{H}(x, 0, -\vec{\Delta}_\perp^2), \quad (7.10)$$

$$\mathcal{E}(x, \vec{b}_\perp) = \int \frac{d^2\Delta_\perp}{2\pi} e^{i\vec{\Delta}_\perp \cdot \vec{b}_\perp} E(x, 0, -\vec{\Delta}_\perp^2). \quad (7.11)$$

The Q^2 dependence is omitted in the notation for simplicity. The three-dimensional IPDs can be interpreted as providing a set of tomographic images of the nucleon. They provide a three-dimensional images of the nucleon in a mixed coordinate-momentum space: the plane of the impact parameter \vec{b}_\perp and the longitudinal momentum x . A qualitative picture of nucleon tomography is the following. For very small x ($x \sim 0.003$) the tomographic image shows sea quark and gluon distributions in the impact parameter space. The valence quarks surrounded by pion cloud are observed for slightly higher values of x ($x \sim 0.03$), while for large x region ($x \sim 0.3$ and higher) mostly the valence quark distributions are seen.

An example of the unpolarised IPD in an unpolarised nucleon, $q(x, \vec{b}_\perp) = \mathcal{H}(x, \vec{b}_\perp)$, calculated in the model from [30], is shown in Fig. 7.2 (left panel) for three different values of x : 0.1, 0.3 and 0.5. The unpolarised quark distribution is symmetric and the effective size of the nucleon in the impact parameter plane decreases with increasing x .

For a transversely polarized nucleon (e.g. polarized in the $+\hat{x}$ -direction) the IPD $q_{\hat{x}}(x, \vec{b}_\perp)$ is no longer symmetric due to the non-zero value of the spin-flip GPD E . This deformation is described by the gradient of the Fourier transform of E :

$$q_{\hat{x}}(x, \vec{b}_\perp) = \mathcal{H}(x, \vec{b}_\perp) - \frac{1}{2M} \frac{\partial}{\partial b_y} \mathcal{E}(x, \vec{b}_\perp). \quad (7.12)$$

Here M is the nucleon mass. The distorted u and d IPDs for a nucleon polarised in the $+\hat{x}$ -direction calculated within the model from [30] are shown in Fig. 7.2 (right panel) again for three different values of x : 0.1, 0.3 and 0.5. E and hence the details of this deformation are not very well known, but its integral over x allows one to relate the average transverse deformation:

$$d_y^q \equiv \int dx d^2b_\perp b_y q_{\hat{x}}(x, \vec{b}_\perp) q_{\hat{x}}(x, \vec{b}_\perp) = \frac{1}{2M} \int dx E^q(x, 0, 0) = \frac{\kappa^q}{2M}, \quad (7.13)$$

to the contribution from the corresponding quark flavor q to the anomalous magnetic moment:

$$\kappa_p^u = 2\kappa_p + \kappa_n = 1.673, \quad \kappa_p^d = 2\kappa_n + \kappa_p = -2.033, \quad (7.14)$$

where the subscripts p and n stand for the proton and neutron, respectively, and the values of the anomalous magnetic moments for the proton and the neutron are: $\kappa_p = 1.793$ and $\kappa_n = -1.913$. The results presented in Fig. 7.2 are model dependent but the sign and the magnitude of the shift does not rely on model predictions because of the relation to the proton/neutron anomalous magnetic moment. Positive κ_p^u implies a shift in $+\hat{y}$ -direction and negative κ_p^d a shift in the $-\hat{y}$ -direction. The size of the shift is of the order of 0.2 fm.

These significant distortions of parton distributions in impact parameter space together with final state interaction (FSI) provides a natural mechanism for the Sivers effect ². This mechanism is called "Chromodynamic lensing" and produces a Sivers asymmetry and dynamically generates k_\perp of partons inside the nucleon. Although in general FSI are very complicated, it is expected to be on average attractive thus translating a position space distortion to the left into a momentum space asymmetry to the right and vice versa. Since the primordial momentum distribution of the quarks (without FSI) must be symmetric, a qualitative connection between the primordial position space asymmetry and the momentum space asymmetry due to FSI is found. A non-zero value of the spin-flip GPD E is a source of distortion of the quark distribution in the impact parameter plane for a transversely polarized nucleon. The non-zero spin-flip E distribution requires non-zero orbital angular momentum of the quarks inside the nucleon. The spatial distortion of the quark distributions is the reflection of the presence of OAM of quarks.

Strictly speaking the Sivers mechanism presented above is only valid in mean field models for the FSI as well as in simple spectator models [276] -[278]. Furthermore, there is in general no one-to-one correspondence between the quark distributions in impact parameter space and the unintegrated parton densities (e.g. Sivers function). They are both connected by an overarching Wigner distribution [27]. They are not Fourier transforms of each other due to the Wilson gauge links in the gauge-independent definitions of the TMDs and GPDs, as was discussed in section 3.2. On the other hand, TMDs and IPDs contain complementary information about three-dimensional images of the nucleon in momenta space (TMDs) and in mixed coordinate-momentum space (IPDs).

The IPDs are transversely distorted also when one considers transversely polarised quarks in an unpolarised nucleon. This distortion leads to the Boer-Mulders asymmetry Higher-twist effects like quark-gluon correlations can also be manifested in quark transverse plane

²The importance of the FSI as a possible source of the single spin asymmetry has been discussed in [275].

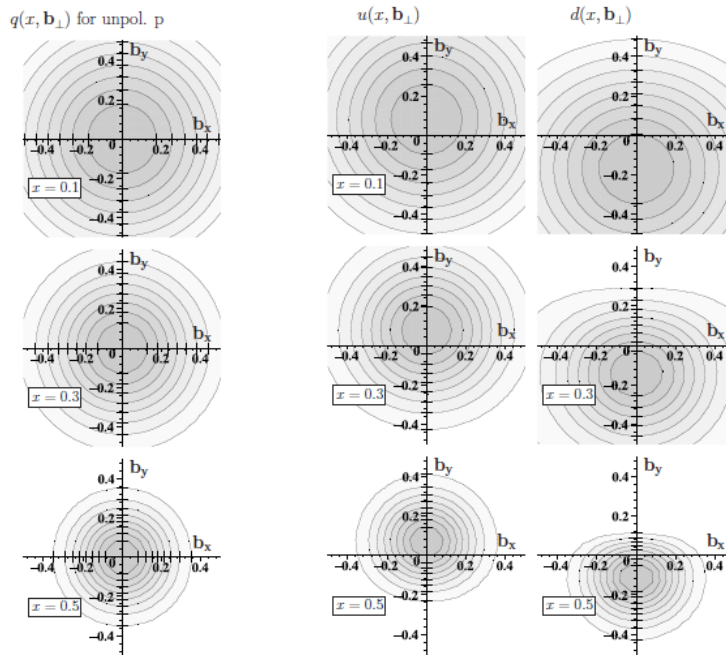


Figure 7.2: Nucleon tomography: left: The symmetric unpolarised valence quark distribution $q(x, \vec{b}_\perp)$ in an unpolarised nucleon shown for three different x values: 0.1, 0.3 and 0.5. Right: The distorted unpolarised u and d quark distributions in the nucleon polarised along $+\hat{x}$ direction. These deformations are due to non-zero value of spin-flip IPD: $\mathcal{E}(x, \vec{b}_\perp)$. (Figs are obtained in the model of [30] and taken from [274]).

distortions.

For a general discussion of parton distributions in impact parameter space and their connection to generalized parton distributions the reader is referred to Refs. [30, 199, 200, 279].

7.2 Controversy on the definition of orbital and total angular momentum

The importance of the orbital motion of the quarks and gluons is obvious in the light of the results obtained for quark and gluon polarisation measurements. However there is a controversy in QCD how to split the total angular momentum into separate quark and gluon components. The problem was recently discussed in many papers [13, 273, 280]. An extensive analysis can be found in [14]. The OAM/TAM in gauge theory, as was pointed out in [31],

should be expressed in terms of gauge invariant, local and covariant operators. A different approach has been proposed in [13, 280] where even in QED the traditional definitions of AM of electrons and photons were questioned. These two approaches lead to different results for the momentum and angular momentum carried by quarks and gluons. For example in the approach from [13, 280] the total momentum carried by gluons is asymptotically ($\mu^2 \rightarrow \infty$) equal to $1/5$ while the so-called Bellinfante definition used in Ji's sum rule (c.f. Eqs: (7.4) and (7.4)), predicts a more conventional result $1/2$. The result that half of the momentum of the nucleon is carried by gluons is very well-established one, tested over a large range of Q^2 . Therefore it is difficult to accept a much smaller prediction. On the other hand, this prediction holds for the asymptotic regime, which is still far from being accessed experimentally.

Below a short summary of the discussion about angular momentum definitions in QCD is given following the review [14]. Three versions of angular momentum operators can be defined: canonical, Bellinfante, used in Eqs (7.4) and (7.4), and as defined by Chen and collaborators in [13]. The main difference is in the field combination used in the construction of AM operators. Canonical (Noether construction from the Lagrangian) may not be gauge invariant. For example the canonical energy-momentum tensor is not gauge invariant because space-dependent gauge transformations do not commute with spatial translations. Bellinfante is built as a gauge-invariant quantity. In Chen's definition the decomposition of gauge boson field into a "physical" part (satisfying Coulomb gauge) and a "pure" field with vanishing rotation is used to construct the angular momentum operator. The corresponding formulae for all three approaches can be found in [14]. To illustrate the idea of these decompositions the formulae for the simpler QED case for electron and photon system are given in appendix 9.4.

There are two kind of problems which appear in the context of the angular momentum. They are those related to any interacting particles and those specific to gauge theories. The general problem for interacting particles (like electrons and photons or quarks and gluons) is how to split the total momentum/angular momentum into two pieces associated with momentum/angular momentum carried by the individual particles. The problem is non-trivial since the particles exchange momentum and angular momentum as a result of their interaction. For example such a splitting for momentum can be done with the canonical version of the relevant operators but these operators are not gauge invariant. The canonical angular momentum operator can be split into orbital and spin parts but the spin operator of photon/gluon field is not gauge invariant. The Bellinfante angular momentum operator is gauge invariant, but does not split into orbital and spin parts. It is generally stated that there is no gauge invariant way of splitting TAM into spin and orbital parts. The

consequence of this fact was presented in section 2.2.2 where the problem of non-existence of twist-2, gauge invariant, local gluonic operators in OPE and problems with the definition of the gluon helicity distribution ΔG were discussed. On the other hand ΔG is measured e.g. via DGLAP evolution equations. The important point is that ΔG does not measure the gluon spin in a nucleon. It measures the gluon spin in a particular gauge in a nucleon. As it was argued in section 2.2.2 for light-cone quantization, ΔG can be interpreted as the gluon helicity distribution or spin of the gluon in the axial gauge. Note that the interpretation of the experimental results is made in the framework of the QCD improved Quark Parton Model which is defined on the light-cone³. Maybe the parton model should be regarded as a picture of QCD in the axial or temporary gauge.

In the third definition of the angular momentum by Chen the spin operator is invariant but it does not make sense as a spin vector. The spin density at a point x depends on the fields throughout all space in this construction. In addition it is not known how to measure the angular momentum defined in this approach.

To conclude: the Bellifante definition seems to be the most practical one because it is gauge invariant and therefore can be directly compared with the results obtained in Lattice QCD approach. In addition, the TAM of quarks and gluons can be related to GPDs via Ji's sum rule, Eqs: (7.4) and (7.4). Very recently a similar relation between the expectation value of the transverse component of the Bellifante version of the angular momentum of a quark in a transversely polarized nucleon in terms of the GPDs H and E has been obtained [281]. The gluon angular momentum in the Bellifante version cannot be split into spin and orbital part in a gauge invariant way. The gluon helicity distribution however can be defined and interpreted as the gluon spin part in a particular gauge, e.g. the axial gauge which is a natural choice for QPM framework.

7.3 Lattice QCD results

Since the 1980's remarkable progress has been made with respect to the theoretical foundations of gauge theories on the lattice as well as with the methods and algorithms required for their numerical implementation and large scale simulations on supercomputers. As a consequence computations of the hadron spectrum can nowadays be performed in full lattice QCD (LQCD) very close to the physical pion mass, and hadron structure calculations have been pushed down to pion masses of around two times of the physical mass of $= 139$ MeV. LQCD results are by now routinely used as input for phenomenology if direct experimental

³Note that in the QCD the asymptotic states of quarks and gluons, used in perturbative calculations, do not exist.

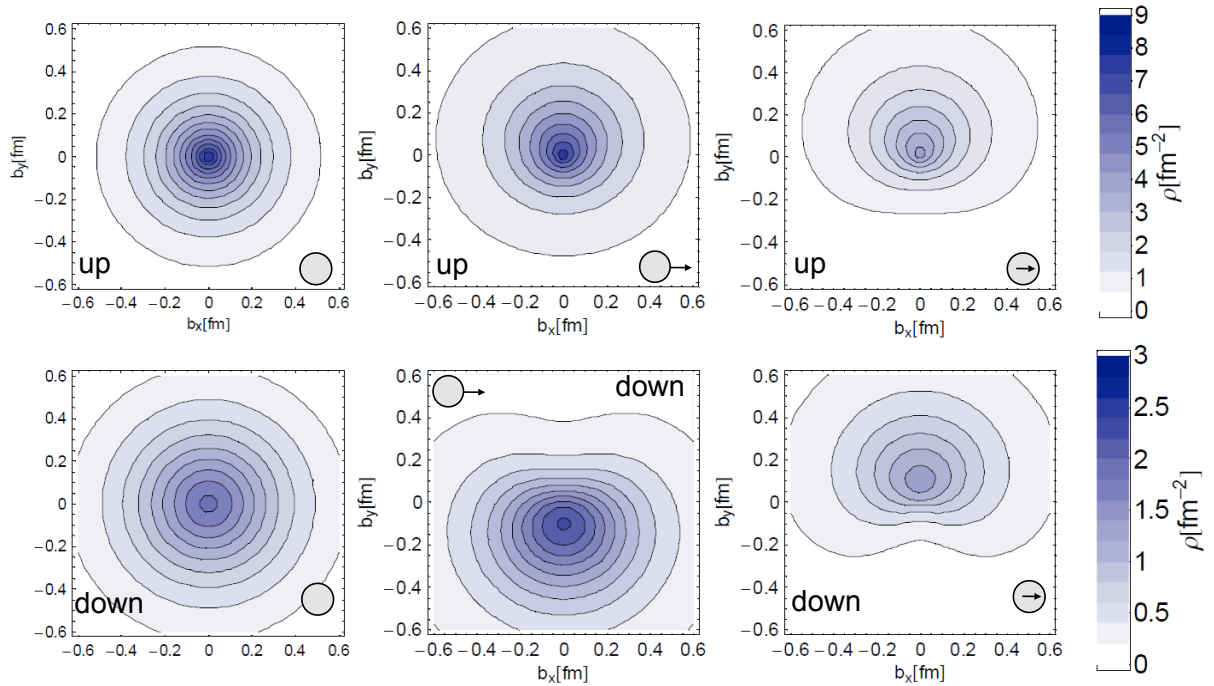


Figure 7.3: Left: u and d quark density distributions in the transverse plane for unpolarised nucleon. Middle: distorted u and d quark density distributions for transversely polarised nucleon (Sivers). Right: distorted u and d quark density distributions for transversely polarised quarks inside unpolarised nucleon (Boer-Mulders). (Figs taken from [283]).

information is not available. A review of LQCD techniques and results can be found in [43]-[45].

Nucleon structure calculations in lattice QCD are important for testing QCD as the fundamental theory of quarks and gluons and making predictions complementary to experimental efforts that aim to measure the full three-dimensional picture of the proton and nucleon. The LQCD calculations can also help in understanding the origin the nucleon spin. Lattice calculations of nucleon structure are pursued by many groups. Recent advances are described in [282].

As an example of LQCD results, the quark density distributions in the transverse plane are plotted in Fig. 7.3. The distortion of the u and d quarks similar to the deformations discussed in sec 7.1 (Fig.7.2) is clearly seen for the unpolarised quarks inside a transversely polarised nucleon (middle panel, Sivers effect) and for transversely polarised quarks inside an unpolarised nucleon (right panel, Boer-Mulders effect).

Lattice QCD has progressed to provide information about the spin fractions and OAM

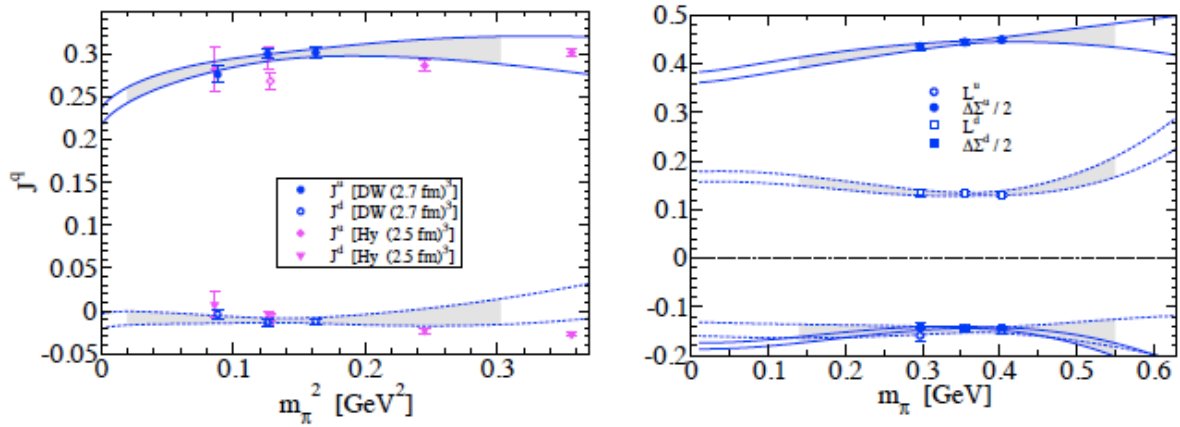


Figure 7.4: Left: u and d quark contributions to the nucleon spin from the domain wall and hybrid action calculations [284]. Right: u and d quark spin and orbital momentum from the domain wall calculations. (Figs taken from [284]).

contributions for u and d quarks in the nucleon at a typical scale $\mu^2 = 4 \text{ GeV}^2$. As an example the quark TAM and separate contributions of u and d quark spin and OAM to the proton spin as a function of the pion mass are shown in Fig.7.4. The pion masses 300 – 400 MeV are still too heavy to be realistic and the LQCD calculations shown in Fig. 7.4 have been performed with some approximations (domain wall and hybrid action calculations [284]).

The angular momentum of d quarks, J^d , is consistent with zero and the OAM and spin parts cancel out for d quarks. The u quark angular momentum is found to be: $J^u = 0.236 \pm 0.006$ [43, 286]; the OAM of u and d quarks are: $L^d \approx -L^u = 0.185 \pm 0.06$. This leads to the surprising LQCD result namely that of a cancellation between OAM of u and d quarks to a total $L^{u+d} \approx 0.030 \pm 0.012$. The LQCD result for $\Delta\Sigma$ is about 0.48, higher than observed experimentally.

Naive model calculations, as for example in the non-relativistic quark model suggests $\Delta\Sigma = 1$. As was discussed in chapter 2 relativistic effects reduce $\Delta\Sigma$ to about two thirds. In Refs [48, 287, 288] a further reduction of $\Delta\Sigma$ has been proposed by including pion cloud contributions and corrections from one gluon exchanges. With such corrections the final result for $\Delta\Sigma$ is consistent with the experimental value.

For the missing 60 – 70% of the nucleon spin an orbital angular momentum of up and down quarks should be responsible. On the other hand L^{u+d} appears to be in contrast to lattice calculations where the orbital angular momentum contribution comes out close to zero [43]. To explain this difference, it was proposed to consider the renormalization scale

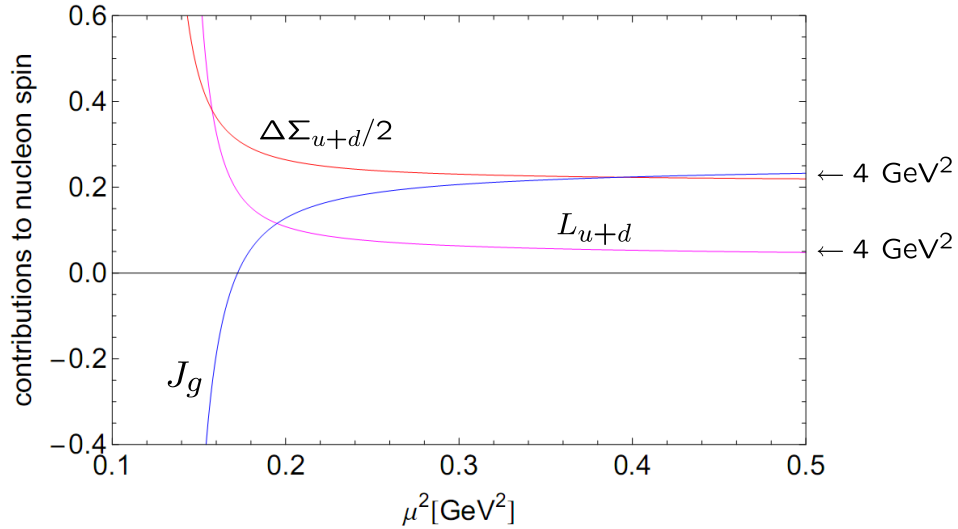


Figure 7.5: The QCD evolution (scale dependence) of the LQCD results obtained at scale $\mu^2 = 4 \text{ GeV}^2$ for $\Delta\Sigma$ and orbital angular momentum of quarks L^{u+d} . Gluons are added to satisfy nucleon spin budget. (Figs are taken from [286]).

dependence of the quantities appearing in the nucleon spin sum rule [48]. Therefore the comparison of the LQCD results with chiral model predictions requires the QCD evolution of lattice results down to the low scales characteristic of model calculations, $\mu^2 \approx 0.2 \text{ GeV}^2$.

Fig.7.5 shows the result of QCD evolution of the LQCD results concerning quark spin and OAM parts, obtained at a scale $\mu^2 = 4 \text{ GeV}^2$. The fully consistent QCD evolution equations for the orbital angular momenta of quarks and gluons at NLO accuracy can be found in [285], where a detailed comparison between LQCD results and relativistic chiral models is presented. The final values for $\Delta\Sigma$, L^q and J^q at the physical pion mass were obtained from extrapolations employing the covariant baryon chiral perturbation theory results [289]. The details of the lattice QCD simulations used in the QCD evolution can be found in [290].

The "matching" scale for the comparison between LQCD results and relativistic quark models is defined as the scale at which gluon contribution to the nucleon spin vanishes due to evolution, see Fig. 7.5⁴. The quark helicity contribution $\Delta\Sigma$ and OAM, L^{u+d} , taken at the scale $\mu^2 \approx 0.17 \text{ GeV}^2$ are equal to: $\Delta\Sigma \approx 0.62$ and $L^{u+d} \approx 0.19$, respectively. The results obtained within the relativistic quark models are very close to these values: $\Delta\Sigma \approx 0.64$ and $L^{u+d} \approx 0.18$ [286].

⁴Effective chiral QCD approximation is used in the chiral models and the pions play role of the Goldstone bosons.

On the other hand the effects from different types of improvements (related to the pion cloud effects, manifestly gauge invariant OAM operators, one-gluon exchange corrections) reduce the value of the $\Delta\Sigma$ to measured one-third, in agreement with the experimental results, and tend to make it increasingly difficult to find a common low matching scale where at least quantitative agreement with the evolved lattice results can be achieved for all of the different spin observables. Also the so-called chiral soliton model [49] gives a different results than is obtained from the LQCD + evolution. There are several reasons for these discrepancies. First, the backward QCD evolution to low scales is very sensitive to the approximation used (LO vs NLO) and to uncertainties related to the calculations of the saturated coupling constant in the small scale regime ⁵. Second; the start point to the backward evolution are LQCD results obtained at $\mu^2 \approx 4 \text{ GeV}^2$, higher than the typical value observed experimentally.

An exception is the isovector orbital angular momentum combination, L^{u-d} , for which systematic lattice errors are minimal. This quantity displays generic behavior with a sign change as it evolves from lattice QCD to low scales, in accordance with the model expectations. For a more complete discussion the reader is referred to [285] and references therein.

The LQCD results that the OAM of quarks is very close to zero seems to be in contradiction with non-zero Sivers effect observed experimentally. This difference may be related to the definitions and interpretation of the orbital angular momentum and orbital motion of quarks. The controversy on the definitions was discussed in the previous section while the possible Sivers effect interpretation as a combination of the chromodynamic lensing (FSI) and the presence of transverse distortion in the quark distributions is discussed in section 7.1. The gauge invariant Bellifante definition of angular momentum is used in LQCD computations. The interpretation of the Sivers effect is given in the framework of the quark parton model and assumes orbital motion of quarks and hence a non-zero GPD E . The gauge invariant lattice QCD angular momentum operator can be different from this related to the gradient of E GPD.

⁵The NNLO approximation in QCD evolution is also discussed in [285] together with coupling constant uncertainties.

Chapter 8

Summary and outlook

This article reviews the spin structure of the nucleon. The large part of this review focuses on the direct gluon polarisation measurements with the COMPASS experiment. The author was deeply involved in these measurements and had key responsibilities for the data analysis. The author's main contributions to the data analyses are: the application of the Artificial Neural Network in the weighted method, the application of the NLO QCD calculations to the determination of the gluon polarisation from the open-charm D meson production, the decomposition of the double helicity asymmetry and a new method to extract the gluon polarisation from the measured asymmetries for inclusive and high- p_T events in the DIS domain. These contributions are presented in detail together with new gluon polarisation results obtained from COMPASS data.

Taking into account all presently available information one can summarize the spin structure of the nucleon as follows:

Precise measurements of the longitudinal spin structure function $g_1(x, Q^2)$ show that quarks contribute only about 1/3 to the spin of the nucleon. This result is also confirmed by QCD fits (which describe data very well) and by an independent measurement of the valence quarks polarization. The valence u and d quarks are polarised longitudinally to high degree and with opposite signs.

The difference between first moment of the g_1 structure function for the proton and neutron defines the Bjorken sum rule which is confirmed by the data. This is a fundamental sum rule because it relies only on $SU(2)$ symmetry between up and $down$ quarks, or isospin invariance. Inclusive measurements allow one to conclude that the strange (anti)quark polarisation is slightly negative while SIDIS results indicate a slightly positive value. The SIDIS flavour decomposition confirms that the polarisation of the sea quarks is very small and that

the asymmetric scenario, $\Delta u = -\Delta d$, is preferred.

Direct measurements point to a small central value of the gluon polarization with large uncertainties so that spin contribution of $0.2 - 0.3$, large enough to solve the "spin crisis" cannot be excluded.

Different types of asymmetries measured with precision at RHIC also indicate that the large gluon polarization scenario is excluded. Therefore the role of axial anomaly is marginal.

The SIDIS data collected on transversely polarised targets give one an access to the transverse structure of the nucleon. The transversity distribution describes the transversely polarised quarks inside the transversely polarised nucleon. The non-zero Collins fragmentation function allows one to measure the transversity in semi-inclusive DIS.

Beyond the collinear approximation and with a finite transverse momentum of the partons inside the nucleon eight transverse momentum dependent PDFs (TMDs) are needed to fully describe the cross section at leading twist and leading order. All these functions lead to azimuthal asymmetries in the distribution of hadrons produced in SIDIS processes on transversely polarised targets and can be disentangled by measuring the different angular modulations. The T -odd Sivers function is of particular interest. This function describes a correlation between the transverse momentum of an unpolarised quark in a transversely polarised nucleon and the nucleon spin vector. The observation of a non-zero Sivers asymmetry suggests the presence of the orbital angular momentum of quarks inside nucleon.

The Collins asymmetry measured on proton targets is sizable for both positive and negative hadrons. A non-zero Sivers asymmetry is seen for positive hadrons, which persists to rather small x values. The COMPASS and HERMES results agree well. The Collins and Sivers results on deuteron targets are compatible with zero. Combined with the non-zero proton results, this suggests a cancellation between the u and d quark contributions.

The TMDs depend on the intrinsic motion of partons inside the nucleon and allow reconstruction of the "three-dimensional" nucleon structure in momentum space. The information from TMDs is combined with complementary information from IPDs - the Fourier transform of the GPDs. The three-dimensional IPDs can be interpreted as providing a set of tomographic images of the nucleon in a mixed coordinate-momentum space. Future precise measurements of TMDs and GPDs (which contains also information about the longitudinal nucleon structure) should allow one to fully reconstruct three-dimensional spin structure of the nucleon.

The observed nucleon spin deficit in the longitudinal data requires one to go beyond the collinear approximation and consider the nucleon as a three-dimensional object. The Quark Parton Model (QPM) is defined in the infinite momentum frame, where the nucleon is moving fast. The understanding that a fast moving nucleon is still a three-dimensional object with

a very rich transverse structure is one of the most important outcomes obtained in the last years. Lorentz-Fitzgerald contraction reduces the spatial size of the nucleon in the direction of its movement and allows one to describe the nucleon in the one-dimensional momentum space in terms of PDFs. However the transverse size of the nucleon is not reduced and similar to the size of the nucleon at rest. The large transverse size allows for complicated correlations e.g. between the spin and transverse motion of quarks and lead to the distortion of the quark transverse distributions (Sivers and Boer-Mulders effects). Some of these are related to the orbital motion of the quarks and gluons. For example the distortion of the quark distributions in impact parameter space together with final state interactions (chromodynamical lensing) provides a natural mechanism for a Sivers asymmetry. The distortion is generated by the spin-flip function GPD E , which is non-zero in the presence of orbital angular momentum of quarks.

Noticeable progress has been made on the lattice QCD approach in the last years. LQCD also provides information about spin fractions and orbital angular momentum contributions for u and d quarks in the nucleon. This approach links the perturbative QCD regime with the non-perturbative chiral limit of QCD, described in many models including Skyrme model and relativistic chiral models. The comparison between LQCD results and the predictions of these models is still far from being perfect and requires backward QCD evolution of the LQCD results to the typical low scale at which chiral models are defined. On the other hand the chiral models with corrections like pion clouds effect and one-gluon exchange contribution are able to reproduce the experimental results e.g. one-third of the nucleon spin carried by quarks.

LQCD results show the cancellation between large orbital angular momenta of u and d quarks (they are opposite in sign). This observation combined with the small value of the gluon polarisation and with the fact that quarks contribute only about 1/3 to the spin of the nucleon allows one to conclude, that the spin of the nucleon is effectively composed of the spins of quarks and of orbital angular momentum of the gluons. On the other hand, there is a general controversy on the definition of angular momentum of quarks and gluons. The LQCD approach is gauge-independent while the interpretation of many results is made in the framework of QPM and in a specific gauge. For example the gluon helicity distribution can be defined and interpreted as the gluon spin part in the axial gauge.

Remarkable progress has been made in the last years in the understanding of the nucleon structure on experimental as well as on theoretical grounds. It is now clear that the simple one-dimensional QPM picture has to be revised and that a complete three-dimensional description is needed. It appears that spin provides the unique opportunity to probe the inner structure of a composite system such as the nucleon.

The main experimental activity in the near future (next 5 years) will be dedicated to the precise measurement of the TMD and GPD functions. The GPDs can be accessed via Deeply Virtual Compton Scattering. The DVCS program is now under preparation at CERN (COMPASS-II proposal) and in JLAB (12 GeV program).

Longer-terms plans are connected with the construction of new electron-ion collider or electron-proton machines. The EIC machine has been proposed in USA (BNL or JLAB). The rich physical program dedicated to precise measurement of distributions of gluons and the quark sea at high energies, containing TMDs, GPDs, nucleon and nuclei tomography, QCD matter under extreme conditions and electroweak physics is discussed. (The EIC Science case: a report on the joint BNL/INT/JLab program). The preliminary studies for Electron-LHC option (eLHC machine) has already started at CERN.

In closing the largest part of the visible mass is due to the nucleons, and less than 30 MeV out of 940 MeV of the nucleon mass originates from the Higgs Boson mechanism. The remaining 97% of the nucleon mass is due to gluons which are massless. Therefore the understanding of the nucleon structure is a fundamental and very important part of elementary physics.

Chapter 9

Appendices

9.1 The helicity dependent DIS cross sections

In this section the cross sections for the DIS processes are formally expressed in the helicity basis. The presented formulae are general and only factorization into PDFs, hard process partonic cross sections, $\hat{\sigma}$, and fragmentation process is assumed. For DIS processes this factorization is proven at least up to NLO QCD approximation. For simplicity the dependence of the kinematic variables are omitted and $\sigma(\hat{\sigma})$ can be the differential or integrated cross section. Convolution integrals are denoted by \otimes . The notation used in this section is the following. p_+ (p_-) defines the PDF for parton p (quark or gluon) with helicity parallel (anti-parallel) to the helicity of the nucleon. σ_{ij} represents DIS cross section with lepton helicity state i and nucleon helicity j ($i, j = +, -$). $\hat{\sigma}_{ij}$ denotes the hard cross section for lepton-parton interaction with lepton helicity state i and parton helicity state j . For example, the cross section σ_{++} corresponds $\sigma^{\rightarrow\rightarrow}$ while σ_{+-} denotes $\sigma^{\rightarrow\leftarrow}$. The produced hadrons are assumed to be unpolarised. However in general, the fragmentation function H can depend on the helicity states of the active parton and the nucleon. A good example is the string fragmentation model [223, 142], where the potential dependence of the spin states in the fragmentation can be forced by non-standard set of fragmentation parameters. Therefore the similar notation as for cross sections is used for fragmentation function. H_{ij} describes the fragmentation process into unpolarised hadrons when the active parton with helicity i is kick out from the polarised nucleon in the j helicity state.

The four DIS cross sections for different helicity configurations can be written:

$$\begin{aligned}
\sigma_{++} &= p_+ \otimes \hat{\sigma}_{++} \otimes H_{++} + p_- \otimes \hat{\sigma}_{+-} \otimes H_{-+}, \\
\sigma_{+-} &= p_- \otimes \hat{\sigma}_{++} \otimes H_{+-} + p_+ \otimes \hat{\sigma}_{+-} \otimes H_{-+}, \\
\sigma_{-+} &= p_+ \otimes \hat{\sigma}_{-+} \otimes H_{++} + p_- \otimes \hat{\sigma}_{--} \otimes H_{-+}, \\
\sigma_{--} &= p_- \otimes \hat{\sigma}_{-+} \otimes H_{+-} + p_+ \otimes \hat{\sigma}_{--} \otimes H_{-+},
\end{aligned} \tag{9.1}$$

where $\hat{\sigma}_{-+} = \hat{\sigma}_{+-}$, $\hat{\sigma}_{++} = \hat{\sigma}_{--}$, $H_{++} = H_{--}$ and $H_{-+} = H_{+-}$. In the COMPASS experiment the two (or three) target cells with opposite polarisations are used while the beam polarisation is kept constant. Therefore the unpolarised part σ and the spin-dependent part $\Delta\sigma$ of the DIS cross sections are:

$$\begin{aligned}
\sigma &= \sigma_{++} + \sigma_{+-} = p_+ \otimes (\hat{\sigma}_{++} + \hat{\sigma}_{+-}) \otimes H_{++} + p_- \otimes (\hat{\sigma}_{++} + \hat{\sigma}_{+-}) \otimes H_{+-}, \\
\Delta\sigma &= \sigma_{++} - \sigma_{+-} = p_+ \otimes (\hat{\sigma}_{++} - \hat{\sigma}_{+-}) \otimes H_{++} - p_- \otimes (\hat{\sigma}_{++} - \hat{\sigma}_{+-}) \otimes H_{+-}.
\end{aligned} \tag{9.2}$$

The standard polarisation-averaged fragmentation functions is defined as $H = \frac{1}{2}(H_{++} + H_{+-})$ while the polarisation-dependent part is $\Delta H = H_{++} - H_{+-}$. Defining unpolarised and polarised PDFs as $p = p_+ + p_-$ and $\Delta p = p_+ - p_-$, respectively, Eq. 9.2 can be easily written as:

$$\begin{aligned}
\sigma &= p \otimes \hat{\sigma} \otimes H + \frac{1}{2}\Delta p \otimes \hat{\sigma} \otimes \Delta H, \\
\Delta\sigma &= \Delta p \otimes \Delta\hat{\sigma} \otimes H + \frac{1}{2}p \otimes \Delta\hat{\sigma} \otimes \Delta H,
\end{aligned} \tag{9.3}$$

where $\hat{\sigma} = \hat{\sigma}_{++} + \hat{\sigma}_{+-}$ and $\Delta\hat{\sigma} = \hat{\sigma}_{++} - \hat{\sigma}_{+-}$. The formulae for unpolarised and polarisation-dependent factorized DIS cross sections are obtained by neglecting ΔH .

9.2 A Neural Network approach

Artificial Neural Networks (ANN) are one of the modern methods of data analysis. Their main characteristic is an ability to learn, similar to the human brain.. Although ANN are a greatly simplified model of the human brain they are capable *e.g.* of modelling an object of unknown characteristics - parametrisation, dividing a set of objects into several groups based on their characteristics - classification, and many more.

An ANN consist of interconnected information processors (neurons). A model of the neuron that is commonly used has been introduced by McCulloch and Pitts in 1943 [291]. A state of every neuron is defined with the help of a so-called activation function, $f(x)$, which is a step function; 0 for $x < 0$ and 1 for $x > 0$. In most applications the original step function is replaced with a continuous sigmoid function like $f(x) = 1/(1 + \exp(-\beta x))$; $\beta > 0$, or a hyperbolic tangent $f(x) = \tanh(\alpha x/2) = (1 - \exp(-\alpha x))/(1 + \exp(-\alpha x))$; $\alpha > 0$. By selection of this activation function the sensitivity of the neural network to the outliers in the input data can be adjusted.

ANN are statistical models that can provide mapping from input to output parameters space. A commonly used architecture is the Multi Layer Perceptron (MLP), with neurons divided into layers. The MLP is a neural network without feedback. The signal is propagated throughout the network in one direction. The external information fed into the input layer is processed in the hidden layers and the result, produced by the output layer, is a classification of the event (or prediction) by the Network. It is worth to say that at least one hidden layer is needed for the MLP to be able to parametrise the exclusive *OR* logic function. However, already two hidden layers are sufficient to enable the network to cope with any parametrisation problem [292].

The training of an ANN is realized by the weights that are assigned to the connections between neurons. During the training procedure the Network tunes the strength of each variable-neuron and neuron-neuron connection. The strengths are obtained by minimising the squared deviation between the expected output and the actual Neural Network prediction, This training process stops when the deviation reaches a stable minimum

The data set on which the ANN is trained is randomly divided into two parts: the “training set” and the “testing set”. The network is trained using the “training set” while the “testing set” is used to monitor the training procedure. When the network errors obtained from the two sets diverge too much, the training is stopped. This prevents situations where the neural network would learn the contents of the “training set” by heart instead of finding more general patterns. The crucial drawback in using MLP for data analysis is choosing the optimal number of neurons (bias-variance problem from machine learning).

The ANN used in the analyses presented in this thesis were prepared using the NetMaker package, [231] and [263]. This package was implemented for COMPASS and for ICARUS neutrino experiment. There are two hidden layers in this Network and the number of neurons in them varies during the training process (dynamic Network). As an input for training and running ANN a set of kinematic observables like Q^2 , y , z_D , $p_T^{D^0}$, x and others have been used.

The program is written in the C#¹ language and optimised for working with large data sets. It provides a graphical interface for the network preparation and for controlling the learning process. After the process is finalised, a file containing the description of the structure of the network, including all the weights, is prepared. It is a text file written in standard XML and is subsequently used later in the COMPASS experiment analysis software.

The ANN approach guarantees that the correlations among the different observables are correctly taken into account.

9.3 NLO QCD fits of $g_1(x, Q^2)$ updated with the NLO open-charm result on $\Delta G/G$

In this section the results of the new NLO QCD fits of the polarised parton distributions, performed with inclusion of the result on $\langle \Delta G/G \rangle^{\text{NLO}}$, Eq.(5.38), obtained at a scale $\langle \mu^2 \rangle \approx 13 \text{ GeV}^2$ are presented. The results are compared with those of Ref. [8] where the gluon helicity distribution was parametrised at a reference Q^2 of 3 GeV^2 in the form

$$\Delta G(x) = \frac{\eta_G x^{\alpha_G} (1-x)^{\beta_G}}{\int_0^1 x^{\alpha_G} (1-x)^{\beta_G} dx}. \quad (9.4)$$

Here η_G is the integral of $\Delta G(x)$, $\eta_G \equiv \Delta G$. To simplify the notation the subscript G in x_G has been omitted. The same parameterization, Eq. (9.4), was used for the singlet, non-singlet quark and gluon helicity distributions except for the singlet quark in the fit with $\eta_G > 0$ where a factor $(1 + \gamma x)$ was added to allow for change of sign. The high x parameter of the gluon helicity distribution was fixed to $\beta_G = 10$. The total number of free parameters was equal to 10. The fits were performed in perturbative QCD at NLO approximation using all inclusive data with $Q^2 > 1 \text{ GeV}^2$. Two solutions with comparable χ^2 probability were found, one with $\eta_G > 0$, the other with $\eta_G < 0$.

In the new fit all the data used in [8] were employed as well as the 15 COMPASS values of A_1^p published later [68]. The reference Q^2 is kept at 3 GeV^2 and the same parameterisations, Eq. (9.4), are used. The total number of free parameters is also equal to 10.

The new open charm result is not attached to a precise value of x and thus its contribution is taken into account by the average

$$\langle R_G \rangle = \int_{0.18}^{0.47} \left[\frac{\Delta G}{G}(x, Q^2 = 13) \right] dx / (0.47 - 0.18) \quad (9.5)$$

¹C# (C sharp) is an object-oriented programming language developed by Microsoft and based on C++ syntax.

which is re-evaluated during the fit for any modification of one of the gluon or singlet quark parameters. The obtained value of $\langle R_G \rangle$ is compared to the open charm result $v_{OC} = -0.20$ with the error $\sigma_{OC} = 0.21$ and the χ^2 of the fit is incremented by $(\langle R_G \rangle - v_{OC})^2 / \sigma_{OC}^2$.

The unpolarised gluon distribution $G(x, Q^2)$ in the denominator of Eq. (9.5) is taken from the MRST04 parameterization [293]. It was used also [8]. In contrast to previous parameterizations by the same group, MRST04 predicts a slower decrease of the gluon distribution at high x , $(1-x)^\beta$ with $\beta \sim 3-4$. For this reason the choice of $\beta_G = 10$ for the fit with $\eta_G > 0$ in Ref. [8] leads to a strongly peaked distribution of $\Delta G/G$ which in turn generates a dip in the fitted distribution of $g_1^d(x)$ around $x = 0.25$ for low values of Q^2 and leads in some cases to very asymmetric errors due to the limits imposed by the positivity condition $|\Delta G(x)| \leq G(x)$. To avoid these unphysical features, β_G is now fixed to 6 in the fit with $\eta_G > 0$.

The fitted distributions of $\Delta G(x)/G(x)$, evolved to $Q^2 = 13(\text{GeV}/c)^2$ are shown in Fig. 5.19, together with error bands corresponding to the statistical errors as derived from the error matrix on the fitted parameters. The present open-charm result is within one standard deviation of the fitted curve for $\eta_G < 0$ and 2.8σ below the one for $\eta_G > 0$. The results of two other global fits, DSSV [47] and LSS [247], which employ both DIS and SIDIS asymmetries are also shown on the same plot. In case of the LSS, two solutions, with positive and with sign-changing ΔG are marked. In the DSSV fit, ΔG changes sign at $x \approx 0.1$ (unlike $G(x)$) and is about 1.5σ above the COMPASS open charm value. The LSS fit cannot distinguish between a positive and a sign-changing ΔG . Both solutions give a positive ΔG at the (x, Q^2) of the present measurement that are about 2 and 2.5σ above the value of it.

The present open charm result has practically no effect on the fit for $\Delta G < 0$, where $\eta_G = -0.32 \pm 0.11$ with- and without that measurement, while it reduces significantly the positive η_G , from $\eta_G = 0.39 \pm 0.07$ to $\eta_G = 0.24 \pm 0.09$ after it is included.

9.4 Angular momentum operator in QED

To illustrate the problem of controversy concerning the definition of quark and gluon angular momentum in QCD the formulae for the three possible angular momentum operators are presented. For simplicity the QED case is considered; the TAM is defined for electron and photon system. As discussed in section 7.2 there are three versions of angular momentum: canonical, Bellinfante and the one proposed by Chen and collaborators in [13]. The canonical angular momentum J_c for electron ψ and photon A fields can be defined as follows:

$$\begin{aligned}
\vec{J}_c &= \int d^3x \psi^\dagger \vec{\gamma} \gamma_5 \psi + \int d^3x \psi^\dagger \left[\vec{x} \times (-i\vec{\nabla}) \right] \psi + \int d^3x (\vec{E} \times \vec{A}) + \int d^3x E^i \left[\vec{x} \times \vec{\nabla} A^i \right] \\
&= \vec{S}_c^e + \vec{L}_c^e + \vec{S}_c^\gamma + \vec{L}_c^\gamma.
\end{aligned} \tag{9.6}$$

The Belfante TAM can be defined and decomposed as follows:

$$\begin{aligned}
\vec{J}_B &= \int d^3x \psi^\dagger \vec{\gamma} \gamma_5 \psi + \int d^3x \psi^\dagger \left[\vec{x} \times (-i\vec{D}) \right] \psi + \int d^3x (\vec{E} \times \vec{B}) \\
&= \vec{S}_B^e + \vec{L}_B^e + \vec{J}_B^\gamma,
\end{aligned} \tag{9.7}$$

and finally Chen's proposition is:

$$\begin{aligned}
\vec{J}_{Ch} &= \int d^3x \psi^\dagger \vec{\gamma} \gamma_5 \psi + \int d^3x \psi^\dagger \left[\vec{x} \times (-i\vec{D}_{pure}) \right] \psi + \int d^3x (\vec{E} \times \vec{A}_{phys}) \\
&+ \int d^3x E^i \left[\vec{x} \times \vec{\nabla} A_{phys}^i \right] = \vec{S}_{Ch}^e + \vec{L}_{Ch}^e + \vec{S}_{Ch}^\gamma + \vec{L}_{Ch}^\gamma.
\end{aligned} \tag{9.8}$$

As usual $D^\mu = \partial^\mu - ieA^\mu$, E and B are electromagnetic fields. In the proposition by Chen and collaborators the photon (gluon) field is decomposed as $\vec{A} = \vec{A}_{phys} + \vec{A}_{pure}$ and:

$$\vec{\nabla} \cdot \vec{A}_{phys} = 0, \quad \vec{\nabla} \times \vec{A}_{pure} = 0. \tag{9.9}$$

The Belfante definition is gauge invariant, but the splitting of the gauge boson angular momentum into a spin and orbital part is not possible. The canonical definition is not gauge invariant but the spin and orbital part can be defined separately. Chen's construction is gauge invariant and allows for splitting into spin and orbital part but the spin operator does not make sense as a spin vector. More details can be found in original papers [13, 280] and in [14].

Bibliography

- [1] W. V. Hughes, Nucl. Phys. A **518**, 371 (1990) and references therein.
- [2] EMC, J. Ashman *et al.*, Phys. Lett. B **206**, 364 (1988).
- [3] J. Ellis, R. L. Jaffe, Phys. Rev. D **9**, 1444 (1974), Phys. Rev. D **10**, 1669 (1974).
- [4] S. A. Larin, Phys. Lett. B **334**, 192 (1994).
- [5] S. L. Adler, Phys.Rev. **177** 2426 (1969), J. S. Bell and R. Jackiw, Nuovo Cim.A **60**, 47 (1969).
- [6] HERMES, A. Airapetian *et al.*, Phys. Rev.D **75**, 012007 (2007); *erratum ibid.* Phys. Rev.D **76**, 039901 (2007).
- [7] SMC, B. Adeva *et al.*, Phys. Rev.D **58**, 112001 (1998).
- [8] COMPASS, V. Yu. Alexakhin *et al.*, Phys. Lett. B **647**,8 (2007).
- [9] E155, P. L. Anthony *et al.*, Phys. Lett. B **463**,339 (1999) and references therein.
- [10] CLAS, K. V. Dharmawardane *et al.*, Phys. Lett. B **641**,11 (2006).
- [11] STAR, B. I. Abelev *et al.*, Phys. Rev. Lett. **100**, 232003 (2008).
- [12] PHENIX, A. Adare *et al.*, Phys. Rev. Lett. **103**, 012003 (2009).
- [13] X.-S. Chen, W.-M. Sun, X.-F. Lu, F. Wang, and T. Goldman *et al.*, Phys. Rev. Lett. **100**, 232002 (2008).
- [14] E. Leader, Phys.Rev. D **83**, 096012 (2011).
- [15] S. D. Bass, "*The spin Structure of the Proton*", World Scientific Publishing Co.Pte.Ltd. 2008.

-
- [16] J. C. Collins, Nucl. Phys. B **396**, 161 (1993).
- [17] BELLE, R. Seidl *et al.*, Phys. Rev. Lett. **96**, 232002 (2006).
- [18] E704, D. L. Adams *et al.*, Phys. Lett. B **261**, 201 (1991); Phys. Lett. B **264**, 462 (1991).
- [19] STAR, B. I. Abelev *et al.*, Phys. Rev. Lett. **101**, 222001 (2008).
- [20] PHENIX, S. S. Adler *et al.*, Phys. Rev. Lett. **95**, 202001 (2005).
- [21] BRAHMS, I. Arsene *et al.*, Phys. Rev. Lett. **101**, 042001 (2008).
- [22] J. Qui and G. Sterman, Phys.Rev. D **59**, 014004 (1999).
- [23] A. Bacchetta *et al.*, JHEP 0702:093 (2007).
- [24] HERMES, A. Airapetian *et al.*, Phys. Rev.Lett. **94**, 012002 (2005).
- [25] COMPASS, E. S. Ageev *et al.*, Nucl. Phys. B **765**, 31 (2007); M. Alekseev *et al.*, Phys. Lett. B **673**, 127 (2009).
- [26] COMPASS, M. Alekseev *et al.*, Phys. Lett. B **692**, 240 (2010).
- [27] G. Lorce, B. Pasquini and M. Vanverhaeghen, arXiv:1102.4704v1, (2011).
- [28] D. Sivers, Phys. Rev. D **43**, 261,(1991).
- [29] D. Müller *et al.*, Fortschr. Phys. **42**, 101 (1994), X. Ji, J.Phys. G **24**.1181 (1998), A. V. Radyushkin, Phys. Rev. D **56**, 5524 (1997).
- [30] M. Burkardt, Int.. J. Mod. Phys. A **18**, 173 (2003), Nucl. Phys. A **735**, 185 (2004), Phys. Rev. D **69**, 074032 (2004).
- [31] X. Ji, Phys. Rev. Lett. **78**, 610 (1997).
- [32] CLAS, S. Stepanyan *et al.*, Phys. Rev.Lett. **87**, 182002 (2001).
- [33] CLAS, S. Chen *et al.*, Phys. Rev.Lett. **97**, 072002 (2006).
- [34] CLAS, F. X. Girod *et al.*, Phys. Rev.Lett. **100**, 162002 (2008).
- [35] HERMES, A. Airapetian *et al.*, Phys. Rev.Lett. **87**, 182001 (2001).
- [36] HERMES, A. Airapetian *et al.*, JHEP. **06**, 066 (2008).

- [37] H1, A. Actas *et al.*, Eur. Phys. J. C **44**, 1 (2005)
- [38] HALL A/HALLA DVCS, C. Munoz *et al.*, Phys. Rev.Lett. **97**, 262002 (2006).
- [39] HALL A, M. Mazouz *et al.*, Phys. Rev.Lett. **99**, 242501 (2007).
- [40] COMPASS, *medium and long-term plans*, CERN-SPSC-2010-014.
- [41] *The Science and Experimental Equipment for 12 GeV Upgrade of CEBAF*, (2005), DOE Science Review, <http://www.jlab.org/12GeV/CDR-for-NSAC-Town-Meeting-r3.pdf>.
- [42] A. Deshpande, R. Milner, R. Venugopalan and W. Vogelsang, Ann. Rev. Nucl. Part. Sci. **55**, 165 (2005); *The Frontiers of Nuclear Science, A long range plan*, (2007), <http://www.er.doe.gov/np/nsac/docs/Nuclear-Science.Low-Res.pdf>;
- [43] Ph. Hagler *et al.*, LHPC and SESAM, Phys. Rev. D **68**, 034505 (2003), LHPC, Phys.Rev. D **77**, 094502 (2008).
- [44] Ph. Hagler, Phys. Rep. **490**, 49 (2010).
- [45] M. Altenbuchinger, Ph. Hagler, W. Weise and E. M. Henley, arXiv:1012.4409.
- [46] D. de Florian, R. Sassot, M. Stratmann and W. Vogelsang, Phys. Rev. Lett. **101**, 072001 (2008).
- [47] D. de Florian, R. Sassot, M. Stratmann, and W. Vogelsang. Phys. Rev. D **80**(3), 034030 (2009).
- [48] A. W. Thomas, Phys. Rev. Lett.**101**, 102003 (2008), Prog. Part. Nucl. Phys. **61**, 219 (2008).
- [49] M. Wakamatsu, Phys. Rev. D **77**, 074011 (2008), Phys. Rev. D **81**, 114010 (2010), Eur. Phys. J. A **46**, 32 (2010) ,Eur. Phys. J. A **44**, 297 (2010).
- [50] K. Kurek, Z. Physik, C **63**, 561 (1994).
- [51] B. Badełek, D. Bardin, K. Kurek and C. Scholtz, Z. Physik, C **66** ,248 (1995).
- [52] M. Anselmino, A. Efremov and E. Leader, Phys. Rep. **261**, 1 (1995).
- [53] R. P. Feynman, Phys. Rev. Lett. **23**, 1415 (1969).
- [54] A. V. Manohar, Proceedings of Lake Louis Winter Institute, Lake Louis, Canada 1992; ed.:B.A. Campbell *et al.*, River Edge, N.Y. World Scientific, 1992.

- [55] D. Adams *et al.*, Nucl. Instr. Meth. A **437**, 23 (1999).
- [56] P. Abbon *et al.*, Nucl. Instr. Meth. A **577**, 455 (2007).
- [57] P. Hoodbhoy, R. L. Jaffe and A. V. Manohar, Nucl. Phys. B **312**, 571 (1989)
- [58] H. Khan and P. Hoodbhoy, Phys. Lett. B **298**,181 (1993).
- [59] J. Kiryluk, Ph.D. thesis, Warsaw University (2000).
- [60] H. Burkhardt and W. N. Cottingham, Ann. Phys. (N.Y.) **56**, 453 (1970).
- [61] S. Wandzura and F. Wilczek, Phys. Lett. B **72**, 195 (1977).
- [62] E155, P. L. Anthony *et al.*, Phys. Lett. B **553**, 18 (2003).
- [63] E94-010, M. Amarian *et al.*, Phys. Lett. Lett. **92**, 022301 (2004).
- [64] E. Leader, *Spin in Particle Physics (Cambridge Monographs on Particle Physics, Nuclear Physics and Cosmology)*, Cambridge University Press, 2001.
- [65] COMPASS, V. Yu. Alexakhin *et al.*, Phys. Lett. B **647**, 330 (2007).
- [66] M. G. Doncel and E. de. Rafael, Nuovo Cimento 4 **A**, 363 (1971).
- [67] B. L. Ioffe, V. A. Khoze and L. N. Lipatov, *Hard Processes*, North Holland, (1984).
- [68] COMPASS, M. G. Alekseev *et al.*, Phys. Lett. B **690**, 466 (2010).
- [69] SMC, D. Adams *et al.*, Phys. Lett. B **336**, 125 (1994).
- [70] E143, K. Abe *et al.*, Phys. Rev. D **58**, 112003 (1998).
- [71] HERMES, A. Airapetian *et al.*, Phys. Rev. D **71**, 012003 (2005).
- [72] SMC, B. Adeva *et al.*, Phys. Rev. D **60**, 072004 (1999);*erratum ibid.*.D **62**, 079902 (2000).
- [73] EMC, J. Ashman *et al.*, Nucl. Phys. B **328**, 1 (1989).
- [74] E155, P.L. Anthony *et al.*, Phys. Lett. B **493**, 19 (2000).
- [75] J. D. Bjorken and E. A. Paschos, Phys. Rev. **185**(5), 1975 (1969).
- [76] J. D. Bjorken, Phys. Rev.**175** (5), 1547 (1969).

- [77] F. Halzen and A. D. Martin, *Quarks and leptons. An Introductory Course in Modern Particle Physics*, John Wiley and sons, N.Y. 1984.
- [78] R. G. Roberts, *The structure of the proton*, Cambridge University Press, 1990.
- [79] R. P. Feynman, *Photon-Hadron Interaction*, W.A. Benjamin Inc., Advanced Book Program 1972.
- [80] Y. L. Dokshitzer, *Sov. Phys. JETP* **46**, 641(1977).
- [81] B. Lampe and E. Reya, *Phys. Rep.* **332**, 1 (2000)
- [82] G. 't Hooft and M. J. G. Veltman, *Nucl.Phys. B* **44**, 189 (1972).
- [83] H-Y. Cheng, *Int. J. Mod. Phys.A* **11**, 5109 (1996).
- [84] R. D. Ball, S. Forte and G. Ridolfi, *Phys. Lett. B* **378**, 255 (1996).
- [85] E. Leader, A. V. Sidorov and D. B. Stamenov, *Phys. Lett. B* **445**, 232 (1998).
- [86] G. Altarelli *et al.*, *Nucl. Phys. B* **143**, 521 (1978); *erratum ibid.* **B 146**, 544 (1978).
- [87] V. N. Gribov and L. N. Lipatov, *Sov.J. Nucl. Phys.* **15**, 438 (1972).
- [88] G. Altarelli and G. Parisi, *Nucl. Phys. B* **126**(2), 298 (1977).
- [89] C. G. Calla and D. J. Gross, *Phys. Rev. Lett.* **22**, 156 (1969).
- [90] M. Glück, E. Reya and W. Vogelsang, *Nucl. Phys. B* **351**, 579 (1991).
- [91] C. Bourrely, J. P. Guillet and P. Chiappetta, *Nuovo Cim. A* **103**, 1337 (1990).
- [92] W. Greiner and A. Schäfer, *Quantum Chromodynamics*, Springer-Verlag, 2-nd edition, 1995.
- [93] R. Mertig and W. L van Neerven, *Z.Phys. C* **70**, 637 (1996); W. Vogelsang, *Phys. Rev. D* **54**, 2023 (1996).
- [94] J. Kodaira, S. Matsuda, T. Muta, K. Sasaaki and T. Uemastu, *Phys. Rev. D* **20**, 627 (1979); J. Kodaira, *Nucl. Phys. B* **165**, 129 (1980).
- [95] E. A. Kureev, L. N. Lipatov and V. Fadin, *Sov. Phys. JETP* **45**, 199 (1977); Ya. Balitskij and L. N. Lipatov, *Sov. J. Nucl. Phys.* **28**, 822 (1978).

- [96] P. D. B. Collins, *Introduction to Regge theory*, Cambridge University Press, 1977.
- [97] F. E. Close and R. G. Roberts, Phys. Lett. B **336**, 257 (1994).
- [98] M. A. Ahmed and G. G. Ross, Phys. Lett. B **56**, 385 (1975).
- [99] J. Bartels, B. I. Ermolaev and M. G. Ryskin, Z. Phys. C **70**, 273 (1996); *ibid.* C **72**, 627 (1998).
- [100] B.I. Ermolaev, M. Greco and S. I. Troyan, Phys. Lett. B **622**, 93 (1999).
- [101] B. Badełek and J. Kwieciński, Phys. Lett. B **418**, 229 (1998).
- [102] J. Kwieciński and B. Ziaja, Phys. Rev.D **60**, 054004 (1999).
- [103] B. Badełek, J. Kiryluk and J. Kwieciński, Phys. Rev.D **61**, 014009 (2000).
- [104] E. Leader, A. V. Sidorov and D. B. Stamenov, Phys. Rev. D **73**, 034023 (2006) .
- [105] G. Farrar and D. R. Jackson, Phys. Rev. Lett. **35**, 1416 (1975).
- [106] H. Avakian, S. J. Brodsky, A. Deur and F. Yuan, Phys. Rev. Lett. **99**, 082001 (2007).
- [107] S. J. Brodsky and I. A. Schmidt, Phys. Lett. B **234**, 144 (1990).
- [108] E97-110, V. Sulkosky, talk given at XVI International Workshop on Deep-Inelastic Scattering and Related Subjects, DIS 2008, 7-11 April 2008, University College London; Ph.D. thesis, College of William and Mary (2007).
- [109] E142, P.L. Anthony *et al.*, Phys. Rev.D **54**, 6620 (1996).
- [110] JLAB Hall A, X. Zheng *et al.*, Phys. Rev. Lett. **92**, 012004 (2004); Phys. Rev.C **70**, 065207 (2004).
- [111] HERMES, K. Ackerstaff *et al.*, Phys. Lett. B **404**, 383 (1997).
- [112] E154, K. Abe *et al.*, Phys. Rev. Lett. **79**, 26 (1997).
- [113] SMC, B. Adeva *et al.*, Phys. Rev.D **62**, 079902 (2000).
- [114] J. D. Bjorken, Phys. Rev. **148**, 1467 (1969); Phys. Rev. D **1**, 1376 (1970).
- [115] Y. Goto *et al.*, Phys. Rev.D **62**, 034017 (2000).
- [116] E. Leader and D. Stamenov, Phys. Rev. D **67**, 037503 (2003).

- [117] C. Amsler *et al.*, (Particle Data Group Collaboration). Phys. Lett. B **667**, 1 (2008).
- [118] A. L. Kataev and V. Starshenko, Mod. Phys. Lett. A **10**, 235 (1995).
- [119] W. A. Bardeen, A. J. Buras, D. W. Duke and T. Muta. Phys. Rev. D **18** (11), 3998 (1978).
- [120] S. A. Larin, T. van Ritbergen and J. A. M. Vermaseren, Phys. Lett. B **404**, 153 (1997).
- [121] R. Machleidt *et al.*, Phys. Rep. **149**, 1 (1987).
- [122] R. L. Jaffe, Phys. Lett. B **365**, 359 (1996).
- [123] A. V. Manohar, Phys. Rev. Lett. **65**, 2511 (1990).
- [124] G. Altarelli and G. G. Ross, Phys. Lett. B **212**, 391 (1988).
- [125] R. D Carlitz, J. C. Collins and A. Mueller, Phys. Lett. B **214**, 229 (1988).
- [126] A. V. Efremov and O. Teryaev, JINR report E2-88-287, Dubna 1988.
- [127] S. D. Bass, B. L. Joffe, N. N. Nikolaev and A. W. Thomas, J. Moscow Phys. Soc. **1**, 317 (1991).
- [128] J. Bartelski and S. Tatur, Acta Phys. Polon. B **33**, 2673 (2002); B **34**, 2731 (2003); B **35**, 647 (2004).
- [129] C. Bourrely, F. Bucella and J. Soffer, Phys. Lett. B **648**, 39 (2007) and references therein; arXiv:1008.5322.
- [130] S.B. Gerasimov, Yad. Fiz **2**, 598 (1965).
- [131] S. D. Drell and A. C. Hearn, Phys. Rev. Lett. **16**, 908 (1996).
- [132] GDH, J. Ahrens *et al.*, Phys. Rev. Lett. **84**, 5950 (2000); Phys. Rev. Lett. **87**, 022003 (2001); Phys. Rev. Lett. **88**, 232002 (2002).
- [133] GDH, H. Dutz *et al.*, Phys. Rev. Lett. **91**, 192001 (2003); Phys. Rev. Lett. **94**, 162001 (2005).
- [134] L. Łukaszuk, Nucl. Phys. A **709**, 289 (2002).
- [135] K. Kurek and L. Łukaszuk, Phys. Rev. C **70**, 065204 (2004).

- [136] L. L. Frankfurt *et al.*, Phys. Lett. B **230**, 141 (1989).
- [137] SMC, B. Adeva *et al.*, Phys. Lett. B **369**, 93 (1996).
- [138] E. Christova and E. Leader, Nucl. Phys. B **607**, 369 (2001).
- [139] A. N. Sissakian, O. Yu. Shevchenko and O. N. Ivanov, Phys. Rev. D **73**, 094026 (2006).
- [140] COMPASS, M. Alekseev *et al.*, Phys. Lett. B **660**, 458 (2008).
- [141] SMC, B. Adeva *et al.*, Phys. Lett. B **420**, 180 (1998).
- [142] T. Sjöstrand, Comp. Phys. Commun. **39**, 347(1986); **43**, 367 (1987).
- [143] A. Kotzinian, Phys. Lett. B **552**, 172 (2003).
- [144] A. Kotzinian, Eur. Phys. J. C **44**, 211 (2005).
- [145] S. D. Bass, Eur. Phys. J. A **5**, 17 (1999); Rev. Mod. Phys. **77**, 1257 (2005).
- [146] C. Bourrely, F. Buccella and J. Soffer, Eur. Phys. J. C **41**, 327 (2005).
- [147] J. C. Peng, Eur. Phys. J. A **18**, 395 (2003).
- [148] D. de Florian, G. A. Navarro and R. Sassot, Phys. Rev. D **71**, 094018 (2005).
- [149] COMPASS, M. Alekseev *et al.*, Phys. Lett. B **680**, 217 (2009).
- [150] COMPASS, M. Alekseev *et al.*, Phys. Lett. B **693**, 227 (2010).
- [151] EMC, M. Arneodo *et al.*, Nucl. Phys. **B321**, 541 (1989).
- [152] R. S. Bhalerao, Phys. Rev. C **63**, 025208 (2001).
- [153] M. Wakamatsu, Phys. Rev. **D67**, 034005 (2003).
- [154] A. D. Martin, W. J. Stirling and R. S. Thorne, Phys.Lett. B **636**, 259 (2006).
- [155] D. de Florian, R. Sassot and M. Stratmann, Phys. Rev. **D75**, 114010 (2007).
- [156] A. Sissakian, O. Shevchenko and O. Ivanov, Eur. Phys. J. C **65**, 413 (2010).
- [157] S. D. Bass and A. W. Thomas, Phys. Lett. B **684**, 216 (2010).
- [158] S. Kretzer, Phys. Rev.D **62**, 054001 (2000).

- [159] C. Bourrely, J. Soffer and F. Buccella, Eur. Phys. J. C **23**, 487(2002).
- [160] S. Kumano and M. Miyama, Phys. Rev. D **65**, 034012. (2002).
- [161] J. Bartelski and S. Tatur, Phys.Rev. D **81**, 054013 (2010).
- [162] J. Bartelski and S. Tatur, Phys.Rev. D **71**, 014019 (2005).
- [163] G Bunce, N. Saito, J. Soffer and W. Vogelsang, Ann. Rev. Nucl. Part. Sci. **50**, 525 (2000).
- [164] D0, W.M. Abazow *et al.* Phys. Rev. Lett. **101**, 211801 (2008).
- [165] F.Abe *et al.* Phys. Rev. Lett. **74**, 850 (1995).
- [166] F.Abe *et al.* Phys. Rev. Lett. **81**, 5754 (1998).
- [167] B. Kamal, Phys. Rev.D **57**, 6663 (1998).
- [168] T. Gehrmann, Nucl. Phyc. B **534**, 21(1998).
- [169] STAR, M. M. Aggarwal *et al.*, Phys. Rev. Lett. **106**, 062002 (2011).
- [170] PHENIX, A. Adare *et al.*, Phys. Rev. Lett. **106**, 062001 (2011).
- [171] D. de Florian and W. Vogelsang, Phys. Rev.D **81**, 094020 (2010).
- [172] MIT-Bates, D. T. Spyde *et al.*, Phys. Rev. Lett. **84**, 1106 (2000).
- [173] S. J. Brodsky, J. Ellis and M. Karliner, Phys. Lett. B **206**, 309 (1998).
- [174] V. Baronne, A. Drago and P. G. Ratcliffe, Phys. Rep. **359**, 1 (2002).
- [175] J. P. Ralston and D. E. Soper, Nucl. Phys. B **152**, 109 (1979).
- [176] X. Artru and M. Mekhfi, Z. Physik,C **45**, 669 (1990).
- [177] R. L. Jaffe and X. Ji, Nucl. Phys. B **375**, 527 (1992).
- [178] M. Anselmino, V. Barone, A. Drago and N. N. Nikolaev, Phys. Lett. B **594**, 97 (2004).
- [179] PAX, V. Barone *et al.*, arXiv:hep-ex/0505054, (2005).
- [180] A. V. Efremov, K. Goeke and P. Schweitzer, Eur. Phys.J. C **35**, 207 (2004).
- [181] R. L. Jaffe, arXiv:hep-ph/0102281, (2001).

- [182] R. Enberg, B. Pire and L. Szymanowski, Eur. Phys. J. C **47**, 87 (2006).
- [183] M. E. Beiyad, B. Pire, M. Segond, L. Szymanowski and S. Wallon, Phys. Lett. B **688**, 154 (2010).
- [184] B. Ermolaev, R. Kirschner and L. Szymanowski, Eur. Phys. J. C **7**, 65 (1999).
- [185] J. Soffer, Phys. Rev. Lett. **74**, 1292 (1995).
- [186] M. Anselmino *et al.*, Phys. Rev. D **75**, 054032 (2007).
- [187] M. Anselmino *et al.*, Nucl. Phys. Proc. Suppl. **191**, 98 (2009).
- [188] A. Kotzinian, Nucl. Phys. B **441**, 234 (1995).
- [189] P. J. Mulders and R. D. Tangerman, Nucl. Phys. B **461**, 197 (1996). *erratum ibid.* B **484**, 538(1997).
- [190] A. Bacchetta *et al.*, JHEP **0702**, 093 (2007).
- [191] COMPASS, M. Alekseev *et al.*, Phys. Lett. B **673**, 127 (2009).
- [192] HERMES, A. Airapetian *et al.* Phys. Rev. Lett. **103**, 152002 (2009).
- [193] HERMES, A. Airapetian *et al.* ,Phys. Lett. B **693**, 11 (2010).
- [194] X. Qian, Ph.D. thesis, Duke University, 2010. Hall A, X. Qian *et al.* Phys. Rev. Lett. **107**, 072003 (2011).
- [195] H. Gao *et al.* Eur. Phys. J. Plus **126**, 2 (2011).
- [196] X. Ji, Phys. Rev. Lett. **91**, 062001 (2003).
- [197] S. Meissner, A. Metz, M. Schlegel and K. Goeke, JHEP **0808**, 038 (2008).
- [198] S. Meissner, A. Metz and M. Schlegel, JHEP **0908**, 056 (2009).
- [199] D. E. Soper, Phys. Rev. D **15**, 1141 (1977).
- [200] M. Burkardt, Phys. Rev. D **62**, 071503, (2000). *erratum ibid.* D **66**, 119903(2002).
- [201] D. Boer and P.J. Muders, Phys. Rev.D **57**, 5780 (1998).
- [202] M. Anselmino *et al.* Phys. Rev. D **73**, 014020 (2006).

- [203] E. Sichtermann and M. Liu, talks given at RIKEN BNL Research Center Workshop: Opportunities for Drell-Yann Physics at RHIC, May 11-13, 2011, Brookhaven National Laboratory.
- [204] H. Avakian *et al.* Phys.Rev.D **77**, 014023 (2008).
- [205] The EIC Science case: a report on the joint BNL/INT/JLab program, editors: D.Boer, M.Diehl, R.Milner,R.Venugopalan and W. Vogelsang, arXiv:1108.1713 [nucl-th].
- [206] C. J. Bomhof, P. J. Mulders and F. Pijlman, Nucl. Phys. B **596**, 277 (2004), Eur. Phys. J. C **47**, 147 (2006).
- [207] A. Bacchetta, C. J. Bomhof, P. J. Mulders and F. Pijlman, Phys. Rev. D **72**, 034030 (2005).
- [208] C. J. Bomhof and P. J. Mulders, Nucl. Phys. B **795**, 409 (2008), JHEP **02**, 029 (2007).
- [209] J. Collins and J. W. Qui, Phys. Rev. D **75**, 114014 (2007).
- [210] T. C. Rogers and P. J. Mulders, Phys. Rev. D **81**, 094006 (2010).
- [211] Z.Kang, J-W Qiu, W. Vogelsang and F. Yuan, Phys. Rev. D **83**, 094001 (2011).
- [212] N. Doble *et al.*, Nucl. Instrum. Meth. A **343**, 351 (1994) .
- [213] A.A. Akhundov, *et al.*, Fortschr. Phys. **44**, 373 (1996).
- [214] P. Abbon *et al.*, *Particle identification with COMPASS RICH-1*, Nucl. Instr. Meth. A, in press (2011).
- [215] SMC, B. Adeva *et al.*, Phys. Rev. D **70**, 012002 (2004).
- [216] HERMES, A. Airapetian *et al.*, Phys. Rev. Lett. **84**, 2584 (2000);
- [217] HERMES, A. Airapetian *et al.*, JHEP **08**, 130 (2010).
- [218] COMPASS, E.S. Ageev *et al.* Phys. Lett. B **633**, 25 (2006).
- [219] COMPASS, M.G. Alekseev *et al.*, Phys. Lett. B **676**, 31 (2009).
- [220] EMC, J.J. Aubert *et al.*, Nucl. Phys. B **213**, 31(1983).
- [221] B. W. Harris, J. Smith and R. Vogt, Nucl. Phys. B **461**, 181(1996).

- [222] COMPASS, M.G. Alekseev *et al.*, in preparation.
- [223] T. Sjöstrand *et al.*, JHEP **0605**, 026 (2006) and references therein.
- [224] A. D. Watson, Z. Phys. C **12**, 123 (1982).
- [225] A. Bravar, K. Kurek and R. Windmolders, Comput. Phys. Commun. **105**, 42 (1997).
- [226] C. Franco, PhD thesis, IST, Universidade Técnica de Lisboa, 2011.
- [227] G. Ingelman *et al.*, Comput. Phys. Commun. **101**, 135 (1997);
see <http://www.isv.uu.se/thep/aroma> for recent updates.
- [228] J. Pretz, to appear in Nucl. Instrum. Meth. A (2011), arXiv:1104.1038v1.
- [229] J. Pretz J and J-M Le Goff, Nucl. Instr. Meth. A **602**, 594 (2009).
- [230] R. Brun *et al.* *GEANT detector description and simulation tool: CERN Program Library Long Writeup* Technical Report W5013 CERN, (1994);
<http://consult.cern.ch/writups/geant>.
- [231] R. Sulej, K. Zaremba, K. Kurek and E. Rondio, Meas. Sci. Technol. **18**, 2486 (2007).
- [232] J-M le Goff and F. Robinet, Compass internal note 2007-8, see
<http://wwwcompass.cern.ch>;
- [233] F. Robinet, PhD thesis, Universite Paris Diderot, Paris 7, UFR de Physique, CEA Saclay, 2008.
- [234] S.J. Brodsky, C. Peterson and N. Sakai, Phys. Rev. D **23**, 2745 (1981).
- [235] J. Alwall, extended version of the talk given at the XIIIth Int. Workshop on Deep Inelastic Scattering, Madison, 2005, arXiv:hep-ph/0508126;
J. Alwall and G. Ingelman, Phys. Rev. D **71**, 094015 (2005).
- [236] ZEUS, S. Chekanov *et al.*, Eur. Phys. J. C **65**, 65 (2010);
H1, F.D. Aaron *et al.*, Phys. Lett. B **686**, 91 (2010).
- [237] H. Jung, Comp. Phys. Comm. **86**, 147 (1995); update:
<http://www.desy.de/~jung/rapgap/> .
- [238] <http://durpdg.dur.ac.uk/HEPDATA/PDF>; projects.hepforge.org/lhapdf/.

- [239] K. Klimaszewski, Ph.D. thesis, Andrzej Sołan Institute for Nuclear Studies, Warsaw, (2010).
- [240] COMPASS, M.G. Alekseev *et al.*, in preparation.
- [241] W. Beenakker, H. Kuijf, W.L. Neerven and J. Smith, Phys. Rev. D **40**, 54 (1989); J. Smith and W.L. Neerven Nucl. Phys. B **374**, 36 (1992).
- [242] I. Bojak and M. Stratmann, Phys. Lett. B **433**, 411 (1998); Nucl. Phys. B **540**, 345 (1999) ; I. Bojak, PhD thesis, University of Dortmund, 2000.
- [243] EMC, J.J. Aubert *et al.*, Phys. Lett. B **167**, 127 (1986).
- [244] BELLE, R. Seuster *et al.*, Phys. Rev. D **73**, 032002 (2006).
- [245] D. de Florian, P. Nadolsky, V. Vogelsang, Berkeley Summer Program on Nucleon Spin Physics June 1-12, 2009, Private communications. See e.g. S. Frixione, B.R. Webber, Cavendish-HEP-08/14, P.Nasson, hep-ph/0409146v1.
- [246] T. Toll, PhD thesis, <http://www-h1.desy.de/psfiles/theses/h1th-519>, (2010).
- [247] E. Leader, A.V. Sidorov and D.B. Stamenov, Phys. Rev. D **82**, 114018 (2010).
- [248] A.D. Martin, R.G. Roberts, W.J. Stirling and R.S.Thorne, Eur. Phys. J. C **4**, 463 (1998).
- [249] E687, P.L. Frabeltti *et al.* Phys. Lett. B **370**, 222 (1996).
- [250] SELEX, M. Iori, Nucl. Phys. B **115**, 103(2003); SELEX, M. Kaya *et al.* Phys. Lett. B **558**, 34 (2003).
- [251] WA82, M. Adamovich *et al.* Phys. Lett. B **305**, 402 (1993); WA89, M. Adamovich *et al.* Eur. Phys. J. C **13**, 247 (2000).
- [252] WA769, G.A. Alves *et al.*, Phys. Rev. Lett. **72**, 812 (1994).
- [253] E791, E.M.Aitala *et al.* Phys. Lett. B **411**, 230 (1997).
- [254] A.M. Halling, Il Nuovo Cim. A **109**,no 6-7, 617 (1996).
- [255] A. Zwyagin, PhD thesis, Ludwig-Maximilians-Universitt, Mnchen, 2010.
- [256] P.Renton and W.S.C.Williams, Ann. Rev. Nucl. Sci., **31**,193 (1981).

- [257] A. Bravar, D.von Harrach and A. Kotzinian, Phys.Lett. B **421**, 349 (1998).
- [258] L. Silva, PhD Thesis, IST, Univ. Técnica de Lisboa, submitted 2011.
- [259] B. Jager, M. Stratmann and W. Vogelsang, Phys. Rev. D **68**, 114018 (2003).
- [260] B. Jager, M. Stratmann and W. Vogelsang, Eur. Phys. J. C **44**, 533 (2005).
- [261] G. Ingelman, A. Edin and J. Rathsman, Comput. Phys. Commun. **101** , 108 (1997).
- [262] COMPASS, E.S. Ageev *et al.*, Phys. Lett. B **612**, 154 (2005).
- [263] R. Sulej, <http://www.ire.pw.edu.pl/rsulej/NetMaker>.
- [264] A.D.Martin, W.J. Stirling, R.S. Thorne and G. Watt, Eur. Phys. J. **C64** ,653 (2009).
- [265] A. A. Akhundov *et al.*, Fortschr. Phys. **44**, 373 (1996).
- [266] CTEQ, H.L. Lai *et al.*, Eur. Phys. J. **C12**, 375 (2000).
- [267] E143, K. Abe *et al.*, Phys. Lett. B **452**, 194 (1999).
- [268] HERMES, A. Airapetian *et al.*, Phys. Lett. B **684**, 114 (2010). A.Kotzinian, Eur. Phys. J. C **44**, 211 (2005).
- [269] C.Bernet, PhD Thesis, Univ. Paris 7, Denis Diderot, Paris, 2005.
- [270] S. Procureur, PhD Thesis, Univ. Paris XI, U.F.R. Scientifique d'Orsay, Paris, 2006.
- [271] K. Goeke, M. V. Polyakov and M. Vanderhaeghen, Prog. Part. Nucl. Phys. **47**, 401, (2001).
- [272] M.Vanderhaeghen, P.A.M.Guichon and M. Guidal, Phys. Rev. Lett. **80**, 5064 (1998); Phys. Rev. D **60**, 094017 (1999).
- [273] M. Wakamatsu, Phys. Rev. D **81**, 114010 (2010).
- [274] M. Burkhardt, talk given at International Workshop on Hadron Structure and Spectroscopy, Paris, 4-6 April, 2011.
- [275] S.J. Brodsky, D.S. Hwang and I. Schmidt, Phys. Lett. B **530**, 99 (2002).
- [276] S.J. Brodsky, D.S. Hwang, and I. Schmidt, Nucl. Phys. B **642**, 344 (2002);

- [277] M. Burkardt and D.S. Hwang, Phys. Rev. D **69**, 074032 (2004); D. Boer, S.J. Brodsky and D.S. Hwang, Phys. Rev. D **67**, 054003 (2003); D. Boer *et al.*, Phys. Rev. D **67**, 054003 (2003).
- [278] L.P. Gamberg *et al.*, Phys. Rev. D **67**, 071504 (2003); L.P. Gamberg *et al.*, Phys. Rev. D **67**, 071504 (2003); A. Bacchetta *et al.*, Phys. Lett B **578**, 109 (2004).
- [279] M. Diehl, Eur. Phys. J. C **25**, 223 (2002).
- [280] X.-S. Chen, W.-M. Sun, X.-F. Lu, F. Wang, and T. Goldman, arXiv:0911.0248. 287 (1976);
I. V. Tyutin, Lebedev Institute preprint 39 (1975) (unpublished).
- [281] E. Leader, arXiv:1109.1230v2, (2011).
- [282] Y. Aoki, T. Blum, H.-W. Lin, S. Ohta, S. Sasaki *et al.*, Phys. Rev. D **82**, 014501(2010); T. Yamazaki *et al.*, Phys. Rev. D **79**, 114505 (2009); A. Lenz, M. Gckeler, T. Kaltenbrunner, and N. Warkentin, Phys. Rev. D **79**, 093007 (2009).
- [283] QCDSF, M. Gockeler *et al.*, Phys. Rev. Lett. **92**, 042002 (2004); Phys. Rev. Lett. **98**, 222001 (2007).
- [284] LHPC DW, S. N. Sirytsyn *et al.*, arXiv:1111.0718, (2011).
- [285] M. Altenbuchinger, Ph. Hagler, W. Weise and E. M. Henley, arXiv:1012.4409v2.
- [286] Ph. Hagler, Talk given at Nucleon Spin Physics Summer Program at Brookhaven National Laboratory, July 14-27 2010.
- [287] F. Myhrer and A. W. Thomas, Phys. Lett. B **663**, 302 (2008).
- [288] A. W. Thomas, Int. J. Mod. Phys. E **18**, 1116 (2009).
- [289] M. Dorati, T. A. Gail and T. R. Hemmert, Nucl. Phys. A **798**, 96 (2008).
- [290] LHPC, J. D. Bratt *et al.*, Phys. Rev. D **82**, 094502 (2010).
- [291] W. S. McCulloch, Biulletin of Mathematical Biophysics **5**, 115 (1943).
- [292] M. Leshno, V. Y. Lin, A. Pinkus and S. Schocken, Neural Networks **6**, 861 (1993).
- [293] A.D. Martin, R.G. Roberts, W.J. Stirling and R.S.Thorne, Phys.Lett. B **604**, 61 (2004).

Acknowledgements

I am grateful to the many persons who directly or indirectly contributed to the analysis and allow me to deeper understood spin physics. In particular, thanks go to Ewa Rondio for constant support and help. Many thanks to [Jan Nassalski](#), Barbara Badełek, Andrzej Sandacz, Marcin Stolarski (for teaching me how unexpected statistics can be) and Konrad Klimaszewski. A very special thanks go to Ernst Sichtermann for his criticism and suggestions and for nice discussions on physics.

The work would not have been possible without the effort of many people in the COMPASS Collaboration, impossible to name all of them. I would like in particular to thank Eva Kabuss, Jean-Marc le Goff, Jorg Pretz, Alain Magnon, Yann Bedfer, Gerhard Mallot and Roland Windmolders - my colleagues from the SMS and COMPASS Collaborations.

I would like to thank Eliot Leader, Mauro Anselmino, Marco Stratmann, Werner Vogelsang, Marcus Diehl, Barbara Pasquini and Philippe Hägler for fruitful discussions about the theoretical and phenomenological aspects of the spin physics. Many thanks to Elke Aschenauer, Feng Yuan and Ernst for giving me an opportunity to participate in two fantastic workshops dedicated to Nucleon Spin Physics and organized in Lawrence Berkeley National Laboratory and in Brookhaven National Laboratory.

A very special thanks to [Leszek Łukaszuk](#), my teacher and my friend, for his patience and support and for showing me how wonderful and deep physics can be.

Many thanks to all my friends who supported my work.

I would like also to thank CERN Laboratory for hospitality during my stays.